Heinrich Heine
Universität
Düsseldorf

Synthesis and characterization of nano- and microsized MIL-101Cr for mixed-matrix membranes

Inaugural-Dissertation

zur Erlangung des Doktorgrades
der Mathematisch-Naturwissenschaftlichen Fakultät
der Heinrich-Heine-Universität Düsseldorf

vorgelegt von

Irina Gruber
aus Kumsangirskij

Düsseldorf, September 2020

aus dem Institut für Anorganische Chemie und Strukturchemie I
der Heinrich-Heine-Universität Düsseldorf

Gedruckt mit der Genehmigung der
Mathematisch-Naturwissenschaftlichen Fakultät der
Heinrich-Heine-Universität Düsseldorf

Berichterstatter:

1. Prof. Dr. Christoph Janiak

2. PD. Dr. Birger Dittrich

Tag der mündlichen Prüfung:

Die vorliegende Arbeit wurde in der Zeit von Oktober 2014 bis September 2020 an der Heinrich-Heine-Universität Düsseldorf im Institut für Anorganische Chemie und Strukturchemie I im Arbeitskreis von Prof. Dr. Christoph Janiak angefertigt.

Eidesstattliche Erklärung

Ich versichere an Eides statt, dass die Dissertation von mir selbstständig und ohne unzulässige fremde Hilfe unter der Beachtung der „Grundsätze zur Sicherung guter wissenschaftlicher Praxis“ an der Heinrich-Heine-Universität Düsseldorf erstellt worden ist. Die aus fremden Quellen direkt oder indirekt übernommenen Gedanken sind als solche kenntlich gemacht. Die Arbeit wurde bisher weder im Inland noch im Ausland in gleicher oder ähnlicher Form einer anderen Prüfungsbehörde vorgelegt. Es wurden keine früheren erfolglosen Promotionsversuche unternommen.

....

Ort, Datum Unterschrift

“Above all, don't fear difficult moments. The best comes from them.”

Rita Levi-Montalcini

Danksagung

An allererster Stelle möchte ich Herrn Prof. Dr. Christoph Janiak meinen besonderen Dank aussprechen für die Möglichkeit meine Promotion in seinem Arbeitskreis anzufertigen. Besonders danke ich ihm für die fruchtbaren Diskussionen, die Korrektur von Manuskripten, die mir gewährten fachlichen Freiräume und das in mich gesetzte Vertrauen in meiner Zeit an seinem Lehrstuhl sowie die Ermöglichung des internationalen wissenschaftlichen Austauschs.
Herrn PD Dr. Birger Dittrich danke ich für die freundliche Übernahme des Korreferats, seinen außerordentlichen Beitrag zu einer gemeinsamen Publikation sowie für die zahlreichen und hilfreichen Denkanstöße und Diskussionen.
Herrn Prof. Dr. Thomas J. J. Müller und Frau Lisa Bensch möchte ich an dieser Stelle für die Bereitstellung von Kristallen zu Derivaten von 9-Hydroxyphenalenon danken, wodurch eine gemeinsame Publikation ermöglicht wurde.
Herrn Prof. Dr. Matthias Karg und Herrn Arne Lerch danke ich für die aufwendigen DLS-Messungen sowie deren Auswertungen.

Für die Korrektur der vorliegenden Dissertation bin ich Ines Dumsch, Sandra Nießing und Marie Klein zu Dank verpflichtet. An dieser Stelle möchte ich mich für die immer freundliche Unterstützung bei Jutta Bourgeois, Birgit Tommes, Annette Ricken, Claudia Schäfer, Beate Rau, Dietmar Frunzke und Marcell Demandt aufs herzlichste bedanken.

Bei Alexander Nuhnen und Tian Zhao möchte ich mich für die erstklassige Hilfe und gute Zusammenarbeit bei den gemeinsamen Publikationen bedanken. Des Weiteren möchte ich mich herzlich bei Lisa Bensch, Franziska Merkt, Natascha Breuer, Beatriz Gil-Hernández, Karsten Klauke, Sebastian Glomb und Mohammed Enamullah für die gemeinsamen Kooperationen bedanken. In diesem Zusammenhang spreche ich auch einen großen Dank aus an Herrn Gamall Makhloufi für seine Zeit und Hilfe, mich in das Thema der Kristallographie einzuarbeiten.

Bei Serkan Gökpinar, Anna Goldman und Hülya Güven möchte ich mich für die schöne Zusammenarbeit während ihrer Abschlussarbeiten bedanken. Den Studierenden in den Laborpraktika möchte ich auch meinen Dank aussprechen. Durch eure Betreuung habe ich sehr viel für eine spätere Position mit Personalverantwortung gelernt.

Ein großer Dank gilt Annika Herbst, die mich während der Diplomarbeit betreut hat und auch im Anschluss mir in verschiedensten Momenten beständig geholfen hat.

Ganz besonders herzlich möchte ich mich bei Ines Dumsch, Sandra Nießing, Maximilian Klopotowski, Mike Lucka, Eduard Preis, Linda Kronenberg, Karsten Klauke und Ralf Bürgel für die wunderbare Promotionszeit und Motivation bedanken - vielen lieben Dank!!

Bei Anna Kautz, Christina Rutz, Raquel Marcos Esteban, Hajo Meyer, Martin Wickenheisser, Janina Dechnik, Sebastian Appel, Christian Heering, Subarna Dey, und Kai Schütte möchte ich mich für die freundliche Aufnahme in den Arbeitskreis bedanken. Selbstverständlich möchte ich mich auch bei allen anderen Mitgliedern des Instituts für die tolle Zeit bedanken – besonders für die schönen Grillnachmittage, Dartspiele, Weihnachtsfeiern, Kaffee- und Kuchenrunden, Karnevalsfeste, MOF-Treffen, Konferenztage, Bastelstunden und für das tolle Fuß- und Volleyballturnier.

Diese Arbeit wäre ohne die Unterstützung von meinen Freunden, meiner Familie und besonders ohne Mohammed Khodeir nicht möglich gewesen – ganz vielen lieben Dank, dass ihr mich immer so fleißig unterstütz habt!

Kurze Zusammenfassung

Metall-organische Gerüstverbindungen (MOFs = Metal-organic frameworks) gehören zu einer relativ neuen Klasse nanoporöser, hybrider Materialien. Unter Berücksichtigung ihrer Multifunktionalität sind diverse Synthesemethoden mit dem Ziel reproduzierbarer und homogener Größenskalierung erprobt worden. Im Folgenden werden Methoden vorgestellt, um prototypische MOFs speziell im Nanobereich zu synthetisieren. Zu diesen Methoden zählen die Synthesen in Emulsionen und die Synthesen unter Zuhilfenahme von Additiven (Modulatoren). Die Wahl der Energiequelle ist ein Parameter, der die Keimbildung und den Wachstumsprozess des Netzwerkes bestimmt. Keimbildung und Wachstumsprozesse beeinflussen Metall-organische Netzwerke hinsichtlich Struktur, Größe, Form, Oberflächenbeschaffenheit und Porosität sowie in ihren chemischen, physikalischen und thermischen Eigenschaften. Ein besonderes Interesse ist der Einsatz von Mikrowellen, um Metall-organische Gerüstverbindungen im Nanobereich herzustellen. Synthesen in der Mikrowelle bilden den Schwerpunkt dieser Arbeit. Dadurch gelang eine Optimierung hinsichtlich Ausbeute, Reaktionszeit, BET-Oberfläche und Partikelgrößenverteilung. Neben der Herstellung wird die Charakterisierung und die Verwendung von MOFs für die membranbasierte Gastrennung näher untersucht. Dazu wurde die Einbettung von unterschiedlich großen MOF-Partikeln in Gemischtmatrixmembranen (Mixed-Matrix-Membranes, MMMs) betrachtet, um die Leistung einer Gemischtgas-Trennung zu untersuchen. Als Beispiel wurde die CO_2/CH_4-Trennung gewählt. Obwohl die Einbeziehung des MOFs MIL-101Cr in MMMs bekannt ist, ist die Wirkung von MIL-101Cr im Nano-/Mikrobereich in MMMs neu und zeigt eine Verbesserung im Vergleich zu Mikrometer-großen MIL-101Cr-Partikeln. Der nanogroße Füllstoff ermöglichte es, eine höhere Beladung zu erreichen, bei der die Permeabilität signifikant über den Vorhersagen von Maxwell und des so genannten Free-Fractional-Volume stieg. Diese Verbesserungen für Gemischtmatrixmembranen auf Basis von MIL-101Cr im Nano-/Mikrobereich sind vielversprechend für andere Gastrennungen.

Ein zweiter Bereich dieser Arbeit hat einen Schwerpunkt in der Analyse von Wasserstoffbrückenbindungen. Die Festkörperstrukturen von drei H-gebundenen Enolformen von 5-substituierten 9-Hydroxyphenalenon (9-HP) wurden untersucht, um

die Position des H-Atoms innerhalb der intramolekularen Wasserstoffbrückenbindung zu bestimmen. Dazu wurden Daten aus der Einkristall-Röntgenbeugung (single-crystal X-ray diffraction, SC-XRD) und aus der Invariom-Modellverfeinerung ausgewertet. Außerdem zeigen Berechnungen aus der Quantenmechanik und Molekularmechanik (quantum mechanics/molecular mechanics, QM/MM), dass Ergebnisse einer früheren standardunabhängigen Atommodellverfeinerung, die auf das Vorhandensein einer resonanzunterstützten Wasserstoffbindung in nicht substituierten 9-Hydroxy-phenalenon basieren, irreführend sind. In allen Festkörperstrukturen ist die niedrigste Energieform die einer asymmetrischen Wasserstoffbrückenbindung. Offensichtliche Unterschiede der Ergebnisse von SC-XRD und anderen Analysemethoden werden erläutert. Während Daten mittels SC-XRD bei Raumtemperatur unter Verwendung des Independent Atom Model (IAM, Unabhängiges Atommodell) für 9-HP anfangs offenbar nicht mit anderen spektroskopischen Ergebnissen übereinstimmten, verfälschten Clusterberechnungen zusätzlich zu früheren SC-XRD-Datenerfassung und -analyse bei niedrigen Temperaturen das Vorhandensein einer C_{2v}-symmetrischen resonanzunterstützten Wasserstoffbrückenbindung in 9-HP (resonance-assisted hydrogen bond, RAHB). Diese Ergebnisse werden vom IAM sowie durch präzise Invariom-Verfeinerungen von drei substituierten 9-HP-Derivaten hier unterstützt. ONIOM-Cluster-Berechnungen ergänzen und bestätigen die Analyse. Die nach der Invariom-Verfeinerung erhaltene Restelektronendichte hat sich in diesem Zusammenhang als nützliches Validierungsinstrument erwiesen. Die jüngsten technischen Fortschritte bei der Auswertung von Einkristall-Röntgenbeugungsdaten liefern ein eindeutiges Ergebnis in voller Übereinstimmung mit anderen spektroskopischen Ergebnissen sowie mit Dichtefunktionaltheorie-Berechnungen (Density functional theory, DFT) an Clustern von Molekülen, die den Festkörper darstellen.

Short summary

This present work mainly deals with metal-organic frameworks and mixed-matrix membranes. Metal-organic frameworks (MOFs) belong to a relatively new class of nanoporous, hybrid materials. Taking into account their multifunctionality, various synthesis methods have been tested with the aim of reproducible and homogeneous size scaling. The following are methods to synthesize prototypical MOFs especially in the nanoscale. These include the syntheses in emulsions and the syntheses using additives (modulators). The choice of energy source is a parameter that determines the nucleation and growth process of the network. Both influence metal-organic networks in terms of structure, size, shape, surface texture and porosity, as well as their chemical, physical and thermal properties. A particular interest is the use of microwaves to produce MOFs in the nanoscale – this is the focus of this work. This succeeded in optimizing the synthesis in terms of yield, reaction time, BET surface and particle size distribution. In addition to manufacturing, the characterization and use of MOFs for membrane-based gas separation will be further investigated. The embedding of MOF particles of different sizes in mixed-matrix membranes (MMMs) was considered in detail. For this purpose, nano/micro-sized MOF particles were synthesized by microwave heating of emulsions for use as a composite material with matrimid mixed-matrix membranes to investigate the performance of a mixed gas separation. The CO_2/CH_4 separation was chosen as an example. Although the inclusion of the MOF MIL-101Cr in MMMs is known, the effect of MIL 101Cr in the nano/micro range in MMMs is new and shows an improvement compared to micro-sized MIL-101Cr particles. The nano-sized filler made it possible to achieve a higher load, where permeability increased significantly above Maxwell's predictions and modeling of the free fractional volume. These improvements for MMMs based on nanoscan-sized MIL-101Cr are promising for other gas deposition.

A second area of this work has a focus on hydrogen bonding. The solid-state structures of three H-bonded enol forms of 5-substituted 9-hydroxyphenalenones were investigated to accurately determine the H atom positions of the intramolecular hydrogen bond. For this purpose, single-crystal X-ray diffraction (SC-XRD) data were evaluated by invariom-model refinement. In addition, QM/MM computations of central molecules in their crystal environment show that results of an earlier standard independent atom model refinement, which pointed to the presence of a resonance-assisted hydrogen bond in unsubstituted 9-hydroxyphenalone, are misleading: in all solid-state structures the lowest energy form is that of an asymmetric hydrogen bond (Cs form). Apparent differences of results from SC-XRD and other analytical methods are explained. While room-temperature SC-XRD using the Independent Atom Model (IAM) for 9-HP apparently disagreed initially with other spectroscopic results, cluster computations in addition to earlier low-temperature SC-XRD data collection and analysis falsify the presence of a C_{2v} symmetric RAHB in 9-HP. These results are fully supported by IAM as well as more precise invariom refinements of three more substituted 9-HP derivatives reported here. ONIOM cluster computations complement and nicely confirm the analysis. Residual electron density obtained after invariom refinement was shown to be a useful validation tool in this context – recent technical progress in evaluating single crystal X-ray diffraction data does provide an unambiguous result in full agreement with other spectroscopic results as well as DFT computations on clusters of molecules that represent the solid state.

List of abbreviations

This list of abbreviations does not list SI units and their symbols/signs/abbreviations (from mathematical or chemical formulas).

bar - Unit of pressure (1 bar ≙ 100000 Pa ≙ 100 kPa)

BET - Brunauer-Emmett-Teller

CCDC - Cambridge Crystallographic Data Centre

CSD - Cambridge Structural Database

CTAB - Cetyltrimethylammoniumbromid

DLS - Dynamic light scattering

DMF - *N,N'*-Dimethylformamide

et al. - et alia

EtOH - Ethanol

h - Hour(s)

9-HP - 9-Hydroxyphenalenone

IAM - Independent Atom Model

IR - Infrared spectroscopy

K - Degree Kelvin

mg - (Milli)gram

MIL - Matériaux de l`Institut Lavoisier

min - -Minute(s)

mL - Milliliter(s)

(m)mol - (Milli)mol, unit of amount of substance (1 mol ≙ 6.022 ・ 1023 particles)

MOF - Metal-organic framework

NL(DFT) - (Nonlocal) density functional theory

nm - Nanometer(s)

NMR - Nuclear Magnetic resonance

(P)XRD - (Powder) X-ray diffraction

QM/MM - Quantum mechanics/molecular mechanics

RAHB - Resonance-assisted hydrogen bond

SEM - Scanning electron microscopy

SBU - Secondary building unit

SC-XRD - Single-crystal X-ray diffraction

TMAOH - Tetramethylammonium hydroxide

wt% - Weight percentage (weight%)

Table of contents

1. Introduction

This chapter is based in parts on the publication: I. Gruber, A. Nuhnen, A. Lerch, S. Nießing, M. Klopotowski, A.Herbst, M. Karg, C. Janiak, *Front. Chem*. **2019**, 7:777.

1.1 Metal-organic frameworks (MOFs)

1.1.1 Origin

The term "metal-organic framework" (MOF) was introduced by Omar Yaghi in 1995.[1] Yaghi said it is a pleasure to see that chemistry could combine molecular beauty and function in such a brilliant way as demonstrated by MOFs.[2] Metal-organic frameworks are a unique class of porous crystalline inorganic-organic hybrid compounds. Before that, the first hybrid frameworks were known as coordination polymers, and early reports regarding porous coordination polymers were published by Kempe, Janiak, and Stock [11–14].[3-6] In short, MOFs are crystalline materials that are built from metal centers and bridging organic ligands. Since 1995, MOFs have attracted attention of numerous researchers in the academic and industrial community.1[,7,8] They have been the focus of a rapidly increasing number of studies and plenty of breakthroughs regarding new syntheses and applications.[9] To this day, researchers which working in the field of manufacturing, agriculture, energy, water treatment, and pharmaceutical engineering are further developing this MOF technology. Some companies have already licensed the technology to use MOFs in their business, like BASF, who was an early promoter of MOF research and is still the global leader in MOF research and a large-scale production vendor. Industrial efforts are now creating a metal-organic framework market with top key players like BASF, MOFapps, and Strem Chemicals. As some metal ions show specific application advantages, the global market is primarily split into zinc-based, copper-based, iron-based, aluminum-based, and magnesium-based MOFs. The key drivers influencing market growth and application in gas storage and gas separation are due to their high-performance in terms of porosity. Some MOFs are able to achieve specific surface areas up to 7000 $m^2\,g^{-1}$ and have methane storage capacity of 240 $cm^3\,cm^{-3}$.[10,11.] Recent technological progress allows not only large-scale production of MOFs, commercially relevant quality, efficiency, and price are also accessible.[12-14]

1.1.2 Design

The ongoing research in the field of MOFs is promoted by their huge variety regarding different structures and properties. MOFs are built from metal nodes (i.e., inorganic centers like metal ions or clusters) and bridging organic linkers, which connect the metal nodes (see Figure 1).[15]

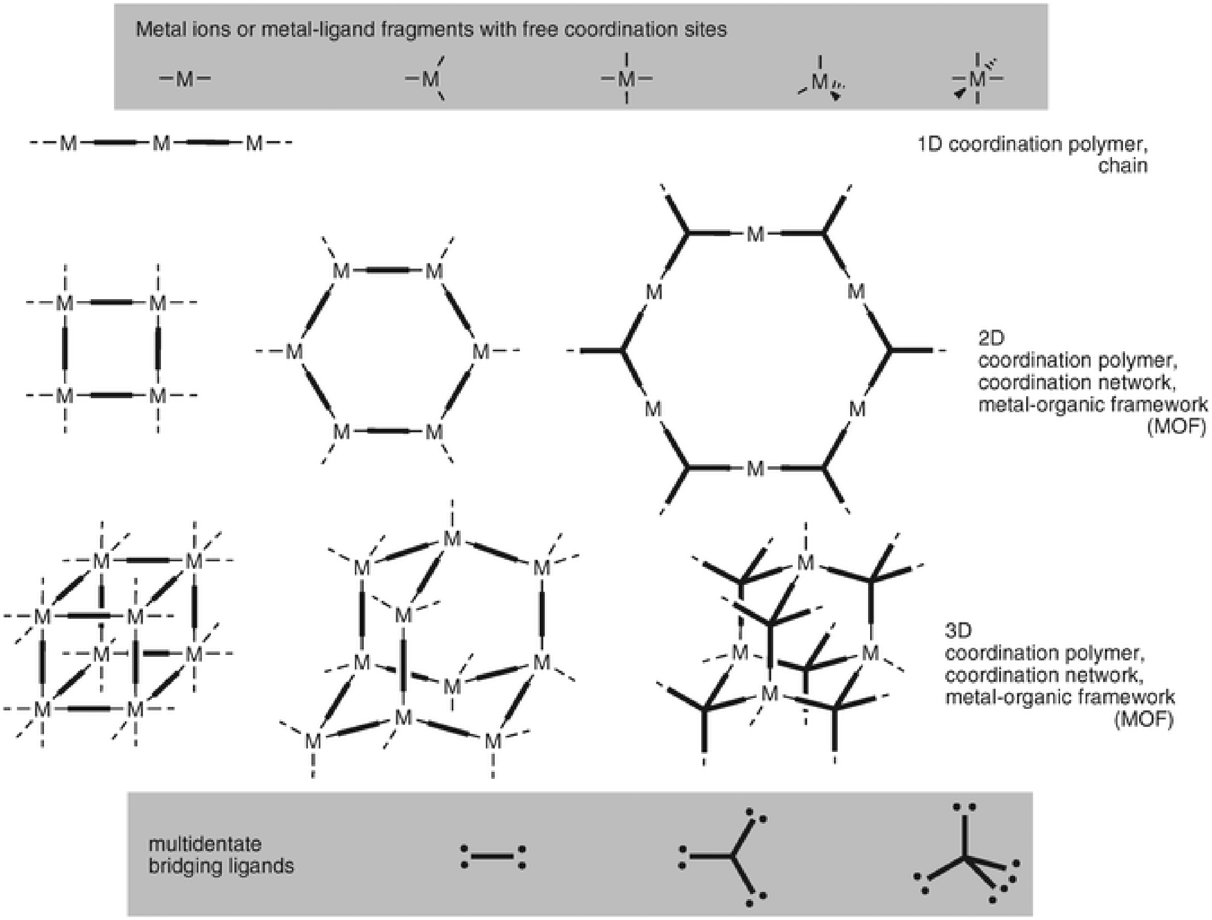

Figure 1. Schematic presentation for the construction of typical coordination polymers/MOFs from molecular building blocks. Reprinted from ref. 16. Copyright 2010, with permission from Royal Society of Chemistry (RSC).

By the sheer endless combination of different metal nodes with different bridging organic linkers, the variety of metal-organic framework is almost unlimited.[17] Due to their influence on the binding and formation of different MOF structures, the reaction conditions are further key factors for the resulting framework.[18] Reaction conditions include the reaction temperature, reaction time, molar ratio and concentrations of the reactants, solvents,[19] and modulators[20]. The last ones are optional but show a high impact on the design and structure.

In a typical synthesis, metal-organic frameworks are synthesized under hydrothermal or solvothermal conditions in polar solvents like water, alcohols, acetonitrile or dimethylformamide at temperatures below 250 °C. The reaction temperature is depending primarily on the decomposition temperature of the solvent and organic linker. The construction of the framework begins with the formation of so-called "metal-containing secondary building units" (metal-containing SBUs) consisting of multi-core metal clusters.[21] The formation of SBUs (organic and metal-containing) is shown in Figure 2. Based on the self-assembly process (i.e., the coordination of organic polytopic linkers to inorganic metal centers), 1-D, 2-D or 3-D frameworks are possible.

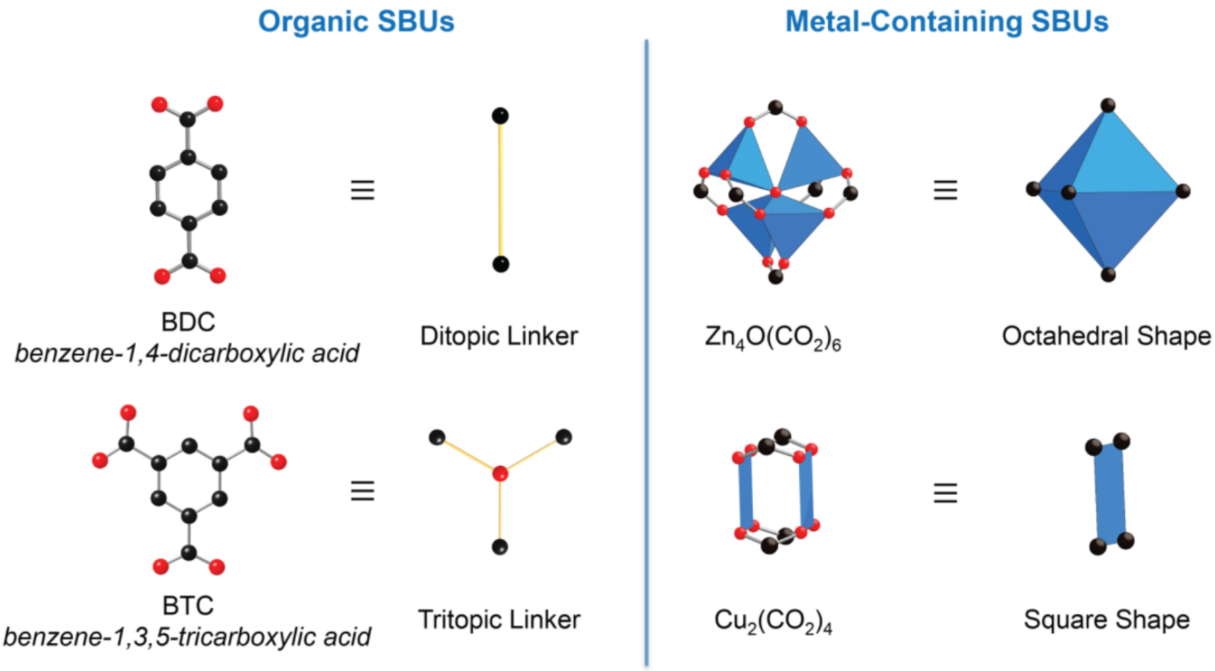

Figure 2. The chemical formula and names are provided for each MOF. Atom colors in molecular drawings: C, black; O, red; N, green; Zn, blue polyhedral; Cu, blue squares. Hydrogen atoms are omitted for clarity. Reprinted from ref. 22. This figure is distributed under the terms of the Creative Commons Attribution 3.0 License, which permits unrestricted use, distribution, and reproduction in any medium, provided the original work is properly cited.

Moreover, there is also the possibility that independent 1-D-, 2-D-, and even 3-D nets interpenetrate each other.[23] Apart from the self-assembly process, MOFs have either a rigid or a flexible structure.

1.1.3 Rigid metal-organic framework

Some metal-organic framework structures consist of rigid networks. A prominent example for a rigid MOF is MIL-101Cr, a MOF from the MIL series (MIL = Matériaux de l'Institut Lavoisier). It is one of the most researched metal-organic frameworks. Crystallites of MIL-101Cr have an octahedral shape, and the framework is built from trinuclear $\{Cr_3(\mu_3\text{-}O)(F,OH)(H_2O)_2\}$ nodes and 1,4-benzenedicarboxylate linkers (see Figure 3A) to give hexagonal (15-16 Å) and pentagonal windows (12 Å) (see Figure 3B), inner cages of 29 Å and 34 Å in diameter (see Figure 3C),[24] and large apparent BET surface area in a zeotypic structure (4100 m^2 g^{-1}, see Figure 3D).

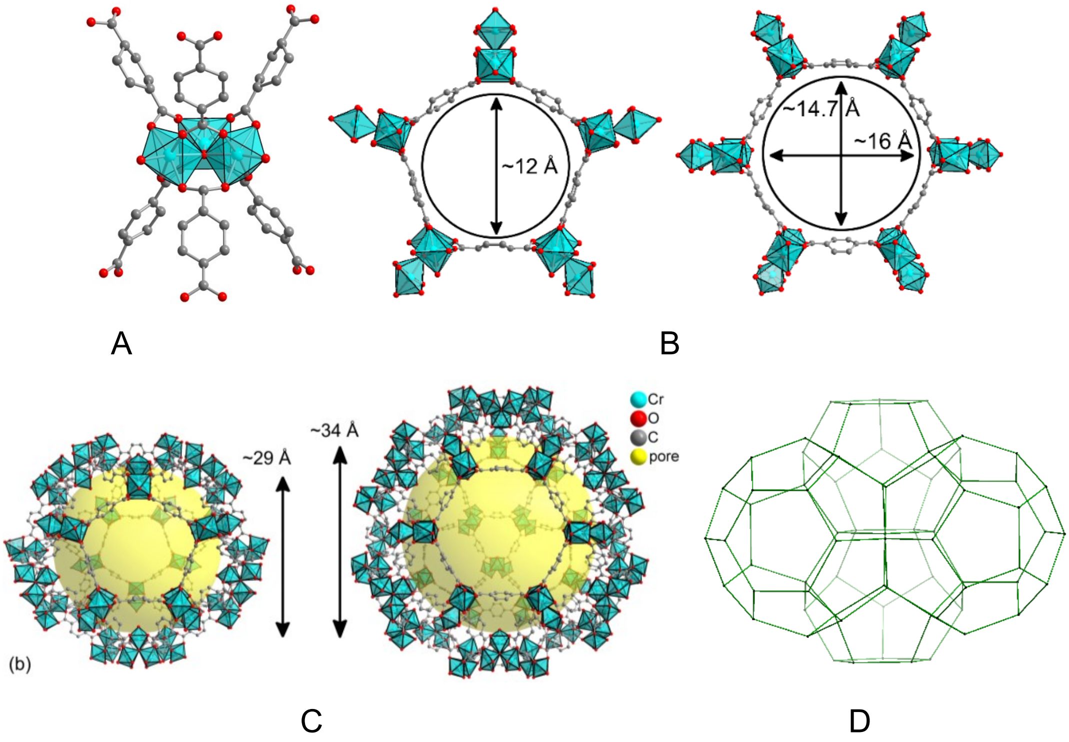

Figure 3. Trinuclear $\{Cr_3(\mu_3\text{-}O)(O_2C\text{-})_6(F,OH)(H_2O)_2\}$ building unit surrounded by bdc linkers in a trigonal prismatic fashion (A); pentagonal and hexagonal cage window apertures with dimensions (B); small cage with pentagonal windows and large cage with pentagonal and hexagonal windows (C); zeotypic network (D). Objects in (A) to (D) are not drawn to scale. Graphics have been created from the deposited cif-file for MIL-101Cr (CSD-Refcode OCUNAK). Graphics have been created from the deposited cif file for MIL 101Cr (CSD Refcode OCUNAK).[25]

It has become one of the most important MOFs.[25,26] For the synthesis of MIL-101Cr long reaction times of 8 h, and temperatures in the region of 160 °C to 220 °C with hydrothermal autoclaving are usually needed.[25] Further, for a typical synthesis of MIL-101Cr hydrofluoric acid is often used as a problematic additive or modifier.[25] Overpressure (autoclaves) and/or heterogeneous reaction mixtures render reaction control difficult and require expensive equipment, especially when it comes to scale-up, hence, are not desirable for large-scale or commercial syntheses.[27] Therefore, a more efficient synthesis of MIL-101Cr is highly wanted.

1.1.4 Flexible metal-organic frameworks

Besides rigid metal-organic frameworks, there are MOFs which can change their pore size and shape depending on environmental conditions. These also include MOFs from the MIL series like MIL-53 and MIL-88.[28,29] Some MOFs in this series show unusual properties in terms of their selective flexibility. Such unusual properties are of crucial importance for the storage and removal of guest molecules in the framework. This behaviour is known as the breathing effect and the gate opening process.[30] Temperature, pressure, pH value and the nature of the guest molecules in the pores have an impact on both, the breathing effect and the gate opening process. These effects are described in Chapter 1.1.4.1 – 1.1.4.2.

1.1.4.1 Breathing effect

The first unusual property of flexible MOFs is the breathing effect. It is based on interactions with guest molecules inside the framework which can cause a change in the structure of the entire crystal lattice (by contracting and expanding). A well-studied MOF showing the breathing effect is MIL-53 (see Figure 4).

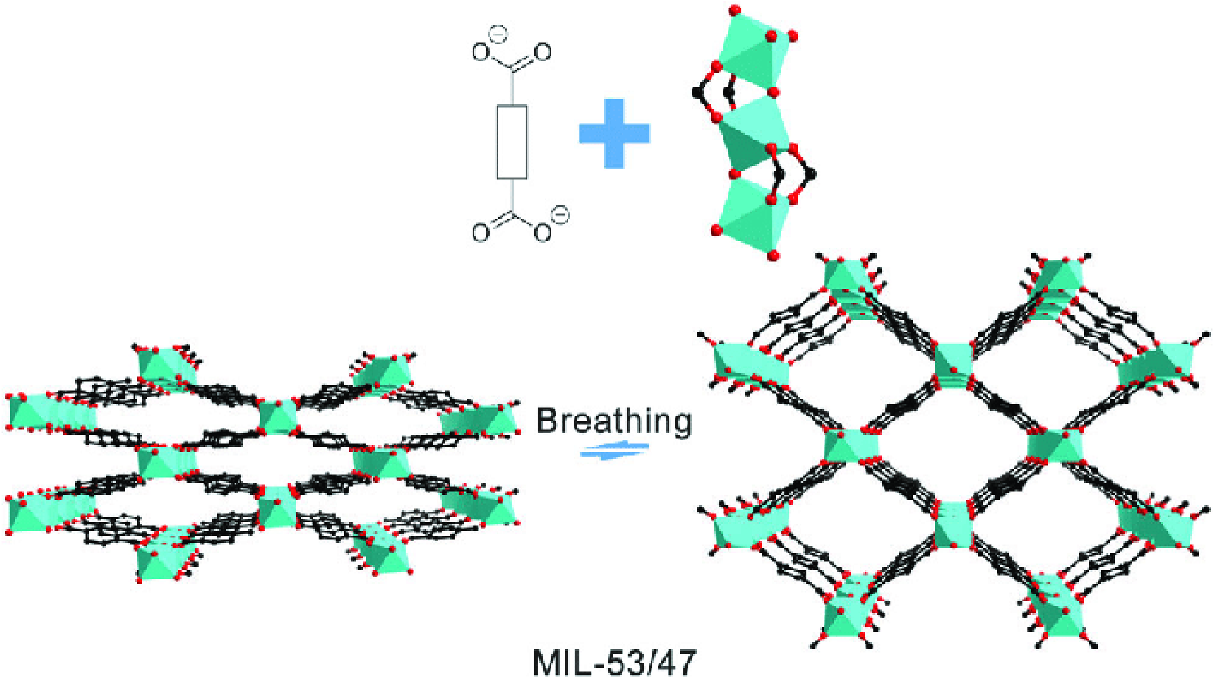

Figure 4. Illustration of the assembly of MIL-53/47 from ditopic carboxylate linkers and infinite chain clusters; metal ions can be Cr^{3+} , Fe^{3+} , Al^{3+} , and V^{4+} (MIL-47). Breathing effect is illustrated. Color scheme: metal (turquoise); O (red); C (black). Reprinted from ref. 31. Copyright 2014, with permission from Royal Society of Chemistry.

1.1.4.2 Gate opening effect

The second unusual property of flexible MOFs is the so-called gate opening effect. The gate opening effect can be triggered among other things by pressure, temperature, light, electric or magnetic fields. An interesting metal–organic framework showing the gate opening effect is LIFM-12 (see Figure 5).[32] Gate opening is an important microscopic phenomenon in understanding adsorption, diffusion, and separation processes.[33] This phenomenon is characteristic of inorganic solids with certain structural flexibility upon interaction with external stimuli. When the gate opening occurs, closed channels (i.e., channels, which connect pores) can be opened and compounds can be adsorbed/removed. Gate opening needs to be activated and is based either on the swinging of organic linkers in combination with rotating of their residual groups or on swinging of organic linkers alone.[32]

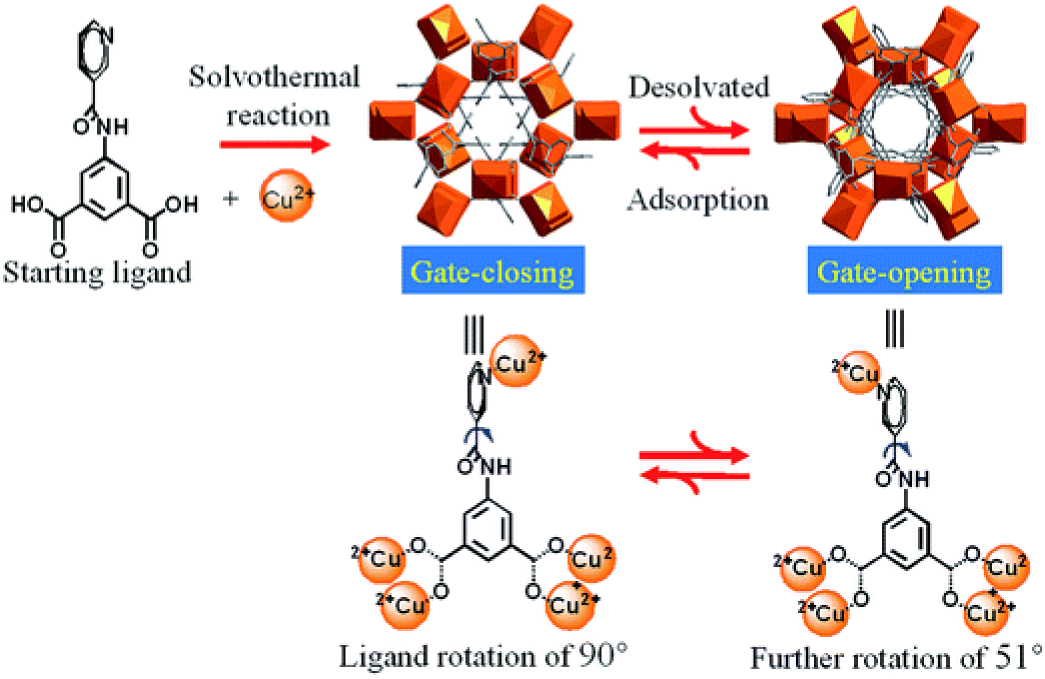

Figure 5. Gate opening/closing *via* guest removal and inclusion processes, controlled by the dynamic rotation of pyridyl ring and amide group of H_2NIA ligand. Reprinted from ref. 34. Published by The Royal Society of Chemistry.

1.1.5 Pores

Size and geometry of the pores in MOF material are influenced by the secondary building unis. Therefore, this chapter describes the pore architecture in detail. Secondary building units can be transformed into extended porous networks. For this transformation, ligand coordination modes and metal coordination environments can be utilized. The geometric and chemical attributes of the secondary building units and linkers have to be considered for the prediction of the framework topology.[35] Among the 1-D, 2-D, and 3-D metal-organic frameworks, the 3-D frameworks are of particular interest. Three-dimensional MOFs have pores (i.e., cavities, see Figure 6) which are crucial for some applications as they are accessible e.g., for small molecules. 3-D MOFs offer an enormous degree of structural and compositional diversity regarding to the mutual control of their porous structure, composition, and functionality.[36] They also offer a large range of chemical and physical properties.

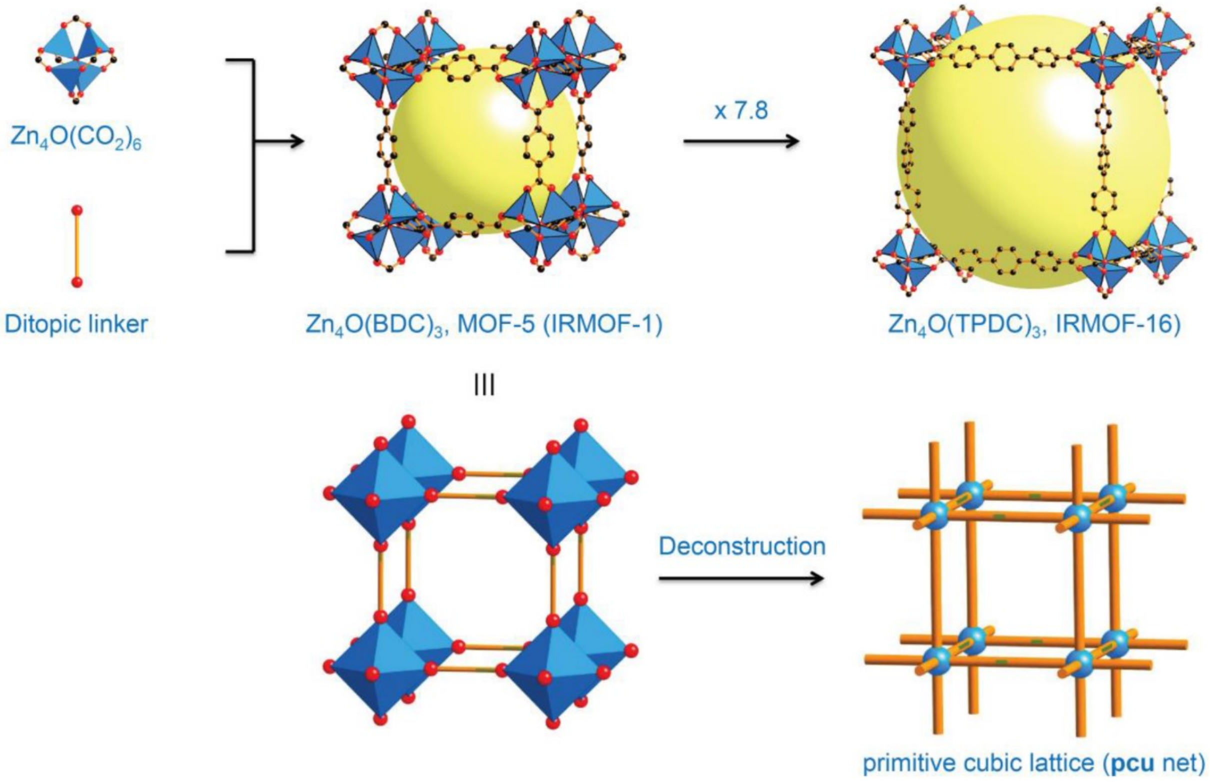

Figure 6. The chemical formula and names are provided for each MOF. Atom colours: C, black; O, red; N, green; Zn, blue polyhedral. Hydrogen atoms are omitted for clarity. The yellow sphere represents the pore. Reprinted from ref. 22. This figure is distributed under the terms of the Creative Commons Attribution 3.0 License, which permits unrestricted use, distribution, and reproduction in any medium, provided the original work is properly cited.

Based on their pore sizes, there are three categories of MOFs. The first category includes microporous MOFs with pores diameters less than 2 nm. Next, there are mesoporous MOFs with pore diameters between 2 and 50 nm. The third category describes macroporous MOFs with pore diameters over 50 nm. The typical porosity of MOFs in the micro-region prevents fast access of molecules (e.g., gas molecules) to the internal surface (see Figure 7). This problem can be overcome by strategies described in the following chapters. Fast access of molecules to the internal surface in larger MOF crystallites can be achieved by two different approaches. The first approach comprises the reduction of the diffusion path length by decreasing the crystal size.[37,38] This approach regarding regarding to the mutual control of their porous structure, composition, and functionality will be examined in chapter 1.2. The second approach is using the enlargement of the pores through defects towards hierarchical micro-meso-macropores[39] and is described elsewhere.[40]

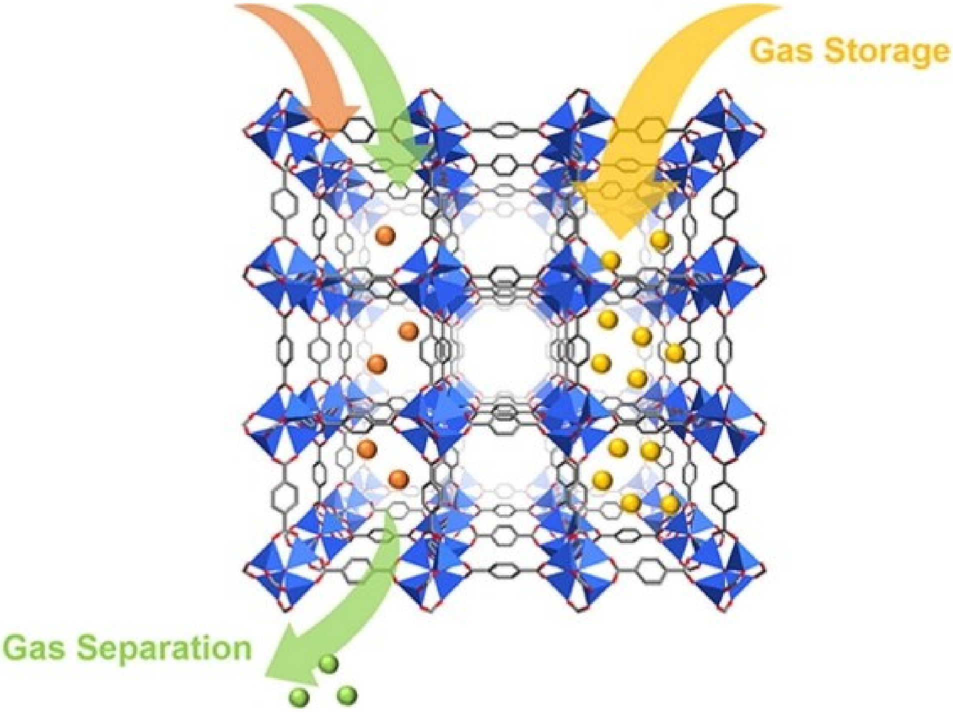

Figure 7. The yellow, green, and orange spheres represent gas molecules inside MOF pores. Reprinted from ref. 41. Copyright 2017. Published by Elsevier Ltd.

1.1.6 Scale chemistry

Nowadays, it is possible to produce extended neutral as well as anionic or cationic porous frameworks with unique defined pore architectures and functions.[42] In this context, the notion of "scale chemistry" occurs. Scale chemistry is based on the existence of building units with different sizes and topologies. Scale chemistry concerns the edification of solids with several building units either inorganic, organic, or hybrid, and the effects they have for the corresponding frameworks and the voids they generate.[43] It is a method of transforming molecular complexes and clusters to extended solids. Moreover, scale chemistry is also needed for the conversion of molecular reactivity into desired physical properties.[44] Finally, scale chemistry is also needed for the translation of molecular geometry into assembled structures. Therefore, stability and robustness are required for chemical and physical functionalities.

1.1.7 Stability and robustness

The stability of metal-organic frameworks depends mainly on the intrinsic structures (i.e., charge density of metal ions, connection numbers of metal ions/clusters, configuration, etc.) and structural dimensionality of the assemblages.[45] A MOF is called robust if the framework remains even in the absence of guest molecules in the cavities. However, not only the crystallographic porosity but also the real gas accessible volume of the compound generated after the removal of solvent molecules are crucial for the manufacturing of porous materials.[46] During the synthesis, solvent molecules and even excess linkers may be trapped in the cavities.[25] In case a MOF is not robust and solvent molecules/excess linkers are being removed from the framework, the framework will collapse due to high surface tension and capillary forces imposed on the MOF structure by the liquid- to-gas-phase transformation of trapped solvent molecules.[47] To access the permanent porosity and high surface areas, the solvent molecules have to be removed — a process termed activation.[48,49] Among the most common activation techniques are the following two practices: Solvent exchange plus vacuum drying[50] and the supercritical drying.[51] As mentioned earlier, high quality MOFs are in demand. In this context, quality equals permanent porosity. Therefore, MOFs must have a permanent porosity to be used in various high-end applications, some of which are presented in the following chapter.

1.1.8 Applications

MOF studies have shown that different strategies can be combined to develop MOFs with unique particle size, functionalities, and pore structures. It depends on the application which metal-organic framework has to be selected and how the various and delicate parameters have to be adapted for synthesizing customized MOFs/pore architectures. MOF technology (for syntheses procedures, see chapter 1.2.5) allows to store, separate, release or protect valuable materials, with academic and industrial research groups improving and developing high-value products. This research can be either driven by curiosity or by applications dealing with small molecule adsorption and storage,[52] drug delivery,[53] gas and liquid separation,[54] sensing,[55] catalysis,[56] heat transformation and other applications.[57,58,59] A schematic representation for various examples are shown in Figure 8.

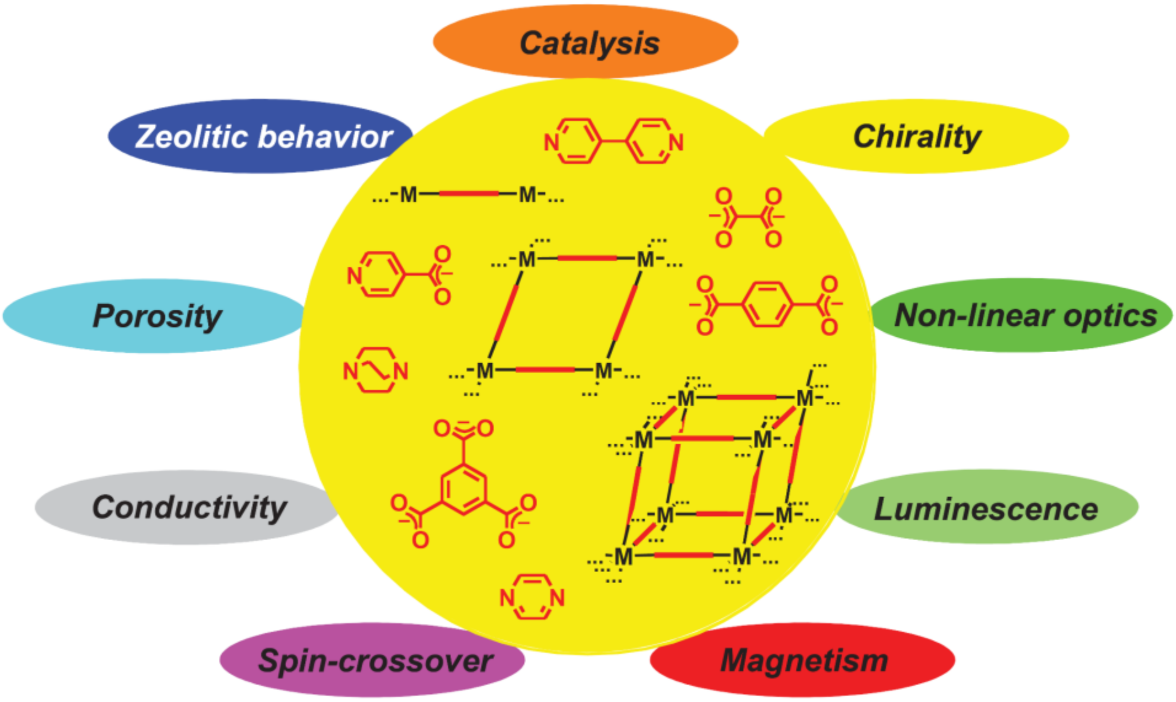

Figure 8. Examples of application-oriented properties of MOFs and examples of common linkers. Reprinted with permission from ref. 16. Copyright 2010, with permission from Royal Society of Chemistry (RSC).

Latest advantages in MOF applications are based on MOF particles in the nano and lower micro range. Such MOF nanoparticles are an emerging class of modular nanomaterials. The aim of the next chapter is therefore to highlight a selection of recent works that provide basic information for understanding the advantages of MOF nanoparticles. The frequently used design strategies for desired applications are also shown in the following chapter.

1.2 Nanotechnology

1.2.1 Nanoparticles

In many different applications, fast access of molecules to the internal surface is required.[60] Fast access can be obtained by decreasing the crystal size. Decreasing particle size to the nano level is an approach that can be achieved by nanotechnology. The term “nano” is a unit prefix and denotes a factor of 10^{-9} or 0.000000001, meaning "one billionth". The general term “nanoparticles” describes small particles with a diameter of 1–100 nm in size in at least one dimension. Nanotechnology, became an important concept in science, and explores materials whose structures show unique improvements concerning physical, chemical, and biological properties.[61] Therefore, the scale-down of metal-organic frameworks (MOFs) to the nano region yields materials that in some cases are more applicable for adsorption, desorption, and storage of small molecules. Unlike their bulk counterparts, MOF nanoparticles have improved properties due to their nano- and microscale architectures (e.g., permanent porosity with enormous internal surface areas, large structural diversities, etc.).[62]

1.2.2 Nanocrystals, nanocomposites, and nanostructured materials

Nano- and also mesostructured MOFs may create more unsaturated metal sites on the internal or external surface of each particle.[63,64] These structures are referred to as nanocrystals if they are referred to as nanocrystals. Such nanocrystals are in most cases single-crystalline and hence have unique optical and electrical characteristics compared to the bulk form.[65] Nanocrystals are complemented by the category of nanocomposites, which consist of different nanocomponents. There are also nanostructured materials which have different properties compared to the macroscopic bulk material due to shape, surface structure, and nano-relevant effects (surface-,[66] optical-[67] or quantum-effects[68]). If bulk materials are reduced to the nanometer size, not only their properties and their behaviour often become size- and shape-dependent,[69] but some effects and forces disappear while other increase. In summary, nanoparticles show size-depending forces, nanoscale effects due to their high external surface-area-to-volume ratio,[70] and typically have an inherent wide size distribution that may affect performance and reliability.[71] While size-depending forces are described elsewhere,[72,73,74] the nanoscale effects are shown here. Among the nanoscale effects, one dominant effect is the strong increase in surface energy. The reduction of the particle size leads to high surface energy. As energetically preferred, nanoparticles show a strong tendency to agglomerate and to aggregate. Agglomeration, as well as aggregation, lead to a loss of specific properties and the properties of agglomerated MOF nanoparticles become more similar to the properties of the analogous bulk material.65 Both effects also lead to two main challenges in MOF nanoparticle technology. The first challenge is the determination of the size,[75] whereas the second challenge is the suppression of agglomeration. The following chapter takes a closer look on both.

1.2.3 Size determination

It is worth to mention that the determination of size is not only depending on which characterization technique is used, it also is based on the conditions under which the nanoparticles are measured.[76] The determination of nanoparticles is therefore not trivial. As a consequence, "the sizes" of nanoparticles are depending on the physical characterization technique performed to measure them. For the exploration of MOF nanoparticles, it is recommended to apply multiple complementary techniques[69] such as solid-state methods (including powder X-ray diffraction, atomic force microscopy, scanning electron microscopy and transmission electron microscopy) and dispersion-based methods (e.g., fluorescence correlation spectroscopy and dynamic light scattering)

1.2.4 Suppression of agglomeration

Next to size determination there is the obstacle of the suppression of agglomeration effect. Most agglomerated clusters are difficult to separate back into individual nanoparticles, and agglomerated macroscopic MOF clusters change or even lose their properties compared with individual MOF nanoparticles. In general, once nanoparticles are dispersed in liquid, they interact with the solvent, e.g., by hydration, ion-adsorption[77] or agglomeration.[78] Through this variety of interactions, the effective size of nanoparticles may significantly change.[79] To prevent agglomeration, the surface of MOF nanoparticles can be functionalized directly after nucleation using organic molecules like long-chain alkyl compounds. Long-chain alkyl compounds are sterically demanding and work as a shell around the MOF nanoparticle. Surfactants or polymers used for the functionalization of these nanoparticles also are helping to prevent the agglomeration effect. Moreover, surfactants and polymers help to limit the process where bigger crystals grow at the expense of smaller ones. This effect is known as Ostwald ripening.[80] State-of-the-art applications, like drug release materials,[81] require MOF nanoparticles with defined diameters, homogeneous shapes, and monodispersed size distributions. In this context, it is also crucial that MOF nanoparticles show almost no tendency for agglomeration. Therefore, improved syntheses are very much in demand. Basic concepts for that goals are provided in the following chapter.

1.2.5 Syntheses of metal-organic framework nanoparticles

1.2.5.1 Overview of the report syntheses

To synthesize MOF nanoparticles with a narrow size distribution, minor agglomeration, and stabilization the nucleation and growth have to be controlled correctly. For that, different syntheses can be used (see Figure 9).

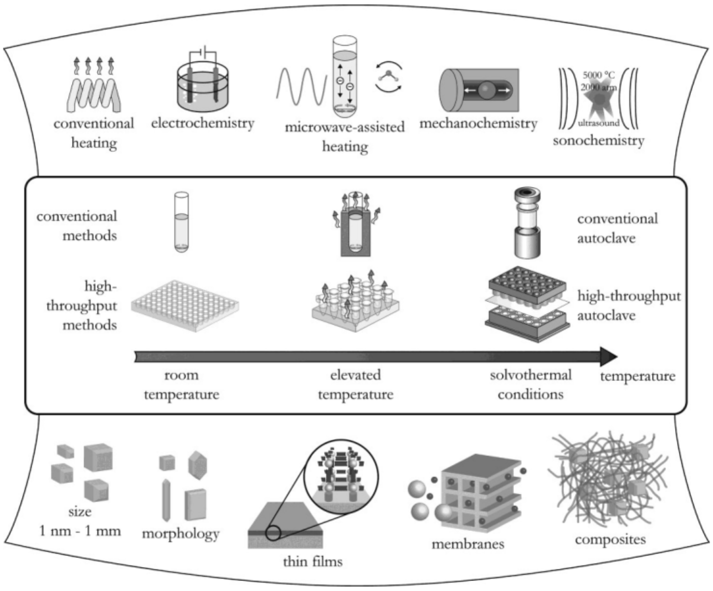

Figure 9 Overview of synthesis methods, possible reaction temperatures, and final reaction products in MOF synthesis. Reprinted with permission from ref. 82. Copyright 2012, with permission from American Chemical Society.

In general, particle engineering for the construction of nanoparticles, i.e., designing the morphology and particle size distribution, can be divided into two approaches. The first one is the so-called top-down approach, and the second one is the so-called bottom-up approach. Elementary details for both approaches are presented in the following sections.

1.2.5.2 Syntheses at atmospheric pressure and spontaneous precipitation

MOF nanoparticles can be achieved by adjusting the reaction time and temperature.[83] The simplest synthesis route takes place at atmospheric pressure (i.e., reactions take place in open vessels).[82] They also can be yielded by a spontaneous precipitation method after mixing the metal salt and organic linker in a solution.[84,85] Spontaneous precipitation of copper-based MOF particles was observed upon the addition of the triethylamine to the synthesis solution containing zinc nitrate hexahydrate and 2-amino terephthalic acid.[86] In addition to these two techniques, there are several other commonly applied practices in chemistry laboratories. MOF nanoparticles can be achieved also by hydro-/solvothermal methods,[87] microwave-assisted routes,[88] surfactant-mediated syntheses,[89] reverse emulsions,[38] direct emulsions,[90] and sonochemistry.[91] Most of the different strategies, which will be described in these chapters, are summarized in Figure 9. In addition, in the following chapters the focus is not only on the various bottom-up/top-down methods but also on the combination of different techniques.

1.2.5.3 Hydrothermal and solvothermal method

Starting with the most commonly used practices, the focus is on liquid-phase syntheses (e.g., the hydrothermal and solvothermal syntheses). In most cases, these syntheses take place under high temperatures, high pressures, and long reaction times. For some MOFs, regular syntheses are sufficient to form nanoparticles and no further adjustments during the synthesis are necessary. The hydrothermal and solvothermal methods are based on the following procedure: Metal salts and organic linker are being dissolved in water or organic solvents, respectively. The solvothermal syntheses are performed in autoclave reactors, which can be made of Teflon or high-grade steel or are Teflon/glass-lined steel reactors. The control over precursor concentration, as well as reaction pressure, reaction time, and reaction temperature are crucial for the formation of uniformly shaped nanoparticles. It was found that also the selected solvent has a strong impact on the formation of the resulting MOF nanoparticles. By controlling the size and shape of the MOF particles, there is the possibility to adjust and tailor the structure and performance of the assemblies.[92]

Although there is the problem that during the solvothermal syntheses solvent molecules remain in the MOF network, molecules inside the pores have also a benefit for the formation of the framework as they have the so-called “template effect” on the framework. The template effect is also known as the “structure-directing effect of solvents” and describes the influence of the solvent molecules on the MOF structure.

Since it was discovered in 1990 that mesoporous silicates can be obtained from supramolecular molecules, attempts were made to apply the principle of supramolecular templating to MOFs. The template effect is based on amphiphilic molecules, e.g., surfactants or copolymers (see chapter 1.2.5.6). Although solvent molecules have become some of the most fascinating phenomena in MOF crystallography and materials science,[93] the complex mechanism involved in these solvent-directed coordination assemblies remains largely unclear.[94] If solvent molecules should be avoided in MOF pores, the solvent can be dispensed. It is a route to yield solvent-free MOF nanoparticles. This method, however, is not transferable for all MOF syntheses. Further details regarding the solvent-free syntheses are shown in the next section.

1.2.5.4 Mechanochemistry

As already mentioned, there are solvent-free syntheses possible. These syntheses are based, among other things, on mechanochemistry (see Figure 10). Here, the MOF nanoparticles are synthesized from the metal salt and the organic linker using the grinding method. Grinding enables the activation of inactive substances and the systematic investigation of solvent-free syntheses, particularly with the focus on the supramolecular template influence on the structure.[95] Results from grinding are comparable to nano-scale solvothermal syntheses.[96] While this solvent-free method has some advantages over the original solvothermal method, mechanochemical syntheses are not transferable for all MOF representatives. In addition, solvothermal and mechanochemical syntheses generally have long reaction times. A 60 min grinding synthesis of MOF-5 was shown by Lv *et al.*[97] Yet, for some MOFs also a grinding time of 1minute is enough. A one min synthesis of Ni-MOF by a mechanical ball milling method was show by Zhanhg *et al.*[98] In order to be applicable to several MOFs and to shorten the generally long reaction times, other synthesis methods like using microwave heating have to be considered. Microwave heating can be used to speed up response times. This highly advanced synthesis procedure is described in the next section.

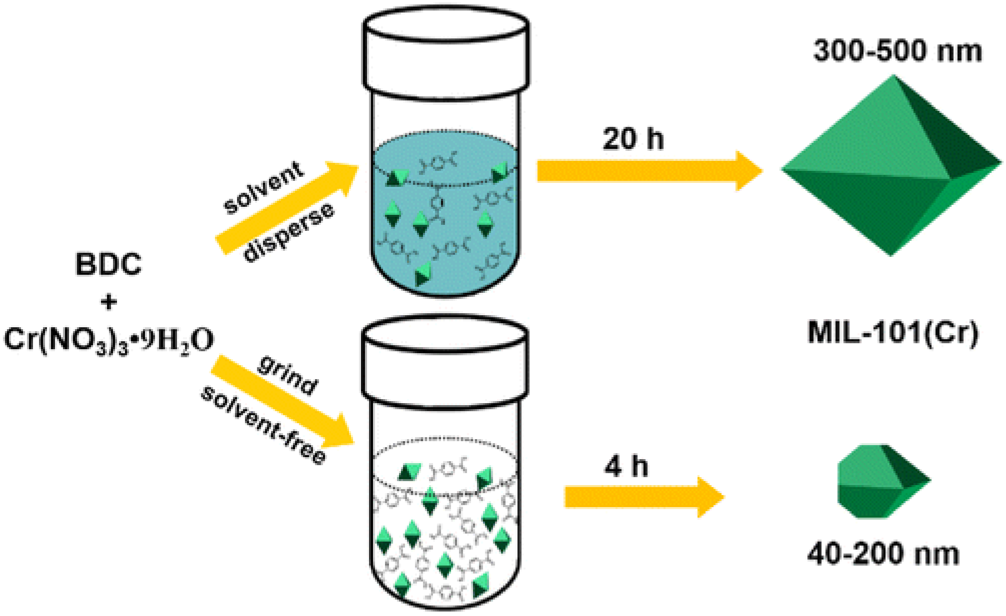

Figure 10. Imaginative diagram about synthetic process of MIL-101(Cr) under different conditions. Reprinted from ref. 99. Copyright 2016, with permission from American Chemical Society.

1.2.5.5 Microwave heating

One important objective producing metal-organic compounds on an industrial scale is to speed up reaction times. Microwave heating allows short reaction times and the required temperatures can be reached within seconds.[100] Syntheses by microwave heating are an efficient alternative to the conventional method due to the conversion of electromagnetic waves into thermal energy. By using microwave heating not only the heating can be controlled (i.e., to a certain extent) but the nucleation and crystal growth can be influenced as well. In typical MOF syntheses, the reaction time requires between 8 h for the production of MIL-101Cr, 24 h for HKUST-1 and UiO-66, and 72 h for NOTT-400.[25,101,102,103] By using microwave heating the reaction time is in the range of minutes. Besides, this method offers the advantages of phase selectivity, simple morphology control, and size scaling. Microwave heating is known to enhance rates of nucleation and crystal growth process, including the acceleration of nucleation over crystal growth.[104] Moreover, microwave heating is an "instant on/instant off" energy source, significantly reducing the risk of overheating reactions.[105] Last but not least, it is a type of a solvothermal synthesis and in combination with surfactants (see next section), microwave heating is one of the most advantageous methods for nanosized MOFs.91[,106]

1.2.5.6 Use of coordinating agents

Including coordinating agents (i.e., modulator molecules) into MOF syntheses, the morphologies and particle size can be tuned.[107,108,109,110] Modulator molecules can be distinguished between surfactants and ionic liquids. Surfactants have a cost advantage and can have basic, acidic, cationic, anionic, or neutral properties. They form weak interactions with the MOF surface and compete with the organic ligands due to their ability to coordinate with the metal centers. Due to a slowdown of the emergences, their ability to coordinate can influence the morphology and the growth of the particles. The modulator method can be combined with all the other methods. It also enables various variations in the design of size, shape, surface quality and pore size. Criteria for choosing the right modulator are the melting point, charge, the ability to coordinate with the metal cation, and to protonate the organic linker. Whether a specific modulator increases or decreases the crystallization of MOF nanoparticles depends not only on the concentration of the modulator but also on the type of MOF and the used metal ions. The modulator method also has the advantage that mesoporous MOFs can be obtained. Mesoporous MOFs are used in energy storage and conversion as well as in the absorption of larger biomolecules. Regarding gas storage, gas separation and catalysis, it is assumed that they outperform previous MOFs in terms of efficiency. If an anionic surfactant is used, both the surfactant and the organic ligand can coordinate with the metal cation as both compete with each other. Anionic surfactants would be, for example, sodium stearate and sodium oleate. Cetyltrimethylammoniumbromid is a cationic surfactant and it is known to slow down the nucleation and growth of MOFs.[111] Triton X-45 is a nonionic surfactant and it is commonly used for to achieving additional mesoporosity.[112]

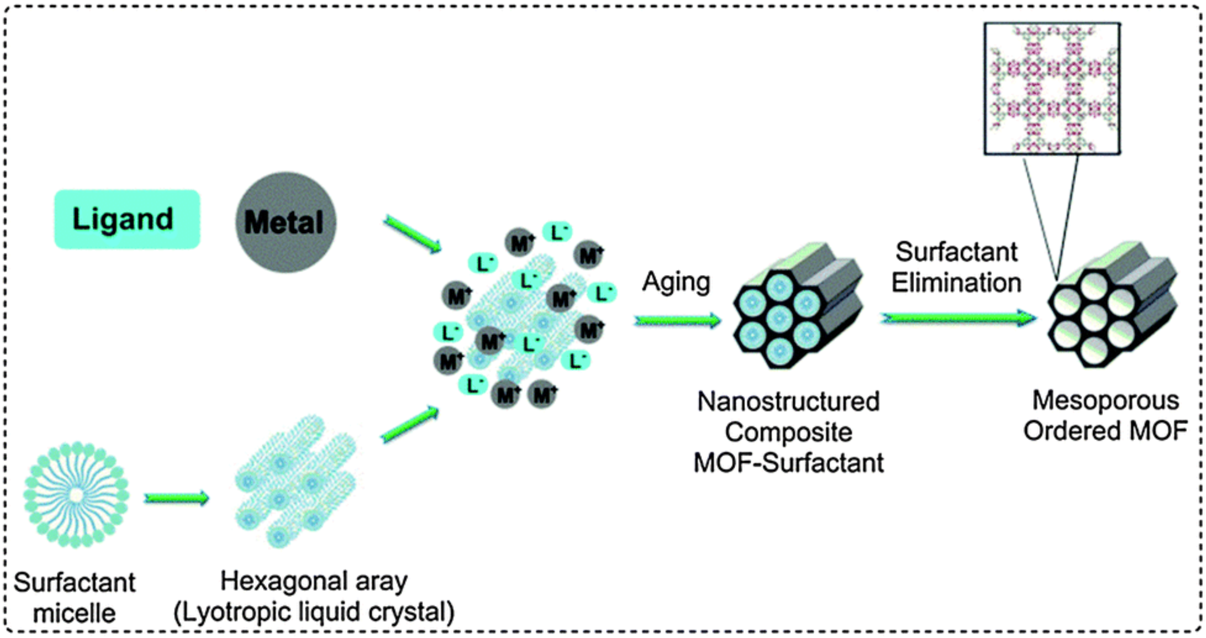

Figure 11. Illustration of the idealized supramolecular templating of mesoporous MOFs arising from co-assembly of the structure-directing agents liquid crystal phase with the metal ions and ligands required for framework formation. Reprinted from ref. 113. Copyright 2014, with permission from Royal Society of Chemistry.

In this context, an alternative synthesis route for safe MOF production is based on the use of ionic liquids. This method was originally reported by Morris *et al.*[114,115] According to his method, the ionic liquid works as a solvent, structure-directing agent and/or charge-compensating group. In MOF syntheses, ionic liquids have inherent advantages over organic solvents as they display no flammability, negligible vapor pressure and low toxicity.[116,117] Size scaling and the homogeneous order of the pores are targeted challenges inside the MOF community.[118] One opportunity to achieve these goals is the use of emulsions which can be combined with the surfactants mentioned in this chapter. Due to their impact on morphology modulation they can optimize synthesis routes.

1.2.5.7 Emulsion techniques

Most critical for MOF technology are the emulsion techniques, through which two goals can be targeted: The first one is the reduction of the particle size, and the second goal is the achievement of high yields. Emulsions can be differentiated between macroemulsions and microemulsions.[119] Macroemulsions are built of dispersed droplets with radii in the range of 1-90 µm, whereas microemulsions are built of dispersed droplets with radii in the range of 5−50 nm.[120] Both can be further differentiated between direct and reverse emulsions. Direct emulsions are given from hydrophobic "oil" droplets dispersed in a hydrophilic medium (water),[121] whereas reverse emulsions are formed from water droplets dispersed in a hydrophobic medium (organic solvent, oil). The size of the droplets depends strongly on the water to surfactant ratio and on the temperature. If a high reaction temperature is required, the coalescence of the droplets will occur and especially microemulsions do not remain intact at high temperatures.[122] Emulsions stabilized by surfactants help to control MOF nucleation and growth through micelles, which can work as nanoreactors.[123] Two processes are known for generating emulsions with small droplets/micelles. The first one is based on low-energy emulsification methods, whereas the second process includes high-energy emulsification methods. Among low energy methods, we can find the most widely used phase inversion temperature method which was first described by Shinoda and Saito.[124] Phase inversion of emulsions means the conversion of oil-in-water to water-in-oil system (or vice versa). The phase inversion temperature method is based on the temperature at which the phase transition occurs. A low temperature favours oil-in-water emulsions and high temperature favours water-in-oil emulsions.[125] For high-energy emulsification methods ultrasound generators are used. Ultrasonication is the topic of the following chapter. Reverse microemulsions have been used for the synthesis of MOFs37 wherein two-micellar systems (different micelles contained either the metal salt or the organic linker) were mixed and the reaction was started through coalescence.[126] The reaction temperature in reverse microemulsion synthesis for MOFs is between 0 °C and 120 °C.[127] Direct emulsion with the phase-inversion-temperature method can also be used for MOF particles in the nano range.[90]

1.2.5.8 Ultrasonication

Ultrasonication is a process that uses sound energy at high frequencies to achieve ultrasonic effects, which are based on acoustic cavitation and so-called hot spots. Cavitation involves the formation, expansion, and implosion of bubbles in a liquid.

Ultrasonication, like the other top-down methods milling/grinding[128,129] is a well-examined synthesis alternative. In MOF chemistry, top-down methods like milling or sonication lead in most cases to a surface area loss and amorphization. Ultrasonication is applicable for bottom-up strategies as well as for top-down approaches. The use of ultrasound from organic chemistry for the bottom-up synthesis of metal-organic compounds was first described by Qiu *et al.*[130] The cavitation collapse causes local temperatures up to almost 5000 °C and pressures of over 1000 atm. The hot spots have the advantage of enormous heating and cooling speed. Since nucleation and particle growth only take place during the hot spots and high-temperature based on cavitation drops within milliseconds, the size of the particles can be limited to the nano level. Using ultrasonication, nanosized MOF particles can be produced with good yields even at atmospheric pressure without an additional heating source. Nanosized MOFs also can be achieved by combining top-down with bottom-up methods.[131] They also introduced technologies and strategies from other scientific fields to yield homogeneous MOF nanoparticles with monodispersed size distribution (e.g., spray-drying strategy).[132] Above that, conventional MOF syntheses can be supplemented by the efficient, inexpensive and environmentally friendly ultrasonication for the preparation and processing of different kinds of nanoparticles. It is particularly effective in breaking up aggregates and in reducing the size and polydispersity of nanoparticles.[133] Furthermore, ultrasonication is a very helpful tool for optimizing the preparations of different other materials beyond MOFs. Among these different materials, the polymeric membranes play an important role. The preparation of polymeric membranes is a highly interesting scientific field. They are not only useful for various industrial applications, but can also be used in combination with MOFs for new high-quality products. The field of polymeric membranes, their properties, applications, etc. are being shown in the next chapter.

1.3 Mixed-Matrix Membranes (MMMs)

1.3.1 Origin

Membranes are thin polymer layers that offer a controlled passage of various compounds (i.e., gas molecules). In case gas molecules permeate through the membrane there are three distinguished principles (see Figure 12): Feed (i.e., liquid mixture whose components shall be separated), retentate (i.e., fluid that is retained by the membrane during the separation process), and permeate (i.e., component which permeates preferentially).[134]

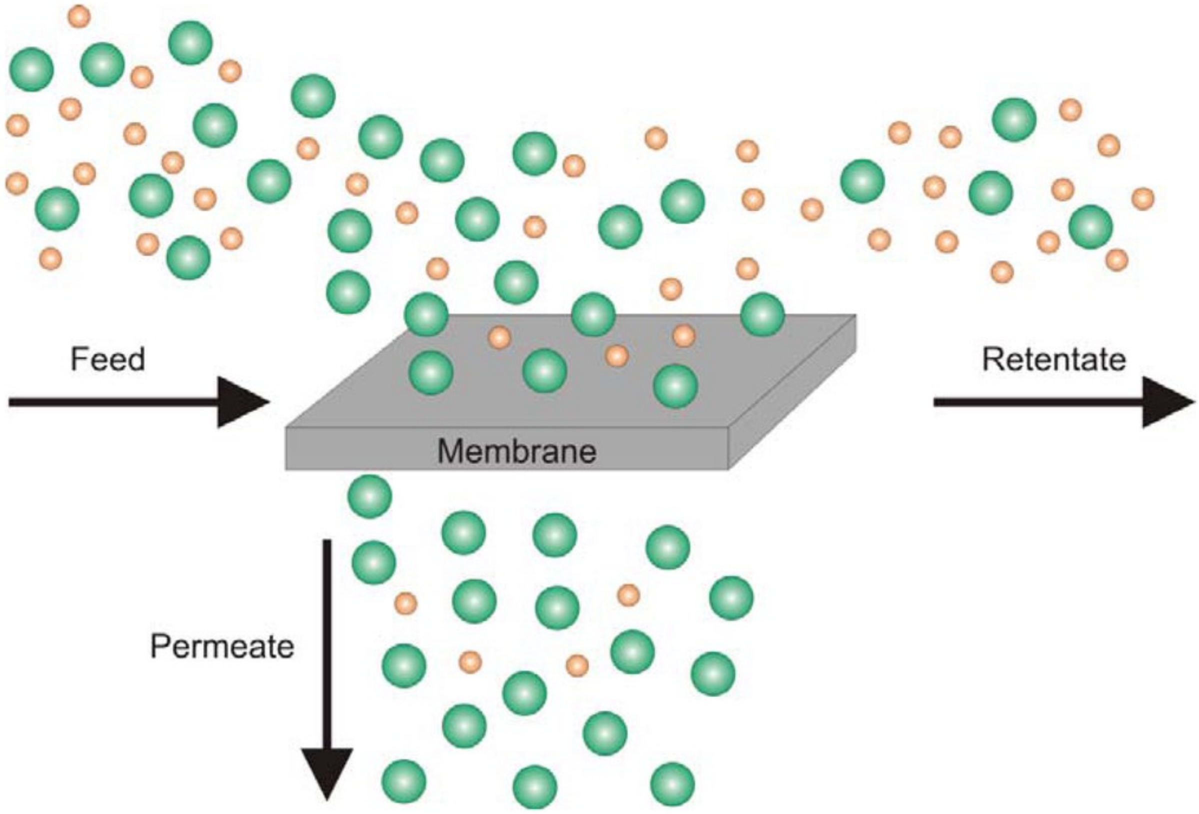

Figure 12. Principles of pervaporation. The liquid feed mixture flows along the membrane and the feed components diffuse into and through the membrane at different rates. The liquid retentate is depleted and the vaporous permeate enriched in the preferentially permeating component. Reprinted from ref. 134. Copyright 2012 by the authors; licensee MDPI, Basel, Switzerland. This figure is distributed under the terms of the Creative Commons Attribution 3.0 License, which permits unrestricted use, distribution, and reproduction in any medium, provided the original work is properly cited.

Since in 1833 Graham's law[135] states that the diffusion rate of a gas is inversely proportional to the square root of its density, several fundamental scientific works linked to gas separation membranes were explored, as summarized in Figure 13.[136]

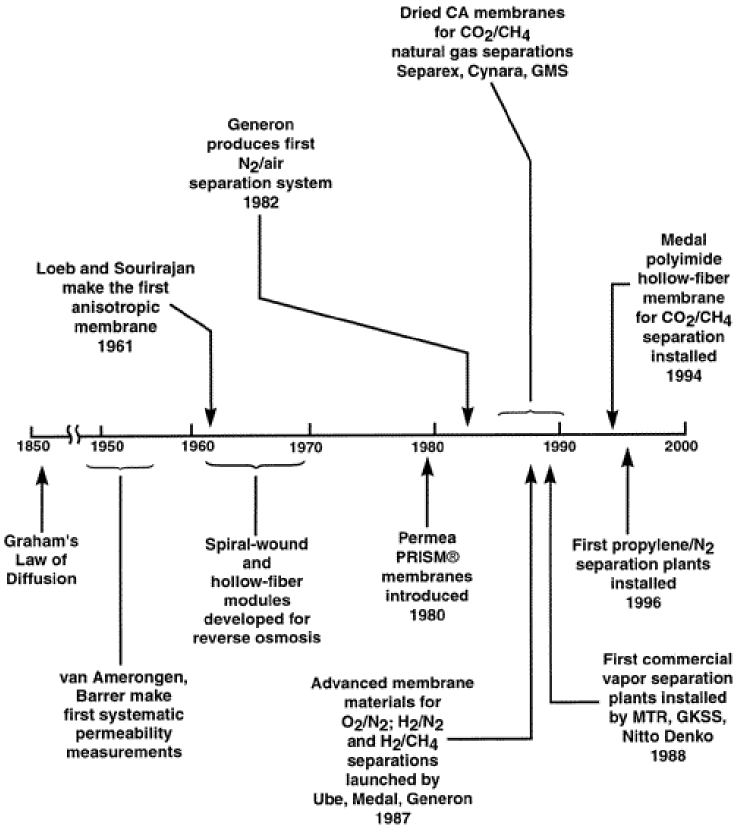

Figure 13. Milestones in the development of membrane gas separations. Reprinted from ref. 136. Copyright 2002, with permission from American Chemical Society.

In 1960, the first breakthrough of asymmetric phase-inverted membranes[137,138] triggered the use of membranes for gas separation in the industrial sector and the development of new membrane materials subsequently began to flourish. Pure organic polymer membranes are already applied for gas separation processes in the industry due to their cost and energy effectiveness, environmentally friendly use, as well as their simple and versatile manufacturing.[139] For making composite membranes (i.e., mixed-matrix membranes, MMMs) molecular sieves (i.e., inorganic fillers, dispersed phase) are incorporated in polymer materials (continuous phase). A schematic illustration of mixed-matrix membranes with dispersed phase embedded in the continuous phase is shown in Figure 14.

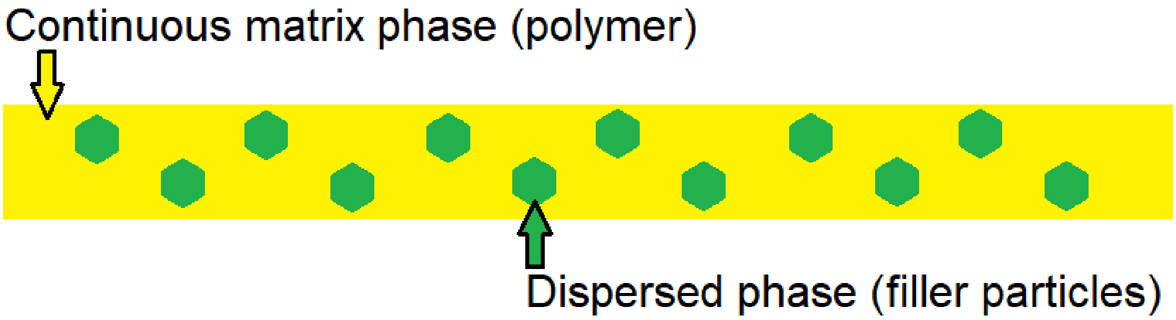

Figure 14. A schematic illustration of mixed-matrix membranes with dispersed phase embedded in the continuous phase.

1.3.2 Gas studies

Composite membranes can be used in gas separations and were firstly produced in 1993 with Polydimethylsiloxane and ethylene propylene diene monomer rubber.[140] Since then, the invention of MMMs with enhanced properties took place and a variety of materials and new technologies have moved into the research of MMMs.[141] Among the newly developed technologies, principles, and measurement innovations a particular interest can be seen in gas studies. Such studies have their roots in single gas measurements. Nowadays, these kinds of measurements run towards mixed-gas measurements (e.g., binary gas mixtures) instead of using single gas techniques. Mixed-gas studies are preferred as gas interaction and plasticization effects are more realistic[142]. Generally, for single and mixed-gas measurement approaches the gas flow through the membrane is either measured at constant pressure and variable volume or with a constant volume and variable pressure.[143] In case mixed-gas is used, the determination of the individual mole fractions of the mixture is a technical challenge as new and sensitive equipment is necessary. Although there is a notable shift towards mixed-gas measurements (i.e., they are state-of-the-art) this particular challenge has not yet been overcome by all research groups. Outdated single gas studies (with adjusted mathematical principles) are published to this day but it is evident that their number decreases.

1.3.3 Membrane materials

Various polymers are available for polymer membranes, and some of the available materials will be presented in this chapter. The immense choice of materials for both phases allows a great diversity of mixed-matrix membranes (MMMs). Therefore, for gas separation and gas storage the gas separation performance and gas molecule interaction with inorganic fillers are the two main factors that need to be targeted by designing desirable MMMs. If the focus of MMMs is on the separation performance, then glassy polymers with high selectivity deliver the required results and rubbery polymers with high permeability properties need to be avoided.[144,145,146] Nevertheless, glassy polymers have rigid structures and the prevention of voids between fillers and polymer as well as an optimal adhesion between both phases is still a challenging task. One of the most investigated polymers for MMMs is Matrimid 5218 (polyimide) which shows high mechanical stability, high chemical resistance, and a good permselectivity.[147] Other commonly used polymers are polysulfone, substituted polycarbonate, and poly(phenylene oxide).[148] There are different inorganic fillers, the most common fillers are mesoporous silica[149], zeolites,[150,151] carbon, carbon molecular sieves,[152,153] nanotubes,[154,155] and metal-organic frameworks.[156,157,158] The latest advances in MMM research show a notable tendency to use MOFs as fillers in the polymer matrix based on their well-defined and tuneable porosity.[159] A trend for the next-generation MMMs follows the incorporation of nanosized fillers,[160] as it is supposed that the quality of MMMs increases, due to the enhanced distribution, less agglomeration, and reduced sedimentation of nanosized MOF particles.[161]

1.3.4 Preparation of mixed-matrix membranes

For the fabrication of MMMs, three preparation techniques are known.[162] The first technique is called *in situ* polymerization and is the easiest method regarding preparation steps. However, this easy routine comes with a great risk of agglomerated filler particles. The risk can be reduced and controlled to a certain extent in case the filler particles have functional groups that can connect with polymer chains by covalent bonds. Generally, the procedure is a one-step method as the filler particles are mixed directly with the organic solvent and the organic monomers. During the stirring of the dispersion, the monomers polymerize, so that the last step – the casting – can carried out. For that, the polymer and filler dispersion are poured onto a flat surface (i.e., casting). After the solvent evaporation is completed, the MMMs are ready to be used as a thin film. For further improvement of the MMMs performance, the membranes are generally dried in a vacuum oven at a specific temperature (depending on the glass transition temperature of the polymer) to remove the remaining solvent. Casting and solvent evaporation can be controlled and have a notable impact on the performance of the thin film.[163] They are the last steps of each preparation technique and therefore will not be mentioned for the next two methods.

The second technique is the solution blending method. Although there are more steps involved, there is still the possibility, that filler particles aggregate again during preparation. The solution blending technique starts by dissolving the polymer in an organic solvent. To the homogeneous solution the inorganic filler is added before the membranes are cast on a flat surface. The solution blending method can be optimized by including the priming method. The priming method is based on two different solutions – one solution of the organic solvent and the polymer and one dispersion of the organic solvent and the filler particles. To the last one, a small amount of the polymer solution is given to enhance the compatibility between filler particles and polymer. By using ultrasonication for the dispersal of the small amount of polymer the distribution becomes more effective.[164]

The third technique is the sol-gel technique. Here, inorganic precursors and organic monomers/polymers are combined in one solution at the same time. One advantage is based on the hydrolyzation of the inorganic precursors and their formation to filler particles right inside the polymer resulting in a homogeneous distribution and homogeneous membranes.

After the materials have been briefly described, the measurement and calculation of their performance must be described. For measuring their performance, various devices are on the market that provide the equipment for single and mixed-gas measurements. However, there are just a small number of accepted and used equations for calculating their performances. They are explained in Chapter 1.3.5.4.

1.3.5 Models and methods for mixed-matrix membranes permeability prediction

1.3.5.1 Adsorption of gas molecules

Since MOF filler particles are used in MMMs, their effects on the adsorption of gas molecules must be described. The adsorption of gas molecules on molecular sieves and especially metal-organic frameworks are dependent on size and shape, molecular polarity, and counter-ions. All these physical properties determine whether and how gas molecules are being adsorbed on the surface of a MOF and how they pass the MOF sieve structure. In case of gas molecules being larger than the pore channels of a MOF, these gas molecules obviously cannot be adsorbed. Therefore, either the MOF shows the breathing and gate opening effect or a MOF with larger pore channels needs to be used. Polar and non-polar gas molecules can be adsorbed favorably under identical conditions. The metal cations of a MOF have two main effects. Firstly, they affect the adsorption of non-polar gas molecules due to the induced electrostatic interactions[165]. Secondly, they have preferred adsorption sites for polar or easily polarizable molecules and therefore, have influence on the electric field inside the pores. All mentioned effects have a high impact on the gas diffusion in polymers. Consequently, the gas diffusion itself needs to be investigated in more detail. The basic assumptions are presented in the next chapter, with particular focus on selectivity and permeability.

1.3.5.2 Selectivity and permeability

Understanding the nature of transport phenomena and the precise evaluation of transport coefficients (permeability, solubility, and diffusivity) is of fundamental and practical interest.[166] Gas diffusion in polymers is as well based on the free volume of the polymer (i.e., gaps between polymer chains) as on pressure and concentration gradients. One of the most important membrane properties is selectivity which can be determined from electrophysiological measurements. The selectivity of polymeric membranes is based mainly on their ability to separate compounds like gas molecules. The selectivity of polymer membranes toward gas "*A*" relative to gas "*B*," can be described as a separation process. By separation, one gas gets a faster permeation rate over a second gas. Another important membrane property is permeability. It is well known that the permeability of gas through MMMs depends on the intrinsic properties of both, the polymer and the filler. Therefore, the permeability can be influenced by the interaction between the polymer matrix with the inorganic filler as well as by the percentage of filler loading in the polymer[167]. By analyzing neat polymer membranes, it is a remarkable fact that permeability and selectivity are inversely correlated to each other such that a rise in permeability usually results in a loss in selectivity and vice versa. Their relationship is described in the next chapter.

1.3.5.3 Robeson upper bound limit

Plotting the gas measurement results, the relationship between both, selectivity and permeability, becomes clear and an upper limit of the membrane performance can be set. The current maximum selectivity for a given permeability is known as the Robeson upper bound limit and today many Robeson plots are available. [168,169]

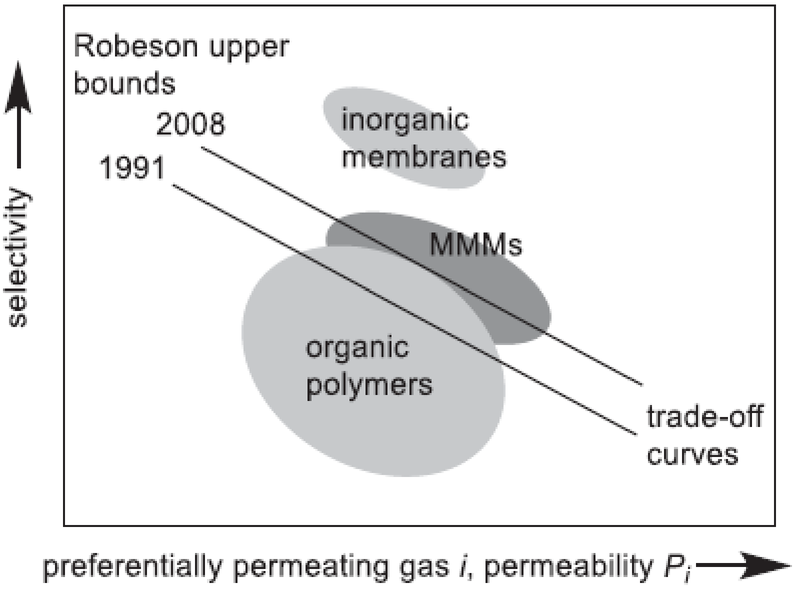

Figure 15. Schematic representation of the relationship between permeability and selectivity, with the 1991 and 2008 Robeson upper bounds shown.[168,169] The distance or position of the commercially interesting area relative to the upper bound can vary depending on the separation problem. Reprinted from ref. 170. Copyright 2012, with permission from Royal Society of Chemistry.

The Robeson plots for gas pairs show the permeability and selectivity of known dense membranes. They also prove that in case of permeability of the membrane increases the selectivity decreases. Also, by using the Robeson plots for pure polymer membranes it becomes obvious that the upper bound limit is difficult to break. One possibility to overcome the Robeson upper bound is seen in combining the organic polymer with porous filler particles (e.g., MOFs, zeolites).142 An ideal MMM should have both high permeability and a high selectivity. The concrete theoretical models are part of the next four chapters.

1.3.5.4 Theoretical model for permeability

Depending on the pore sizes in the polymeric matrix, there are a few fundamental transport mechanisms in gas separation. Among them there are the following which are described elsewhere: Poiseuille flow,[171] the Knudsen diffusion,[172] molecular sieving,[173] solution-diffusion.[174] For solution-diffusion there are the following principles for MMM: diffusion,168 sorption,[175] and selectivity.[176] The gas transport through a mixed-matrix membrane is a complex issue. And the separation process can take place through different mechanisms.172,[177] An effective MMM for natural gas separation should have good resistance against plasticization (e.g., induced by CO_2) and an inherently high permselectivity for mixed-gas processes (e.g., CO_2 and CH_4).[178]

A brief introduction on plasticization helps to understand the important effects gas molecules like CO_2 can have on membranes. Resistance against plasticization helps to prevent deterioration of separation performances at high pressure[179] and can be reduced by polymer cross-linking.164 Plasticization also describes the effect that the permeability of both gases increases and the selectivity decreases. This is due to an increase in the segmental motion of polymer chains at high feed pressures caused by the presence of one or more gas sorbates.[180] CO_2 which is highly condensable gas causes such plasticization,[181] less so CH_4 or N_2. In order to predict the gas permeability through membranes, many theoretical models are recommended. Using the following equation provided by Koros and Shimidzu, it is possible to calculate the permeability and selectivity for binary gas mixtures.[182] For permselectivity, permeability as well as separation are the two key parameters for the characterization of MMMs. To provide some details for both key parameters, it should be mentioned first, that permeability is the rate at which penetrants permeate through the membrane. The permeability of penetrant A (P_A) equals the diffusive flux of penetrant A ($Flux_A$) normalized by the change in partial pressure, ΔpA (cmHg), per unit thickness of the membrane, 1 (cm):

$$P_A = \frac{Flux_A \cdot 1}{\Delta_{pA}} \tag{1}$$

The values of polymer membranes for gas permeability are usually reported in Barrer units (1 Barrer = 1×10^{-10} cm^3 (STP) cm cm^{-2} s^{-1} cm Hg^{-1} = 3.348×10^{-16} mol m m^{-2} Pa-1 s^{-1}). The ideal selectivity (α) of a MMM for a gas mixture of two gases (gas A and gas B) is the ratio of the permeability of gas A (P_A) over the permeability of gas B (P_B). The efficiency of the membrane in enriching a gas over another gas can be expressed as a quantity (also described as separation factor, α). For a binary gas mixture that permeates through a membrane, the selectivity of the membrane toward gas "*A*" relative to gas, "*B*," can be described as ideal selectivity or ideal permselectivity, $\alpha_{(A/B)}$. In case the downstream pressure is negligible compared to the upstream one, $\alpha_{(A/B)}$ can be written as the ratio of permeabilities of gas penetrants A and B:

$$\alpha_{(A/B)} = \frac{P_A}{P_B} \tag{2}$$

Under these conditions, $\alpha_{(A/B)}$ is also called the ideal separation factor, which provides a fundamental measure of membranes performance.

The separation factor α_{AB} shows the ability of a MMM to separate a binary gas mixture. For the permeation of a gas mixture it can be calculated using the following equation:

$$\alpha_{A,B} = \frac{\gamma_{a,permeate} \,/\, \gamma_{b,permeate}}{\gamma_{a,retentate} \,/\, \gamma_{b,retentate}} \tag{3}$$

Here, $\gamma_{a,permeate}$ and $\gamma_{b,permeate}$ are the molar ratios of the gas A and B in permeate, $\gamma_{a,retentate}$ and $\gamma_{b,retentate}$ are the molar ratios of gas A and B in retentate.

The morphology of the MMM interface is also an important factor as it determines the transport properties. MMMs with ideal and nonideal interfaces have to be distinguished. To understand the properties of the interface not only gas permeation and sorption experiments are necessary but also appropriate modeling is needed.

1.3.5.5 MMMs with an ideal interface

The original concepts are based on ideal interfaces i.e., MMM with no voids around the filler particles. The model developed by James Clerk Maxwell for the prediction of steady-state dielectric properties in a conducting suspension of identical spheres can be used for MMMs separation performance prediction as there are analogue principles.[183,184,185] Therefore, the ideal MMM gas permeability can be calculated using the following equitation for effective permeability of MMMs with a dilute concentration of the dispersed phase:[186]

$$P_{eff} = P_c \left[\frac{nP_d + (1-n)P_c - (1-n)\Phi_d\,(P_c - P_d)}{nP_d + (1-n)P_c + n\Phi_d\,(P_c - P_d)}\right] \qquad (4)$$

Here, P_{eff} stands for effective permeability of a gas penetrant in a MMM with a volume fraction (Φ_d) of the dispersed phase (filler, d) in the continuous matrix phase (polymer, c), P_c and P_d show the gas penetrant permeability in the continuous and dispersed phases, respectively. n is the shape factor of the dispersed phase (n = 0 corresponds to the transport of gas through a MMM made of side-by-side layers of the two phases). The Maxwell model is based on ideal circumstances and implicates that there are no defects (i.e., holes) in the MMM. A defect-free polymer−particle contact of dispersed fillers in a polymer matrix is, however, difficult to achieve.

For the dilute suspension of spherical particles (n = is the shape factor of the dispersed phase = 1/3), the equation can be rewritten as the well-known Maxwell equation:

$$P_{eff} = P_c \left[\frac{P_d + 2P_c - 2\Phi_d\,(P_c - P_d)}{P_d + 2P_c + \Phi_d\,(P_c - P_d)}\right] \qquad (5)$$

The Maxwell model is used to predict the permeation properties of MMMs when the dispersion and distribution of filler particles in polymer matrix are homogeneous.

1.3.5.6 Mixed-matrix membranes with non-ideal interface

Mixed-matrix membranes with non-ideal interface have voids around the filler particles. Since dispersions of filler particles are not ideal in some cases, theoretical models have to be adapted in order to achieve realistic results. In addition to ideal effects, there are different effects associated with the incorporation of filler particles into a polymeric matrix. Such effects are for instance that the dispersed phase may create voids at the interface or have an impact on the rigidification in the polymer. Therefore, the incorporation of filler particles has a notable impact on the properties of the polymer phase.[187,184,188]

Before describing the impact on these, there are the following five various MMM morphologies: the ideal, void (between the filler particles and the polymer matrix), rigidified, with pore blocking, and agglomeration combined with pore blocking. All these different morphologies have a distinguished influence on the gas transport properties and different effects can be observed. Starting with the voids and low filler loading: here, an increase in gas permeability can be detected but with no noteworthy changes regarding the selectivity property. In case the filler loading is high and filler particles are not distributed homogeneously in the polymeric matrix, clusters of aggregated particles could be observed in combination with drastically decrease in selectivity. Rigidification is known to increase the selectivity but to decrease the permeability. For pore-blocking there is a special observation. The higher the pore blocking the more reduced becomes the permeability, while the selectivity rises. All non-ideal effects have their roots predominantly in thermal effects, solvent evaporation after casting, and/or clogging of the dispersed filler particles.[189] As for the synthesis of MMM large and small pore fillers can be used, they show channel defects and pore blocking.[190] The interface has a high impact on the transport property of MMMs even though the interface between the polymer matrix and inorganic filler particles occupies just a minor volume fraction around and less than 10^{-10} %.[141,144,175,191] Due to these non-ideal effects, there is need to obtain more accurate reproductions of experimental results. To accomplish this need and to determine the transport in more complex MMM systems (concerning defects, voids, and rigidification), next-generation (i.e., modified) permeation models based on Maxwell, Bruggeman,[192] and Pal[193] must be taken into consideration.

Proceeding from the fact that there are non-ideal effects the void permeability can be estimated using Knudsen approach:[194,]189

$$P_l = DS \tag{6}$$

$$D = D_{Knudsen}\left(1 - \frac{\sigma}{2l_l}\right) \tag{7}$$

$$D = D_{Knudsen}\left(d_{pore}/3\right)\left(8RT/\pi M_l\right)^{1/2} \tag{8}$$

$$S = \frac{1}{RT}\left(1 - \frac{\sigma}{2l_l}\right) \tag{9}$$

Here, P_l is the voids gas permeability, D is the modified Knudsen diffusion, S is the molecular solubility (concentration), σ_p is the Lennard-Jones diameter of gaseous penetrant, l_l is effective thickness of the formed void around the filler particles, d_{Pore} is pore diameter which is approximated as $2l_l$, R is the universal gas constant, T is the absolute temperature and M_l is the molecular weight of penetrant. With the knowledge of filler particles and voids, the effective P_{eff} (effective permeability of fillers particles) can be calculated according to the following equitation:[195] Φs is the volume fraction of the molecular sieve phase in the combined phase and is given by a simple expression:

$$P_{eff} = P_l \left[\frac{P_d + 2P_c - 2\Phi_d\,(P_l - P_d)}{P_d + 2P_l + \Phi_S\,(P_l - P_d)}\right] \tag{10}$$

$$\Phi_S = \frac{\Phi_d}{\Phi_d + \Phi_l} = \left(\frac{r_d}{r_d + r_l}\right)^3 \tag{11}$$

Here, P_{eff} is the permeability of the combined molecular sieve and interface phase, P_d is the permeability of the dispersed or sieve phase, P_l is the permeability of the interface, Φ_d is the volume fraction of the molecular sieve phase, Φ_i is the volume fraction of the interface (voids in the total MMM volume), and Φ_s is the volume fraction of the molecular sieve phase in the combined phase (filler particles in the voids), r_d is the average radius of filler particles. At last, the Maxwell model can easily be applied a second time to these more complicated structures of MMMs. Hence, the value of the combined permeability of molecular sieve and interface (voids), Peff can then be used with the continuous polymer phase permeability, Pc to calculate the permeability of the three-phase mixed-matrix membranes, PMMM:[196,197,198]

$$P_{MMM} = P_C \left[\frac{P_{eff} + 2P_C - 2(\Phi_d + \Phi_I)(P_C - P_{eff})}{P_{eff} + 2P_C + (\Phi_d + \Phi_I)(P_C - P_{eff})}\right] \tag{12}$$

The predictions according to the modified Maxwell model corresponded well with the experimental observations.

1.3.5.7 Free Fractional Volume

Another way to analyze permeation properties is to take a look at the so called Free Fractional Volume (FFV). The FFV is defined as the sum of the volume weighted FFV of the polymer and the volume weighted FFV of the filler (eq. 13).

$$\text{(Total) FFV} = \text{FFV}_{\text{polymer}} \cdot \phi_c + \text{FFV}_{\text{filler}} \cdot \phi_d \tag{13}$$

Whereby the FFV of the polymer can be deduced by the Bondi method, which is described in detail in the literature and was determined as 0.17 for Matrimid[199,200]. The FFV of the filler can be calculated by multiplying the pore volume of the filler with the density of the MOF, to yield a dimensionless entity. Equation (14) shows the correlation of the FFV and the permeability *P*:

$$P = A_p \cdot \exp^{(-\frac{B_p}{\text{FFV}})} \tag{14}$$

After linearization:

$$\lg P = \lg A_p - \frac{B_p}{2.303\text{FFV}} \tag{15}$$

Hence, lg *P* plotted against the inverse FFV should give a linear correlation with slope − $B_p/2.303$ and intercept lg A_p if indeed the FFV determines the permeability.

By using the described models and previously mentioned measurements, it is possible to design unique MMMs for specific applications. In combination with metal-organic frameworks/metal-organic frameworks nanoparticles, which were the subject of the first chapter, new materials can be developed and even outstanding technologies can be improved. In order to get an insight into some interesting MMM applications, the next chapter contains some interesting facts.

1.3.6 Application of metal-organic framework nanoparticles as additives in Mixed-Matrix Membranes

One of the most interesting applications of MOFs is their use in mixed-matrix membranes (MMM)[201]. Essential processes in the chemical and energy industries are gas separations, e.g., *n*-butane has to be separated from *iso*-butane by destillation. There is also the essential process of natural gas purification, whereby amine scrubbing is necessary to meet the pipeline specifications. Pure membranes for gas separations are already known for hydrogen recovery, air separation, and CO_2/CH_4 separation, but face challenges for H_2S removal and butane isomer separation. Advanced membrane materials are based on specific polymers that incorporate highly selective and permeable molecular sieve particles. The molecular sieve particles enable specific transport properties and interphase compatibility with the polymer and can be chosen according to the application. Zeolites can be incorporated into membranes to separate butane isomers, but show poor compatibility with organic polymers. Here, the MOFs come into play because they offer some very interesting opportunities in combination with polymers.[202] They are used for CO_2 removal from natural gas (i.e., natural gas sweetening), hydrogen isolation and recovery, and oxygen and nitrogen enrichment from the air.[203]

For usage in membrane technology, MOFs with high water stability are necessary. MIL-101Cr which was described above meets the requirement.57 Regarding the CO_2/CH_4 separation, the adsorption of CO_2 in MIL-101 is higher than that of CH_4 because of the higher polarization and quadrupole moment of CO_2.[204] Other MOFs meet also the requirement; therefore, it can provide promising opportunities for developing MMMs with original MOFs. Especially regarding permeability and selectivity the limits have not yet been reached. Additionally, the use of MOFs in MMMs provides numerous potential advantages over other inorganic fillers as for example the superior compatibility with the polymer matrix.[205]

1.4 Resonance-assisted hydrogen bonds

This chapter is based in parts on the publication: I. Gruber, L. Bensch, T. J. J. Müller, C. Janiak, B. Dittrich, *Z. Kristallogr.* **2020**, 235.[206]

1.4.1 Hydrogen bond

The hydrogen bond is unique in its importance for numerous processes in chemistry and biochemistry.[207-210] A strong or classic hydrogen bond occurs when there is an interaction between an electron-rich center (A) and a sufficiently positively polarized H atom, which is part of a covalent bond with an electronegative atom (D). The D-H···A hydrogen bond can appear either between different molecules (intermolecular) or in the same molecule (intramolecular). In both cases, the D-H bond distance is to some extent elongated compared to equivalent distances where the acceptor atom (A) is missing. A special kind of hydrogen bond has been reported where the proton is shared equally between the atoms D and A (D···H···A). Here, short H···O distances lead to effective coupling between two covalent and one ionic valence bond structures in a low barrier hydrogen bond (LBHB, see Figure 16).[211,212]

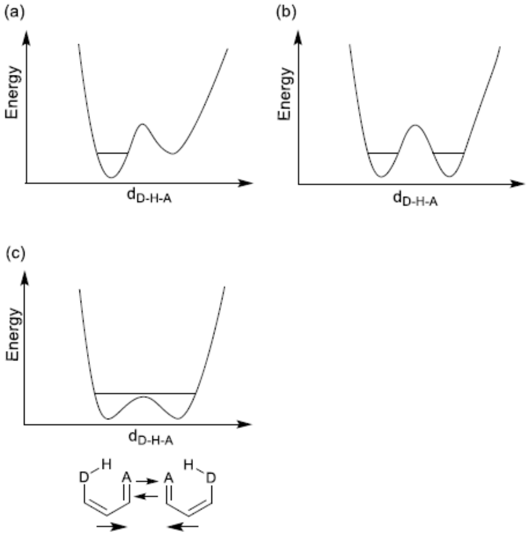

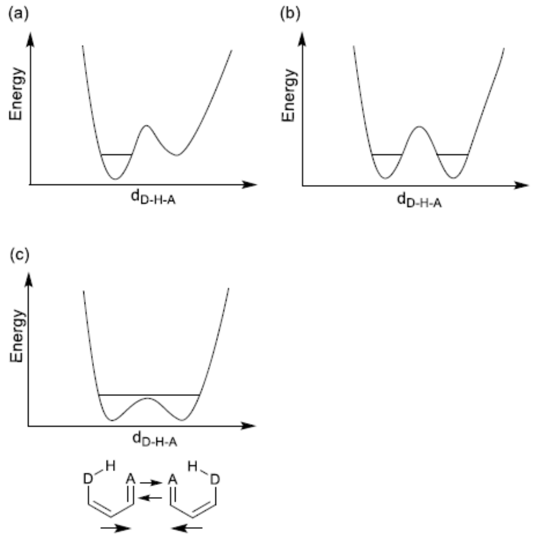

Figure 16. Schematic potential-energy curves for hydrogen bonds (D-H···A). Asymmetric double-well potential (a), symmetric double-well potential (b) and low barrier hydrogen bond LBHB (c). In the LBHB case two proton normal modes D-H···A and A···H-D are shown. The thick arrows indicate the transverse dipole moment which inverts with tautomerization.

1.4.2 Low barrier hydrogen bond

Four characteristics for such a low barrier hydrogen bonds have been defined:[213,214] Firstly, the distances between the atoms in D···H···A are longer compared with normal D-H and H-A covalent bonds and secondly, the D···H···A bonds are based on two energetically equivalent valence bond resonant forms. Thirdly, the resonance through D···H···A leads to an energetic stabilization, which grants the fourth feature, namely that also the D···A distance is shorter than in a normal hydrogen bond. Although the last criterion leads to an increase in the interatomic repulsion, the resonance-based stabilization is able to compensate this repulsion. Such special or near-symmetric hydrogen bonds are often formed between charged moieties.[215] For O-H···O systems these special hydrogen bonds are often found when O···O distances are very short (below 2.5 Å). For cases where a short-strong hydrogen bond exists, Gilli *et al.* introduced the term resonance-assisted hydrogen bond (RAHB) in 1989 as a particular case of an intramolecular hydrogen bond, which is supported by a conjugated π-electron system (see Figure 17) and where six-, eight-, or ten-membered neutral rings are formed.[216,217,218]

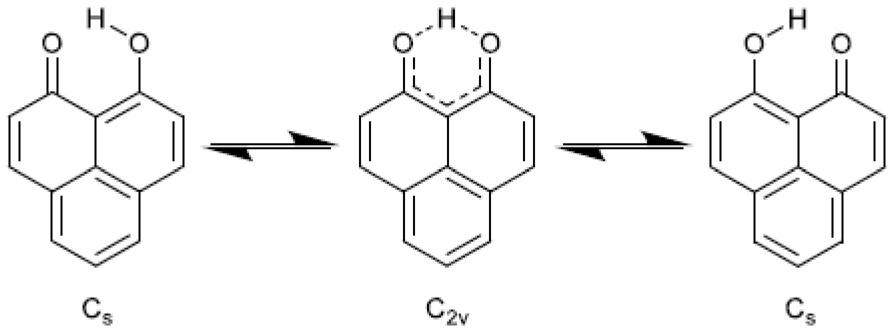

Figure 17. Interconversion between two equivalent minimum energy (C_s) structures with asymmetric hydrogen bridges in 9-hydroxyphenalen-1-one as an example of an enolized diketone or hydroxyl ketone. The interconversion occurs through a symmetric (C_{2v}) (transition-state) intermediate.

1.4.3 Resonance-assisted hydrogen bond

Another work published in 2009 by Gilli *et al.* further differentiated the hydrogen bond between RAHBs. Here, the two oxygen atoms are interconnected by a system of π-conjugated double bonds (-O-H···O=), charged assisted hydrogen bonds (CAHB, divided into negative (-O-H···O⁻-) and positive (=O···H⁺···O=), also known as (–/+)CAHB), and low barrier hydrogen bonds.[219,220] A detail representation is shown in Figure 18.

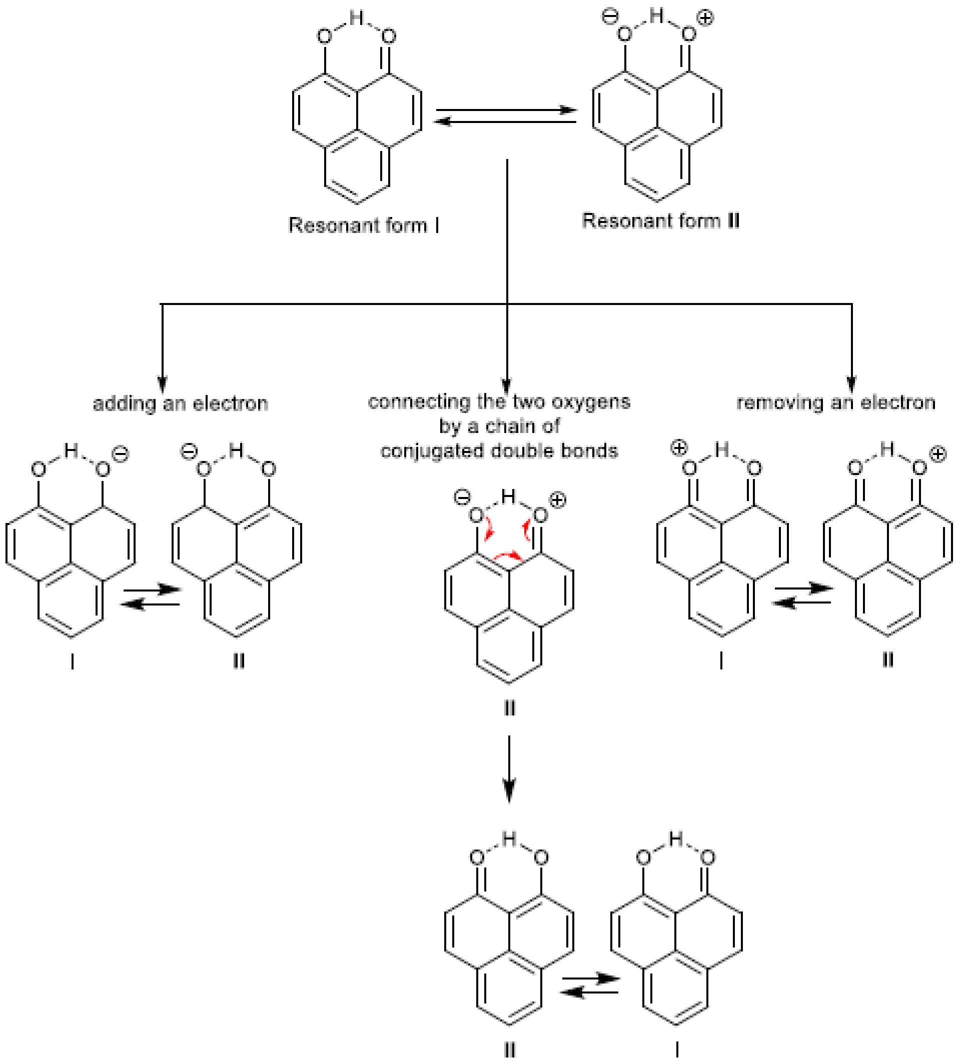

Figure 18. Two resonant forms I and II and three possible ways to interconvert them.

According to Emsley's empirical studies the delocalization of the π-conjugated system becomes greater in case the hydroxyl ketone unit forms either intramolecular or infinite-chain intermolecular hydrogen bonding.215 For investigations of such strong hydrogen bonds of keto-enols, 9-hydroxyphenalenone is a suitable example. The molecule contains a hydroxyl ketone unit[221] and is an electron acceptor, known for its ability to react as a radical anion,[222,223] but is also known for forming metal complexes.[224,225,226,227,228] It was first synthesized by Koelsch in 1941.[229] Derivatives are used for many different applications,[224] in particular, for catalytic reactions[230] and as neutral radical conductors.[231] The functionalization in the 5-positions of 9-HP has remained rather rare,224,[232] but considering electronic and photophysical properties was systematically investigated by Bensch et al,[233] who have also performed DFT computations. Bensch *et al.* also highlighted that conjugated 5-substituted 9-HP systems are synthetically accessible without unusual protection of the hydroxyl group due to a strong intramolecular hydrogen bond.221 The strength of this hydrogen bond was also characterized by IR spectroscopy, where no O-H stretching band could be found in an experimental IR spectrum.227

For the unsubstituted 9-hydroxyphenalenone, an earlier crystal structure analysis indicated that a symmetric intramolecular hydrogen bond could be present (also called symmetric C_{2v} form.[234,235] Variable-temperature NMR studies on hydrogenated malonaldehyde and its deuterated form already uncovered that a fast interconversion might occur between asymmetrically hydrogen bonded structures of this bistable molecule, resulting in rapid prototropy between two equivalent tautomers (also called asymmetric C_s forms).[236,237] The ^1H and ^{13}C NMR studies showed that unsubstituted 9-HP has C_{2v} symmetry in solution down to 130 K. However, it was pointed out that the C_{2v} symmetry could be due to fast interconversion among the two asymmetrically C_s forms. Here π-electrons could probably adapt to the proton motion in combination with reorganization of carbon-oxygen bond lengths and angles. Moreover, it has been calculated that the proton experiences a tunneling effect and therefore a double minimum potential, implying structural alteration regarding the equilibrium configuration and the transition state.[238,239] Ab initio SCF calculations on 9-HP supported the existence of two equivalent minimum-energy structures with an asymmetric hydrogen bridge. According to these computations the interconversion between the two minima occurs through a symmetric (C_{2v}) intermediate which is 5.20 kcal/mol above the minimum-energy C_s structures.[240] How do the results from SC-XRD fit into this picture is the subject of the second focus of this thesis.

2. Objectives of this work

Two research focuses have emerged that define the agenda of this thesis. The first one considers an improved synthesis route for nano/microsized MIL-101Cr. The first research focus also includes the application of theses nano/microsized MIL-101Cr in mixed-matrix membranes. The second research focuses consider the improved determination of a C_{2v} symmetric resonance-assisted hydrogen bond in 9-hydroxyphenalenones.

The main objectives of this work are:

- Shortened syntheses of nano/microsized metal-organic framework (MOF) particles with consistent or improved properties. In summary, the size of the prototypical MOF MIL-101Cr can be adjusted in the nano-micro-range below 100 nm by using microwave heating in combination with a direct emulsion technique, surfactants, and ultrasonication.

- Application of these MOF particles in mixed-matrix membranes in order to improve gas separation. The use of nano/microsized MIL-101Cr in Matrimid mixed-matrix membranes allowed for the preparation of 24 wt% filler mixed-matrix membranes compared to a maximum of 20 wt% for microsized MIL-101Cr. All in all, the thesis highlights the potential of MOF nano/micro particles in mixed-matrix membranes with wider implications.

- The solid-state structures of three H-bonded enol forms of 5-substituted 9-hydroxyphenalenones were investigated to accurately determine the H atom positions of the intramolecular hydrogen bond. Therefore, single-crystal X-ray diffraction data were evaluated by invariom-model refinement and QM/MM computations were studied.

3. Cumulative part

The following sections (3.1–3.9) present the published works of this thesis. The published work is self-contained with a short introductory part and in case for section 3. 1 and 3.2 a separate list of references. Before each section, a short overview is given. A statement about the author's share of work is presented. For the publications as co-author (section 3.3–3.9), only a brief summary and description of the contribution to the publication is given.

3.1 Synthesis of nano/microsized MIL 101Cr through combination of microwave heating and emulsion technology for mixed matrix membranes

Irina Gruber, Alexander Nuhnen, Arne Lerch, Sandra Nießing, Maximilian Klopotowski, Annika Herbst, Matthias Karg, Christoph Janiak
Front. Chem. 7 (2019), 777, 1-19
DOI: 10.3389/fchem.2019.00777

Nano/microsized MIL-101Cr was synthesized by microwave heating of emulsions for the use as a composite with Matrimid mixed-matrix membranes (MMM) to enhance the performance of a mixed-gas-separation. As an example we chose CO_2/CH_4 separation. Although the incorporation of MIL-101Cr in MMMs is well known, the impact of nanosized MIL-101Cr in MMMs is new and shows an improvement compared to microsized MIL-101Cr under the same conditions and mixed-gas permeation. In order to reproducibly obtain nanoMIL-101Cr microwave heating was supplemented by carrying out the reaction of chromium nitrate and 1,4-benzenedicarboxylic acid in heptane-in-water emulsions with the anionic surfactant sodium oleate as emulsifier. The use of this emulsion with the phase inversion temperature (PIT) method offered controlled nucleation and growth of nanoMIL-101 particles to an average size of less than 100 nm within 70 min offering high apparent BET surface areas (2900 $m^2\ g^{-1}$) and yields of 45 %.

Author's share of work:

- Designing and performing of the synthetic work and evaluation of the MOF results.
- The mixed gas measurements and calculations were performed by A. Nuhnen
- Writing of the manuscript and drawing of the figures, graphs and tables except for:
    - figure 7, 9, 10, S2, S28-S30: done by A. Nuhnen,
    - figure S17 - S23: done by A. Lerch, and
    - figure S4: done by C. Janiak.
- Editing of the manuscript regarding the reviewers' comments by I. Gruber, A. Nuhnen, and C. Janiak.

Synthesis of nano/microsized MIL-101Cr through combination of microwave heating and emulsion technology for mixed-matrix membranes

Irina Gruber[1], Alexander Nuhnen[1], Arne Lerch[2], Sandra Nießing[1], Maximilian Klopotowski[1], Annika Herbst[1], Matthias Karg[2] and Christoph Janiak[1]*

[1]Institut für Anorganische Chemie und Strukturchemie, Heinrich-Heine-Universität Düsseldorf, Düsseldorf, Germany.
[2]Institut für Physikalische Chemie, Heinrich-Heine-Universität Düsseldorf, Düsseldorf, Germany.

*** Correspondence:**
Prof. Dr. Christoph Janiak
janiak@uni-duesseldorf.de

Keywords: Metal-organic framework (MOF), MIL-101Cr, nano/microsized MOF, microwave heating, emulsion, surfactants, mixed-matrix membranes (MMMs).

Abstract

Nano/microsized MIL-101Cr was synthesized by microwave heating of emulsions for the use as a composite with Matrimid mixed-matrix membranes (MMM) to enhance the performance of a mixed-gas-separation. As an example we chose CO_2/CH_4 separation. Although the incorporation of MIL-101Cr in MMMs is well known, the impact of nanosized MIL-101Cr in MMMs is new and shows an improvement compared to microsized MIL-101Cr under the same conditions and mixed-gas permeation. In order to reproducibly obtain nanoMIL-101Cr microwave heating was supplemented by carrying out the reaction of chromium nitrate and 1,4-benzenedicarboxylic acid in heptane-in-water emulsions with the anionic surfactant sodium oleate as emulsifier. The use of this emulsion with the phase inversion temperature (PIT) method offered controlled nucleation and growth of nanoMIL-101 particles to an average size of less than 100 nm within 70 min offering high apparent BET surface areas (2900 m^2 g^{-1}) and yields of 45 %. Concerning the CO_2/CH_4 separation, the best result was obtained with 24 wt% of nanoMIL-101Cr@Matrimid, leading to 32 Barrer in CO_2 permeability compared to 6 Barrer for the neat Matrimid polymer membrane and 21 Barrer for the maximum possible 20 wt% of microMIL-101Cr@Matrimid. The nanosized filler allowed reaching a higher loading where the permeability significantly increased above the predictions from Maxwell and free-fractional-volume modelling. These improvements for MMMs based on nanosized MIL-101Cr are promising for other gas separations.

Introduction

New porous materials have been constructed from metal-organic and –inorganic cluster building blocks by a smart choice regarding the building units. Now it is possible to produce extended anionic, cationic and neutral porous frameworks with unique pore architectures and functions (Yaghi et al., 1998). Moreover, there are also the opportunities that independent one-, two-, and even three-dimensional nets interpenetrate each other in many solid-state structures of polymeric, hydrogen-bonded nets and coordination polymers (Batten and Robson, 1998). The existence of building units with different sizes with close topologies results into the definition of the notion of “scale chemistry” which concerns the edification of solids with several building units, either inorganic, organic, or hybrid, and the consequences it has for the corresponding frameworks and the voids they generate (Férey, 2000). For chemical and physical functionalities robustness of a metal-organic framework is required even in the absence of guest molecules in the cavities. The stability depends mainly on the structural dimensionality of the assemblages (Kitagawa and Kondo, 1998). The method of transforming molecular complexes and clusters to extended solids is essential to translate molecular geometry into assembled structures as well as to converting molecular reactivity into desired physical properties (Yaghi et al., 2000). Secondary building units are molecular complexes and cluster entities. Ligand coordination modes and metal coordination environments can be utilized in the transformation of secondary building units into extended porous networks using polytopic linkers. Consideration of the geometric and chemical attributes of the secondary building units and linkers leads to prediction of the framework topology (Eddaoudi et al., 2001). Metal-organic frameworks (MOFs) are a unique class of porous crystalline organic-inorganic hybrid compounds build from metal nodes and bridging organic linkers (Yaghi et al., 2003). They promise applications in small molecule adsorption and storage (Li et al, 2009), gas and liquid separation (Tanh Jeazet et al., 2012 (a)), catalysis (Beyzavi et al., 2015), sensing (Chen et al., 2009), drug delivery (Horcajada et al., 2012), heat transformation and other applications (Janiak and Henninger, 2013; Erucar and Keskin, 2018; Azar and Keskin 2018). However, the inherent microporosity of most metal-organic frameworks prevents a fast access of molecules to the internal surface in larger MOF crystallites. A faster access of molecules to the internal surface is desirable for application in adsorption/desorption and storage and can be achieved by reduction of the diffusion path length by decreasing the crystal size (Rieter et al., 2006; Lin et al., 2009) or by enlargement of the pores through defects towards hierarchical micro-meso-macropores (Shen et al., 2015). In this work, we focus on the reduction of the diffusion path length through decreasing the particle size. There are various approaches to control the MOF particle size, i.e., microwave-assisted routes (Khan et al., 2011), surfactant-mediated syntheses (Huang et al., 2003), reverse microemulsions (Lin et al., 2009), and sonochemistry (Khan and Jhung 2015). Among those strategies microwave heating and the use of surfactants have been the most advantageous method (Khan et al., 2015; Huang et al., 2018). Microwave heating is known to enhance rates of nucleation and crystal growth process, including acceleration of nucleation over crystal growth (Diring et al., 2010). Moreover, in microwave reactions the required temperatures can be reached within seconds (Galema, 1997) and microwave heating is an "instant on/instant off" energy source, significantly reducing the risk of overheating reactions (Bogdal, 2006).

Most critical was the emulsion technique, through which we tried to achieve two goals: The first one was the reduction of the particle size, the second goal was good yields. As shown in **Table S1** in the Supplementary Material, already published results for MIL-101Cr via microwave heating show particle sizes between 49 – 200 nm. A view on the described yields shows relatively low yields (35-38 %) (Khan et al., 2011) or no statement concerning the yield (Wuttke et al., 2015). Emulsions stabilized by surfactants also help to control MOF nucleation and growth through micelles, which can work as nanoreactors (Khan et al., 2010)]. Emulsions can be differentiated between macroemulsions (= emulsions) and microemulsions (Wu et al., 2017). Macroemulsions are built of dispersed droplets with radii in the range of 1-90 µm, whereas microemulsions are built of dispersed droplets with radii in the range of 5−50 nm (Carr and Shantz, 2005). Both can be further differentiated in direct and reverse emulsions (**Figure 1** and **Figure S6**).

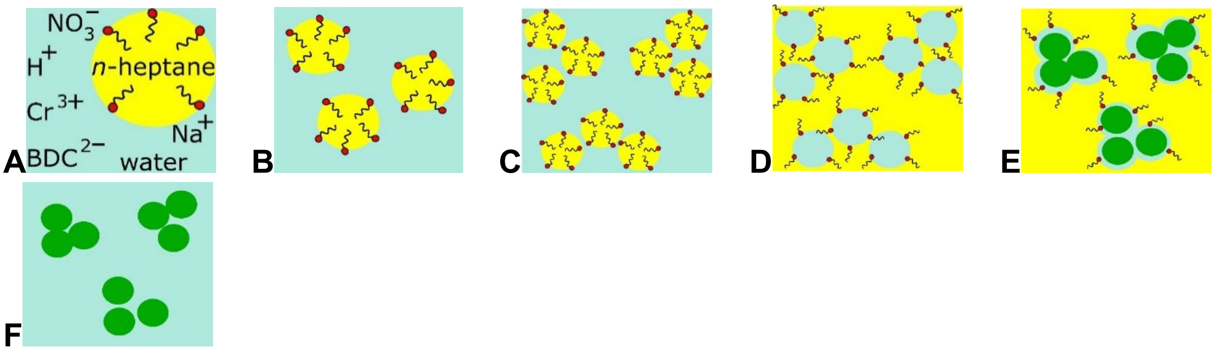

Figure 1 The anticipated direct emulsion mechanism for the formation of nanoMIL-101Cr (depicted as green spheres). BDC^{2-} = benzene-1,4-dicarboxylate, Cr^{3+} = chromium salt, NO_3^- = nitrate ion, and micelles with hydrophobic groups of sodium oleate oriented towards the center of heptane oil droplets (hydrophilic groups = red spheres). MOF precursors are in the aqueous phase **(A)**. At higher temperature, the heptane droplets expand rapidly **(B)**, at the PIT (phase inversion temperature) the size of the heptane droplet reaches a minimum **(C)**, phase inversion occurs **(D)**, reverse micelles work as nanoreactors for nanoMIL-101Cr and in addition coalescence occurs **(E)**, isolated and agglomerated nanoMIL-101Cr particles in water after washing procedure **(F)**.

Direct emulsions are given from hydrophobic "oil" droplets dispersed in a hydrophilic medium (water) (Salvia-Trujillo et al., 2018), whereas reverse emulsions are formed from water droplets dispersed in a hydrophobic medium (organic solvent, oil). The size of the droplets or micelles depends strongly on the water to surfactant ratio and on the temperature. If a high reaction temperature is required, coalescence of the micelles will occur and especially microemulsions do not remain intact at high temperature (Whitby et al., 2012). Therefore, we speak only generally of emulsions here and do not use the term microemulsion, because droplet sizes vary during the reaction procedure. So far, only reverse microemulsions have been used for the synthesis of MOFs (Rieter et al., 2006) wherein two-micellar systems (different micelles contained either the metal salt or the organic linker) were mixed and the reaction was started through coalescence (Wang et al., 2018). The reaction temperature in reverse microemulsion synthesis for MOFs was between 0 °C and 120 °C (Taylor et al., 2008). There are no reverse emulsion syntheses for MOFs known, where higher temperatures (> 180 °C) were used.

Two processes are known for generating emulsions with small droplets. The first one is based on high-energy emulsification methods (e.g., ultrasound generators), whereas the second process includes low-energy emulsification methods. Among low energy methods, we can find the most widely used phase inversion temperature (PIT) method which was first described by Shinoda and Saito (Shinoda and Saito, 1969). Phase inversion of emulsions means the conversion of oil-in-water to water-in-oil system (or vice versa) as shown in **Figure 1** and **Figure S6**. The PIT method is based on the temperature at which the phase transition occurs, such that for example a low temperature favors oil-in-water emulsions and a high temperature favors water-in-oil emulsions (Kale and Deore, 2017). This method leads to a reduction of the interfacial tension of the surfactant, providing droplet fragmentation and inverting the water-in-oil emulsion phase to an oil-in-water emulsion. At the PIT the droplet size and the interfacial tension reaches a minimum. Important information about phase structures in the phase inversion temperature (PIT) range were presented by Benton et al. (Benton et al., 1986). Other examples of inversion in the PIT range are “abnormal emulsions”. Here, the surfactants are preferentially located in the dispersed phase of an emulsion (Sajjadi et al., 2004). The PIT depends on surfactant concentration (Izquierdo et al., 2002) as well as on the type of oil and the hydrophilic chain length of the surfactants. Therefore, in the case of an oil-in-water emulsion, the stability increases significantly with the chain length of the hydrophile–lipophile group of the surfactant and the emulsion droplets are usually negatively charged because of the selective adsorption of OH^- onto the droplet surfaces (Mei et al., 2011). The PIT method is mostly used in combination with non-ionic surfactants but recent studies have shown that a specific oil emulsion can be produced by using combinations of sodium caseinate and Tween 20 (Su and Zhong, 2016). Also, a nonionic/anionic surfactant blend exhibits a higher PIT than the corresponding nonionic-only system. This result can be attributed to the hydrophilic nature of anionic surfactants. Mishra et al. studied the effect on PIT of an oil-in-water emulsion stabilized by anionic surfactant (Kundu et al., 2013). Moreover, Kale et al. also showed the influence on PIT of an oil-in-water emulsions stabilized by an anionic surfactant (Kale and Deore, 2017). Studies also have shown that the formation and properties of emulsions prepared according to the PIT approach can be modulated by using a combination of nonionic and cationic surfactants. With increasing cationic surfactant concentration not only the PIT increased but also the positive charge on the oil droplets after emulsion formation (Mei et al., 2011). Positively charged oil-in-water emulsions were prepared by Sun et al. by adding a cationic surfactant to the system. The cationic molecules raise the PIT above 100 °C (Mei et al., 2011).

One of the most interesting applications of MOFs is their use in mixed-matrix membranes (MMM) (Sorribas et al., 2014). Pure organic polymer membranes are already applied for gas separation processes in industry due to their cost and energy effectiveness, environmentally friendly use, as well as their simple and versatile manufacturing (Seoane et al., 2015). Essential processes in the chemical and energy industries are gas separations, e.g., n-butane has to be separated from iso-butane by distillation. There is also the essential process of natural gas purification, whereby amine scrubbing is necessary to meet the pipeline specifications. Pure membranes for gas separations are already known for hydrogen recovery, air separation and CO2/CH4 separation, but face challenges for H2S removal and butane isomer separation. Advanced membrane materials are based on specific polymers which incorporate highly selective and permeable molecular sieve particles. The molecular sieve particles enable specific transport properties and interphase compatibility with the polymer and can be chosen according to the application. Zeolites can be incorporated into membranes to separate butane isomers, but show poor compatibility with organic polymers. Here the MOFs come into play, because they offer some very interesting opportunities in combination with polymers (Liu et al., 2018). They are used for CO_2 removal from natural gas (natural gas sweetening), hydrogen isolation and recovery, and oxygen and nitrogen enrichment from air (Miricioiu et al., 2019). However, permeability and selectivity of neat polymer membranes are inversely correlated to each other such that a rise in permeability usually results in a loss in selectivity and vice versa. The current maximum selectivity for a given permeability is known as the Robeson upper bound limit (Robeson, 1991; Robeson, 2008). One possibility to overcome the Robeson upper bound is seen in combining the organic polymer with porous filler particles (e.g., MOFs, zeolites) as an additive in so-called mixed-matrix membranes (Dechnik et al., 2017). Latest advances in MMM research use MOFs as fillers in the polymer matrix based on their well-defined and tuneable nanoporosity (Zornoza et al., 2013). One of the most investigated polymers for MMMs is Matrimid 5218 (**Figure S3**) which shows high mechanical stability, high chemical resistance, and a good permselectivity (Nuhnen et al., 2018). A trend for the next-generation MMMs follows the incorporation of nanosized fillers (Carreon et al., 2017), as it is supposed that the quality of MMMs increases, due to the enhanced distribution, less agglomeration, and reduced sedimentation of nanosized filler particles (Zornoza et al., 2011).

For use in membrane technology MOFs with high water stability are necessary and MIL-101Cr (**Figure S4**) meets the requirement (Janiak and Henninger, 2013). With a view on CO_2/CH_4 separation, the adsorption of CO_2 in MIL-101 is higher than that of CH_4, because of the higher polarization and quadrupole moment of CO_2 (Chowdhury et al., 2012). Moreover, Zhao et. al. have achieved with nanosized MIL-101Cr a significant enhancement of CO_2 adsorption compared to bulk MIL-101 due to the 'nano-effect' of porous materials for gas adsorption (Zhao et al., 2018). Hence, MIL-101Cr is an appropriate filler in MMMs for CO_2/CH_4 gas separation. To the best of our knowledge, there is no study on the nanoMIL-101Cr in Matrimid (nanoMIL-101Cr@Matrimid) for CO_2/CH_4 mixed-gas separation. In the present work, the formation of nanoMIL-101Cr (corresponds to MOFs with a size in the nano- and lower micrometer range) was achieved by the combined approach of surfactant emulsion and ultrasonication followed by microwave heating. MicroMIL-101Cr (corresponds to MOFs with a size in the middle micrometer range) was synthesized according to the literature (Yang et al., 2010). Subsequently, we show an improved mixed-gas permeation performance of nano- over microMIL-101Cr@Matrimid membranes towards the separation of the binary gas mixture of CO_2 and CH_4.

Materials and Methods

Materials

All chemicals were obtained commercially and were used without further purification: $Cr(NO_3)_3 \cdot 9H_2O$ (Acros Organics, 99 %), HNO_3 (Grüssing, 65 wt%), 1,4 benzenedicarboxylic acid (H_2BDC, Acros Organics,> 99 %), tetramethylammoniumhydroxid (TMAOH , 25 wt.% in water, Sigma Aldrich), sodium oleate (Tokyo Chemical Industry, >97 %), hexadecyltrimethylammonium bromide (CTAB, Sigma Aldrich, 95 %), Triton X-45 (Sigma Aldrich), Matrimid® 5218 powder (Huntsman, **Figur S3**), n-heptane (Sigma Aldrich, p.a.), DMF (VWR, p.a.), ethanol

(VWR, p.a.), and dichloromethane (DCM, Fisher Chemical, 99.9 %). All experimental work was performed in air. De-ionized (DI) water was used.

Instrumentation

Powder X-ray diffraction (PXRD) patterns were obtained on a Bruker D2 Phaser powder diffractometer equipped with a flat silicon, low background sample holder using Cu−K_α radiation (λ = 1.5418 Å, 30 kV, 10 Ma, ambient temperature). With this sample holder at 2θ <~10° the beam spot is strongly broadened so that only a fraction of the reflected radiation reaches the detector; hence lower relative intensities are measured in this range. For all samples 2θ angles between 5 and 50° over a time of 105 min, that is 0.007°/sec, were measured. Simulated patterns of MIL-101Cr were calculated with CCDC Mercury 3.9 program using the single crystal data of MIL-101Cr obtained by Rietveld refinement (CCDC no. 605510, Refcode OCUNAC) (Férey et al., 2005). **Nitrogen physisorption** (**N_2**) isotherms were obtained with a Nova 4000e from Quantachrome at 77 K. For measuring the isotherms, the MOF powders were loaded into glass tubes and weighted before they were degassed at 150 ° for 2 h under vacuum. After that, the glass tubes were weighted again. At last, they were transferred to the analysis port of the sorption analyzer. Apparent Brunauer-Emmett-Teller (BET) surface areas were calculated from the adsorption branch of the nitrogen physisorption isotherms. In this work we refer to the microporous MOF surface areas from Type I isotherms as 'apparent BET' based on reference (Thommes et al., 2015), where it is noted that 'the BET-area derived from a Type I isotherm must not be treated as a realistic probe accessible surface area' but 'represents an apparent surface area, which may be regarded as a useful adsorbent “fingerprint” ' Nonlinear (NL-)DFT calculations for pore size distribution curves were done with the native NovaWin 11.03 software using the ‘N_2 at 77 K on carbon, slit pore, nonlinear density functional theory (NLDFT) equilibrium’ model (Gelb et al., 1999). Note that the NL-DFT calculations only yield pore size distributions in the micropore (< 2 nm, 20 Å) to low mesopore (< 10 nm, 100 Å) regime. BET surface areas and pore volumes (measured at $P \cdot P_0^{-1} = 0.95$) were calculated from N_2 sorption isotherms. **Infrared (IR)** spectra were obtained with a Bruker FT-IR Tensor 37 in attenuated total reflection (ATR) mode in the range 4000−500 cm^{-1}. **Scanning electron microscopic (SEM)** images were recorded with a Zeiss DSM 982 and a Jeol JSM-6510LV QSEM Advanced electron microscope with a LAB-6 cathode at 20 keV. The microscope was equipped with a Bruker Xflash 410 silicon drift detector and the Bruker ESPRIT software for EDX analysis. The membrane cross-sections were prepared through freeze-fracturing after immersion in liquid nitrogen. The membrane fractions were mounted on a sample holder (**Figure S1**) and coated with gold by a Jeol JFC 1200 fine-coater at an approximate current of 20 mA for 20−30 s. Dark and light areas around cross-section of membranes depend on mounting on SEM sample holder. Light areas are a consequence of the nearby metal sheet which for stability purpose is screwed close to the membrane (**Figure S1**). **Transmission electron microscopy** (**TEM**) micrographs were taken at room temperature with a Zeiss E902 ATEM. Samples were deposited on 200 µm carbon-coated copper grids. The size distribution was calculated from a manual diameter determination over a minimum of 50 isolated particles. **Dynamic light scattering** (**DLS**) experiments were conducted with a 3D LS Spectrometer operated in 2D mode (LS Instruments,, Fribourg, Switzerland) using a HeNe-laser (λ=632.8 nm) with a maximum constant output power of 35 mW as light source. The measurements were performed at scattering angles from θ=30°-140° and at a constant temperature of

25 °C, which was achieved by a heat-controlled decalin bath connected to a circulating water bath (Julabo CF31). The light scattered by the sample was detected by two avalanche photodetectors operating in pseudo-cross-correlation mode. For all measurements dust-free, disposable culture tubes made of borosilicate glass (Fisher Scientific, Schwerte, Germany) were used. Samples for light scattering experiments were prepared by redispersion of freeze-dried particles in water using ultrasonication and filtration with a syringe filter (5 µm pore size, PTFE, hydrophobic). Temperature stability was achieved by equilibration of the samples for at least 30 min in the decalin bath before the measurements. All measurements were repeated three times using acquisition times of 60 s each. The resulting intensity-time autocorrelation functions were analyzed by the CONTIN algorithm using the software AfterALV 1.0e (Dullware, Wageningen, the Netherlands) yielding the relaxation rate distributions G(Γ). For an angle dependent diffusion analysis the mean relaxation rates Γ of the dominating species in the intensity-weighted G(Γ) were plotted versus the squared scattering vector q^2 to analyze whether translational diffusion is probed. The polydispersity index (PDI) is shown in the supplementary material (calculated according Kozlov et al., 2017, PDI = (standard deviation/ average nanoparticle size)^2). As a **microwave reactor** a CEM Mars 6 with 55 mL sample tubes used. A **Sonics vibra-cell** VCX 750 ultrasound generator with Microtip 630-0419, Amplitude 20 %) was employed for both emulsion types.

Mixed gas permeation

The membranes were placed inside the membrane module composed of two stainless steel parts with a cavity (4.5 cm in diameter) in which a macroporous disk support (20 µm nominal pore size, Mott Corp.) is gripped inside with Viton o-rings. Before the measurement, the membranes were heated for 1 h in a vacuum oven at 150 °C for removing residual moisture traces through storage. The composition of the feed gas mixtures and the purge gas flow (sweep gas) were controlled by an **OSMO Inspector** device (Convergence Industry B.V; **Figure S2**). Gas concentrations in the outgoing stream were evaluated by an Agilent 490µGC on-line **gas micro-chromatograph** equipped with a thermal conductivity detector (TCD). Gas concentrations in the permeate were measured every 30 minutes until steady state was reached (up to 8 hours). Permeability results in Barrer (1 Barrer = 1 x 10^{-10} cm^3 (STP)cm/(cm^2 s cmHg) were obtained from the concentrations in steady state. The real separation selectivity of the mixtures was calculated as the ratio of the mole fractions of the components in the permeate and the feed stream. Permeation measurements were performed at 25 °C controlled by a flexible heating coil. The carrier gas was Helium. After the mixed-gas permeation investigations, the thickness of the membranes was measured at ten different places using a micrometer screw as a **thickness measuring device**. A binary mixture of CO_2 and CH_4 (50 % of CO_2) was used as a feed gas in permeability and selectivity measurements. Permeation experiments were conducted at 25 °C,4 bar feed pressure and 1 bar permeate pressure. The permeability of the membranes was calculated by the following two equations (Abedini et al., 2014):

$$\boldsymbol{P_{CH_4} = \frac{2.73.15 \times 10^{10}\left(1 - y_{CO_2}\right)VL}{760\,AT\,[\left(1 - x_{CO_2}\right)(P_0 \times 76)/14.7]}\left(\frac{dP}{dt}\right)}$$

$$P_{CO_2} = \frac{2.73.15 \times 10^{10} y_{CO_2} VL}{760\, AT\, [\, x_{CO_2} (P_0 \times 76)/14.7]} \left(\frac{dP}{dt}\right)$$

P_{CH4} and P_{CO2} (Barrer): permeability of gases in Barrer;
L (cm): membrane thickness;
T (°C): experiment temperature;
V (cm^3): constant volume vessel;
A (cm^2): membrane surface area;
P_o (cmHg): feed pressure;
(dP/dt): slope of pressure versus time.

The selectivity was calculated by the following equation:

$$\alpha_{A/B} = \frac{y_A/y_B}{x_A/x_B}$$

x: mole fractions in the feed gas; y: mole fractions in the permeate.

Maxwell model and Bruggeman model

The Maxwell model can be used to describe the gas transport through a dense composite membrane (Bouma et al., 1997).

For spherical particles the permeability of the composite membrane P_{eff} can be calculated as follows:

$$P_{eff} = P_c \frac{P_d \cdot (1+2\phi_d) + P_c \cdot (2-2\phi_d)}{P_d \cdot (1-\phi_d) + P_c \cdot (2+\phi_d)}$$

With P_c as permeability of the continuous phase, P_d is the dispersed phase permeability and ϕ_d is the volume fraction of the filler.

In cases where the permeability of the filler is much higher than the permeability of the continuous phase ($P_d >> P_c$) the upper equation can be written as follows:

$$P_d \gg P_c;\ \frac{P_{eff}}{P_c} = \frac{(1+2\phi_d)}{(1-\phi_d)}$$

As in the Maxwell model no filler-filler particle interactions are considered, the model is only valid for low filler loadings up to a volume fraction of about 0.2 for the filler (ϕd) (Pal, 2008).
The volume fraction of the filler in the dispersed phase can be calculated as follows:

$$\phi_d = \frac{w_d/\rho_d}{\left(\frac{w_c}{\rho_c}\right) + \left(\frac{w_d}{\rho_d}\right)}$$

Where, w_d and w_c are the weight percentages, ρ_d and ρ_c the densities of the filler and the polymer, respectively.

The Bruggeman model is based on the effective medium theory and does consider the presence of nearby particles for the permeation properties. Hence, the Bruggeman model is valid for high filler loadings especially.

The permeability for composite membranes can be calculated as follows:

$$\left(\frac{P_c}{P_{eff}}\right)^{\frac{1}{3}} = (1-\phi_d) \cdot \left(\frac{P_d}{P_c} - 1\right)$$

For fillers with distinctly higher permeabilities compared to the continuous phase ($P_d >> P_c$) the equation simplifies to:

$$P_{eff} = \frac{P_c}{(1-\phi_d)^3}$$

Dynamic light scattering

We performed DLS measurements at different scattering angles θ and thus at different magnitudes of the scattering vector q:

$$|\vec{q}| = \frac{4\pi n}{\lambda} \sin\frac{\theta}{2}$$

Here λ corresponds to the wavelength of the incident light and n to the refractive index of the dispersing medium. Analysis of the q-dependence of the relaxation rate Γ allows for a diffusion analysis.

For purely translational diffusion, Γ scales with the square of q:

$$D_t = \frac{\Gamma}{q^2}$$

The diffusion coefficient D_t can then be used to calculate the hydrodynamic radius R_h of the particles in dilute dispersion using the Stokes–Einstein equation (Cao, 2003):

$$R_h = \frac{kT}{6\pi\eta D_t}$$

Here k is the Boltzmann constant, T the absolute temperature and η the solvent viscosity.

Synthesis of nanoMIL 101Cr in direct emulsion

The chosen parameters led to positive results using our microwave reactor and the tubes provided for this purpose. It should be mentioned, that other research groups with different microwave reactors/tubes might have used different parameters.

Direct emulsion contains DI water, *n*-heptane, surfactant, HNO_3, and the starting material for MIL-101Cr. First, a solution of H_2BDC (0.33 g, 2 mmol), $Cr(NO_3)_3 \cdot 9H_2O$ (0.80 g, 2 mmol), 5 mL water, and 1.0 equivalent of HNO_3 (with respect to chromium nitrate) were mixed together. This solution was combined with a solution of sodium oleate (0.14 g, 0.34 mmol), 5 mL of water, and ultrasonicated with *n*-heptane (5 mL) for one minute. The pH value was 4. After the ultrasonication the solution was transferred into microwave ractor tubes with a volume of 55 mL. The direct emulsion was heated to 180 °C within 30 min and kept at this temperature for 10 min (another batch was kept at 180 °C for 40 min). Other direct emulsons were prepared as discribed above but heated to 210 °C for 30 min and kept at 210 °C for 10 min (another batch for 40 min). After cooling to RT within 15 min the green MIL-101Cr powder was collected by centrifugation and purified as follows: Washing with water (1.00 g MOF to 1.50 L water) by stirring the dispersion for 24 h in order to remove the sodium oleate.

Then, the product was washed with hot DMF and hot ethanol two times (2 x 50 mL, 24 h) to remove remaining terephthalic acid. The product was activated under vacuum (50 mbar) at 150 °C for 24 h. The reactions were carried out several times to ensure reproducibility. Syntheses without the presence of HNO_3, syntheses by replacing HNO_3 with NaOH (to get pH 7), syntheses without *n*-heptane, and direct emulsion in combination with CTAB and Triton X-45 yielded no MIL-101Cr product.

Attempted synthesis of nanoMIL 101Cr in reverse emulsion

In a one-micellar system, where all reactants are in one micelle, the reaction starts by increasing the temperature or triggering the reaction through other parameters (Anjali and Basavaraj, 2018). Because of the fact that at high temperature micelles coalesce anyway, there is no point in separating the MOF precursors in different micelles at the beginning. Therefore, we suspended all MOF precursors in the same aqueous phase before forming the emulsion (**Figure S5** and **Figure S6**).
The reverse emulsion experiments were carried out in a water-in-oil emulsion of chromium(III) nitrate nonahydrate, terephthalic acid and nitric acid in a PTFE- (Teflon-) lined vessel at 180 °C for 70 min reaction time under microwave heating.

A solution of H_2BDC (0.33 g, 2 mmol), $Cr(NO_3)_3{\cdot}9H_2O$ (0.80 g, 2 mmol), 4 mL DI water, and 1.0 equivalent HNO_3 (with respect to chromium nitrate) were mixed together. This solution was combined with a solution of one of the modulators, sodium oleate (1.00 g, 3.28 mmol), CTAB (1.00 g, 2.73 mmol), or Triton X-45 (1.00 g, 2.47 mmol) in 4 mL of DI water and ultrasonicated with *n*-heptane (40 mL) for 1 min. The pH value was 4. After the ultrasonication the solution was dived into three parts and all transferred into microwave ractor tubes with a volume of 55 mL. The reaction was initiated by an increase in temperature up to 180 °C for 30 min (heating ramp) in closed 55 mL Teflon vessels by microwave heating at 600 W. After finishing the heating ramp the reaction was hold at 180 °C for 40 min (dwelling time). Further steps follow the same route mentioned above. It should be mentioned that with lower amounts of sodium oleate the stability of the direct emulsion gets lost and with a higher amount of sodium oleate or with an increase of temperature higher 210 °C only amorphous material was obtained. To verify the relevance of an acidic modulator, we tried to synthesize nanoMIL-101Cr according to the direct emulsion method using NaOH instead of HNO_3. We also tried to synthesize nanoMIL-101Cr according to the direct emulsion method without HNO_3. Also we tried to carry out the synthesis without heptane and just in water with additives. After microwave heating there was no MIL-101Cr material at all. Different variations of direct/reverse emulsions are listed in the Supplementary Material.

Synthesis of microMIL 101Cr with TMAOH (conventional synthesis)

The hydrothermal synthesis of MIL-101Cr was adapted from the literature (Yang et al., 2010). H_2BDC (0.332 g, 2 mmol) was added to an alkali solution of 10 mL deionized water (DI water) and tetramethylammonium hydroxide (5 mL, 0.05 mol/L) and stirred at RT for 5 min. $Cr(NO_3)_3{\cdot}9H_2O$ (0.8 g, 2 mmol) was added to the mixture and stirred for 5 min. The resulting mixture was transferred into a 20 ml Teflon-lined autoclave for 24 h at a heating temperature of 180 °C. The green powder was collected by repeated centrifugation and thorough washing with 50 mL DMF at 150 °C, 50 mL ethanol at

100 °C, and 50 mL DI water at 100 °C. The product was activated under vacuum at 150 °C for 24 h.

Preparation of Matrimid membranes

For the pure Matrimid membrane a certain amount of polymer and DCM were mixed together and stirred for 24 h. The yellowish solution was not further treated before it was cast into 8 cm diameter metal rings, which were placed on a flat glass surface. Next, the rings were covered with funnels with some paper tissue until the membrane was dry (after approximately 1.5 h).

The funnels were used to prevent contamination by dust particles during the evaporation of the solvent and also to control the evaporation rate. As soon as all solvent was evaporated, the membranes were removed from the metal rings and the glass surface by flushing the rings with deionized water. The membranes were kept in a vacuum oven for another 24 h at 150 °C and 50 mbar to remove the residual solvent. After the membranes were naturally cooled to ambient temperature they have been tailored to the size of the sample holder (4.5 cm in diameter) and stored in air and RT for characterization and permeation tests. Details for the specific amounts of polymer and solvent are listed in **Table 2**.

Table 2 Weight and mass content of Matrimid and MOF in mixed-matrix membranes**.**

MOF [wt%]	Matrimid [g]	DCM (Matrimid) [ml]	MOF [g]	DCM (MOF) [ml]	Matrimid-DCM[a] for priming [ml]
0	0.80	7.0	-	-	-
8	0.80	7.0	0.07	9.0	0.67
16	0.80	7.0	0.15	9.0	1.34
24	0.80	7.0	0.25	9.0	2.01

[a] Taken from the prepared Matrimid-DCM solution.

Preparation of mixed-matrix membranes

For all MMMs nanoMIL-101Cr was used which was obtained by direct emulsion and sodium oleate (210 °C, 70 min). MMMs were fabricated by a dense film casting method using a “priming” technique (Mahajan and Koros, 2002). This technique involves the addition of low amounts of polymer to the MOF-DCM-suspension prior to the incorporation of the particles into the polymer matrix. Priming has shown to support greater affinity between the filler and the polymer, resulting in a symmetric MMM with improved transport properties.

By using the priming technique, a Matrimid-DCM-solution was prepared for each MOF/Matrimid membrane sample (8 wt%, 16 wt%, and 24 wt%) and stirred for 24 h. This solution was then combined with an already prepared nanoMIL-101Cr-DCM-suspension in two steps. For the MOF-DCM-suspension certain amount of MIL-101 was suspended in DCM and stirred for 24 h. Then, the MOF-suspension was sonicated for 15 minutes with high power ultrasound before stirring it for another 45 minutes. This procedure was repeated three times. Next, the green suspension was combined with a specific fraction of the previously prepared Matrimid-DCM-solution and stirred again for 24 h (corresponding to the first step of priming). After that, the blend was sonicated for 15 minutes and stirred for 45 minutes (here also a repetition of another 2 times was conducted). Before casting, the leftover Matrimid-DCM-solution was combined with the MOF-DCM-Matrimid-suspension and kept under stirring for 1 h. This final suspension was casted into metal rings. After the solvent was evaporated the membranes were detached, tailored, dried overnight and stored as described above. Details for the specific amounts of MOF, solvent, and polymer are listed in **Table 2**. The experiments were made on mixed-matrix membranes containing 8, 16 and 24 wt% of MIL-101. Each type of membrane was prepared and measured three times to provide reliable error estimates.

Results and Discussion

MIL-101Cr syntheses

MIL-101Cr (MIL = Matériaux de l'Institute Lavoisier) has become one of the most important MOFs (Férey et al., 2005; Zhao et al., 2015). It is hydrothermally very stable (Khutia et al., 2013), offers good adsorption of gases (Khutia and Janiak, 2014), water (Wickenheisser et al., 2013), and organic compounds (Rezk et al., 2013), catalytic Lewis- and Brønsted-acid activity (Herbst and Janiak, 2016), and polymer compatibility in mixed-matrix membranes (MMMs) (Tanh Jeazet et al., 2012 (b)). The MIL-101Cr crystallites have an octahedral shape, and the framework is built from trinuclear {$Cr_3(\mu_3\text{-}O)(F,OH)(H_2O)_2$} nodes and 1,4-benzenedicarboxylate (bdc) linkers (**Figure S4A**) to give hexagonal (15-16 Å) and pentagonal windows (12 Å) (**Figure S4B**), inner cages of 29 Å and 34 Å in diameter (**Figure S4C**) (Wickenheisser and Janiak, 2015), and large apparent BET surface area (4100 $m^2\ g^{-1}$) in a zeotypic structure (**Figure S4D**). For the synthesis of MIL-101Cr long reaction times of 8 h, and temperatures in the region of 160 °C to 220 °C with hydrothermal autoclaving are usually needed (Férey et al., 2005). Further, for a typical synthesis of MIL-101Cr hydrofluoric acid is often used as a problematic additive or modifier (Férey et al., 2005). Overpressure (autoclaves) and/or heterogeneous reaction mixtures render reaction control difficult and require expensive equipment, especially when it comes to scale-up, hence, are not desirable for large-scale or commercial syntheses (Jeremias et al., 2016). Therefore, a more efficient synthesis of MIL-101Cr is highly wanted. For example, nitric acid, HNO_3 was also shown to act as mineralizing agent and increased crystallinity and yield (Zhao et al., 2015).

In order to decrease reaction time and particle size we tested microwave heating in combination with emulsion techniques. Nanosized particlesof MIL-101Cr can be synthesized by microwave heating alone (Khan et al., 2011), yet in our hands the use of microwave heating alone did not lead to reproducible results. Although there are syntheses published to obtain MIL-101Cr with microwave heating and water alone, we could not synthesize MIL-101Cr adopting the published procedures for our microwave reactor. Therefore, we tried to adjust the syntheses and used the direct and reverse emulsion technique in combination with microwave heating. With both techniques we were able to obtain MIL-101Cr in our microwave reactor. To the best of our knowledge we present here the first report where microwave heating, emulsions, and ultrasonication are used in combination for the synthesis of MIL-101Cr nano/microparticles, leading to good yields (45 %) in short reaction times (~70 min) without the use of HF or a steel autoclave. Because no HF was used for the syntheses, the formula of the MIL-101Cr framework should be $[Cr_3(O)(OH)(bdc)_3(H_2O)_2]$.

For the stabilization of the emulsions we tested three different surfactants, which are generally utilized for MOF emulsion synthesis (**Figure 2**).

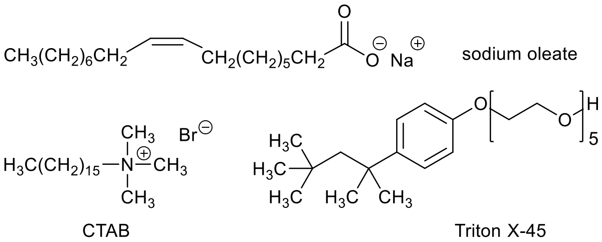

Figure 2 Chemical formulas of the used surfactants sodium oleate, cetyltrimethylammonium bromide (CTAB), and Triton X-45.

Sodium oleate was chosen exemplarily for a monocarboxylic acid and anionic-surfactant, because it should strongly interact with the MOF surface via coordinative bonds and attractive electrostatic forces to open metal sites. This interaction should lead to an adsorption on the MOF surface and inhibits further growth and aggregation (Diring et al., 2010). CTAB was chosen due to its cationic nature and because it is known to slow down the nucleation and growth of MOFs (Jiang et al., 2011). Triton X-45 was tested as a nonionic surfactant to achieve additional mesoporosity (Du et al., 2016).

The direct and reverse emulsions were employed under identical temperature and reaction time conditions. All experiments were carried out with 2 mmol each of chromium(III) nitrate nonahydrate and terephthalic acid in a PTFE- (Teflon-) lined vessel at 180 – 210 °C for 40 - 70 min (see SI). Using direct emulsion, we mixed the MOF precursors and the surfactant together in a heptane-in-water emulsion; for reverse emulsion in a water-in-heptane emulsion. The emulsions were ultrasonicated before heating, otherwise heptane and water would quickly separate again as bulk phases. Ultrasonication achieved sufficient dispersion of the respective droplets in the continuous phase yielding long-time stable emulsions. Baloch et al. have shown that an increase in ultrasonification time increases the number of *n*-heptane droplets and decreases their average size and the degree of dispersity, hence improves the emulsion quality (Baloch and Hameed, 2005). Once the reaction was finished, the MIL-101Cr powder was purified and activated.

It turned out that only the direct emulsion technique in combination with sodium oleate as surfactant gave reproducible and satisfying yields (45 %) together with crystalline products of high apparent BET surface areas around 2900 $m^2\ g^{-1}$ (**Table 1**).

Table 1 Reaction conditions and results for the synthesis of nanoMIL-101Cr.

conditions[a] **surfactant,**[b] **temp.**	**Time**[c] **[min]**	**S_{BET}**[d] **[$m^2 \cdot g^{-1}$]**	**Size**[e] **[nm]**	**V_{pore}**[f] **[$cm^3 \cdot g^{-1}$]**	**Yield**[g] **[%]**
direct emulsion					
SO (180°C)	40	1337	<100	0.55	34
second batch		1032		0.50	23
SO (180°C)	70	2269	<100	1.05	43
second batch		2400		1.08	30
SO (210°C)	40	1744	<100	0.73	37
second batch		1555		0.75	25
SO (210°C) [h]	70	2923	<100	1.32	45
second batch		2663		1.19	31
reverse emulsion					
SO (180°C)	70	561	<100	0.31	36
second batch		417		0.21	21
CTAB (180°C)	70	862	n.d.	0.42	20
second batch		706		0.35	33
TX-45 (180°C)	70	401	n.d.	0.21	22
conventional synthesis (see SI for details) [Fehler! Textmarke nicht definiert.]					
microMIL-101Cr [h]	24 h	2741	350±70	1.25	64

[a] All synthesis and other details are given in the Supporting Information. Stated reactions have been carried out in duplicate to ensure reproducibility. [b] SO: sodium oleate; CTAB: cetyltrimethylammonium bromide; TX-45: Triton X-45. [c] Time for heating ramp plus dwelling time. [d] Apparent BET surface area calculated in the pressure range $0.05 < p/p_0 < 0.2$ from N_2 sorption isotherms at 77 K with an estimated standard deviation of ± 50 $m^2\ g^{-1}$. [e] Particle size based on SEM pictures, for microMIL-101Cr statistic based on 50 particles. [f] Total pore volume calculated from N_2 sorption isotherms at 77 K ($p/p_0 = 0.4$) for pores ≤ 3.2 nm. [g] Yield is based on Cr. [h] Used in mixed-matrix membrane fabrication. n.d. not determined.

This result may be based on the phase inversion, whereby the oil-in-water emulsion inverts into a water-in-oil emulsion and provides nanoreactors for MOF particles (**Figure 1**). From FTIR-ATR the infrared band assignments of sodium oleate can still be seen in nanoMIL-101Cr but only as a minor contribution (**Figure S7**) (Roonasi et al., 2010). Concering the yield we note that in the original synthesis procedure by Férey et al. (Férey et al., 2005) the problematic modulator HF was used and a yield of only ~50% was stated after separation of MIL-101Cr from the terephthalic acid. Many small-scale literature syntheses follow this original hydrothermal synthesis procedure with a yield of ~50% (Férey et al., 2005). Hence, yields around 45% are competitive with many literature syntheses of MIL-101Cr. Also, the yields of about 45 % are slightly higher than for MIL-101Cr samples synthesized by microwave heating alone (Iglesia et al., 2016). The use of microwave heating led to a drastic decrease concerning reaction time (70 min) and temperature (210 °C and lower). Attempts to shorten the reaction times to 40 min suffered from a loss in surface area and porosity (García-Márquez et al., 2012) (**Table 1**).

For comparison, nanoMIL-101Cr was synthesized via reverse emulsion and microMIL-101Cr via the conventional hydrothermal route as described in the Supplementary Material. Particles of nanoMIL-101Cr via reverse emulsion were small, but displayed poor porosity characteristics (**Table 1**).

Powder X-ray diffraction (PXRD) confirmed the identity, crystallinity and phase purity of nanoMIL-101Cr synthesized using direct emulsions (**Figure 3A**).

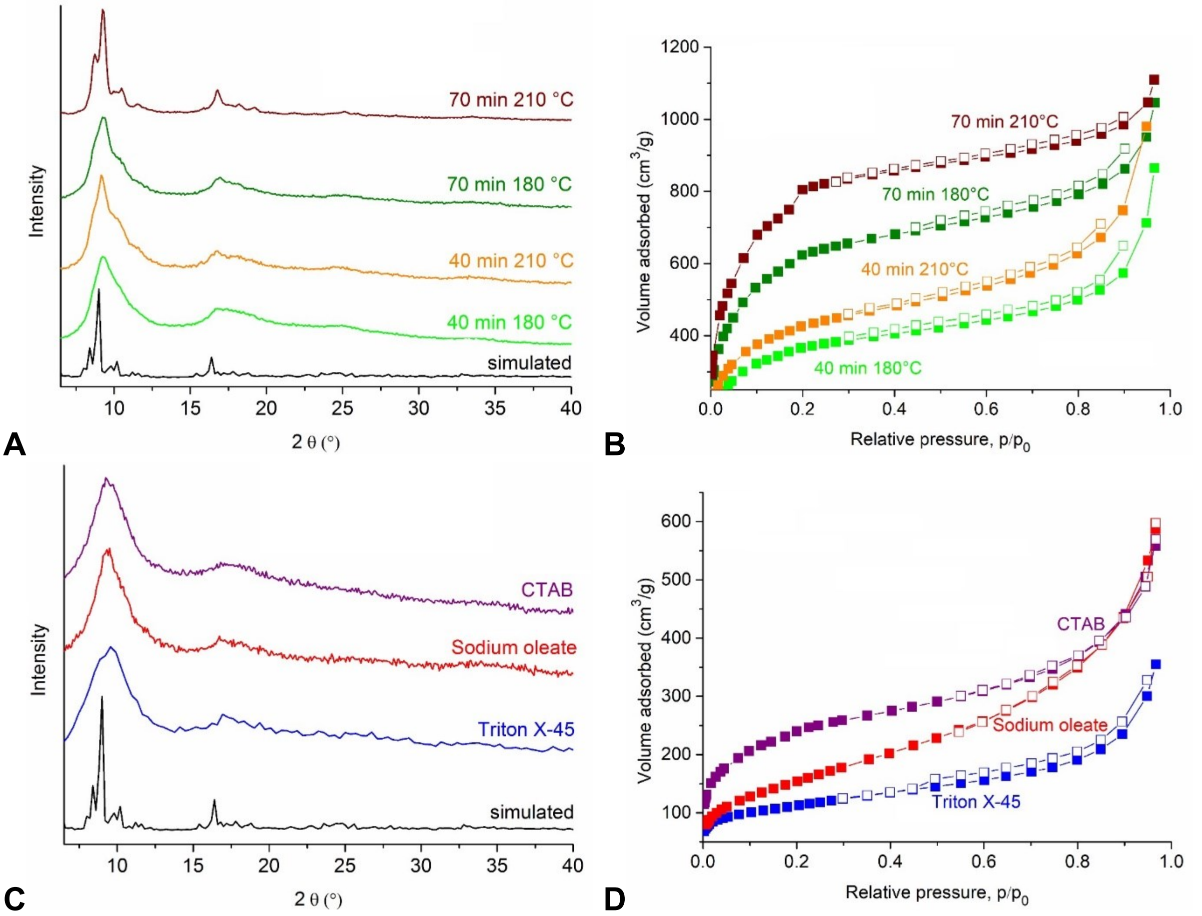

Figure 3 PXRD patterns and N_2 sorption isotherms of nanoMIL-101Cr synthesized in direct emulsion **(A**,**B)** for 40 min at 180 °C (light green), 40 min at 210 °C (orange), 70 min at 180 °C (dark green), 70 min at 210 °C (brown). PXRD patterns and N_2 sorption isotherms of nanoMIL-101Cr synthesized in reverse emulsions **(C**,**D)** by using sodium oleate (red), CTAB (purple), Triton X 45 (blue). Simulated PXRD pattern based on the cif-file of MIL-101Cr, CCDC number: 605510, (black) (**Férey et al., 2005**). For the N_2 sorption isotherms the samples were activated at 150 °C under vacuum for 12 h. Filled symbols depict adsorption, empty symbols desorption.

It is observed that a higher temperature (210 °C) and longer reaction time (70 min) improved crystallinity and porosity (**Table 1**). As Burrows et al. already have described, the broad Bragg reflections of the XRD patterns of the samples are attributed to the small particle size effects, and indeed the lines get broader as the nano/microparticle size decreases (Jiang et al., 2011). The porosity characteristics were determined from

N_2 adsorption-desorption isotherms of the purified and activated nanoMIL-101Cr (**Figure 3B**). The apparent BET surface area could be increased up to 2900 m^2 g^{-1} by a 70 min synthesis at 210 °C.

The N_2 isotherms of the higher surface area samples after 70 min reaction time are of the Type I(b) up to $p/p_0 \approx 0.4$ with the characteristic step between $0.1 < p/p_0 < 0.2$ due to the presence of the two kinds of microporous windows/mesoporous cages as in pure MIL-101Cr (Férey et al., 2005). For $p/p_0 > 0.4$ the increasing uptake which appears to increase without limit when $p/p_0 = 1$ is the result of unrestricted monolayer-multilayer adsorption due to the macroporous voids in the interparticle space so that the isotherm becomes of Type II (Thommes et al., 2015).

Hence, we determined the pore volume at $p/p_0 = 0.4$ and not as suggested in the latest IUPAC report for gas sorption at $p/p_0 = 0.95$, in order not to overestimate the pore volume (Thommes et al., 2015). Micrometer sized MIL-101Cr from the literature exhibits the typical Type I(b) isotherm for MIL-101Cr, reaching its plateau at $p/p_0 = 0.4$ (Zhao et al., 2015). Therefore, it is ensured that pore filling is already completed at $p/p_0 = 0.4$. Possibly due to retained surfactant, as mentioned above, the pore volume is smaller than expected. The NL-DFT calculations yielded pore widths largely below ~25 Å (2.5 nm) (**Figure S8**), which is smaller than the expected 2.9 and 3.4 nm (**Figure S4B**) but match with literature reports (Horcajada et al., 2007) and with our results on microMIL-101Cr from conventional hydrothermal syntheses (**Figure S10**) (Huang et al., 2012). With shorter reaction times of 40 min not only does the porosity decrease, but the pore size distributions extent also into the mesopore region (above 20 Å, 2 nm) (**Figure S8A and S8C**). Thus, products from short reaction times seem to have a hierarchically porosity with micropores below 20 Å width and pores sizes between 20 Å and 100 Å (**Figure S11**).

From reverse emulsion no satisfactory BET surface area, crystallinity and yield could be reached compared to direct emulsion and conventional syntheses. These results may be based on the phase inversion, whereby the water-in-oil emulsion inverts into an oil-in-water emulsion and as a consequence nanoreactors for MOF particles are no longer available (**Figure S6**). From PXRD it is evident that the crystallinities of the samples synthesized in reverse emulsion were all very poor (**Figure 3C**). Still the PXRD patterns with strongly broadened reflections are similar to those for nanosized MIL-101Cr particles reported by other researchers, when using microwave heating or surfactants (**Table S1**). Broad Bragg diffraction peaks may indicate either a low crystallinity or small (nano)particles (Iglesia et al., 2016).

Nitrogen sorption experiments of nanoMIL-101Cr from reverse emulsions yield low BET surface areas of less than 900 m^2 g^{-1} and total pore volumes of less than 0.2 cm^3 g^{-1} (**Table 1**, **Figure 3D**). The low porosity values are in accordance with the lower crystallinity deduced from the PXRD patterns and are in about the same range as those for nanosized MIL-101Cr particles reported by other researchers, when using microwave heating or surfactants (see summary in **Table S1**). The nitrogen adsorption isotherms are a combination of Type IV at low p/p_0 (for mesoporous solids) and Type II at high p/p_0 (Thommes et al., 2015), which is characteristic for macrporous solids with interparticular porosity (**Figure S9**). When the reverse emulsion is exposed to high temperature (> 100 °C), heptane vaporizes and expands rapidly, thereby the surface area of the oil within the water increases and an enhanced contact of surfactant molecules with metal salt and organic linker components occurs. This can lead to further competition concerning the coordination equilibrium on the crystal surface, especially for the monocarboxylic acid sodium oleate. All reverse emulsion samples show pore size distributions about 1 nm (10 Å) to over 10 nm (100 Å) with a large pore volume fraction, especially for nanoMIL-101Cr from sodium oleate in the lower mesopore region (between 2 to 10 nm) (**Figure 9A**). Yields of MIL-101Cr from reverse emulsion were below 36 % (**Table 1**).

The morphology and particle size was assessed by scanning electron microscopic (SEM), transmission electron microscopy (TEM) and dynamic light scattering (DLS). SEM images of MIL-101Cr from direct emulsion with sodium oleate show the formation of nano/microparticles with rather uniform diameters around 100 nm and spherical morphology (**Figure 5**).

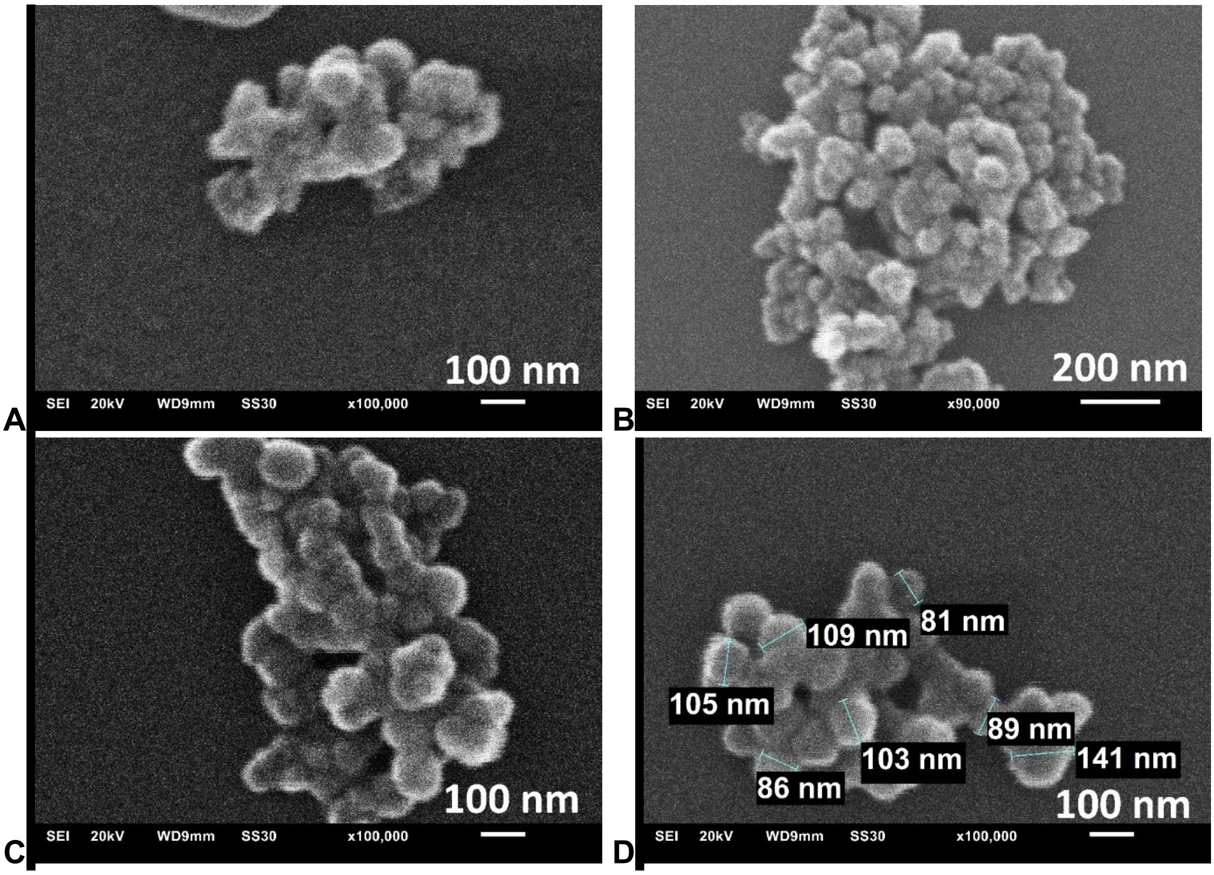

Figure 5 SEM images of the sample prepared in direct emulsion for 40 min at 180 °C **(A)**, 70 min at 180 °C **(B)** and 70 min at 210 °C **(C**,**D)**.

TEM images agree with sizes obtained from SEM (**Figure S12** and **Figure S13**). The TEM-histograms of nanoMIL-101Cr particles (**Figure S12E** and **Figure S13E**) show that the average particle size and its standard deviation are 73±15 and 86±15 nm diameter for direct emulsion at 210 °C for 40 min and 70 min reaction time, respectively. TEM images are similar to other TEM images already published by other research groups (Wuttke et al., 2006). For MIL-101 powder gained by reverse emulsion the SEM results, TEM results, and a histogram are shown in **Figure S14** and **Figure S15**, respectively. For microMIL-101Cr the PXRD, N$_2$, SEM results and a histogram are shown in **Figure 4A**, **Figure 4B** and **Figure S16,** respectively.

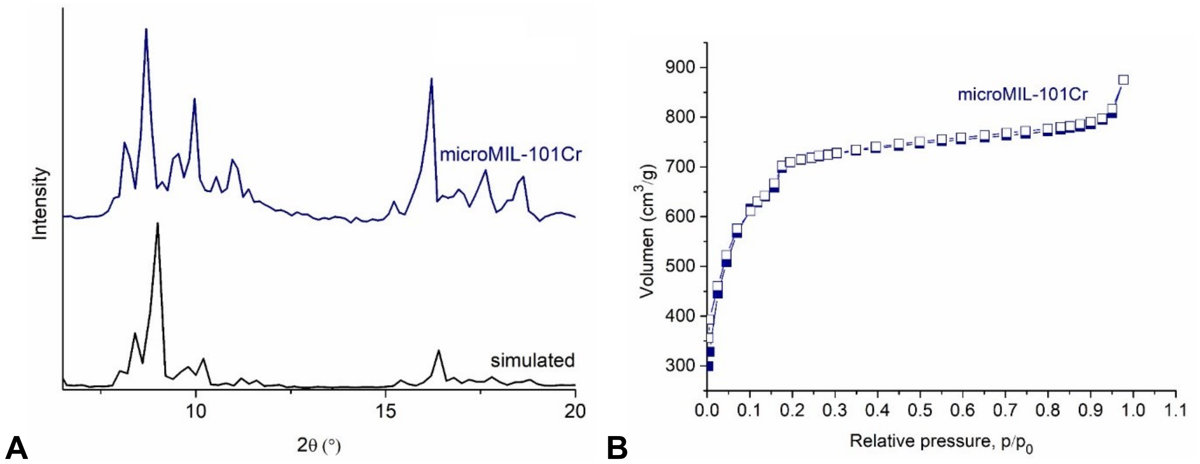

Figure 4 PXRD patterns (navy blue for microMIL-101Cr **(A)**, black for simulated PXRD pattern from the cif-file of MIL-101Cr, CCDC number: 605510) (**Férey et al., 2005**). N_2 sorption isotherms of microMIL 101Cr **(B)**. Filled symbols depict adsorption, empty symbols desorption.

We also used dynamic light scattering (DLS) as a non-destructive ensemble measurement technique to determine the hydrodynamic radius of particles from dilute dispersion. The SEM and TEM images showed aggregates of the small primary particles that may have formed during sample preparation. Since the intensity of scattered light in DLS scales with the diameter at the 6th power, DLS is extremely sensitive to the presence of aggregates or impurities like dust. Indeed the recorded intensity-time autocorrelation functions and the corresponding distribution functions of the hydrodynamic radii $G(R_h)$ obtained from CONTIN analysis shown in **Figure S17-Figure S23** in the Supplementary Material reveal the presence of small fractions of larger aggregates in all samples. These aggregates appear with average sizes on the order of a few microns. It is also possible that these contributions stem from impurities like dust that were not efficiently removed by the filtration process applied prior to the DLS measurements. However, we want to note that these larger contributions have low intensities and are clearly not the dominating species in the samples. The diffusion and size of the dominating species (strongest peak in $G(R_h)$) in DLS were analyzed using angle dependent measurements. For each sample we determined the mean relaxation rate and observed a linear dependence on the square of the magnitude of the scattering vector q indicating that we only probe translational diffusion. This allowed us to precisely determine the hydrodynamic radii. For the different nanoMIL-101Cr samples from direct emulsion with sodium oleate DLS gave rather uniform hydrodynamic radii between 137 to 155 nm (274 to 310 nm in diameter). It is also evident that by increasing the reaction temperature from 180 °C to 210 °C or decreasing the reaction time from 70 min to 40 min no significant change of particle size was observed. The determined hydrodynamic radii match nicely to the sizes determined from electron microscopy although slightly smaller values were determined in the latter. This deviation is indeed expected as DLS probes the diffusion of the particles including their solvating shell (Khan et al., 2010).

MIL-101Cr@Matrimid mixed-matrix membrane

The mixed-gas permeation performance of neat Matrimid membranes and MIL-101Cr MMMs were investigated with a binary gas mixture of CO_2 and CH_4. Mixed-gas studies instead of single-gas studies are preferred, since the ideal selectivities from single-gas studies can differ from those of mixed-gases due to gas interaction and plasticization effects (Dechnik et al., 2017). Plasticization describes the effect that the permeability of both gases increases and the selectivity decreases. This is due to an increase in the segmental motion of polymer chains at high feed pressures caused by the presence of one or more gas sorbates (Wind et al., 2002), CO_2 in particular causes such plasticization, less so CH_4 or N_2.

Neat Matrimid membranes and MIL-101Cr@Matrimid MMMs were fabricated with different loadings of the MOF (8, 16 and 20 or 24 wt%). For comparison, nanoMIL-101Cr from direct emulsion with sodium oleate and microMIL-101Cr from conventional hydrothermal conditions were used to prepare nanoMIL-101Cr@Matrimid MMMs and microMIL-101Cr@Matrimid MMMs, respectively. For the MMM fabrication chosen amounts of MOF and Matrimid (**Table 2**) were first mixed with dichloromethane, DCM, and stirred, before the suspension was casted into metal rings. After covering the rings with funnels and evaporation of the solvent (**Figure S24**), the membranes were detached, tailored, dried and stored. The detailed procedure is described in the Supplementary Material.

A major difference was already noticed for the preparation of the highly loaded MMMs where it was not possible to produce microMIL-101Cr-MMMs with 24 wt% MOF because of their extreme brittleness (**Figure S24B** and **Figure S24C**). Hence, we could only produce and measure microMIL-101Cr@Matrimid MMMs with 8, 16 and 20 wt% MOF loading.

The XRD diffractogram of pure Matrimid shows a broad reflection around 2 $\Theta = 20°$ with low intensity based on the semi-crystalline structure (Amooghin et al., 2015). For MMMs, all the intense reflections of MIL-101Cr and the broad reflection of Matrimid can be observed (**Figure S25A**). The MIL-101 reflections confirm that the MOF material were not affected by the preparation of the membranes. For details regarding the infrared analysis of the MMMs see Figure S26 in Supp. Material.

SEM images in combination with energy-dispersive X-ray spectroscopy (EDX) of cross-sections of the membranes confirm the homogeneous distribution of nanoMIL-101Cr particles (**Figure 6**).

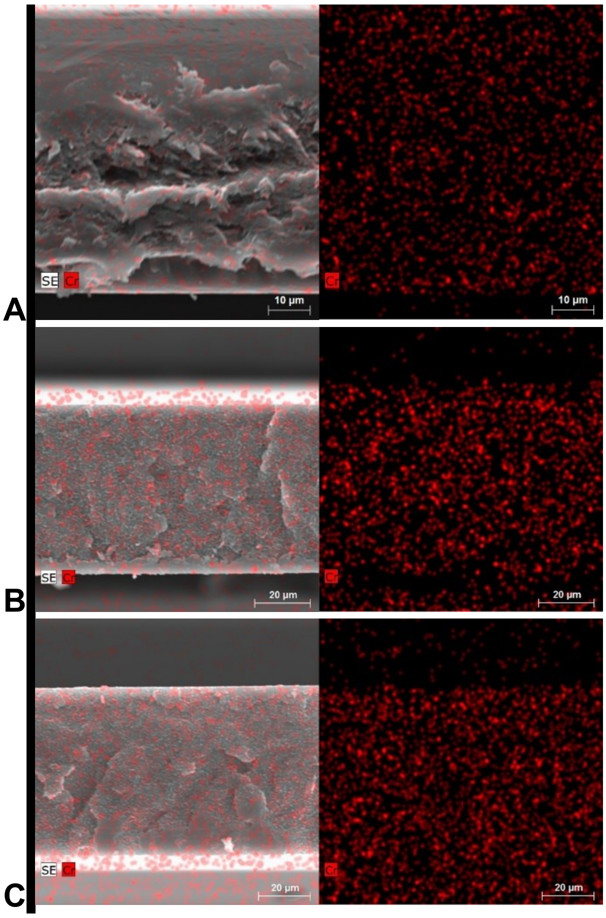

Figure 6 SEM/EDX images of the cross-section of nanoMIL-101Cr@Matrimid membrane with 8 wt% MOF **(A)**, 16 wt% MOF **(B)**, and 24 wt% MOF **(C)**. Left: SEM/EDX images superimposed. Right: EDX element mapping (Cr = red). The bottom of the cross-sections in the image corresponds to the bottom of the membrane when casted. The cross-section of a pure Matrimid membrane is shown in **Figure S25B**. Dark and light areas around cross-section of membranes depend on mounting on SEM sample holder (see Figure S2).

The uniform distribution is due to the organic-inorganic structure of the MOF filler particles, which disperse well within the continuous polymer phase. SEM images of cross-sections and EDX of the membranes fabricated with conventional synthesized microMIL-101Cr are shown in **Figure S26**. Even larger microMIL-101Cr in Matrimid MMMs lead also to a homogeneous distribution in the polymer matrix.

Mixed-gas permeation performance

The mixed-gas permeation performance of neat Matrimid membranes and mixed-matrix membranes were investigated with a binary gas mixture of CO_2 and CH_4. Before the measurement, the membranes were again heated for 1 h in a vacuum oven at 150 °C. The results for the permeability and selectivity for the MIL-101Cr@Matrimid membranes are shown in **Table 3** and **Figure 7**.

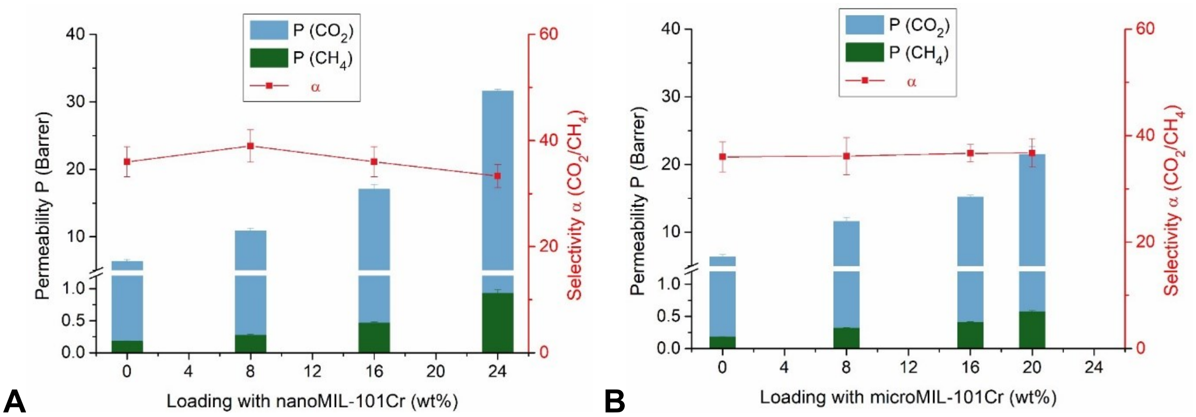

Figure 7 Separation properties of nanoMIL-101Cr@Matrimid **(A)** and microMIL-101Cr@Matrimid **(B)** MMMs with different MOF loadings for a 50:50 v:v gas mixture of CO_2 and CH_4 at 25 °C and a feed pressure of 4 bar. Error bars of the permeability correspond to the standard deviation; error bars of the selectivity were calculated via error propagation.

Table 3 Summary of the separating properties of nanoMIL-101Cr@Matrimid and MIL-101Cr@Matrimid membranes for a 50:50 v:v gas mixture of CO_2 and CH_4.[a]

MOF	**Membrane Thickness[c] [µm]**	**MIL-101 loading**	**P (CO_2) [Barrer]**	**P (CH_4) [Barrer]**	**S (CO_2/CH_4)**
-	59-60	Pure Matrimid	6.6±0.3	0.18±0.01	36±3
nanoMIL-101Cr	68-70	8 wt%	10.8±0.4	0.28±0.01	39±3
	69-79	16 wt%	17.0±0.7	0.47±0.02	36±3
	78-88	24 wt%	31.6±0.2	0.93±0.06	33±2
microMIL-101Cr	67-69	8 wt%	11.6±0.6	0.31±0.01	36±4
	75-75	16 wt%	15.2±0.3	0.41±0.01	37±2
	70-81	20 wt%	21.5±0.1	0.58±0.01	37±3

[a] At 25 °C and a feed pressure of 4 bar. Each type of membrane was prepared and measured three times to provide reliable error estimates. [b] Errors for CO_2 and CH_4 permeabilities deduce from standard deviations of the three measured membranes, errors for CO_2/CH_4 selectivity were calculated by error propagation [c] Each membrane was measured at ten different places using a thickness measuring device.

Nano- and microMIL-101Cr@Matrimid MMMs show a similar rise in CO_2 and CH_4 permeability with increasing MOF loading. Furthermore, the selectivity remains unaltered for all measured MMMs. By comparing our results for CO_2 and CH_4 permeability with already published results (**Table S2** in the Supplementary Material) it can be noticed, that with our nanoMIL-101Cr mixed-matrix membranes we have achieved very high CO_2 and CH_4 permeability results with an almost steady selectivity. By taken into account the results for selectivity of the already published studies it is obvious that their selectivity results are sometimes high sometimes low without any correlation concerning the MOF loading. Therefore, the achievement of almost steady selectivity without great changes is worth to be mentioned.

However, we note again that it was not possible to produce MMMs with 24 wt% microMIL-101Cr. The CO_2 permeability increased from about 6 Barrer for pure Matrimid to over 31 Barrer for the 24 wt% nanoMIL-101Cr membrane, but to only 21 Barrer for the 20 wt% microMIL-101Cr membrane. Thus, at 24 wt% loading of nanoMIL-101Cr, the permeability of the membrane for both gases increased almost five times with respect to the pure Matrimid membrane. However, at 20 wt% loading of microMIL-101Cr, the permeability for both gases increased only three times with respect to the pure Matrimid membrane. The permeability increase can be traced to the added free fractional volume, which is introduced by the incorporation of the porous MIL-101Cr filler particles. Furthermore, one can observe only a negligible reduction in the CO_2/CH_4 selectivity of around 36 for both MOF variations.

For comparison, single-gas and mixed-gas permeation measurements for CO_2/CH_4 separation of different MOF@Matrimid and MIL-101Cr@polymer MMMs are collected in **Table S2**. The CO_2 permeability and CO_2/CH_4 selectivity of the membranes fabricated in this study together with MOF@Matrimid MMMs from the literature summarized in a Robeson chart (**Figure 8**). From this chart it is obvious that MMMs with MIL-101Cr@Matrimid compare well in performance with already published results. Yet, the nanoMIL-101Cr-MMM with 24 wt% surpasses all other MOF@Matrimid MMMs in its CO_2 permeability even though some of these other MOF-MMMs have MOF weight percentages of 30 or even 40 wt% (Rajati et al., 2018; Perez et al., 2009; Zhang et al., 2008; Naseri et al., 2015).

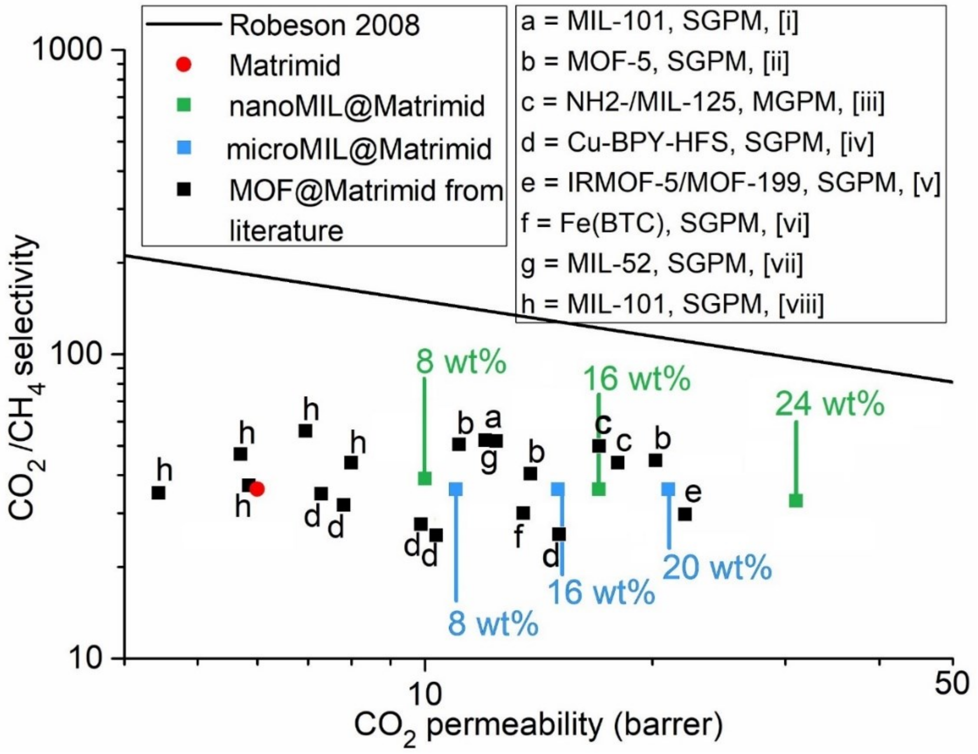

Figure 8 CO_2/CH_4 separation performance of nanoMIL-101Cr@Matrimid (green), microMIL-101Cr@Matrimid (light blue), and neat Matrimid (red) compared with published results for mixed-matrix membranes based on MOF@Matrimid (black). The upper bound for polymer performances as defined by Robeson in 2008 is given as a black line (Robeson, 2008). SGPM = single-gas permeation measurement.

MGPM = mixed-gas permeation measurement. References: a = (Rajati et al., 2018), b = (Perez et al., 2009), c = (Anjum et al., 2016), d = (Zhang et al., 2008), e = (Nik et al., 2012), f = (Shahid and Nijmeijer, 2014), g = (Dorosti et al., 2014), and h = (Naseri et al., 2015).

Modelling

Figure 9 shows the comparison between predicted Maxwell and Bruggeman model (see Supp. Material for details) and experimental relative CO_2 permeabilities for nanoMIL-101Cr@Matrimid MMMs.

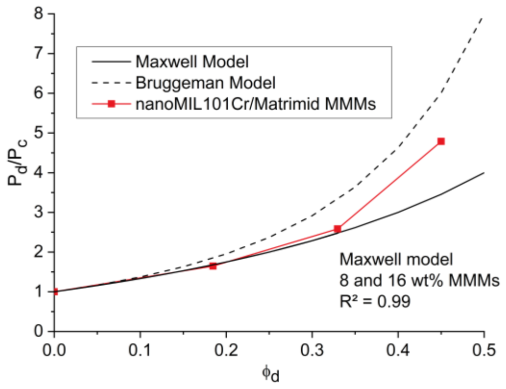

Figure 9 Relative experimental CO_2 permeabilities (referenced to the permeability P_c of the pure polymer membrane) for nanoMIL-101Cr@Matrimid (red curve) with different filler volume fraction ϕ_d. The black solid line gives the theoretical CO_2 permeabilities for porous fillers based on the Maxwell Model and the black dashed line gives the theoretical CO_2 permeabilities for porous fillers based on the Bruggeman Model.

The very high pore volume of 1.32 cm^3 g^{-1} for nanoMIL-101Cr results in a low crystal density for MIL-101 and therefore the used weight percentages of 8, 16 and 24 wt% roughly double when converted into filler volume. Thus, MMMs loaded with 8, 16 and 24 wt% MOF give a filler volume of 0.18, 0.32 and 0.45, respectively. We note, that for an effective increase in permeability the filler volume, in which the free volume (pore volume) of the filler is of high relevance, is more important than the usually given wt% loading of the membrane. The relative CO_2 permeabilities for the MMMs with lower filler loadings follow exactly the predicted values for the Maxwell model. This is in good agreement with previous studies, where composite membranes for filler loadings up to 0.2 and even slightly above mostly follow the Maxwell model (Nuhnen et al., 2018). For higher filler loadings above 0.2 the relative CO_2 permeabilities starts to deviate from the Maxwell model and approach the calculated values based on the Bruggeman model. Since the Maxwell model does not consider filler-filler particle interaction, it is not suitable for filler loadings significantly above 0.2. In contrary the Bruggeman model is explicitly used for higher filler loadings in MMMs and also considers the effects of filler-filler particle interactions (Shen and Lua, 2013). Hence, the permeation data displays a good agreement for both models in their respective filler loading range. Relative CH_4 permeabilities show the same trend (**Figure S28**).

A comparison between predicted Maxwell and Bruggeman model and experimental relative CO_2 and CH_4 permeabilities for microMIL-101Cr@Matrimid MMMs, presented in **Figure S29** and **Figure S30**, yields slightly different results. For lower filler volumes the experimental data follows the Maxwell model and with rising filler volume it surpasses the values calculated for the Maxwell model, but does not reach the calculation derived by the Bruggeman model. For the studied MMMs it is observed, that the filler loading, where filler-filler particle interactions influence the permeation performance in a significant manner, is somewhere between 0.35 and 0.45. In this range of the filler loading the permeability starts to rise sharply. This shows in the permeation performance of nanoMIL-101Cr@Matrimid MMMs, which is superior to the regular microMIL-101Cr@Matrimid MMMs, as it is possible to reach higher filler loadings to achieve this sharp rise in permeability.

Another way to analyze permeation properties, is to take a look at the so called Free Fractional Volume (FFV). The FFV is defined as the sum of the volume weighted FFV of the polymer and the volume weighted FFV of the filler (eq. 1).

$$(\boldsymbol{Total})\ \boldsymbol{FFV} = \boldsymbol{FFV_{polymer}} \cdot \boldsymbol{\phi_c} + \boldsymbol{FFV_{filler}} \cdot \boldsymbol{\phi_d}$$

Whereby the FFV of the polymer can be deduced by the Bondi method, which is described in detail in the literature and was determined as 0.17 for Matrimid (Kanehashi et al. 2015; Huang et al., 2006). The FFV of the filler can be calculated by multiplying the pore volume of the MOF, here obtained by nitrogen sorption of nanoMIL-101Cr and microMIL101-Cr, with the density of the MOF, to yield a dimensionless entity. Equation (2) shows the correlation of the FFV and the permeability *P*:

$$\boldsymbol{P = A_p \cdot exp^{(-\frac{B_p}{FFV})}}$$

After linearization:

$$\mathbf{lg}\, \boldsymbol{P} = \mathbf{lg}\, \boldsymbol{A_p} - \frac{\boldsymbol{B_p}}{\mathbf{2.303}\boldsymbol{FFV}}$$

Hence, lg P plotted against the inverse FFV should give a linear correlation with slope − B_p/2.303 and intercept lg A_p. if indeed the FFV determines the permeability. **Figure 10** shows the plot of lg P versus 1/FFV for the nano- and microMIL-101Cr@Matrimid MMMs.As the FFV rises with increasing filler volume, the inverse FFV decreases.

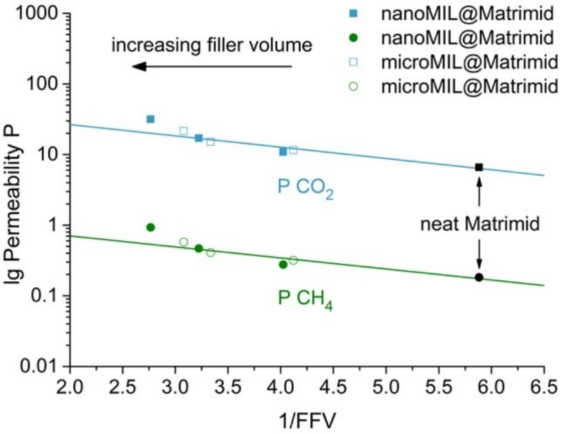

Figure 10 Experimental CO_2 and CH_4 permeabilities of nano- and microMIL-101Cr@Matrimid MMMs as a function of the inverse FFV. The neat polymer has 1/FFV = 5.9, the 20 wt% microMIL-MMMs has 1/FFV = 3.1, the 24 wt% nanoMIL-MMM has 1/FFV = 2.8. The added straight lines are intended as guides to the eye.

For filler volumes between 0 and 16 wt% MOF the reduction of the inverse FFV and the rise in permeability show a good linear correlation, displayed by the straight line. The nanoMIL-MMM with 24 wt% MOF however, has a higher than expected permeability. This is in good agreement with the previous observation that for MMMs with 24 wt% filler loading a sharp increase in permeability takes place which leads to a significant deviation from the used FFV model. As it seems, similar to the Maxwell model, the FFV model is no longer applicable for MMMs with higher filler loadings, where filler-filler interaction start to occur. Such filler-filler interaction would add an additional FFV (yielding an even smaller 1/FFV value). A similar effect could be observed in the work of Kanehashi et al. were they plotted lg*P* versus 1/FFV for several MOFs and carbons materials (Kanehashi et al., 2015). For example, a Cu-BTC MMMs with the highest filler loadings of 30 wt% showed a distinct increase in CO_2 and CH_4 permeability compared to the given 1/FFV (Kanehashi et al., 2015).

Conclusion

In summary, we demonstrated that the size of MIL-101Cr can be adjusted in the nano-micro-range below 100 nm by using microwave heating in combination with a direct emulsion technique, surfactants, and ultrasonication. Direct emulsion with the phase-inversion-temperature method and sodium oleate as surfactant yielded nanoMIL-101Cr particles of less than 100 nm and high apparent BET-surface areas (2900 $m^2\ g^{-1}$) in good yields (45 %). Furthermore, we observed, that with increasing reaction time and temperature, the particles became more crystalline and showed higher N_2 uptakes, as well as larger total pore volumes. Thereby we prepared nanoMIL-101Cr for application as a filler in mixed-matrix membranes. The use of nanoMIL-101Cr in Matrimid MMMs allowed for the preparation of 24 wt% filler MMMs compared to a maximum of 20 wt% for microMIL-101Cr in order to still have a defect-free membrane. The increased filler amount improved the gas permeability. Permeation modelling studies based on the Maxwell model and the free fractional volumes indicate a significant permeability increase beyond the 20 wt% filler content. Our approach, to surpass the normally obtainable filler wt% fraction by a nanosized filler in a mechanically still stable membrane, is a promising result with wider implications.

Conflict of Interest

The authors declare that the research was conducted in the absence of any commercial or financial relationships that could be construed as a potential conflict of interest.

Author Contributions

I. Gruber: synthesized/fabricated the nano/microsized MOF as well as the mixed-matrix-membranes, performed/discussed the powder X-ray diffraction/nitrogen physisorption/infrared experiments and wrote the manuscript; A. Nuhnen: performed/discussed the mixed-gas permeation and wrote the manuscript part concerning the mixed-matrix-membranes; A. Lerch: performed/discussed the DLS experiments and results given by the 3D LS spectrometer; S. Nießing, M. Klopotowski: performed the scanning electron microscopy, SEM and EDX analysis; A. Herbst: contributed the idea of emulsion and microwave heating based synthesis of MIL-101 and ran pilot tests; M. Karg, C. Janiak: proofreading and refining of manuscript.

Acknowledgments

The authors acknowledge the Center for Advanced Imaging (Cai, Heinrich-Heine-University) for access to the TEM instruments and the financial support of the Federal German Ministry of Education and Research (BMBF) in the project Optimat under grant no. 03SF0492C. A.L. and M.K. acknowledge financial support from the German Research Foundation (DFG) through the project KA 3880/3-1. The open access publication fee was covered from a library fund at the Heinrich-Heine-Universität Düsseldorf.

Supplementary Material

The Supplementary Material for this article can be found online at: https://www.frontiersin.org/articles/10.3389/fchem.2019.00777/full#supplementary-material

References

Yaghi, O. M., Li, H., Davis, C., Richardson, D., Groy, T. L. (1998). Synthetic strategies, structure patterns, and emerging properties in the chemistry of modular porous solids. Acc. Chem. Res. 31, 474-484. doi: 10.1021/ar970151f.

Batten, S. T., Robson, R. (1998). Interpenetrating nets: Ordered, periodic entanglement. Angew. Chem. Int. Edn Engl. 37, 1460–1494. doi: 10.1002/(sici)1521-3773(19980619)37:11<1460::aid-anie1460>3.0.co;2-z.

Ferey, G. (2000). Building units design and scale chemistry. J. Solid State Chem. 152, 37–48. doi: 10.1006/jssc.2000.8667.

Kitagawa, S., Kondo, M. (1998). Functional micropore chemistry of crystalline metal complex-assembled compounds. Bull. Chem. Soc. Jpn 71, 1739–1753. doi: 10.1246/bcsj.71.1739.

Yaghi, O. M., O'Keeffe, M., Kanatzidis, M. G. (2000). Design of Solids from Molecular Building Blocks: Golden Opportunities for Solid State Chemistry. J. Solid State Chem. 152, 1–2. doi: 10.1006/jssc.2000.8733.

Eddaoudi, M., Moler, D. B., Li, H., Chen, B., Reineke, T. M., O'Keeffe, M., Yaghi, O. M. (2001). Modular chemistry: Secondary building units as a basis for the design of highly porous and robust metal-organic carboxylate frameworks. Acc. Chem. Res. 34, 319–330. doi: 10.1021/ar000034b.

Yaghi, O.M., O'Keeffe, M., Ockwig, N.W., Chae, H.K., Eddaoudi, M., Kim, J. (2003). Reticular synthesis and the design of new materials. Nature 423, 705-714. doi: 10.1038/nature01650

Li, J.-R., Kuppler, R.J., Zhou, H.-C. (2009). Selective gas adsorption and separation in metal–organic frameworks. Chem. Soc. Rev. 38, 1477-1504. doi: 10.1039/B802426J

Tanh Jeazet, H.B., Staudt, C., Janiak, C. (2012) (a). Metal–organic frameworks in mixed-matrix membranes for gas separation. Dalton Trans. 41, 14003-14027. doi: 10.1039/C2DT31550E

Beyzavi, M.H., Stephenson, C.J., Liu, Y., Karagiaridi, O., Hupp, J.T., Farha, O.K. (2015). Metal–organic framework-based catalysts: Chemical fixation of CO_2 with epoxides leading to cyclic organic carbonates. Front. Energy Res. 2:63. doi: 10.3389/fenrg.2014.00063

Chen, B., Wang, L., Xiao, Y., Fronczek, F.R., Xue, M., Cui, Y., Qian, G. (2009). A Luminescent Metal–Organic Framework with Lewis Basic Pyridyl Sites for the Sensing of Metal Ions. Angew. Chem. Int. Ed. 48, 500-503. doi: 10.1002/anie.200805101

Horcajada, P., Gref, R., Baati, T., Allan, P.K., Maurin, G., Couvreur, P., Férey, G., Morris, R. E., Serre, C. (2012). Metal–Organic Frameworks in Biomedicine. Chem. Rev. 112,1232-1268. doi: 10.1021/cr200256v

Janiak, C., and Henninger, S.K. (2013). Kühlen mit Sonnenlicht. Nachr. Chem. 61, 520-523. doi: 10.1002/nadc.201390159

Erucar, I., and Keskin, S. (2018). High-Throughput Molecular Simulations of Metal Organic Frameworks for CO_2 Separation: Opportunities and Challenges. Front. Mater. 5:4. doi: 10.3389/fmats.2018.00004

Azar, A.N.V., and Keskin S. (2018). Computational Screening of MOFs for Acetylene Separation. Front. Chem. 6:36. doi: 10.3389/fchem.2018.00036

Rieter, W.J., Taylor, K.M.L., An, H., Lin, W., Lin, W. (2006). Nanoscale Metal−Organic Frameworks as Potential Multimodal Contrast Enhancing Agents. J. Am. Chem. Soc. 128, 9024-9025. doi: 10.1021/ja0627444

Lin, W., Rieter, W.J., Taylor, K.M.L. (2009). Modular Synthesis of Functional Nanoscale Coordination Polymers. Angew. Chem. Int. Ed. 48, 650-658. doi: 10.1002/anie.200803387.

Wuttke, S., Braig, S., Preiß, T., Zimpel, A., Sicklinger, J., Bellomo, C., Rädler, J.O., Vollmar, A.M., Bein, T. (2015). MOF nanoparticles coated by lipid bilayers and their uptake by cancer cells. Chem. Commun. 51, 15752-15755. doi: 10.1039/C5CC06767G

Jiang, D., Burrows, A.D., Edler, K.J. (2011). Size-controlled synthesis of MIL-101(Cr) nanoparticles with enhanced selectivity for CO_2 over N_2. CrystEngComm 12, 6916-6919. doi: 10.1039/C1CE06274C

Shen, T., Luo, J., Zhang, S., Luo, X., Environ. J. (2015). Hierarchically mesostructured MIL-101 metal–organic frameworks with different mineralizing agents for adsorptive removal of methyl orange and methylene blue from aqueous solution. Chem. Eng. 3, 1372-1383. doi: 10.1016/j.jece.2014.12.006

Khan, N.A., Kang, I.J., Seok, H.Y., Jhung, S.H. (2011). Facile synthesis of nano-sized metal-organic frameworks, chromium-benzenedicarboxylate, MIL101. Chem. Eng. J. 166, 1152-1157. doi: 10.1016/j.cej.2010.11.098

Huang, L., Wang, H., Chen, J., Wang, Z., Sun, J., Zhao, D., Yan, Y. (2003). Synthesis, morphology control, and properties of porous metal–organic coordination polymers. Microporous Mesoporous Mater. 58, 105-114. doi: 10.1016/S1387-1811(02)00609-1

Khan, N.A., and Jhung, S.H. (2015). Synthesis of metal-organic frameworks (MOFs) with microwave or ultrasound: Rapid reaction, phase-selectivity, and size reduction. Coord. Chem. Rev. 285, 11-23. doi: 10.1016/j.ccr.2014.10.008

Khan, N.A., Haquea, E., Jhung, S.H. (2010). Rapid syntheses of a metal–organic framework material Cu3(BTC)2(H2O)3 under microwave: a quantitative analysis of accelerated syntheses. Phys. Chem. Chem. Phys. 12, 2625-2631. doi: 10.1039/B921558A

Huang, A., Wan, L., Caro Mater. J. (2018). Res. Bull. 98, 308-313. doi: 10.1016/j.materresbull.2017.10.038

Diring, S., Furukawa, S., Takashima, Y., Tsuruoka, T., Kitagawa, S. (2010). Microwave-assisted synthesis of well-shaped UiO-66-NH 2 with high CO 2 adsorption capacity. Chem. Mater. 22,4531-4538. doi: 10.1021/cm101778g

Galema, S.A. (1997) Chem. Soc. Rev. 26 (1997). Microwave chemistry. 233-238. doi: 10.1039/CS9972600233

Bogdal, D. (2006). Microwave-Assisted Organic Synthesis. New York: Elsevier.

Wu, Y.-S., Ngai, S.-C., Goh, B.-H., Chan, K.-G., Lee, L.-H., Chuah, L.-H. (2017). Anticancer Activities of Surfactin and Potential Application of Nanotechnology Assisted Surfactin Delivery. Front. Pharmacol. 8:761. doi: 10.3389/fphar.2017.00761

Carr, C.S., and Shantz, D.F. (2005). Non-ionic-microemulsion mediated growth of zeolite A. Microporous Mesoporous Mater. 85, 284-292. doi: 10.1016/j.micromeso.2005.06.029

Salvia-Trujillo, L., Artiga-Artigas, M., Molet-Rodríguez, A., Turmo-Ibarzand, A., Martín-Belloso, O. (2018). Emulsion-Based Nanostructures for the Delivery of Active Ingredients in Foods. Front. Sustain. Food Syst. 2:79. doi: 10.3389/fsufs.2018.00079

Whitby, C.P., Lotte, L., Lang, C. (2012). Structure of concentrated oil-in-water Pickering emulsions. Soft Matter 8, 7784-7789. doi: 10.1039/C2SM26014J

Wang, S., McGuirk, C.M., d'Aquino, A., Mason, J.A., Mirkin, C.A. (2018). Metal–Organic Framework Nanoparticles. Adv. Mater. 30, 1-14. doi: 10.1002/adma.201800202.

Taylor, K.M.L., Rieter, W.J., Lin, W. (2008). Manganese-Based Nanoscale Metal−Organic Frameworks for Magnetic Resonance Imaging. J. Am. Chem. Soc. 130, 14358–14359. doi: 10.1021/ja803777x

Shinoda, K., and Saito, H. (1969). The Stability of O/W type emulsions as functions of temperature and the HLB of emulsifiers: The emulsification by PIT-method. J. Colloid Interface Sci. 30, 258-263. doi: 10.1016/S0021-9797(69)80012-3

Kale, S.N., and Deore, S.L. (2017). Emulsion Micro Emulsion and Nano Emulsion: A Review. Sys. Rev. Pharm. 8 (1), 39-47. doi: 10.5530/srp.2017.1.8

Benton, W.J., Raney, K.H., Miller, C.A. (1986). Enhanced videomicroscopy of phase transitions and diffusional phenomena in oil-water-nonionic surfactant systems. J. Colloid Interf. Sci. 110, 363-388. doi: 10.1016/0021-9797(86)90390-5

Sajjadi, S., Jahanzad, F., Yianneskis, M. (2004). Catastrophic phase inversion of abnormal emulsions in the vicinity of the locus of transitional inversion. Colloids Surf. A 240, 149-155. doi: 10.1016/j.colsurfa.2004.03.012

Izquierdo, P., Esquena, J., Tadros, T.F., Dederen, C., Garcia, M.J., Azemar, N., Solans, C. (2002). Formation and Stability of Nano-Emulsions Prepared Using the Phase Inversion Temperature Method. Langmuir 18, 26-30. doi: 10.1021/la010808c

Mei, Z., Liu, S., Wang, L., Jiang, J., Xu, J., Sun, D. (2011). Preparation of positively charged oil/water nano-emulsions with a sub-PIT method. J. Colloid Interf. Sci. 361, 565-572. doi: 10.1016/j.jcis.2011.05.011

Su, D., and Zhong, Q.X. (2016). Lemon oil nanoemulsions fabricated with sodium caseinate and Tween 20 using phase inversion temperature method. J. Food Eng. 171, 214-221. doi: 10.1016/j.jfoodeng.2015.10.040

Kundu, P., Agrawal, A., Mateen, H., Mishra, I.M. (2013). Stability of oil-in-water macro-emulsion with anionic surfactant: Effect of electrolytes and temperature. Chem. Eng. Sci. 102, 176-185. doi: 10.1016/j.ces.2013.07.050

Sorribas, S., Zornoza, B., Téllez, C., Coronas, J. (2014). Mixed matrix membranes comprising silica-(ZIF-8) core–shell spheres with ordered meso–microporosity for natural- and bio-gas upgrading. J. Membr. Sci. 452, 184-192. doi: 10.1016/j.memsci.2013.10.043

Seoane, B., Coronas, J., Gascon, I., Etxeberria Benavides, M., Karvan, O., Caro, J., Kapteijn, F., Gascon, J. (2015). Metal–organic framework based mixed matrix membranes: a solution for highly efficient CO_2 capture? Chem. Soc. Rev. 44, 2421-2454. doi: 10.1039/C4CS00437J

Miricioiu, M.G., Iacob, C., Nechifor, G. Niculescu, V.-C. (2019). High Selective Mixed Membranes Based on Mesoporous MCM-41 and MCM-41-NH2 Particles in a Polysulfone Matrix. Front. Chem. 7:332. doi: 10.3389/fchem.2019.00332

Robeson, L. M. (1991). Correlation of separation factor versus permeability for polymeric membranes. J. Membr. Sci. 62, 165-185. doi: 10.1016/0376-7388(91)80060-J

Robeson, L. M. (2008). The upper bound revisited. J. Membr. Sci. 320, 390-400. doi: 10.1016/j.memsci.2008.04.030

Dechnik, J., Sumby, C.J., Janiak, C. (2017). Enhancing Mixed-Matrix Membrane Performance with Metal–Organic Framework Additives. Cryst. Growth Des. 17, 4467-4488. doi: 10.1021/acs.cgd.7b00595

Zornoza, B., Tellez, C., Coronas, J., Gascon, J., Kapteijn, F. (2013). Microporous Mesoporous Mater. 166, 67-78. doi: 10.1016/j.micromeso.2012.03.012

Nuhnen, A., Dietrich, D., Millan, S., Janiak, C. (2018). Role of Filler Porosity and Filler/Polymer Interface Volume in Metal–Organic Framework/Polymer Mixed-Matrix Membranes for Gas Separation. ACS Appl. Mater. Interfaces 10, 33589-33600. doi: 10.1021/acsami.8b12938

Carreon, M., Dahe, G., Feng, J., Venna, S.R. (2017). World Scientific Series in Membrane Science and Technology: Biological and Biomimetic Applications, Energy and the Environment. Chapter 1: Mixed Matrix Membranes for Gas Separation Applications. ISBN: 9789813207707. doi:10.1142/9789813207714_0001

Zornoza, B., Gorgojo, P., Casado, C., Tellez, C., Coronas, J. (2011). Mixed matrix membranes for gas separation with special nanoporous fillers. Desalin. Water Treat. 27, 42-47. doi: 10.5004/dwt.2011.2045

Chowdhury, P., Mekala, S., Dreisbach, F., Gumma, S. (2012). Adsorption of CO, CO_2 and CH_4 on Cu-BTC and MIL-101 metal organic frameworks: Effect of open metal sites and adsorbate polarity. Microporous Mesoporous Mater. 152, 246-252. doi: 10.1016/j.micromeso.2011.11.022

Zhao, T., Li, S.-H., Shen, L., Wang, Y., Yang, X.-Y. (2018). The sized controlled synthesis of MIL-101(Cr) with enhanced CO_2 adsorption property. Inorg. Chem. Commun. 96, 47-51. doi: 10.1016/j.inoche.2018.07.036

Yang, J., Zhao, Q., Li, J., Dong, J. (2010). Synthesis of metal–organic framework MIL-101 in TMAOH-$Cr(NO_3)_3$-H_2BDC-H_2O and its hydrogen-storage behavior. Microporous Mesoporous Mater. 130, 174-179. doi: 10.1016/j.micromeso.2009.11.001

Thommes, M., Kaneko, K., Neimark, A.V., Olivier, J. P., Rodriguez-Reinoso, F., Rouquerol, J., Sing, K.S. (2015). Physisorption of gases, with special reference to the evaluation of surface area and pore size distribution (IUPAC Technical Report). Pure Appl. Chem. 87, 1051–1069. doi: 10.1515/pac-2014-1117

Gelb, L.D., Gubbins, K.E., Radhakrsihan, R., Sliwinska-Bartowiak, M. (1999). Phase separation in confined systems. Rep. Prog. Phys. 62, 1573-1659. doi: 10.1088/0034-4885/62/12/201

Abedini, R., Omidkhah, M., Dorosti, F. (2014). Highly permeable poly(4-methyl-1-pentyne)/NH_2-MIL 53 (Al) mixed matrix membrane for CO_2/CH_4 separation. RSC Adv. 4, 36522-36537. doi: 10.1039/C4RA07030E

Bouma, R.H.B., Checchetti, A., Chidichimo, G., Drioli, E. (1997). Permeation through a heterogeneous membrane: the effect of the dispersed phase. J. Membr. Sci. 128, 141-149. doi: 10.1016/S0376-7388(96)00303-1

Pal, R. (2008). Permeation models for mixed matrix membranes. J. Colloid. Interface Sci. 317, 191-198. doi: 10.1016/j.jcis.2007.09.032

Cao, A. (2003). Light Scattering. Recent Applications. Light scattering, Recent applications, Anal Lett 36, 3185-3225. doi: 10.1081/AL-120026567

Anjali, T.G., and Basavaraj, M.G. (2018). Influence of pH and Salt Concentration on Pickering Emulsions Stabilized by Colloidal Peanuts. Langmuir 34 13312-13321. doi: 10.1021/acs.langmuir.8b02913

Mahajan, R., and Koros, W.J. (2002). Mixed matrix membrane materials with glassy polymers. Part 1. Polym. Eng. Sci. 42, 1420-1431. doi: 10.1002/pen.11041

Férey, G., Draznieks, C.M., Serre, C., Millange, F., Dutour, J., Surble, S., Margiolaki, I. (2005). A Chromium Terephthalate-Based Solid with Unusually Large Pore Volumes and Surface Area. Science 309, 2040-2042. doi: 10.1126/science.1116275

Zhao, T., Jeremias, F., Boldog, I., Nguyen, B., Henninger, S.K., Janiak, C. (2015). High-yield, fluoride-free and large-scale synthesis of MIL-101(Cr). Dalton Trans. 44, 16791-16801. doi: 10.1039/C5DT02625C

Khutia, A., Rammelberg, H.U., Schmidt, T., Henninger, S., Janiak, C. (2013). Water Sorption Cycle Measurements on Functionalized MIL-101Cr for Heat Transformation Application. Chem. Mater. 25, 790-798. doi: 10.1021/cm304055k

Khutia, A., and Janiak, C. (2014). Programming MIL-101Cr for selective and enhanced CO_2 adsorption at low pressure by postsynthetic amine functionalization. Dalton Trans. 43, 1338-1347. doi: 10.1039/C3DT52365A

Wickenheisser, M., Jeremias, F., Henninger, S.K., Janiak, C. (2013). Grafting of hydrophilic ethylene glycols or ethylenediamine on coordinatively unsaturated metal sites in MIL-100(Cr) for improved water adsorption characteristics. Inorg. Chim. Acta 407, 145-152. doi: 10.1016/j.ica.2013.07.024

Rezk, A., Al-Dadah, R., Mahmoud, S., Elsayed, A. (2013). Investigation of Ethanol/metal organic frameworks for low temperature adsorption cooling applications. Appl. Energy 112, 1025-1031. doi: 10.1016/j.apenergy.2013.06.041

Herbst, A., and Janiak, C. (2016). Selective glucose conversion to 5-hydroxymethylfurfural (5-HMF) instead of levulinic acid with MIL-101Cr MOF-derivatives. New J. Chem. 40, 7958-7967. doi: 10.1039/C6NJ01399F

Tanh Jeazet, H.B., Staudt, C., Janiak, C. (2012) (b). A method for increasing permeability in O_2/N_2 separation with mixed-matrixmembranes made of water-stable MIL-101 and polysulfone. Chem. Commun. 48, 2140-2142. doi: 10.1039/C2CC16628C

Wickenheisser, M., Janiak, C. (2015). Hierarchical embedding of micro-mesoporous MIL-101(Cr) in macroporous poly(2-hydroxyethyl methacrylate) high internal phase emulsions with monolithic shape for vapor adsorption applications. Microporous Mesoporous Mater. 204, 242-250. doi: 10.1016/j.micromeso.2014.11.025

Jeremias, F., Henninger, S.K., Janiak, C. (2016). Ambient pressure synthesis of MIL-100(Fe) MOF from homogeneous solution using a redox pathway. Dalton Trans. 45 (20), 8637-8644. doi: 10.1039/C6DT01179A

Jiang, D., Mallat, T., Krumreich, F., Baiker, A. (2011). Polymer-assisted synthesis of nanocrystalline copper-based metal–organic framework for amine oxidation. Catal. Commun. 12, 602-605. doi: 10.1016/j.catcom.2010.12.010

Du, S., Li, F., Sun, Q., Wang, N., Jia, M., Yu, J. (2016). A green surfactant-assisted synthesis of hierarchical TS-1 zeolites with excellent catalytic properties for oxidative desulfurization. Chem. Commun. 52, 3368-3371. doi: 10.1039/C5CC08441E

Baloch, M.K., and Hameed, G. (2005). Emulsification of oil in water as affected by different parameters. J. Colloid Interf. Sci. 285, 804-813. doi: 10.1016/j.jcis.2004.11.070

Roonasi, P., Yang, X., Holmgren, A. (2010). Competition between sodium oleate and sodium silicate for a silicate/oleate modified magnetite surface studied by in situ ATR-FTIR spectroscopy. J. Colloid Interf. Sci. 343, 546-552. doi: 10.1016/j.jcis.2009.12.002

Iglesia, O. de la, Sorribas, S., Almendro, E., Zornoza, B., Tellez, C., Coronas, J. (2016). Renew. Energ. 88, 12-19. doi: 10.1016/j.renene.2015.11.025

García-Márquez, A., Demessence, A., Platero-Prats, A.E., Heurtaux, D., Horcajada, P., Serre, C., Chang, J.-S., Férey, G., de la Peña-O'Shea, V.A., Boissière, C., Grosso, D., Sanchez, C. (2012). Metal-organic framework MIL-101(Cr) based mixed matrix membranes for esterification of ethanol and acetic acid in a membrane reactor. Eur. J. Inorg. Chem. 2012 (32), 5165-5174. doi: 10.1002/ejic.201200710

Horcajada, P., Surblé, S., Serre, C., Hong, D.-Y., Seo, Y.-K., Chang, J.-S., Grenèche, J.-M., Margiolaki, I., Férey, G. (2007). Synthesis and catalytic properties of MIL-100(Fe), an iron(III) carboxylate with large pores. Chem. Commun. 27, 2820-2822. doi: 10.1039/B704325B

Huang, X.-X., Qiu, L.-G., Zhang, W., Yuan, Y.-P., Jiang, X., Xie, A.-J., Shena, Y.-H., Zhub, J.-F. (2012). Hierarchically mesostructured MIL-101 metal–organic frameworks: supramolecular template-directed synthesis and accelerated adsorption kinetics for dye removal. CrystEngComm 14, 1613-1617. doi: 10.1039/C1CE06138K

Dechnik, J., Gascon, J., Doonan, C.J., Janiak, C., Sumby, C.J. (2017). Mixed-Matrix Membranes. Angew. Chem. Int. Ed. 56, 9292-9310. doi: 10.1002/anie.201701109

Wind, J.D., Staudt-Bickel, C., Paul, D.R., Koros, W.J. (2002). The Effects of Crosslinking Chemistry on CO_2 Plasticization of Polyimide Gas Separation Membranes. Ind. Eng. Chem. Res. 41, 6139-6148. doi: 10.1021/ie0204639

Amooghin, A.E., Omidkhah, M., Kargari, A. (2015). Enhanced CO_2 transport properties of membranes by embedding nano-porous zeolite particles into Matrimid®5218 matrix. RSC Adv. 5, 8552-8565. doi: 10.1039/C4RA14903C

Shen, Y., and Lua, A.C. (2013). Theoretical and experimental studies on the gas transport properties of mixed matrix membranes based on polyvinylidene fluoride. AIChE J. 59, 4715-4726. doi: 10.1002/aic.14186

Kanehashi, S., Chen, G.Q., Scholes, C.A., Ozcelik, B., Hua, C., Ciddor, L., Southon, P.D., D'Alessandro, D.M., Kentish, S.E. (2015). Enhancing gas permeability in mixed matrix membranes through tuning the nanoparticle properties. J. Membr. Sci. 482, 49-55. doi: 10.1016/j.memsci.2015.01.046

Huang, Y., Wang, X., Paul, D.R. (2006). Physical aging of thin glassy polymer films: Free volume interpretation. J. Membr. Sci. 277, 219-229. doi: 10.1016/j.memsci.2005.10.032

Rajati, H., Navarchian, A.H., Tangestaninejad, S. (2018). Preparation and Characterization of Mixed Matrix Membranes based on Matrimid/PVDF blend and MIL-101(Cr) as filler for CO 2 /CH 4 separation. Chem. Eng. Sci. 185, 92-104. doi: 10.1016/j.ces.2018.04.006

Perez, E.V., Balkus Jr., K.J., Ferraris, J.P., Musselman, I.H. (2009). Mixed-matrix membranes containing MOF-5 for gas separations. J. Membr. Sci. 328, 165-173. doi: 10.1016/j.memsci.2008.12.006

Anjum, M.W., Bueken, B., De Vos, D., Vankelecom, I.F. (2016). MIL-125(Ti) based mixed matrix membranes for CO_2 separation from CH4 and N2. J. Membr. Sci. 502, 21-28. doi: 10.1016/j.memsci.2015.12.022

Zhang, Y., Musselman, I.H., Ferraris, J.P., Balkus Jr., K.J. (2008). Gas permeability properties of Matrimid (R) membranes containing the metal-organic framework Cu-BPY-HFS. J. Membr. Sci. 313, 170-181. doi: 10.1016/j.memsci.2008.01.005

Nik, O.G., Chen, X.Y., Kaliaguine, S. (2012). Functionalized metal organic framework-polyimide mixed matrix membranes for CO_2/CH_4 separation. J. Membr. Sci. 4213, 48-61. doi: 10.1016/j.memsci.2012.04.003

Shahid, S., and Nijmeijer, K. (2014). High pressure gas separation performance of mixed-matrix polymer membranes containing Highmesoporous FE(BTC). J. Membr. Sci. 459, 33-44. doi: 10.1016/j.memsci.2014.02.009

Dorosti, F., Omidkhah, M., Abedini, R. (2014). Fabrication and characterization of Matrimid/MIL-53 mixed matrix membrane for CO 2 /CH 4 separation. Chem. Eng. Res. Des. 92, 2439-2448. doi: 10.1016/j.cherd.2014.02.018

Naseri, M., Mousavi, S.F., Mohammadi, T., Bakhtiari, O. (2015). Synthesis and gas transport performance of MIL-101/Matrimid mixed matrix membranes. J. Ind. Eng. Chem. 29, 249-256. doi: 10.1016/j.jiec.2015.04.007

Kozlov, N. K., Natashina, U. A., Tamarov, K. P., Gongalsky, M. B., Solovyev, V. V., Kudryavtsev, A. A., Sivakov, V., Osminkina, L. A. (2017). Recycling of silicon: from industrial waste to biocompatible nanoparticles for nanomedicine. Mater. Res. Express 4, 095026, 1-6. doi: 10.1088/2053-1591/aa8c33.

Liu, G., Chernikova, V., Liu, Y., Zhang, K., Belmabkhout, Y., Shekhah, O., Zhang, C., Yi, S., Eddaudi, M., Koros, W. J. (2018). Mixed matrix formulations with MOF molecular sieving for key energy-intensive separations. Nature Materials, 17, 283-289. doi: 10.1038/s41563-017-0013-1.

Supplementary Material

Synthesis of nano/microsized MIL-101Cr through combination of microwave heating and emulsion technology for mixed-matrix membranes

Data Content

- Instrumentation
- Additional Data (i.a., published BET results and Gas (CO_2/CH_4) permeation data)
- Structure features of MIL-101Cr
- Additional information for the syntheses of nano/microsized- and microMIL-101Cr
- Additional analysis for nano/microsized- and microMIL-101Cr
- Mixed-matrix membranes
- Additional analysis for mixed-matrix membranes

Instrumentation

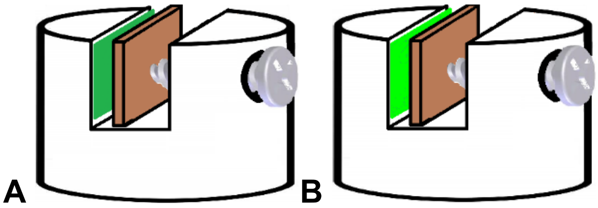

Figure S1 Schematic illustration of a SEM 90-degree sample mount to mount the cross-section of membranes (green/light green squares) directly against the vertical side of the mount. Open slot with the bottom of the cross-section facing the screw and metal sheet (brown square) **(A)** and open slot with the bottom of the cross-section facing away from the screw and metal sheet **(B)**.

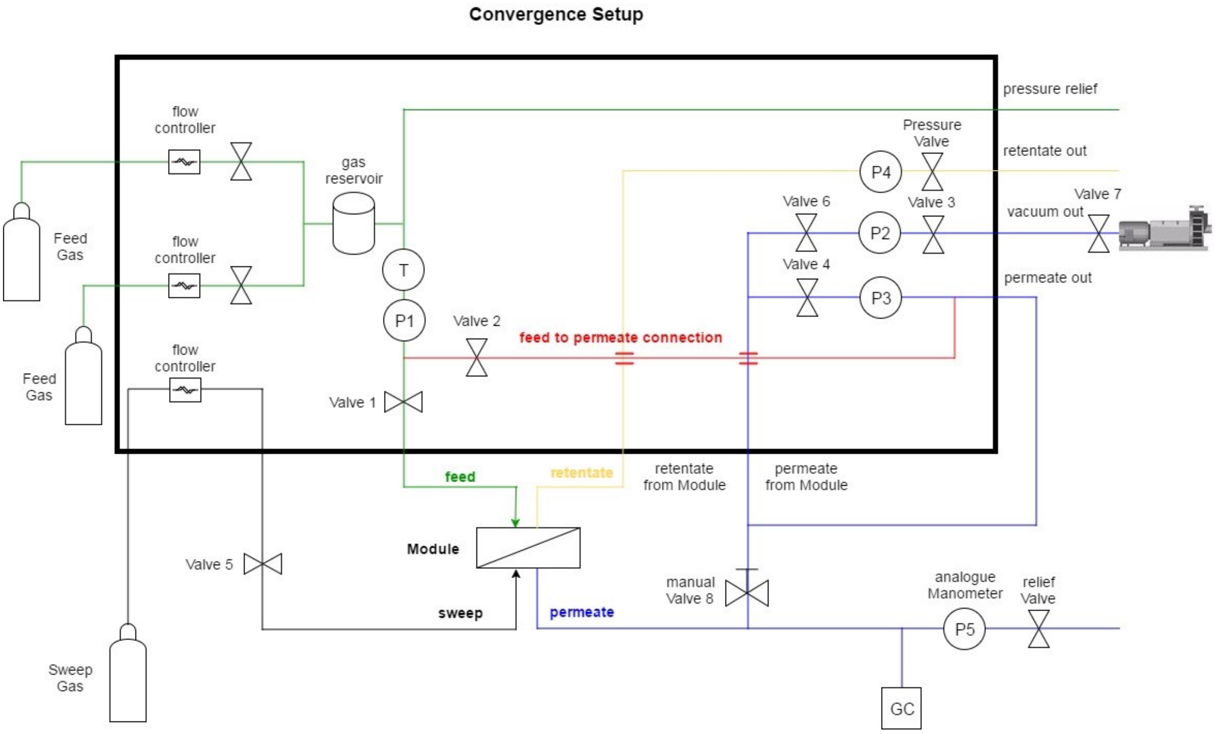

Figure S2 Schematic illustration of the mixed-gas permeation pilot. Black boarded area represents the OSMO Inspector.

Additional Data

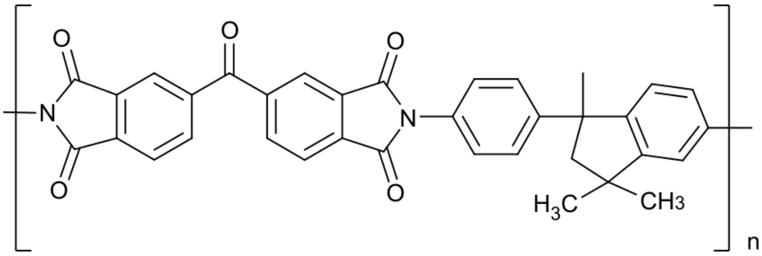

Figure S3 Repeating unit of Matrimid 5218.

Published BET results and particle sizes for MIL 101Cr synthesized via conventional and microwave heating

The following table (**Table S1**) shows the results for BET and particle sizes as well as additional published results by other working groups with and without the use of modulators. Thereby a possible comparison can be eased.

Table S1 Data for MIL-101Cr synthesized via conventional and microwave heating already published by other groups.

Sample name [a]	Synthesis condition heating/temp./time	Surfactant	Particle size [nm]	BET $[\mathrm{m^2 \cdot g^{-1}}]$	Ref.
A1	CE/220 °C/8 h	None	n.d.	2962	i
A2				2439	
A3				2345	
A4				1724	
A5		CTAB	n.d.	846	
A6				609	
B1				619	
B2				717	
C1				465	
C2				1026	
A0	CE/220 °C/12 h	None	n.d.	2341	ii
A1		CTAB	n.d.	1804	
A2				1596	
A3				1560	
B0		None	n.d.	3514	
B2		CTAB	n.d.	1454	
B3				1144	
A	CE/ 210 °C/6 h	None	800	2735	iii
B	CE/ 210 °C/24 h		400	3160	
C	CE/210 °C/ 24 h		200	ND	
D	MW/ 210 °C/15 min		200	3071	
E	MW/ 210 °C/1 h		200	3196	
F	MW/210 °C/1 h		100	ND	
G	CE/ 210 °C/4 h		400	3160	
H	CE/ 210 °C/24 h		100	ND	
J	MW/ 210 °C/15 min		200	3071	
K	MW/ 210 °C/15 min		50	3223	
(a)	CE/180 °C/8 h	None	50 (9)	2944	iv
(b)		Stearic Acid	19 (4)	2691	
(c)		4-Methoxybenzoic acid	25 (6)	2646	
(d)		Benzoic acid	28 (6)	2923	

Sample name [a]	Synthesis condition heating/temp./time	Surfactant	Particle size [nm]	BET [$m^2 \cdot g^{-1}$]	Ref.
(e)		4-Nitrobenzoic acid	36 (7)	2692	
(f)		Perfluorobenzoic acid	73 (8)	2893	
MIL-101Cr nanoparticles	MW/180 °C/6 min	None	49±20 nm	3205	v

[a] Sample name according to the reference shown in the right column. n.d. not determined. i = (Huang et al., 2012); ii = (Shen et al., 2015); iii = (Khan et al., 2011); iv = (Jiang et al., 2011); v = (Wuttke et al., 2015).

Published results for MMMs

Table S2 Gas (CO_2/CH_4) permeation data of mixed-matrix membranes with different MOFs and different polymers from literature.

SGPM MGPM [a]	Polymer	MOF	MOF [wt %]	P (CO2) [Barrer]	P (CH4) [Barrer]	S (CO2/CH4)	Ref.
SGPM	Matrimid			7.33	0.21	34.90	i
	PVDF			2.11	0.08	26.37	
	Matrimid/PVDF(3 %)			9.42	0.22	42.81	
	Matrimid	MIL-101	10	12.01	0.23	52.21	
	Matrimid/PVDF(3 %)	MIL-101	10	14.87	0.24	61.95	
SGPM	Matrimid	MOF-5	10	11.1	0.22	50.5	ii
			20	13.8	0.34	40.5	
			30	20.2	0.45	44.7	
MGPM (50:50)	Matrimid	MIL-125	15	18	0.41	44	iii
		NH_2-MIL-125	15	17	0.34	50	
SGPM	Matrimid	Cu-BPY-HFS	0	7.29	0.21	34.7	iv
			10	7.81	0.24	31.9	
			20	9.88	0.36	27.6	
			30	10.36	0.38	25.4	
			40	15.06	0.59	25.6	
SGPM	Matrimid	IRMOF-5	30	20.2	0.45	44.7	v
		MOF-199	30	22.1	0.74	29.8	
SGPM	Matrimid	Fe(BTC)	30	13.5	0.45	30	vi
SGPM	Matrimid	MIL-53	15	12.43	0.24	51.8	vii
SGPM	Matrimid	MIL-101	0	4.44	0.126	35	viii
			10	6.95	0.125	56	
			15	5.70	0.120	47	
			20	5.85	0.155	37	
			30	7.99	0.181	44	

[a] SGPM = single-gas permeation measurement. MGPM = mixed-gas permeation measurement. Permeability data have been obtained out at different feed pressures Results are shown in **Figure 8** in the manuscript. i = (Rajati et. al., 2018); ii = (Perez et. al., 2009); iii = (Anjum et. al., 2016); iv = (Zhang et. al., 2008); v = (Nik et. al., 2012); vi = (Shahid and Nijmeijer 2014); vii = (Dorosti et. al., 2014); viii = (Naseri et. al., 2015).

Structure features of MIL-101Cr

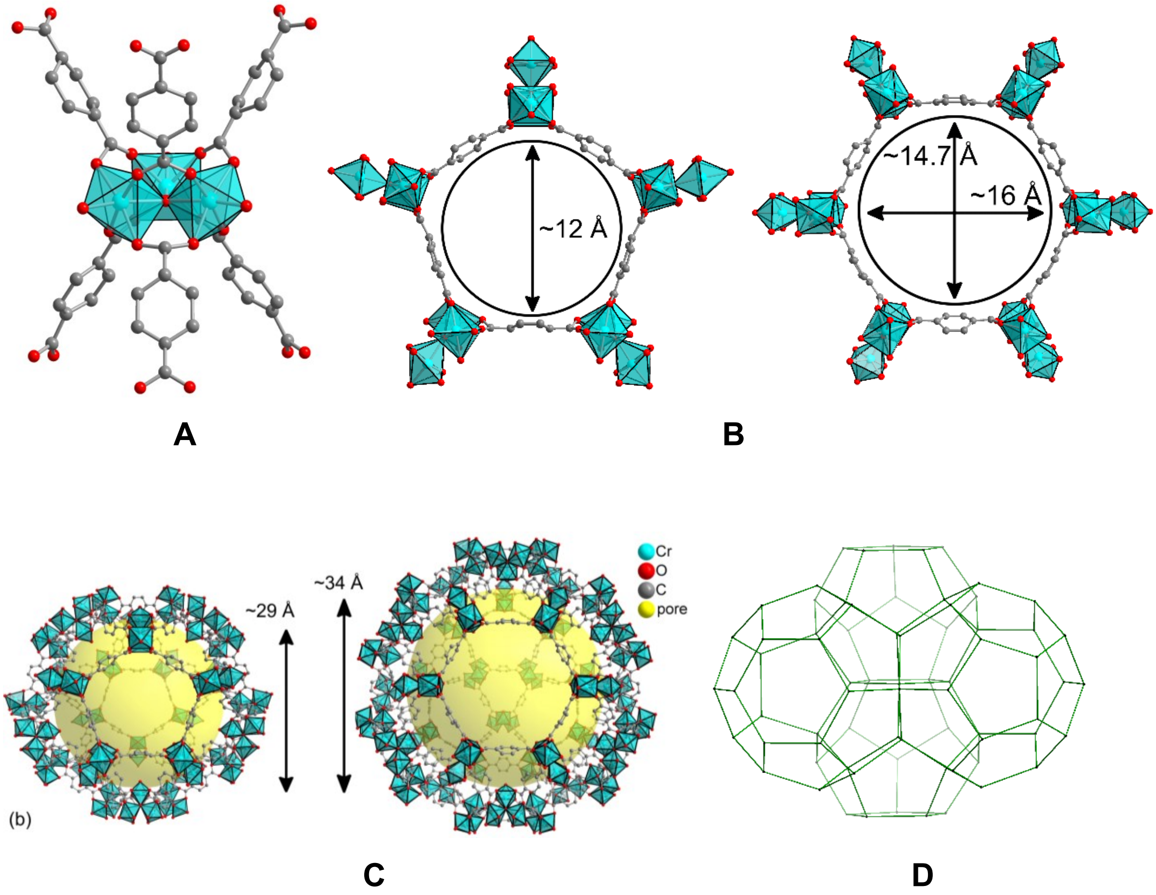

Figure S4 Trinuclear $\{Cr_3(\mu_3\text{-}O)(O_2C\text{-})_6(F,OH)(H_2O)_2\}$ building unit surrounded by bdc linkers in a trigonal prismatic fashion **(A)**; pentagonal and hexagonal cage window apertures with dimensions **(B)**; small cage with pentagonal windows and large cage with pentagonal and hexagonal windows **(C)**; zeotypic network **(D)**. Objects in **(A)** to **(D)** are not drawn to scale. Graphics have been created from the deposited cif-file for MIL-101Cr (CSD-Refcode OCUNAK) (Férey et al., 2005).

Additional information for the syntheses of nano/microsized and microMIL-101Cr

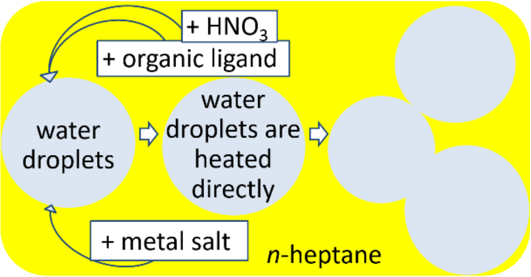

Figure S5 Schematic illustration of water droplets with MOF precursors in heptane of a reverse emulsion. The ater droplets expand and micronize rapidly when heated under microwave irradiation, hence, surface area of water droplets increases, and contact between surfactant and MOF increases (see **Figure S6**).

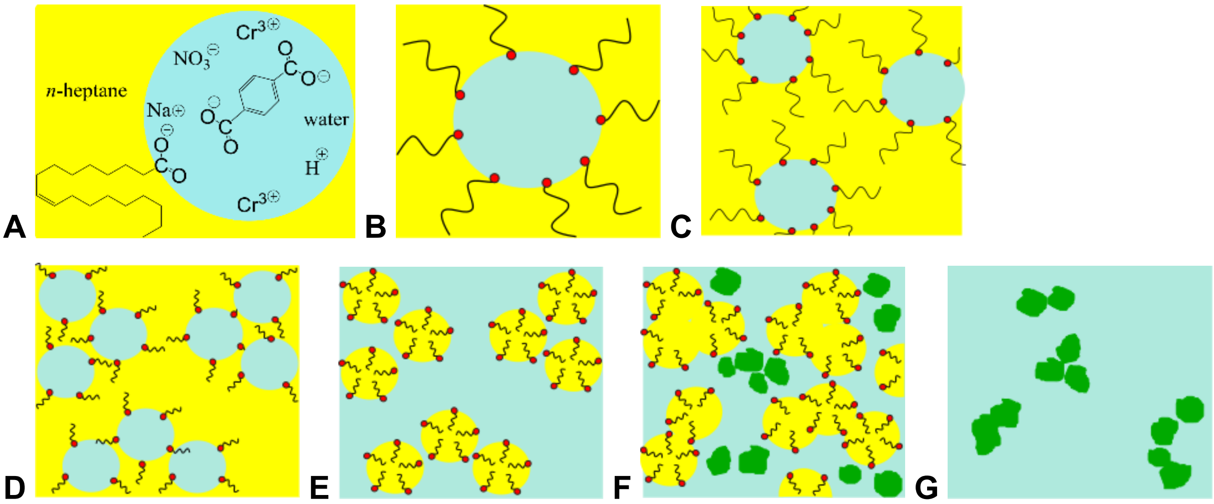

Figure S6 The anticipated reverse emulsion mechanism for the formation of nanoMIL-101Cr (depicted as green domains). BDC^{2-} = benzene-1,4-dicarboxylate, Cr^{3+} = chromium salt, NO$_3^-$ = nitrate ion, and inverse micelles with hydrophobic groups of sodium oleate (hydrophilic groups = red spheres) oriented away from the center (center = water droplets with MOF precursors). Reverse micelle with sodium oleate in n-heptane **(A**,**B)**. At higher temperature the heptane droplets expand rapidly **(C)**. At the PIT (phase inversion temperature) the size of the water droplet reaches a minimum **(D)**, phase inversion occurs **(E)**, coalescence of micelles and formation of nanoMIL-101Cr in the continuous phase **(F)**. Isolated and agglomerated nanoMIL-101Cr particles in water after washing procedure **(G)**.

Different variations of direct/reverse emulsions

We also tried to vary the emulsion parameters for further improvement of our above results. Details for the optimization attempts included (a) synthesis of MIL-101Cr in reverse emulsion without HNO_3, (b) synthesis of MIL-101Cr in reverse emulsion with NaOH, (c) synthesis of MIL-101Cr in direct emulsion without HNO_3, (d) synthesis of MIL-101Cr in direct emulsion with NaOH, and (e) synthesis of MIL-101Cr in direct emulsion without heptane. As no green MIL-101Cr material could be collected by centrifugation from these synthesis routes we will not discuss the syntheses in detail. Moreover, as no material could be obtained without HNO_3 or the swelling effect of heptane we conclude that both are crucial for the emulsion technique.

Synthesis of MIL-101Cr in direct emulsion without HNO3.

A solution of H_2BDC (0.33 g, 2 mmol), $Cr(NO_3)_3{\cdot}9H_2O$ (0.80 g, 2 mmol), and 5 mL water was combined with a solution of sodium oleate (0,14 g, 0.34 mmol) in 5 mL of water and ultrasonicated with heptane (5 mL) for one minute. The direct emulsion was heated to 180 °C/210 within 30 min and kept at this temperature for 10 min/40 min by microwave heating at 600 W. No green MIL-101Cr material was collected by centrifugation.

Synthesis of MIL-101Cr in direct emulsion with NaOH.

A solution of H_2BDC (0.33 g, 2 mmol), $Cr(NO_3)_3{\cdot}9H_2O$ (0.80 g, 2 mmol), 5 mL water, and 10 µL of 20 % NaOH was combined with a solution of sodium oleate (0,14 g, 0.34 mmol) in 5 mL of water and ultrasonicated with heptane (5 mL) for one minute. The direct emulsion was heated to 180 °C/210 within 30 min and kept at this temperature for 10 min/40 min by microwave heating at 600 W. No green MIL-101Cr material was collected by centrifugation.

Synthesis of MIL-101Cr in direct emulsion with HNO3 but without heptane.

A solution of H_2BDC (0.33 g, 2 mmol), $Cr(NO_3)_3{\cdot}9H_2O$ (0.80 g, 2 mmol), 5 mL water, and 10 µL of 65 % HNO_3 was combined with a solution of sodium oleate (0,14 g, 0.34 mmol) in 10 mL of water and ultrasonicated for one minute. The direct emulsion was heated to 180 °C/210 within 30 min and kept at this temperature for 10 min/40 min by microwave heating at 600 W. No 3green MIL-101Cr material was collected by centrifugation.

Synthesis of MIL-101Cr in reverse emulsion without HNO3.

A solution of H_2BDC (0.33 g, 2 mmol), $Cr(NO_3)_3{\cdot}9H_2O$ (0.80 g, 2 mmol), and 4 mL water was combined with a solution of one of the surfactants, sodium oleate (1.00 g, 3.28 mmol), CTAB (1.00 g, 2.73 mmol), or Triton X-45 (1.00 g, 2.47 mmol) in 4 mL of water, ultrasonicated with *n*-heptane (40 mL) for 1 min, and heated as mentioned above. No green MIL-101Cr material was collected by centrifugation.

Synthesis of MIL-101Cr in reverse emulsion with NaOH.

A solution of H_2BDC (0.33 g, 2 mmol), $Cr(NO_3)_3 \cdot 9H_2O$ (0.80 g, 2 mmol), 4 mL water, and 10 µL of 20 % NaOH was combined with a solution of one of the surfactants, sodium oleate (1.00 g, 3.28 mmol), CTAB (1.00 g, 2.73 mmol), or Triton X-45 (1.00 g, 2.47 mmol) in 4 mL of water and ultrasonicated with *n*-heptane (40 mL) for 1 min. The reverse emulsion was heated to 180 °C within 30 min and kept at this temperatur for 40 min by microwave heating at 600 W (Mars-6 microwave reactor from CEM). No green MIL-101Cr material was collected by centrifugation.

Additional analysis for nano/microsized and microMIL-101Cr

Fourier transform infrared-attenuated total reflectance spectroscopy (FTIR-ATR)

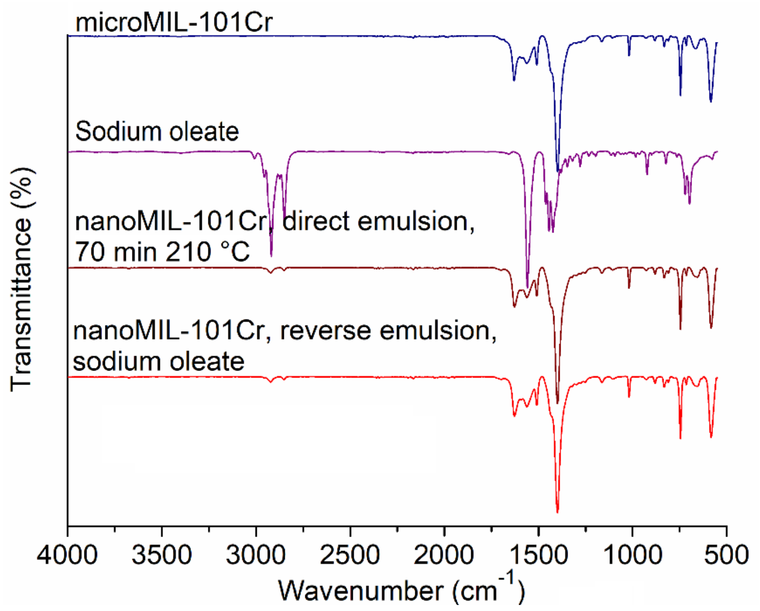

Figure S7 FTIR-ATR spectra of micrMIL-101 (navy blue), sodium oleate (dark violet), nanoMIL-101Cr via direct emulsion (brown) and nanoMIL-101Cr via reverse emulsion (red).

Pore-size distribution

The following data (**Figure S8 – Figure S10**) show the results for the pore-size distribution of nanoMIL-101Cr via direct and reverse emulsion, and microMIL-101Cr synthesized via a conventional procedure, respectively.

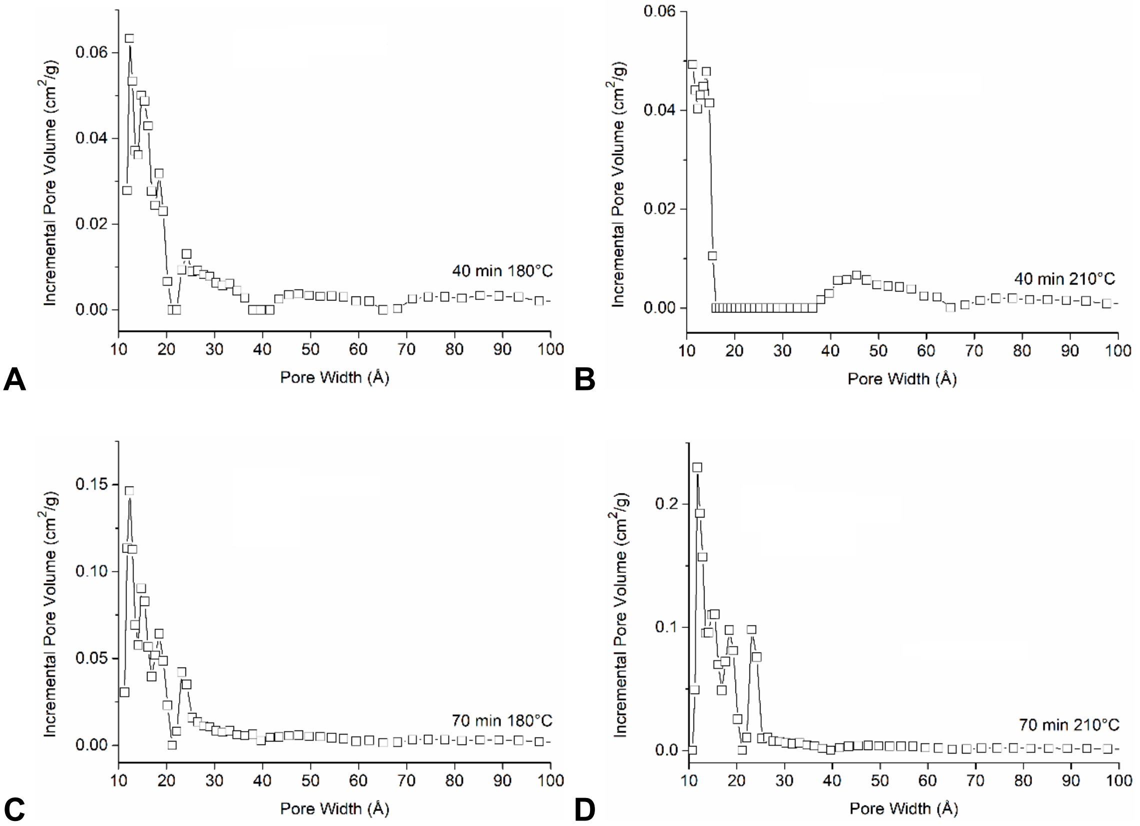

Figure S8 NL-DFT pore-size distribution of nanoMIL-101Cr in direct emulsions prepared for 40 min at 180 °C **(A)**, 70 min at 180 °C **(B)**, 40 min at 210 °C **(C)**, and 70 min at 210 °C **(D)**.

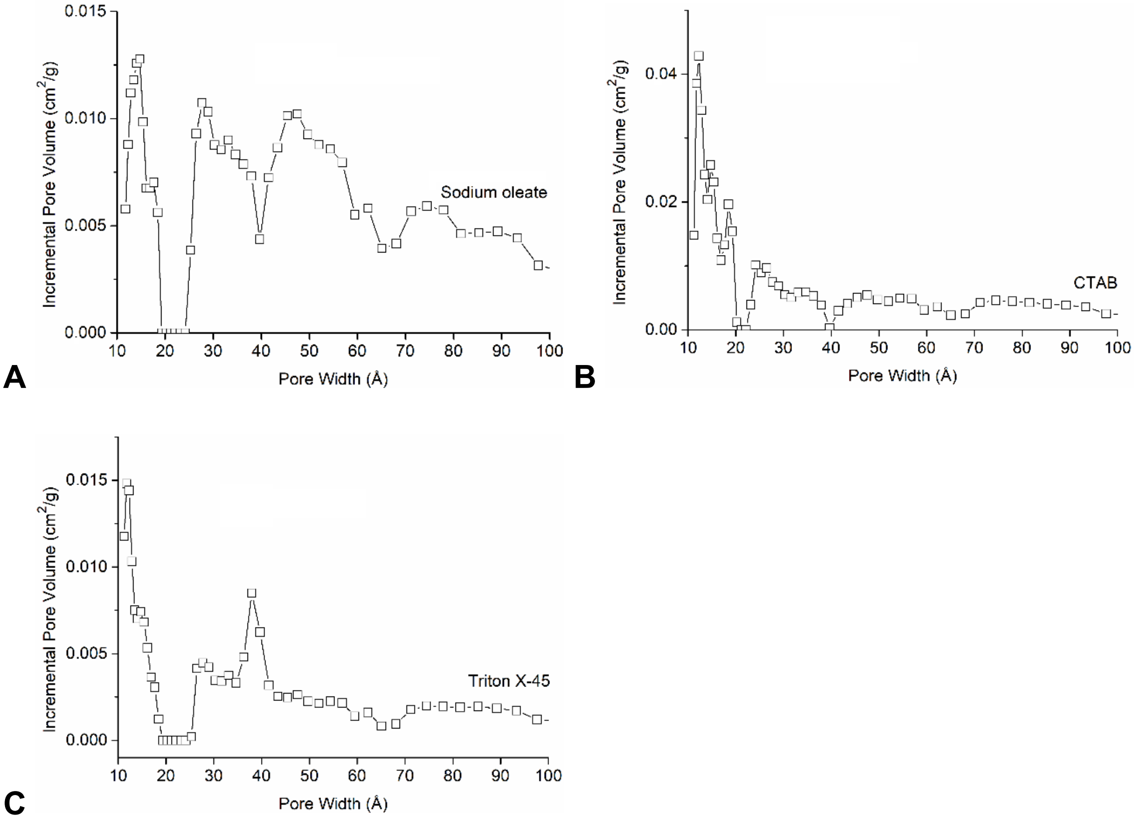

Figure S9 DFT pore-size distribution of nanoMIL-101Cr in reverse emulsions prepared by using sodium oleate **(A)**, CTAB **(B)**, and Triton X-45 **(C)**.

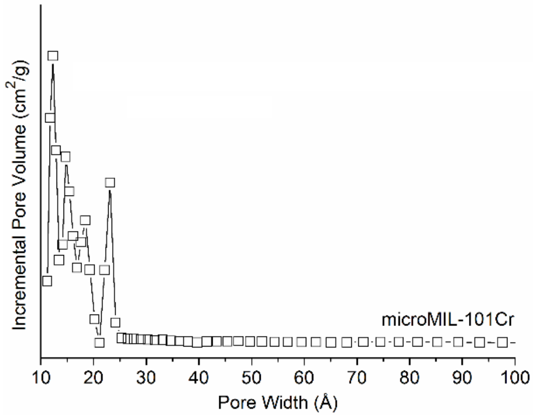

Figure S10 DFT pore-size distribution curves of microMIL-101Cr through conventional synthesis with TMAOH.

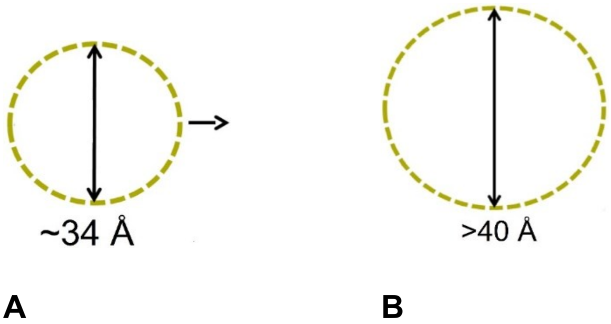

Figure S11) The comparison between the normal pore size **(A)** and the pore size given here by using surfactants **(B)** for MIL-101(Cr.

Scanning electron microscopic (SEM) and transmission electron microscopy (TEM)

Scanning and transmission electron microscopy (SEM, TEM) images show aggregates of small primary particles which may be due to sample preparation, see **Figure 5** and **Figure S12 – Figure S16**. The following data show the images and histograms gotten from TEM measurements of nanoMIL 101Cr samples synthesized via direct and reverse emulsion.

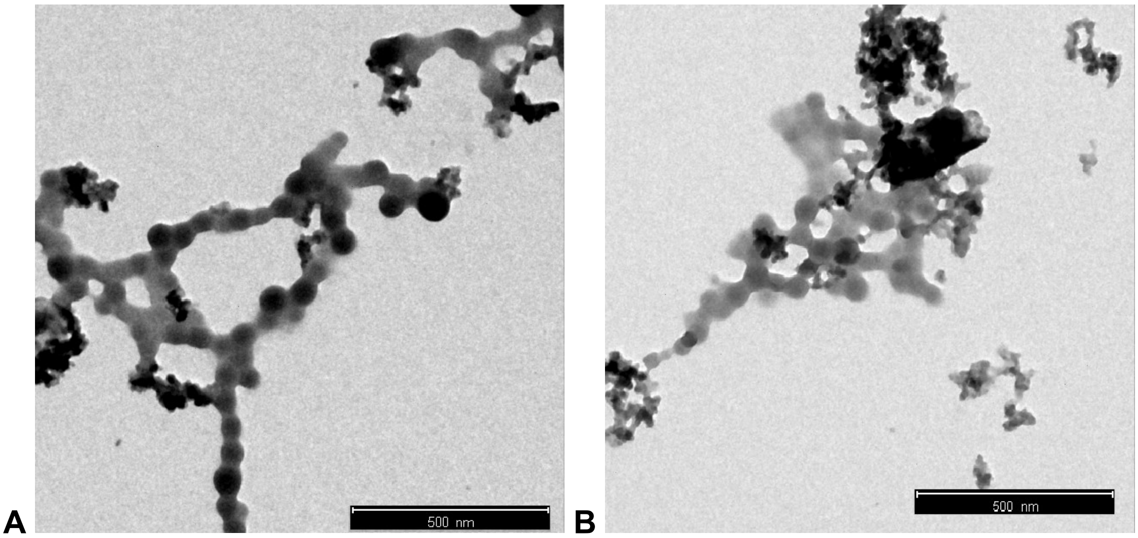

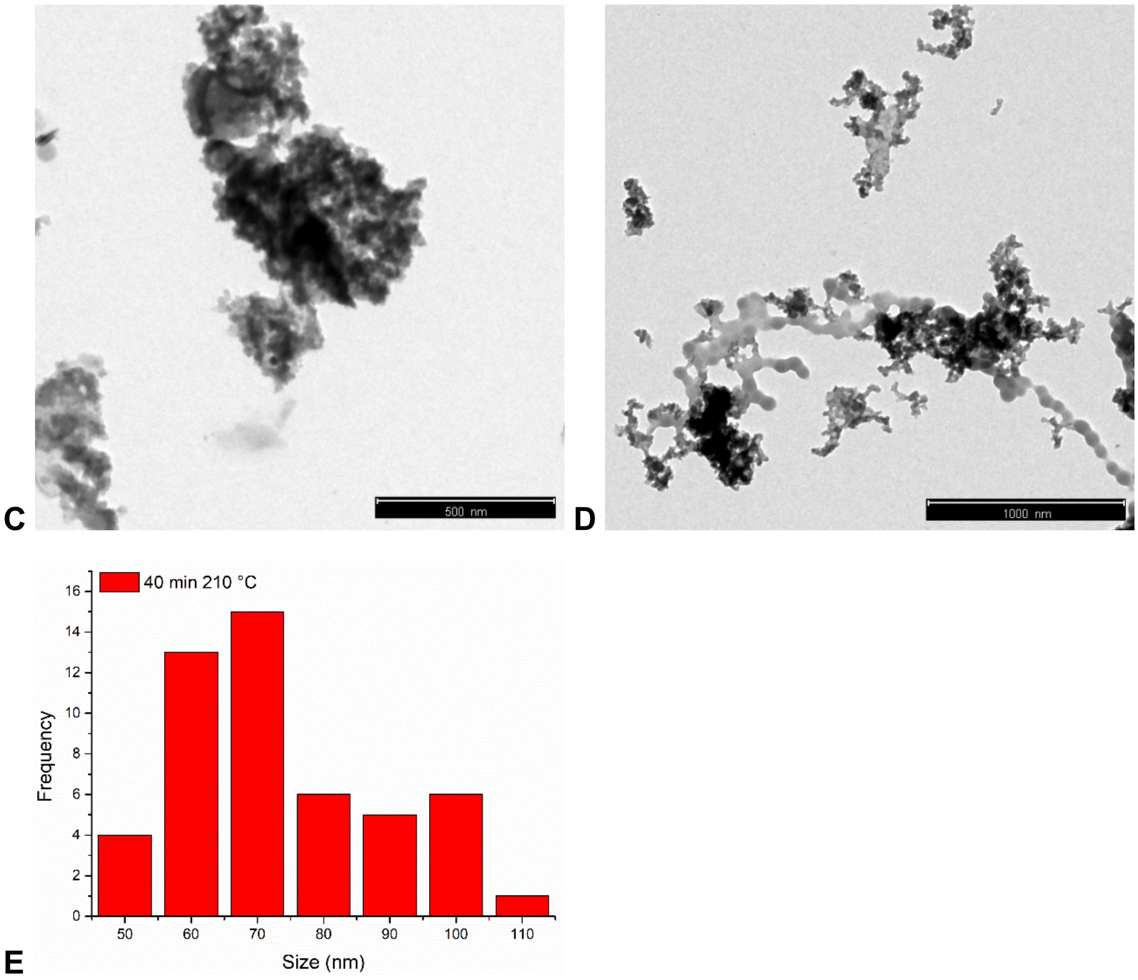

Figure S12 TEM images of nanoMIL-101Cr synthesized in direct emulsion with sodium oleate for 40 minutes at 210° C. Scale bar 500 nm (A-C) and 1000 nm (D). Histogram of nanoMIL-101Cr (E). Statistic based on 50 particles. Polydispersity index (PDI) = 0.04.

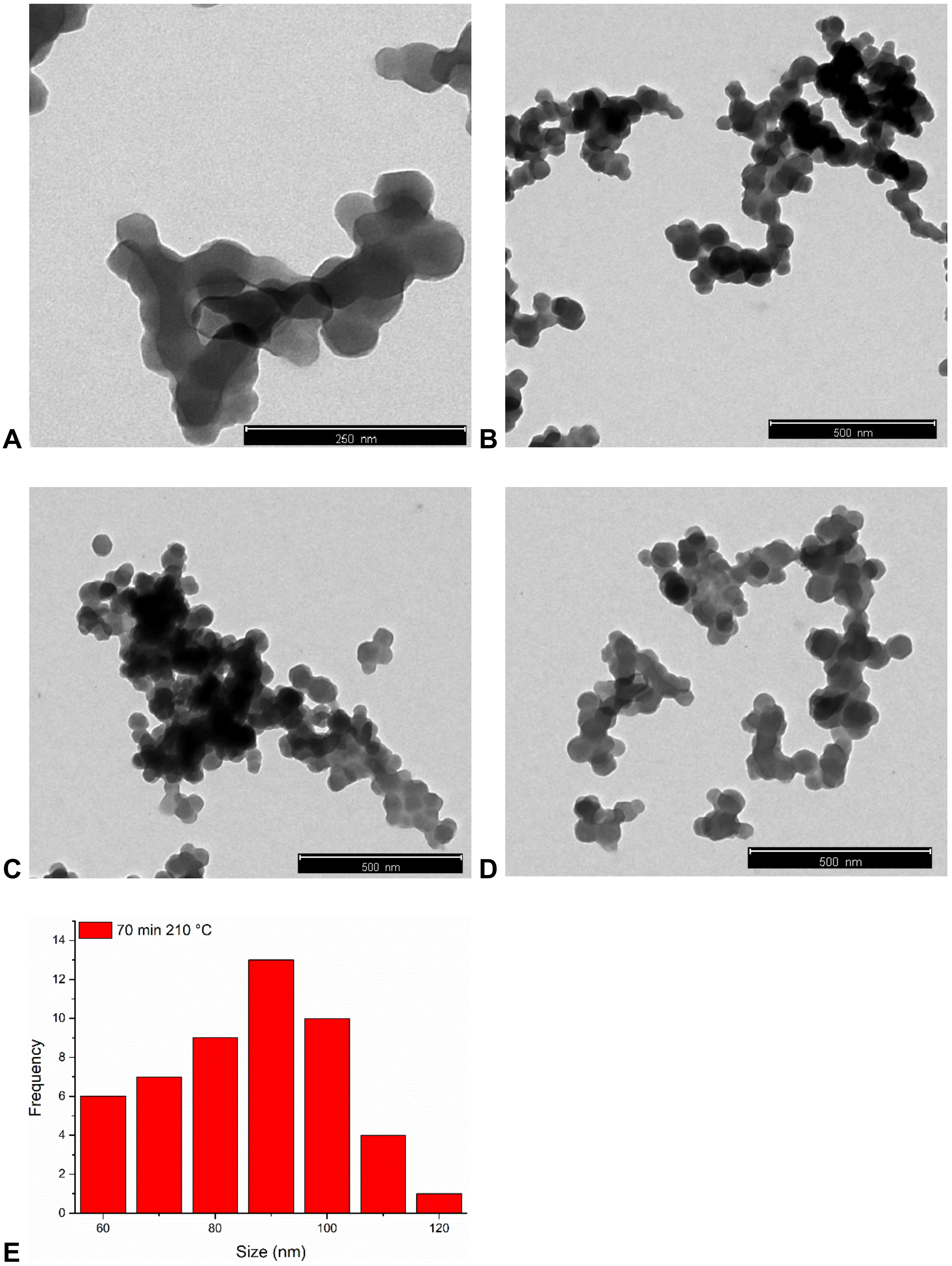

Figure S13 TEM images of nanoMIL-101Cr synthesized in direct emulsion with sodium oleate for 70 minutes at 210° C **(A)**. Scale bar 250 nm **(A)**, 500 nm **(B-D)**. Histogram of nanoMIL-101Cr **(E)**. Statistic based on 50 particles. Polydispersity index (PDI) = 0.02.

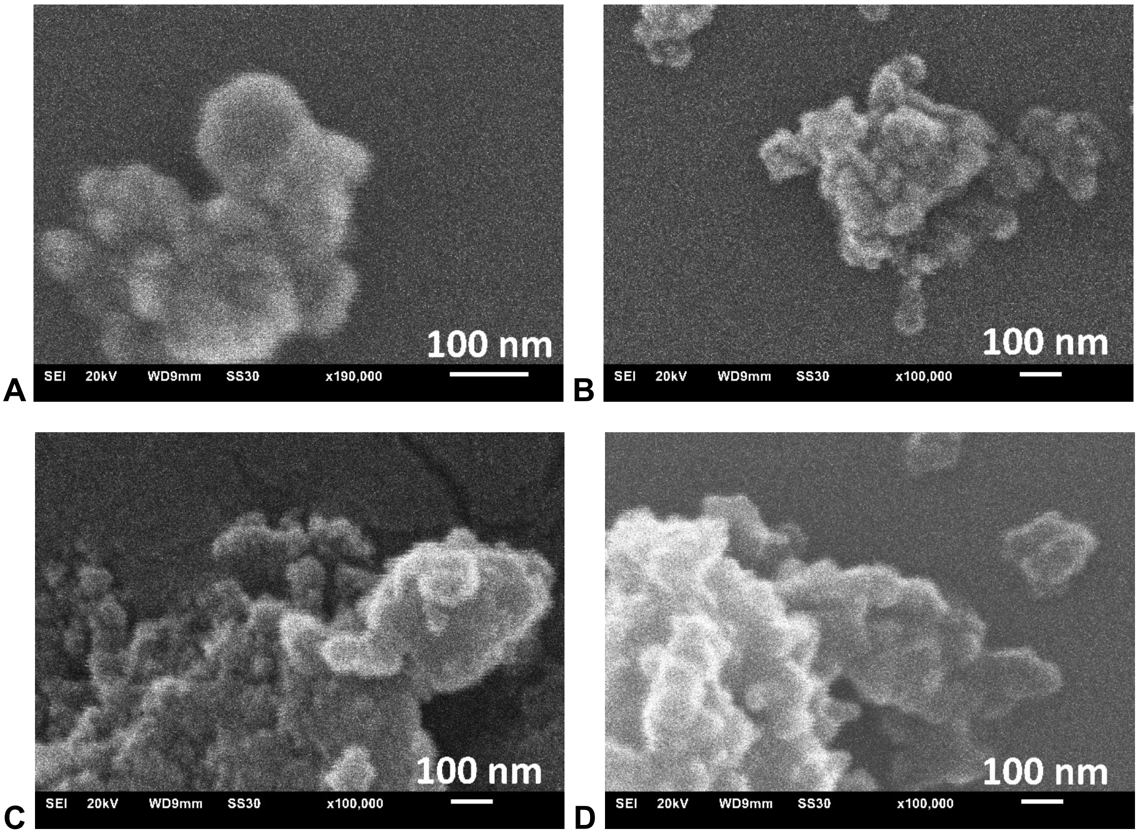

Figure S14 SEM images of the nanoMIL-101Cr prepared in reverse emulsion with sodium oleate **(A**,**B)**; CTAB **(C)**, and Triton X-45 **(D)**.

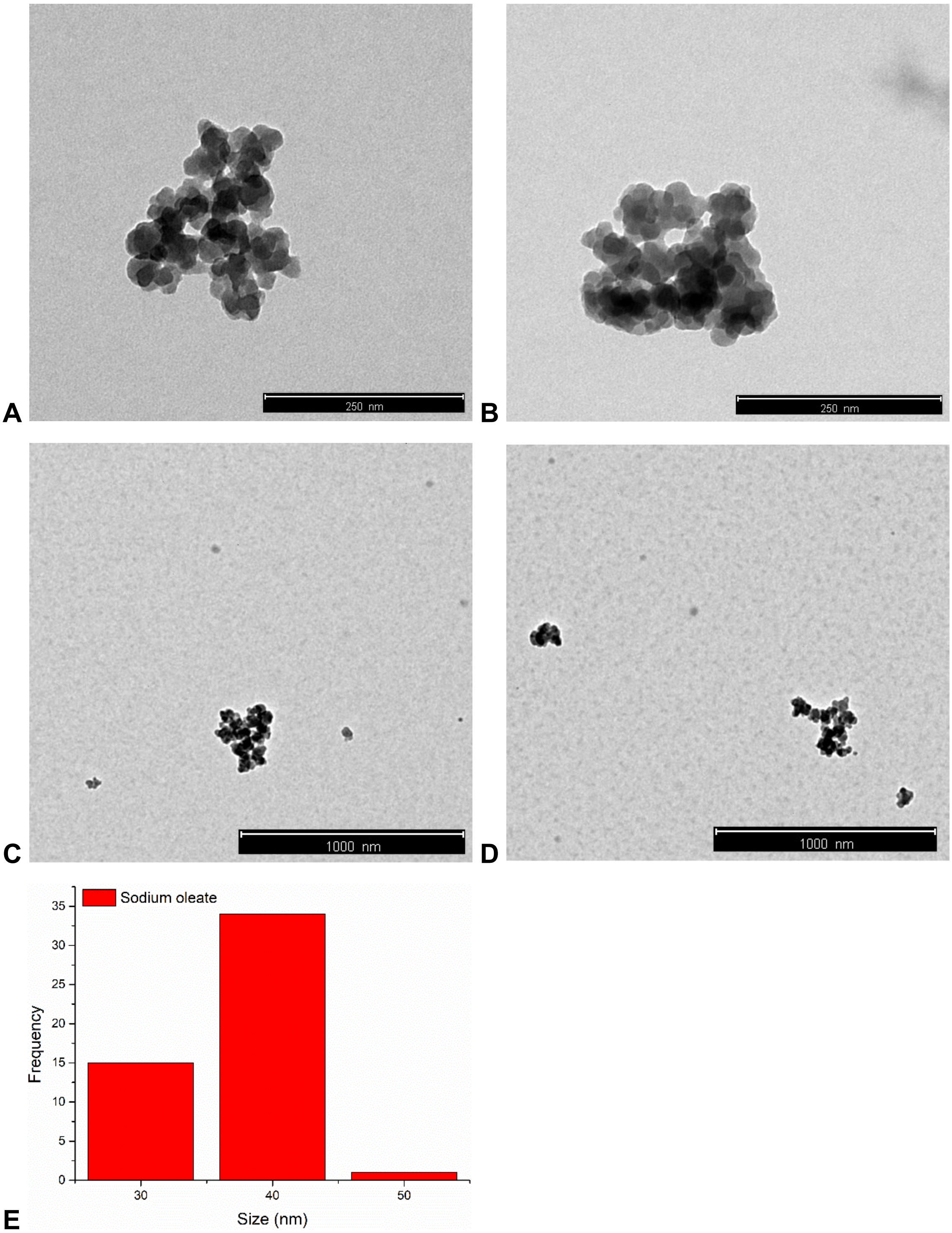

Figure S15 TEM images of nanoMIL-101Cr synthesized in reverse emulsion with sodium oleate. Scale bar 250 nm **(A**,**B)** and 1000 nm **(C,D)**. Histogram of nanoMIL-101Cr **(E)**. Statistic based on 50 particles. Polydispersity index (PDI) = 0.01.

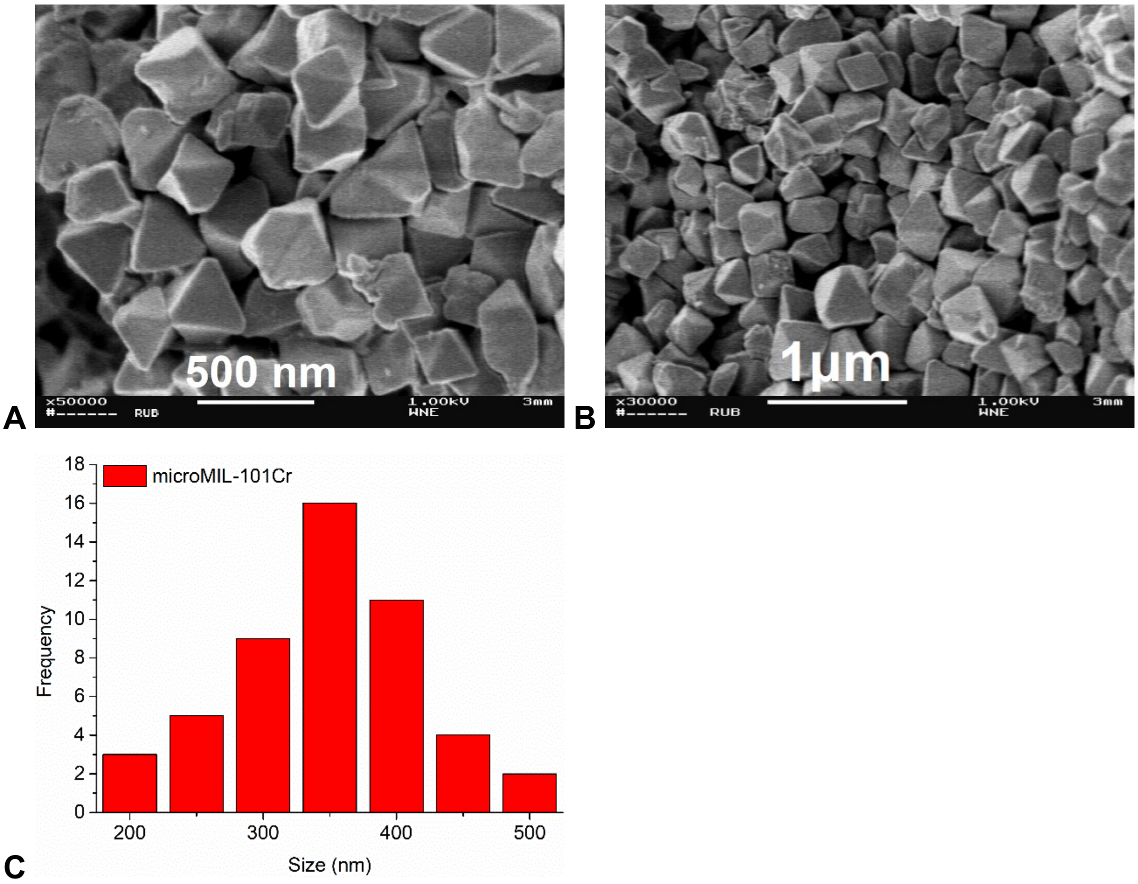

Figure S16 SEM images for microMIL-101Cr **(A,B)**. Histogram of microMIL-101Cr **(C)**. Statistic based on 50 particles. Polydispersity index (PDI) = 0.04.

Dynamic light scattering (DLS)

The following figures (**Figure S17** Figure S– **Figure S23**) show representative intensity-time autocorrelation functions recorded at θ = 90° **(A)**,the corresponding hydrodynamic radius distribution functions calculated from the relaxation rate distribution functions G(Γ) obtained from CONTIN analysis **(B)** as well as the plots of the mean relaxation rate Γ of the dominating scattering species as a function of q^2 **(C)** from DLS measurements of nanoMIL-101Cr samples synthesized via direct and reverse emulsion.

In general, we measure typical intensity-time autocorrelation functions that decay to zero at large decay times for all samples. The CONTIN fits (black solid lines) nicely describe each function. The intensity-weighted radius distribution functions obtained from the CONTIN analysis reveal mostly two contributions: 1) a dominating contribution with sizes in the range of hundreds of several hundreds of nm and 2) a contribution at significantly larger radii, in the micron range. In some cases (**Figure S22** and **Figure S23**), also a third contribution close to 100 nm is observed. Thus the correlation functions are clearly multimodal with two or three contributions. The contributions in the micron size range is most likely caused by the presence of a small fraction of aggregates or impurities from e.g. dust that where not removed by the applied filtration process. However, this contribution is only a minor one for each sample and given the fact that the presented results come from an intensity-weighted analysis, can be neglected. Thus we focus in the following on analysis of the dominating contribution and use angular dependent analysis to study the diffusion behavior and finally determine the hydrodynamic particle size. Therefore, the meanrelaxation rates Γ for the dominating species as obtained from the CONTIN analysis were plotted against the squared scattering vector q^2. For all samples a linear dependence of Γ as a function of q^2 is observed. Thus, we can conclude that we probe only translational diffusion (see equation S10) for all nanoMIL-101Cr samples. The respective translational diffusion coefficients D_t obtained from the slope of the linear regressions in each plot are mentioned in each figure caption, respectively. From D_t we also calculated the respective hydrodynamic radii according to equation S11. The corresponding radii are mentioned in the figure captions. For samples prepared in direct and reverse emulsions with sodium oleate as the surfactant the obtained R_H lie in a range 120-150 nm. For MIL101-Cr samples prepared with CTAB and Triton X-45 as the surfactant values of 726 nm and 440 nm, respectively (**Figure S22** and **Figure S23**) were obtained.

We note that, even small traces of agglomerated particles are able to distort a DLS measurement (Hall et al., 2007). It was shown by Grobelny et. al that the detection of smaller nanoparticles in the presence of a few percent of larger ones by DLS is difficult. Moreover, particles with the size of 10 nm could appear four times as large (~40 nm) while, for example, particles of 80 nm could appear only 1.3-times larger than the particle size by TEM analysis (Tomaszewska et al., 2013). As a consequence, it was not possible to detect the signal coming from 95% of smaller particles in the presence of 5% bigger particles. Other publications also mentioned DLS particle sizes 1.7-times larger than the primary particle size by TEM analysis (Foldbjerg et al., 2009; Chalati et al., 2011). In summary, DLS is very sensitive to traces of larger or agglomerated particles and the detection of smaller particles is easily concealed by a small percentage of agglomerated particles.

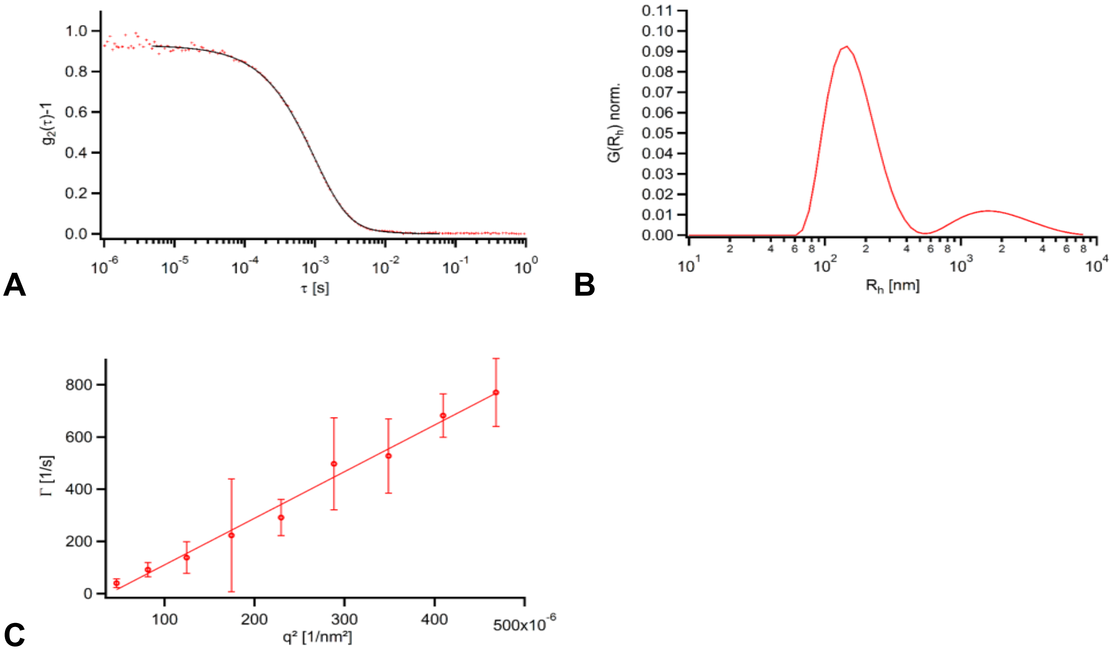

Figure S17 DLS measurement of MIL-101Cr prepared by direct emulsion technique and using sodium oleate as surfactant (40 min, 180 °C). **(A)** Autocorrelation function recorded at 25 °C and a scattering angle of $\theta = 90$ °, **(B)** corresponding hydrodynamic radius distribution function calculated from the relaxation rate distribution function (intensity-weighted). **(C)** Γ vs q^2, the slope of the regression line provides D_t. R_h is calculated using the Stokes-Einstein equation. $R_h = 137.25$ nm, with $\eta(H_2O) = 0.889$ mPa*s and $D_t = 1.7861 \cdot 10^6$ nm²/s.

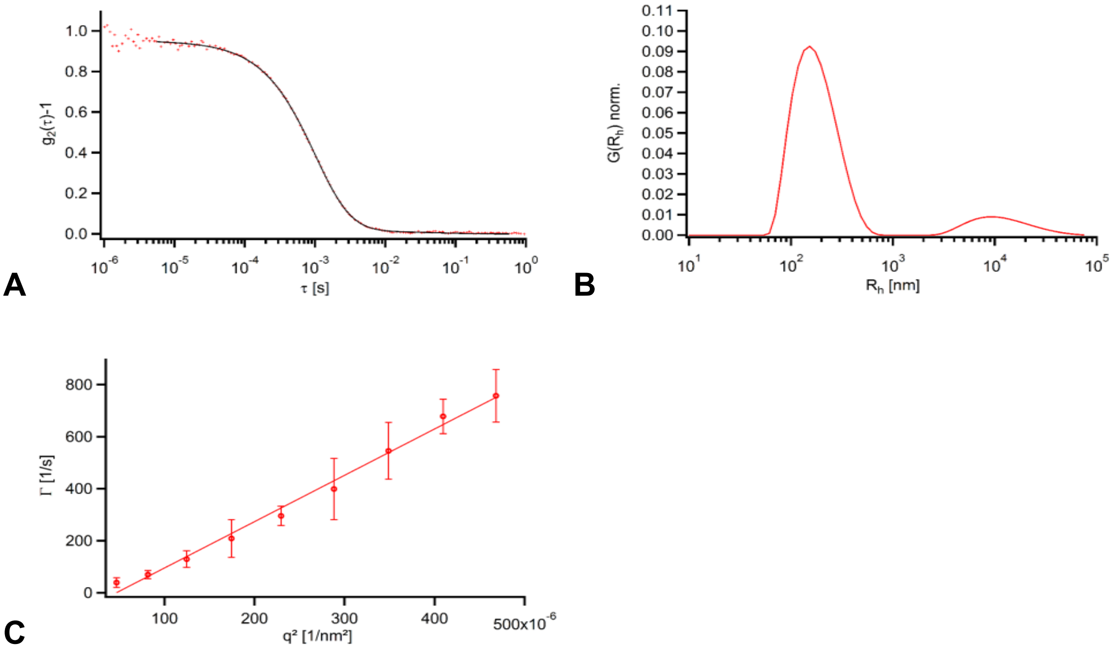

Figure S18 DLS measurement of MIL-101Cr prepared by direct emulsion technique and using sodium oleate as surfactant (70 min, 180 °C). **(A)** Autocorrelation function recorded at 25 °C and a scattering angle of θ = 90 °, **(B)** corresponding hydrodynamic radius distribution function calculated from the relaxation rate distribution function (intensity-weighted). **(C)** Γ vs q^2, the slope of the regression line provides D_t. R_h is calculated using the Stokes-Einstein equation. $R_h = 137.61$ nm, with $\eta(H_2O) = 0.889$ mPa*s and $D_t = 1.7814*10^6$ nm²/s.

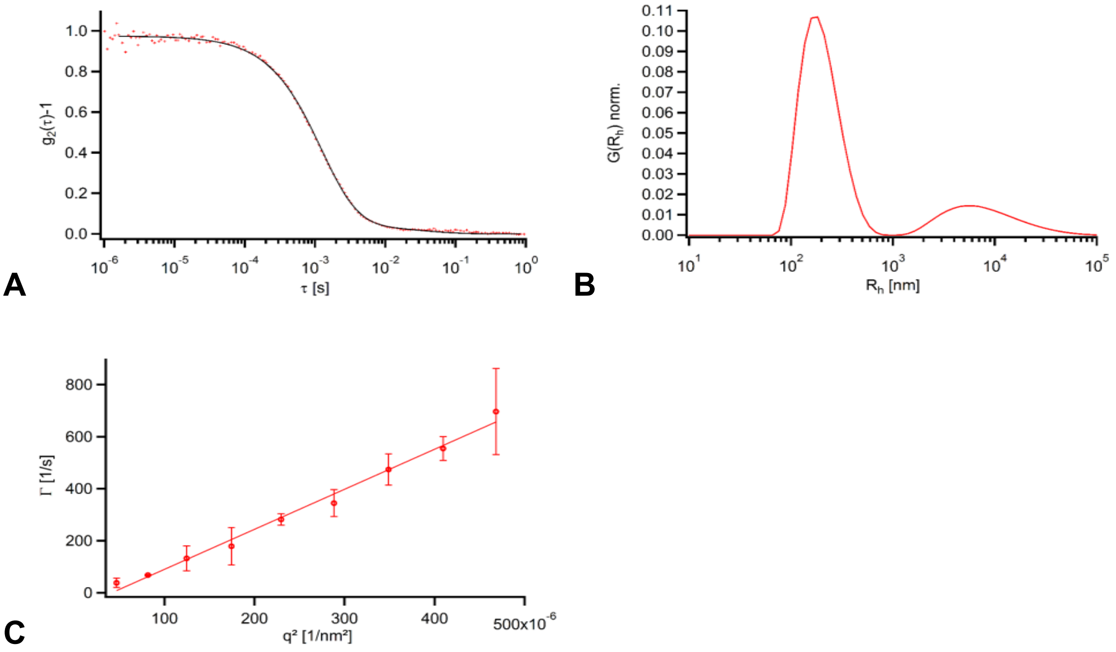

Figure S19 DLS measurement of MIL-101Cr prepared by direct emulsion technique and using sodium oleate as surfactant (40 min, 210 °C). **(A)** Autocorrelation function recorded at 25 °C and a scattering angle of $\theta = 90$ °, **(B)** corresponding hydrodynamic radius distribution function calculated from the relaxation rate distribution function (intensity-weighted). **(C)** Γ vs q^2, the slope of the regression line provides D_t. R_h is calculated using the Stokes-Einstein equation. $R_h = 155.04$ nm, with $\eta(H_2O) = 0.889$ mPa*s and $D_t = 1.5811*10^6$ nm²/s.

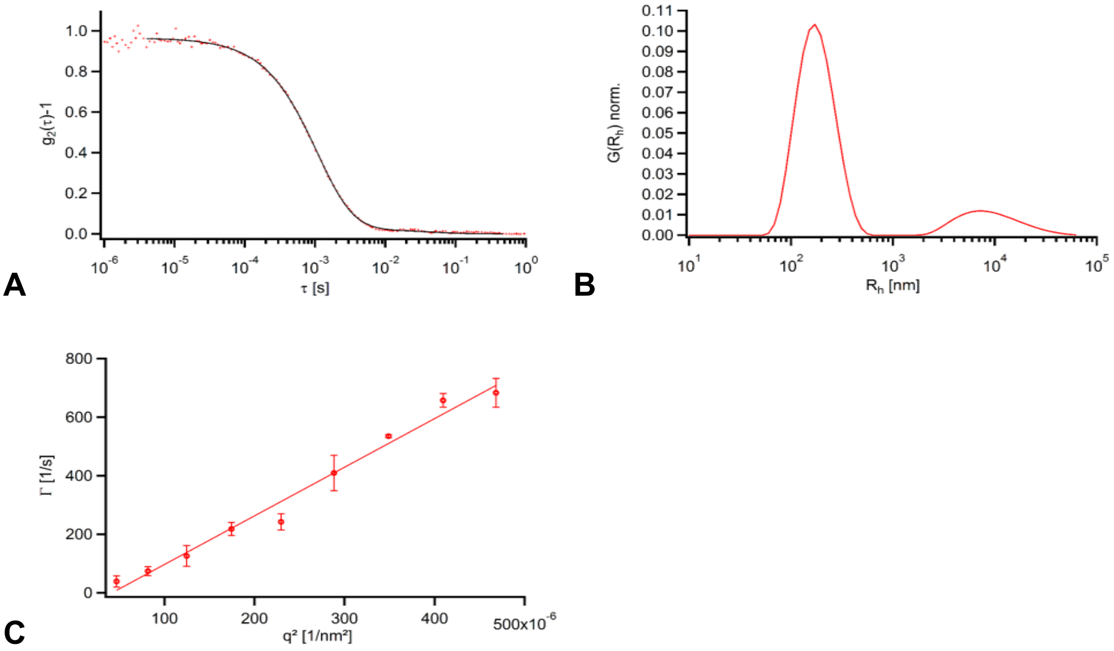

Figure S20 DLS measurement of MIL-101Cr prepared by direct emulsion technique and using sodium oleate as surfactant (70 min, 210 °C). **(A)** Autocorrelation function recorded at 25 °C and a scattering angle of θ = 90 °, **(B)** corresponding hydrodynamic radius distribution function calculated from the relaxation rate distribution function (intensity-weighted). **(C)** Γ vs q², the slope of the regression line provides D_t. R_h is calculated using the Stokes-Einstein equation. R_h = 145.36 nm, with η(H_2O) = 0.889 mPa*s and D_t = 1.6853*10^6 nm²/s.

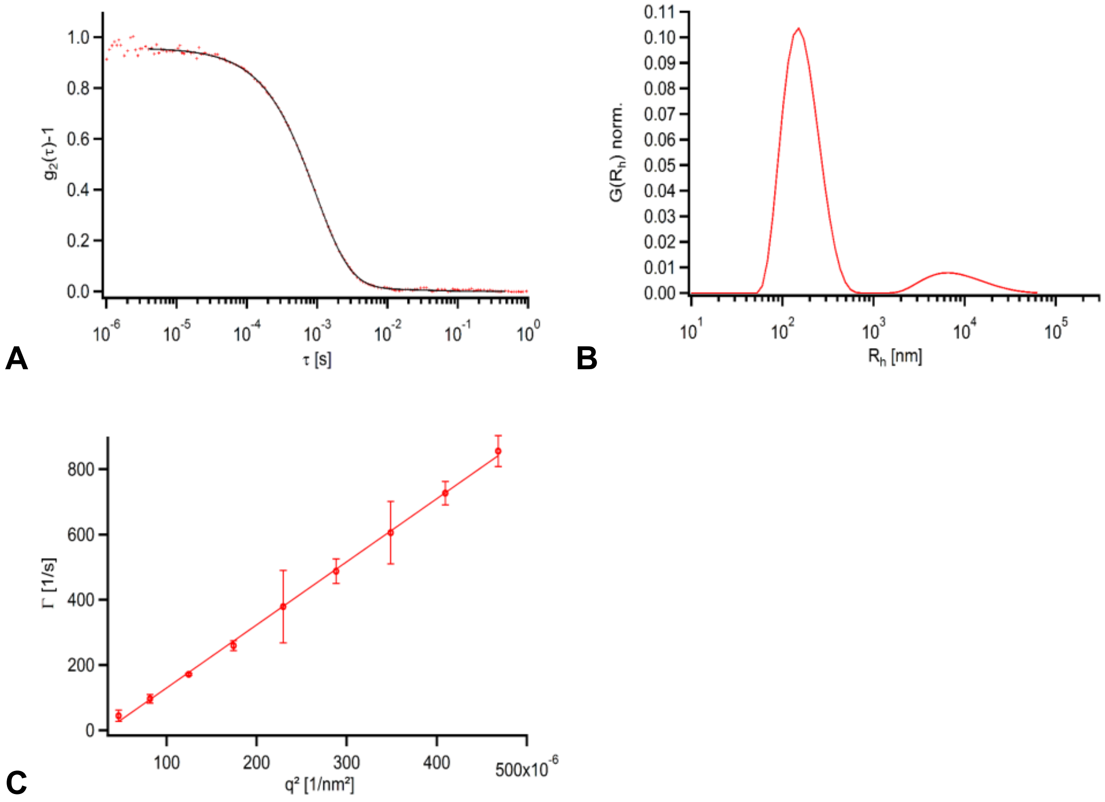

Figure S21 DLS measurement of MIL-101Cr prepared by reverse emulsion technique and using sodium oleate as surfactant. **(A)** Autocorrelation function recorded at 25 °C and a scattering angle of θ = 90 °, **(B)** corresponding hydrodynamic radius distribution function calculated from the relaxation rate distribution function (intensity-weighted. **(C)** Γ vs q², the slope of the regression line provides D_t. R_h is calculated using the Stokes-Einstein equation. R_h = 126.86 nm, with η(H_2O) = 0.889 mPa*s and D_t = 1.9323*10^6 nm²/s.

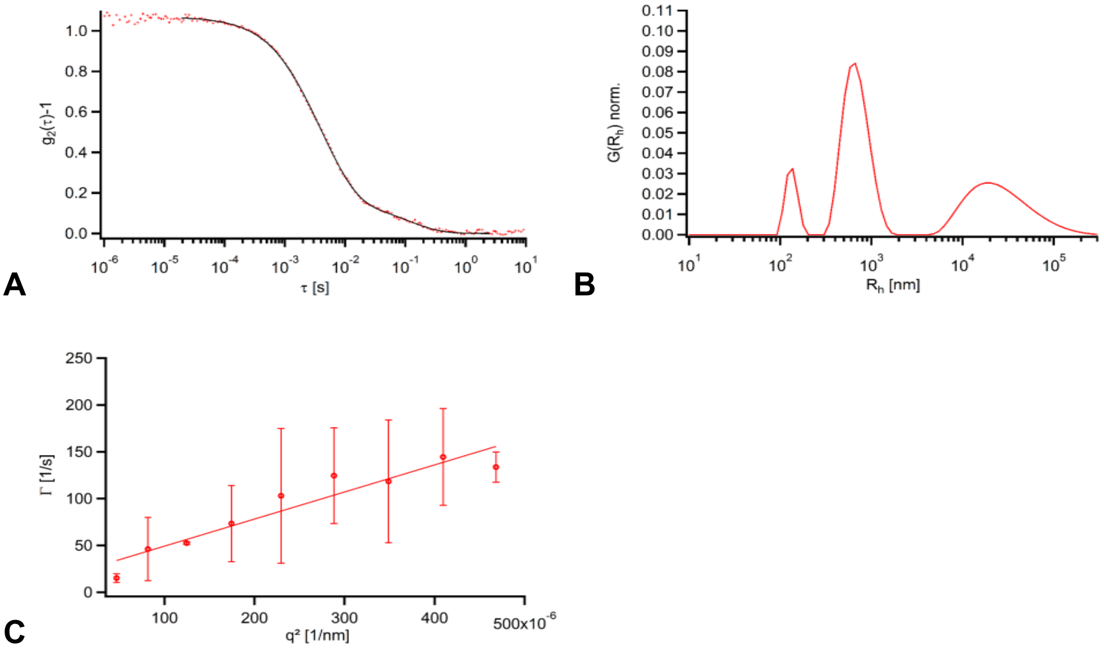

Figure S22 DLS measurement of MIL-101Cr prepared by reverse emulsion technique and using CTAB as surfactant. **(A)** Autocorrelation function recorded at 25 °C and a scattering angle of θ = 90 °, **(B)** corresponding hydrodynamic radius distribution function calculated from the relaxation rate distribution function (intensity-weighted). **(C)** Γ vs q², the slope of the regression line provides D_t. R_h is calculated using the Stokes-Einstein equation. R_h = 726.90 nm, with $\eta(H_2O)$ = 0.889 mPa*s and $D_t = 3.3724*10^5$ nm²/s.

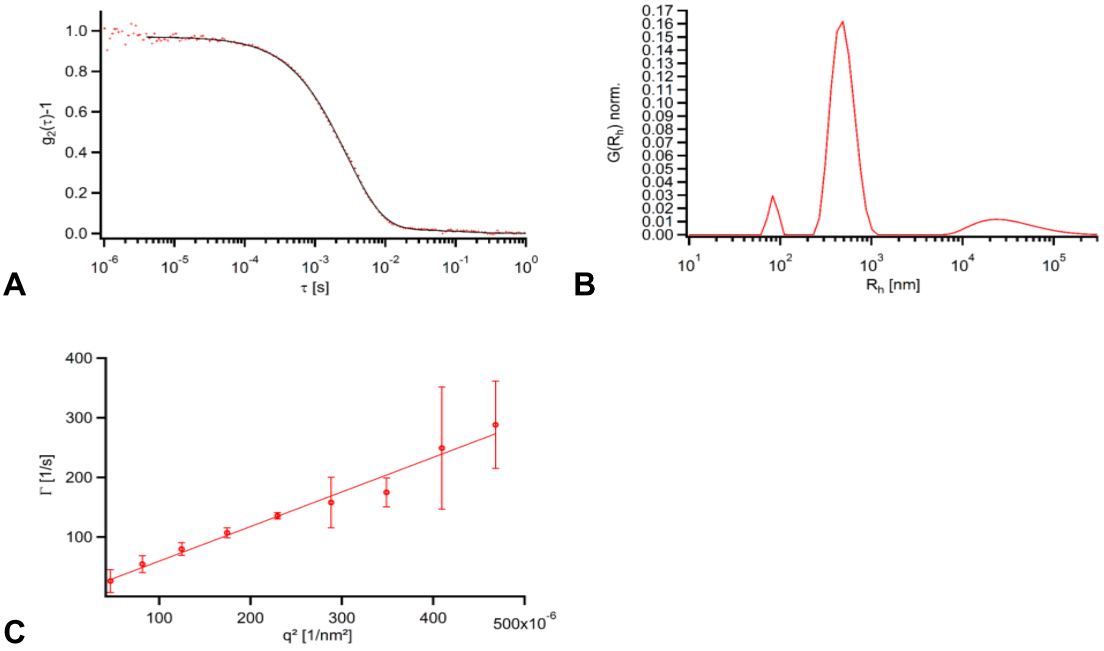

Figure S23 DLS measurement of MIL-101Cr prepared by reverse emulsion technique and using Triton X-45 as surfactant. **(A)** Autocorrelation function recorded at 25 °C and a scattering angle of θ = 90 °, **(B)** corresponding hydrodynamic radius distribution function calculated from the relaxation rate distribution function (intensity-weighted). **(C)** Γ vs q², the slope of the regression line provides D_t. R_h is calculated using the Stokes-Einstein equation. $R_h = 441.31$ nm, with $\eta(H_2O) = 0.889$ mPa*s and $D_t = 5.5548*10^5$ nm²/s.

Mixed-matrix membranes

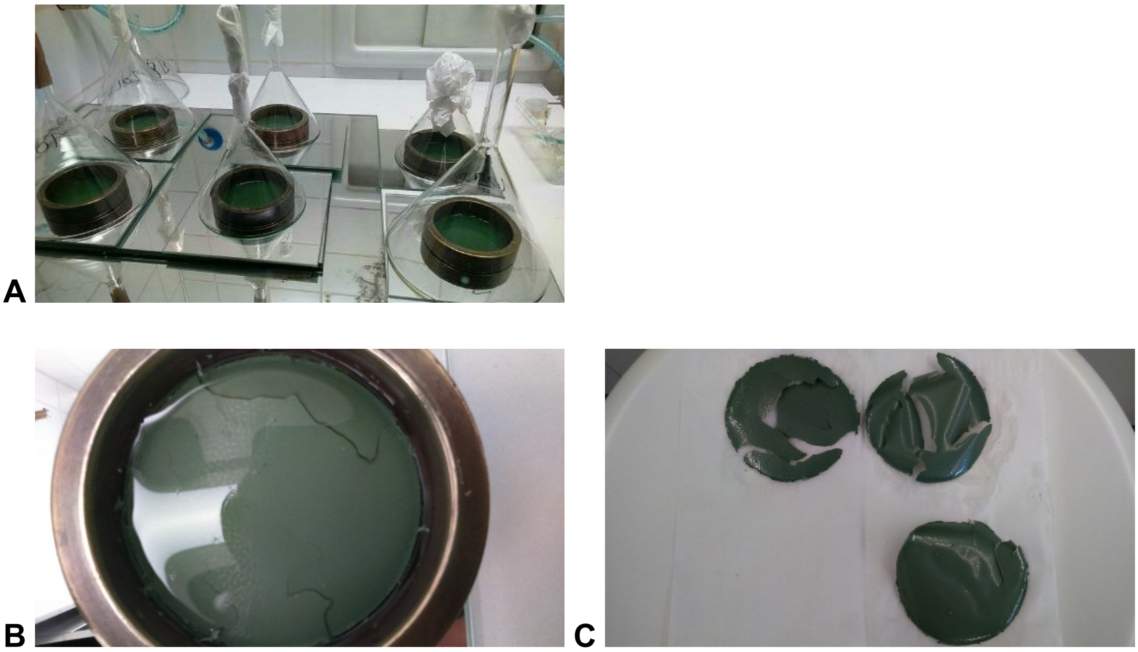

Figure S24 Metal rings with MMM suspension covered with funnels **(A)**. Cracked MMM with 24 wt% of MIL-101Cr **(B**,**C)**.

Additional analyses for mixed-matrix membranes

Powder X-ray diffraction, scanning electron microscopic (SEM), and Infrared analysis (IR)

Detail information for the fabrication of Matrimid membranes and mixed-matrix membranes are listed in **Table 2**. Separation properties are summarized in **Table 3**. The results for the PXRD and FTIR-ATR gotten from the MMMs are shown in **Figure S27**. Also, a cross-section of the pure Matrimid membrane is presented in **Figur S25**. Moreover, gas permeation data for CO_2/CH_4 of already published MMM with different MOFs and MAtrimid are listed in **Table S2**.

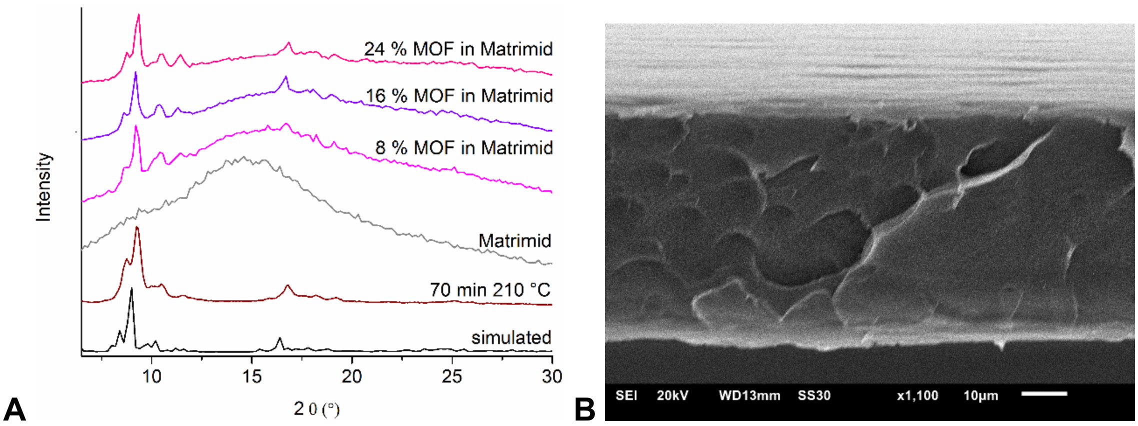

Figure S25 XRD patterns **(A)** of synthesized nanoMIL-101Cr (brown), Matrimid (grey), MMM with 8 wt % MOF (pink); with 16 wt % MOF (violet), with 24 wt % MOF (magenta), simulated pattern (black) (Férey et al., 2005). SEM images of the cross-section of Matrimid membrane **(B)**. Scale bar 10 µm.

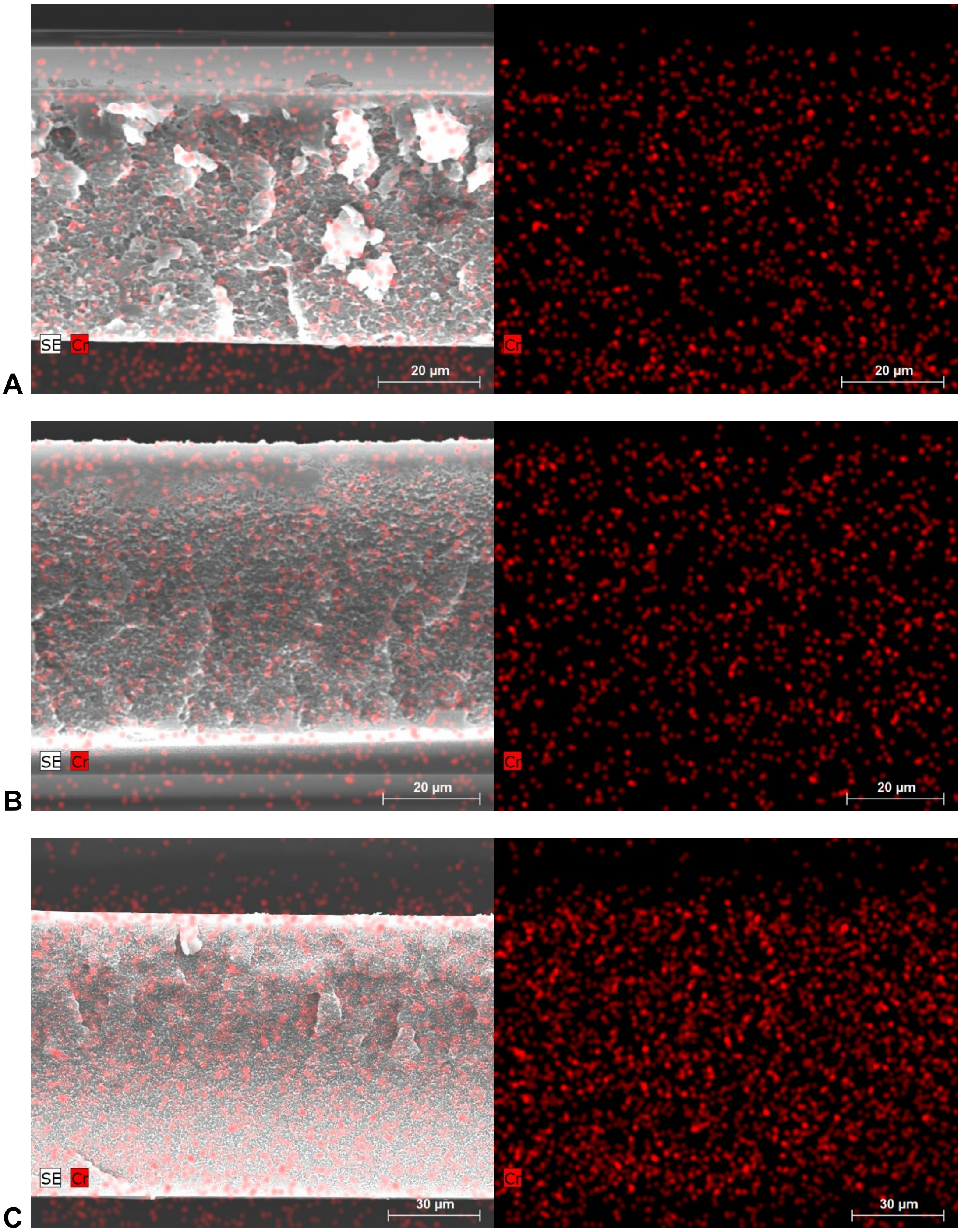

Figure S26 SEM images of the cross-section of microMIL-101Cr@Matrimid membrane: with 8 wt % MOF **(A)**; with 16 wt % MOF **(B)**, and with 20 wt % MOF **(C)**. Images of only EDX mapping (Cr = red) are shown on the left for a clearer representation. The bottom of the cross-sections in the image corresponds to the bottom of the membrane when casted. Cross-section of pure Matrimid is shown in **Figure S25B**.

The FTIR-ATR results for MIL-101Cr, nanoMIL-101Cr, Matrimid, and MMMs show that the characteristic bonds match with those described in the literature (**Figure S27**) (Rajati et al., 2018). The symmetric and asymmetric stretching bonds of the C=O groups of the imide can be observed at 1780 cm^{-1} and 1717 cm^{-1}. The symmetric stretch vibration of benzophenone carbonyl is shown at 1669 cm^{-1}. The bands at 1363 cm^{-1} and 1089 cm^{-1} are for the stretching modes of the C-N-C of the imide 5-membered ring (Inagaki et al., 2013). The band at 1396 cm^{-1} is based on the symmetric O-C-O vibrations of organic linker in the MOF. The bands observed between 1294 cm^{-1} and 1089 cm^{-1} are matching Matrimid bands Inagaki et al. showed previously (Inagaki et al., 2013). The bands at 1366 and 1089 cm^{-1} are for the stretching modes of the C-N-C of the imide 5-membered ring. Between 2800 cm^{-1} and 3000 cm^{-1} comprises C-H stretching including symmetric and asymmetric stretching of CH_2 and CH_3 entities. The vinylic =C-H band can be seen above 3000 cm^{-1}. The carboxylate asymmetric and the symmetric stretching frequencies are located at about 1550 cm^{-1} and 1420 cm^{-1}, respectively. Within this region also bands due to the symmetric and asymmetric bending of methylene and methyl groups appear (Gong et al., 1992).

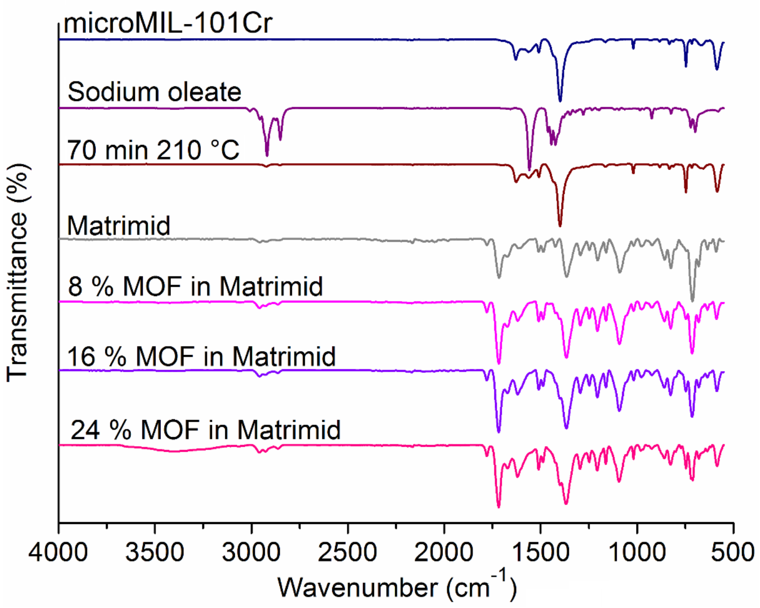

Figure S27 FTIR-ATR spectra of microMIL-101 (navy blue), sodium oleate (dark violet), nanoMIL-101Cr (brown), Matrimid (grey), MMM with 8 wt % MOF (pink); with 16 wt % MOF (violet), with 24 wt % MOF (magenta).

Maxwell and Bruggeman model

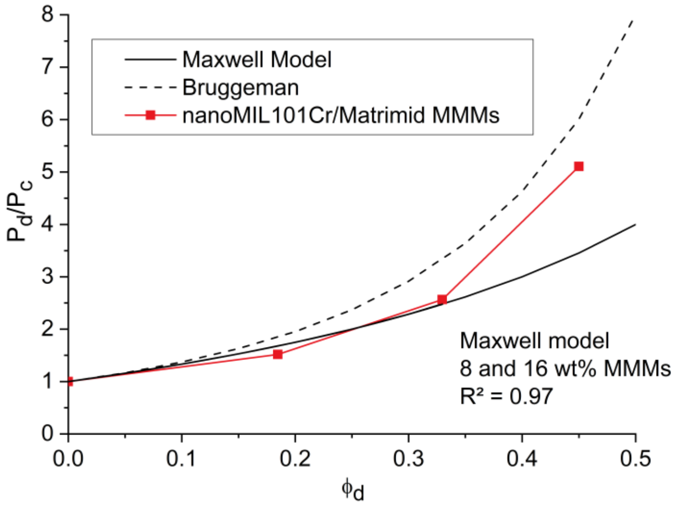

Figure S28 Relative experimental CH_4 permeabilities (referenced to the permeability P_c of the pure polymer membrane) for nanoMIL-101Cr-101Cr@Matrimid (red curve) with different filler volume fraction ϕ_d. The black solid line gives the theoretical CH_4 permeabilities for porous fillers based on the Maxwell Model and the black dashed line gives the theoretical CH_4 permeabilities for porous fillers based on the Bruggeman Model.

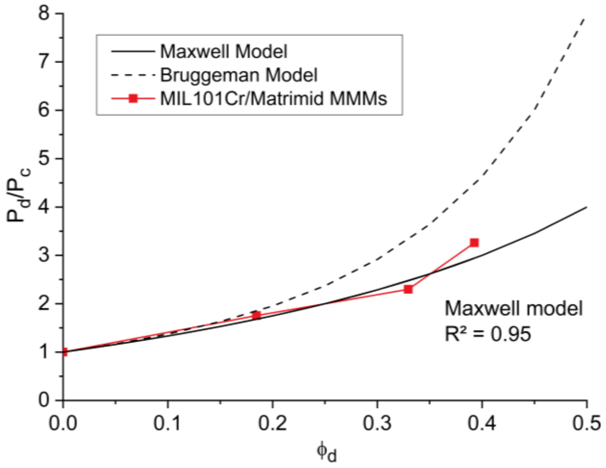

Figure S29 Relative experimental CO_2 permeabilities (referenced to the permeability P_c of the pure polymer membrane) for microMIL-101Cr@Matrimid (red curve) with different filler volume fraction ϕ_d. The black solid line gives the theoretical CO_2 permeabilities for porous fillers based on the Maxwell Model and the black dashed line gives the theoretical CO_2 permeabilities for porous fillers based on the Bruggeman Model.

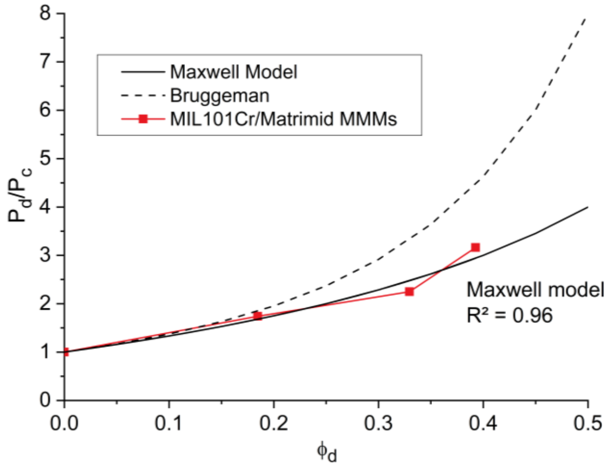

Figure S30 Relative experimental CH_4 permeabilities (referenced to the permeability Pc of the pure polymer membrane) for microMIL-101Cr@Matrimid (red curve) with different filler volume fraction ϕd. The black solid line gives the theoretical CH_4 permeabilities for porous fillers based on the Maxwell Model and the black dashed line gives the theoretical CH_4 permeabilities for porous fillers based on the Bruggeman Model.

References

Huang, X.-X., Qiu, L.-G., Zhang, W., Yuan, Y.-P., Jiang, X., Xie, A.-J., Shena, Y.-H., Zhub, J.-F. (2012). Hierarchically mesostructured MIL-101 metal–organic frameworks: supramolecular template-directed synthesis and accelerated adsorption kinetics for dye removal. CrystEngComm 14, 1613-1617. doi: 10.1039/C1CE06138K

Shen, T., Luo, J., Zhang, S., Luo, X., Environ. J. (2015). Hierarchically mesostructured MIL-101 metal–organic frameworks with different mineralizing agents for adsorptive removal of methyl orange and methylene blue from aqueous solution. Chem. Eng. 3, 1372-1383. doi: 10.1016/j.jece.2014.12.006

Khan, N.A., Kang, I.J., Seok, H.Y., Jhung, S.H. (2011). Facile synthesis of nano-sized metal-organic frameworks, chromium-benzenedicarboxylate, MIL101. Chem. Eng. J. 166, 1152-1157. doi: 10.1016/j.cej.2010.11.098

Jiang, D., Burrows, A.D., Edler, K.J. (2011). Size-controlled synthesis of MIL-101(Cr) nanoparticles with enhanced selectivity for CO_2 over N_2. CrystEngComm 12, 6916-6919. doi: 10.1039/C1CE06274C

Wuttke, S., Braig, S., Preiß, T., Zimpel, A., Sicklinger, J., Bellomo, C., Rädler, J.O., Vollmar, A.M., Bein, T. (2015). MOF nanoparticles coated by lipid bilayers and their uptake by cancer cells. Chem. Commun. 51, 15752-15755. doi: 10.1039/C5CC06767G

Rajati, H., Navarchian, A.H., Tangestaninejad, S. (2018). Preparation and Characterization of Mixed Matrix Membranes based on Matrimid/PVDF blend and MIL-101(Cr) as filler for CO 2 /CH 4 separation. Chem. Eng. Sci. 185, 92-104. doi: 10.1016/j.ces.2018.04.006

Perez, E.V., Balkus Jr., K.J., Ferraris, J.P., Musselman, I.H. (2009). Mixed-matrix membranes containing MOF-5 for gas separations. J. Membr. Sci. 328, 165-173. doi: 10.1016/j.memsci.2008.12.006

Anjum, M.W., Bueken, B., De Vos, D., Vankelecom, I.F. (2016). MIL-125(Ti) based mixed matrix membranes for CO_2 separation from CH_4 and N_2. J. Membr. Sci. 502, 21-28. doi: 10.1016/j.memsci.2015.12.022

Zhang, Y., Musselman, I.H., Ferraris, J.P., Balkus Jr., K.J. (2008). Gas permeability properties of Matrimid (R) membranes containing the metal-organic framework Cu-BPY-HFS. J. Membr. Sci. 313, 170-181. doi: 10.1016/j.memsci.2008.01.005

Nik, O.G., Chen, X.Y., Kaliaguine, S. (2012). Functionalized metal organic framework-polyimide mixed matrix membranes for CO_2/CH_4 separation. J. Membr. Sci. 4213, 48-61. doi: 10.1016/j.memsci.2012.04.003

Shahid, S., and Nijmeijer, K. (2014). High pressure gas separation performance of mixed-matrix polymer membranes containing Highmesoporous FE(BTC). J. Membr. Sci. 459, 33-44. doi: 10.1016/j.memsci.2014.02.009

Dorosti, F., Omidkhah, M., Abedini, R. (2014). Fabrication and characterization of Matrimid/MIL-53 mixed matrix membrane for CO 2 /CH 4 separation. Chem. Eng. Res. Des. 92, 2439-2448. doi: 10.1016/j.cherd.2014.02.018

Naseri, M., Mousavi, S.F., Mohammadi, T., Bakhtiari, O. (2015). Synthesis and gas transport performance of MIL-101/Matrimid mixed matrix membranes. J. Ind. Eng. Chem. 29, 249-256. doi: 10.1016/j.jiec.2015.04.007

Férey, G., Draznieks, C.M., Serre, C., Millange, F., Dutour, J., Surble, S., Margiolaki, I. (2005). A Chromium Terephthalate-Based Solid with Unusually Large Pore Volumes and Surface Area. Science 309, 2040-2042. doi: 10.1126/science.1116275

Hall, J.B.; Dobrovolskaia, M.A., Patri, A.K., McNeil, S.E. (2007). Characterization of nanoparticles for therapeutics. Nanomedicine, 2, 789-803. doi: 10.2217/17435889.2.6.789

Tomaszewska, E., Soliwoda, K., Kadziola, K., Tkacz-Szczesna, B., Celichowski, G., Cichomski, M., Szmaja, W., Grobelny, J. (2013). Detection Limits of DLS and UV-Vis Spectroscopy in Characterization of Polydisperse Nanoparticles Colloids. J. Nanomater. 60, 1-10. doi: 10.1155/2013/313081

Foldbjerg, R., Olesen, P., Hougaard, M., Dang, D.A., Hoffmann, H.J., Autrup, H. (2009). PVP-coated silver nanoparticles and silver ions induce reactive oxygen species, apoptosis and necrosis in THP-1 monocytes. Toxicol. Lett. 190, 156-162. doi: 10.1016/j.toxlet.2009.07.009

Chalati, T., Horcajada, P., Gref, R., Couvreur, P., Serre, C. (2011). Optimisation of the synthesis of MOF nanoparticles made of flexible porous iron fumarate MIL-88A. J. Mater. Chem. 21, 2220-2227. doi: 10.1039/C0JM03563G

Inagaki, M., Ohta, N., Hishiyama, Y. (2013). Aromatic polyimides as carbon precursors. Carbon 61, 1-21. doi: 10.1016/j.carbon.2013.05.035

Gong, W.Q., Parentich, A., Little, L.H., Warren, L.J. (1992). Adsorption and Immobilization of Cytochrome c on Nanodiamonds. Langmuir 8, 118-124. doi: 10.1021/la0495736

3.2 Studying of the hydrogen atom position in the strong-short intramolecular hydrogen bond of 5-substituted 9-hydroxyphenalenone derivatives by invariom-model refinement and ONIOM cluster computations

Irina Gruber, Lisa Bensch, Thomas J. J. Müller, Christoph Janiak, Birger Dittrich,
Z. Kristalogr. (2020), 235, 225–235
DOI: 10.1515/zkri-2020-0022

The structures of the H-bonded enol forms of 5-substituted 9-hydroxyphenalenones were investigated by the use of invariom-model refinement to determine the H atom position of the intramolecular hydrogen bond. Invariom-model refinement shows that the first impression after the standard independent atom model (IAM) refinement, which pointed to the presence of a resonance-assisted hydrogen bond, is not correct. Only an asymmetric hydrogen bond (C_s forms) is found.

<u>Author's share of work:</u>

- Carrying out the X-ray crystallography measurements, evaluating crystal data, structure refinement and displaying the X-ray molecular structures
- Writing of the manuscript and drawing of the figures, graphs and tables except for figure 5, figure above table 3, and figure 6 which were done by Birger Dittrich.
- Editing of the manuscript regarding the reviewers' comments by Irina Gruber, Birger Dittrich, and Christoph Janiak.

Reprinted with permission from ref. 206.

Studying of the hydrogen atom position in the strong-short intramolecular hydrogen bond of pure and 5-substituted 9-hydroxyphenalenones by invariom-model refinement and ONIOM cluster computations

Irina Gruber,[a] Lisa Bensch,[b] Thomas J. J. Müller,[b] Christoph Janiak,[a] Birger Dittrich[c]

[a] *Institut für Anorganische Chemie und Strukturchemie, Heinrich-Heine-Universität Düsseldorf, Universitätsstraße 1, 40225 Düsseldorf, Germany. E-mail: janiak@hhu.de.*

[b] *Institut für Organische Chemie und Makromolekulare Chemie, Heinrich-Heine-Universität Düsseldorf, Universitätsstraße 1, 40225 Düsseldorf, Germany. E-mail: ThomasJJ.Mueller@hhu.de.*

[c] *Institut für Anorganische Chemie und Strukturchemie II, Heinrich-Heine-Universität Düsseldorf, Universitätsstraße 1, 40225 Düsseldorf, Germany, E-mail: dittrich@hhu.de.*

Abstract

The solid-state structures of three H-bonded enol forms of 5-substituted 9-hydroxyphenalenones were investigated to accurately determine the H atom positions of the intramolecular hydrogen bond. For this purpose, single-crystal X-ray diffraction (SC-XRD) data were evaluated by invariom-model refinement. In addition, QM/MM computations of central molecules in their crystal environment show that results of an earlier standard independent atom model refinement, which pointed to the presence of a resonance-assisted hydrogen bond in unsubstituted 9-hydroxyphenalone, are misleading: in all our three and the earlier solid-state structures the lowest energy form is that of an asymmetric hydrogen bond (C_S form). Apparent differences of results from SC-XRD and other analytical methods are explained.

Keywords: intramolecular hydrogen bond; ONIOM QM/MM computations; single-crystal X-ray diffraction; 5-substituted 9-hydroxyphenalenone derivatives; invariom refinement.

1 Introduction

The hydrogen bond is unique due to its adaptable combination of electrostatics and covalency. Moreover, it is important for numerous processes in chemistry and biochemistry [1–4]. A strong or classic hydrogen bond occurs when there is an interaction between an electron-rich atom (A), and a sufficiently positively polarized H atom, which is part of a covalent bond with an electronegative atom (D). The D–H···A hydrogen bond can appear either between different molecules (intermolecular) or within the same molecule (intramolecular). In both cases, the D–H bond distance is to some extent elongated when compared to equivalent distances where the acceptor atom (A) is absent. A special kind of hydrogen bond has been reported where the proton is shared equally between the atoms D and A (D···H···A). Here short H···A distances lead to an effective coupling between two covalent, and one ionic valence bond structures in a low barrier hydrogen bond (LBHB, see Figure 1) [5–8]. Four characteristics for such LBHBs have been defined [9, 10]: firstly, the D···H and H···A distances between the atoms in D···H···A are longer compared with normal D–H and H–A covalent bonds and secondly, the D···H···A bonds are based on two energetically equivalent atomic arrangements, where each can be formally described by different mesomeric Lewis structures. Thirdly, the fast equilibrium through the D···H···A transition state leads to an energetic stabilization, which grants the fourth feature, namely that also the D···A distance is shorter than in a normal hydrogen bond. Enolized diketones, which are stabilized by intramolecular OHO hydrogen bonds, are usually thought of as being centered, linear hydrogen bonds that are involved in the delocalized π-system to give "aromatic" systems [11]. Such special or near-symmetric hydrogen bonds are often formed between charged moieties. For O–H···O systems these special hydrogen bonds can be frequently found when O···O distances are short (below 2.5 Å). For cases where a short-strong hydrogen bond exists, Gilli et al. introduced the term resonance-assisted hydrogen bond (RAHB) as a particular case of an intramolecular hydrogen bond in 1989. RAHBs are supported by a conjugated π-electron system (see Figure 2) where six-, eight-, or ten-membered neutral rings are formed [12–14].

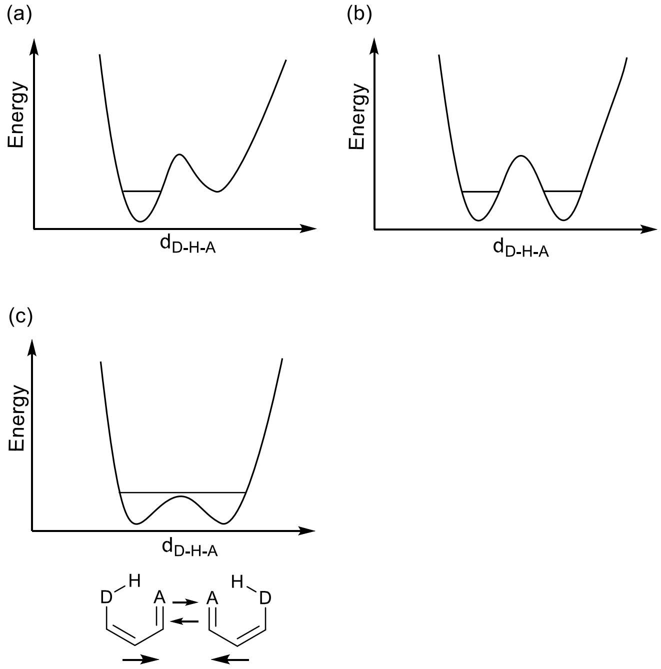

Figure 1: Schematic potential–energy curves for hydrogen bonds (D–H···A). Asymmetric double-well potential (a), symmetric doublewell potential (b) and low barrier hydrogen bond LBHB (c). In the LBHB case two proton normal modes D–H···A and A···H–D are shown. The thick arrows indicate the transverse dipole moment which inverts with tautomerization.

The unsubstituted enolized diketone 9-hydroxyphenalen-1-one (9-HP) can exist in C_{2v} or C_S form with a sixmembered H-bonded ring. In solution, as shown by ^{1}H and ^{13}C NMR studies [15], 9-HP appears to have C_{2v} symmetry down to a temperature of 130 K. The higher symmetry could of course be due to rapid interconversion between its two C_S forms. An IR spectroscopic investigation of both solution and solid state found no absorption for the O–H stretching band due to the presence of very strong intramolecular hydrogen bonding with the carbonyl oxygen [16]. Studies using single-crystal Xray diffraction (SC-XRD) have shown that 9-HP possesses a short O–O distance (<2.5 Å) [17], and that there is a phase transition between a low-temperature C_S form with four molecules in the asymmetric unit (Z' = 4, CSD refcode HXPHOL11, 215 K), and a room-temperature C_{2v} structure with Z' = 2 where one molecule is disordered, whose H-atoms were omitted in the deposition refcode HXPHOL [18].

The combined use of ^{13}C and ^{2}H spin-lattice relaxation times provides a convenient means of determining quadrupole coupling constants of intramolecular bridging deuterons in planar molecules in the liquid phase. In systems of the type D–2 H···A (2H = deuteron), the strength of the “hydrogen bond” is related to the position of the deuteron relative to D and A, which, in turn, controls the magnitude of the quadrupole coupling constant. Thus, values of this coupling constant provide a qualitative criterion of the strengths of hydrogen bonds in series in which D and A are held constant [19]. The D···H···A linear motion may strongly couple with the other two-proton normal modes (D–H···A and A···H–D), producing a three-dimensional oscillation. There might also be strong anharmonic coupling between D···H···A and the oxygenatom normal modes due to the fact that the proton at the top of the barrier undergoes a subtle balance of forces [20]. For the intramolecular proton exchange in 9-HP, tunneling can be calculated from the energy difference between the gerade–ungerade pair. Such a calculation is based on the proton, which will spend equal time in each well, and tunneling will depend on the frequency with which the proton oscillates between the wells [21]. Gilli et al. differentiated three ways for making the two resonant forms of intramolecular hydrogen bonds equivalent (see Figure 3) [22] and further categorized hydrogen bonds as:

– resonance-assisted hydrogen bonds (RAHBs, here the two oxygen atoms are interconnected by a system of πconjugated double bonds (–O–H···O=),

– charged assisted hydrogen bonds (CAHB, divided into negative (–O–H···O^-–) and positive (=O···H^+···O=), also known as (−/+)CAHB), and

– low barrier hydrogen bonds (LBHB) [23].

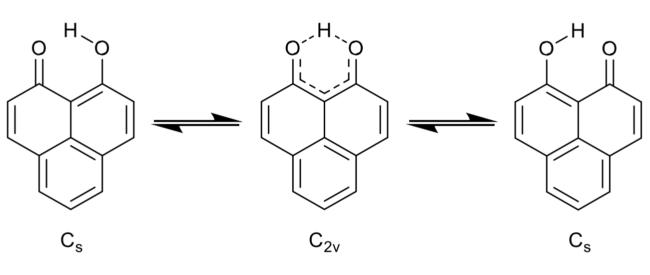

Figure 2: Interconversion between two equivalent minimum energy (C_S) structures with asymmetric hydrogen bridges in 9- hydroxyphenalen-1-one as an example of an

enolized diketone or hydroxyl ketone. The interconversion occurs through a symmetric (C_{2v}) (transition-state) intermediate.

According to Emsley's empirical studies, the delocalization of the π-conjugated system becomes greater in case the hydroxyl-ketone unit forms either intra-molecular, or infinite-chain intermolecular hydrogen bonds [11]. 9-Hydroxyphenalenone and its derivatives are suitable examples for investigating such strong hydrogen bonds of keto–enols. The molecule contains a hydroxyl ketone unit [24] and is an electron acceptor, known for its ability to react as a radical anion [25, 26], but is also known for forming metal complexes [27–30]. It was first synthesized by Koelsch in 1941 [31]. Derivatives are used for many different applications [25], in particular as ligand in transition metal catalysts [32] and as neutral radical conductors [33]. The functionalization in the 5- positions of 9-HP has remained rather rare [27, 34], but was systematically investigated by DFT computations by Bensch et al., who considered electronic and photophysical properties [35], and also highlighted that conjugated 5-substituted 9- HP systems are synthetically accessible without the necessity of protecting the hydroxyl group due to the strong intramolecular hydrogen bond. For 9-HP, the high temperature structure [18] indicates that a symmetric intramolecular hydrogen bond is present (symmetric C2v form, Figure 2). Since an O–H stretching band could not be found in the IR spectrum due to the presence of a very strong intramolecular hydrogen bonding with the carbonyl oxygen [16], and since 9-HP exhibits ^{1}H and ^{13}C NMR spectra which are consistent with either C_{2v} symmetry or with existence of rapidly equilibrating C_S tautomers [36], the question arises how the results from different spectroscopic techniques and SC-XRD can be joined, understood and consistently united. Variable-temperature NMR studies on 9- HP and hydrogenated malonaldehyde, the latter also in its deuterated form, also support occurrence of fast interconversion between asymmetrically hydrogen bonded structures of such bistable molecules, resulting in rapid prototropy between two equivalent tautomers (see Figure 3) [15, 36]. X-ray photoelectron spectroscopy (XPS) spectra showed that the H atom remains localized on one oxygen atom for at least a few O–H vibrational periods [16]. These results have been validated by deuteron quadrupole coupling constants which were shown to be linearly related to the squares of stretching frequencies for the corresponding X–H bonds and suggest that 9-HP involves hydrogen bonds with double-well potentials. Vibronically resolved fluorescence and fluorescence excitation spectra of 9-HP show strong spectral changes when the phenolic proton is deuterated, implying that the proton motion is coupled to a rearrangement of the oxygen-carbon molecular framework, and double-minimum potential energy curve shapes were calculated for both ground and electronically excited state [20]. Moreover, it has been calculated that the proton experiences a tunneling effect and therefore a double minimum potential, implying structural alterations regarding the equilibrium configuration and the transition state [37]. Ab initio SCF calculations on 9-HP supported the existence of two equivalent minimum-energy structures with an asymmetric hydrogen bridge (C_S, Figure 2). According to these computations the interconversion between the two minima occurs through a symmetric (C_{2v}) intermediate which is 5.20 kcal/mol above the minimum-energy C_S structures [38]. How do the results from SC-XRD fit into this picture? 9-HP contains a strong intramolecular hydrogen bond forming a fourth six-membered ring. While all spectroscopic methods and gas-phase computations agree on the hydrogen bonds in 9-HP having double-well potentials and two discrete minima, the high-temperature form of the crystal shows a symmetric intramolecular hydrogen bond [18, 39]. Hence, we set out to investigate three recently synthesized 9-HP derivatives with substituents in the 5-position (summarized in Table 1) by SC-XRD, and complemented the experimental studies by QM/MM cluster computations which take into account the influence of the solid state. These computations were also performed on 9-HP. SC-XRD studies made use of invariom [40] aspherical scattering factors that permit obtaining more precise especial results than IAM refinement [41]. Using invariom-model refinement [42], which relies on the Stewart–Hansen– Coppens multipole model [43, 44] we thus aim for an accurate determination of the position of the hydrogen atoms participating in the strong hydrogen bond, and will find an encompassing explanation for the apparently contradictory spectroscopic and crystallographic results.

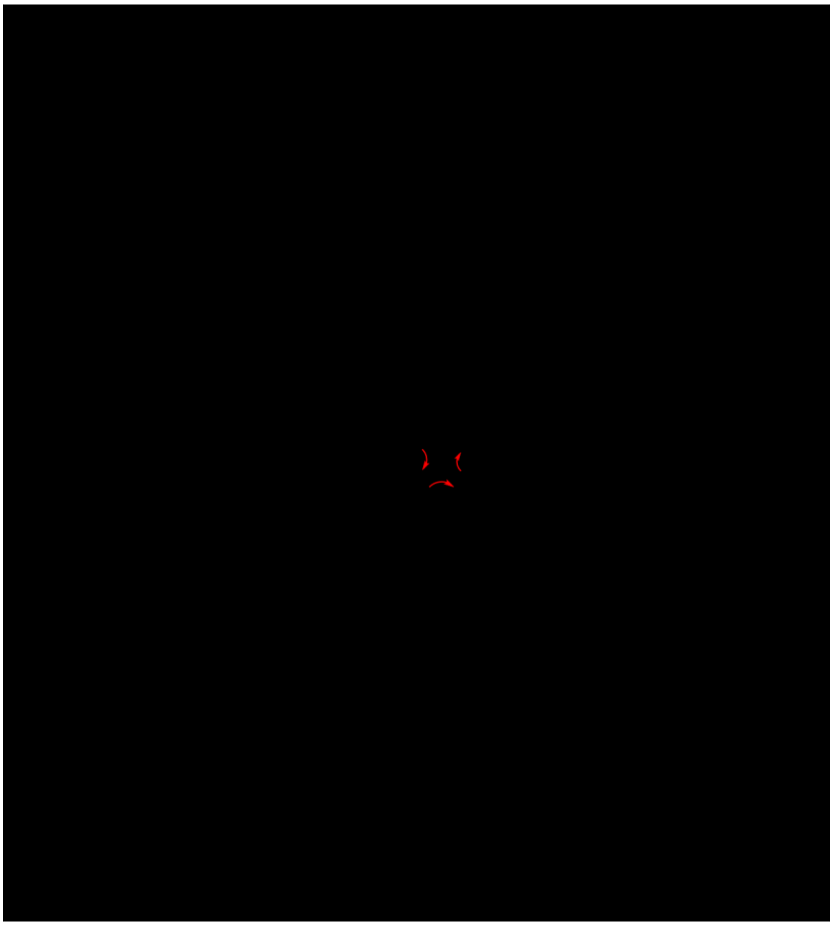

Figure 3: Two resonant forms I and II and three possible ways to interconvert them.

2 Experimental

2.1 Materials

Single crystals of 9-hydroxy-5-(4-methoxyphenyl)-1H-phenalen-1-one (**I**), 9-hydroxy-5-(1-methyl-1H-pyrazol-4-yl)-1H-phenalen-1-one (**II**) and 5-[4-(9H-carbazol-9-yl) benzyl]-9-hydroxy-1H-phenalen-1-one (**II**) were prepared as described elsewhere [33, 45].

Table 1: 5-substituted 9-hydroxyphenalenones studied here by SCXRD.

[redacted]

2.2 SC-XRD data collection

All single-crystals were carefully selected under a polarizing microscope and mounted in oil on a loop. Data for initial structure solution were collected using ω-scans on a Bruker Kappa APEX2 CCD Duo diffractometer with microfocus sealed tube, using Cu–Kα radiation (λ = 1.54178 Å) for **I**, and Mo–Kα radiation (λ = 0.71073 Å) for **II** and **III**. In order to have diffraction data of similar quality and resolution for all three compounds, X-ray diffraction data for **I**–**III** were then re-measured at a temperature of 100 ± 2 K at the SLS synchrotron beamline X10SA with a wavelength of 0.6358 Å using 360 degree Φ scans with a DECTRIS Pilatus 6M detector. Cell refinement, and data reduction employed the XDS program [46]. Preliminary refinement was done by full-matrix least squares on F2 using SHELXL-2016 [47]. Empirical (multi-scan) absorption correction was achieved with SADABS [48]. Crystal structure and refinement data are presented in Table 2.

2.3 Least-squares refinement and electron density modeling using invarioms

All non-hydrogen positions for **I–III** were refined with anisotropic displacement parameters. For later comparison with the invariom model [40] SHELXLindependent atom model (IAM) refinement was repeated with the XD program suite [50]. In addition, the IAM result provided input for subsequent invariom [42] least-squares refinement with Stewart–Hansen– Coppens [43, 44] aspherical scattering factors predicted by DFT computations. IAM and invariom refinement in XD were carried out using the same X-ray diffraction intensities (merged for **I** and **II**, but not **III**), weighting schemes and cutoff settings. Since the scattering factors for some of the more unusual model compounds were not initially present in the invariom database, several missing model compounds were added. A Holstein assignment diagram that contains the central molecule, the model compounds with their SMILES [51] code and the respective IUPAC name are shown exemplarily for molecule **I**. The other Holstein plots can be foundin the supplementaryinformation. For all geometry optimizations underlying the database, the same M06/def2TZVP DFT method/basis set combination was chosen. Computations using the program GAUSSIAN09 [52] and subsequent Fourier transform with the TONTO program [53] permitted to generate static structure factors from the wavefunctions obtained; each model compound was then fitted with a multipole model; the multipole parameters with their local pseudoatom coordinate system then constitute a scattering factor database entry. The program XDLSM [49] was employed for both the aspherical-atom refinements on the 'simulated' theoretical data, as well as the later refinements with the experimentally measured data. Concerning the treatment of hydrogen atoms in the experimental XDLSM refinement, riding hydrogen atom positions from the IAM were initially used as starting point. The X–H bonds were then elongated to the M06/def2TZVP optimized result, with freely adjusted isotropic displacement parameters. Finally, for finding the hydrogen atom of the strong O–H···O hydrogen bond, ultimately all hydrogen atom positions were allowed to adjust in addition to their isotropic displacement parameters. XD input files were generated with the preprocessor program Invariomtool [54]. Structural data for this paper have been deposited with the Cambridge Crystallographic Data Center (CCDC-numbers 1831535 (**I**), 1831536 (**II**), 1831537 (**III**)). These data can be obtained free of charge via www.ccdc.cam.ac.uk/data_request/cif.

Table 2: Crystal structure and refinement data for **I-III**, the three 5-substituted 9-HP samples used in this study.

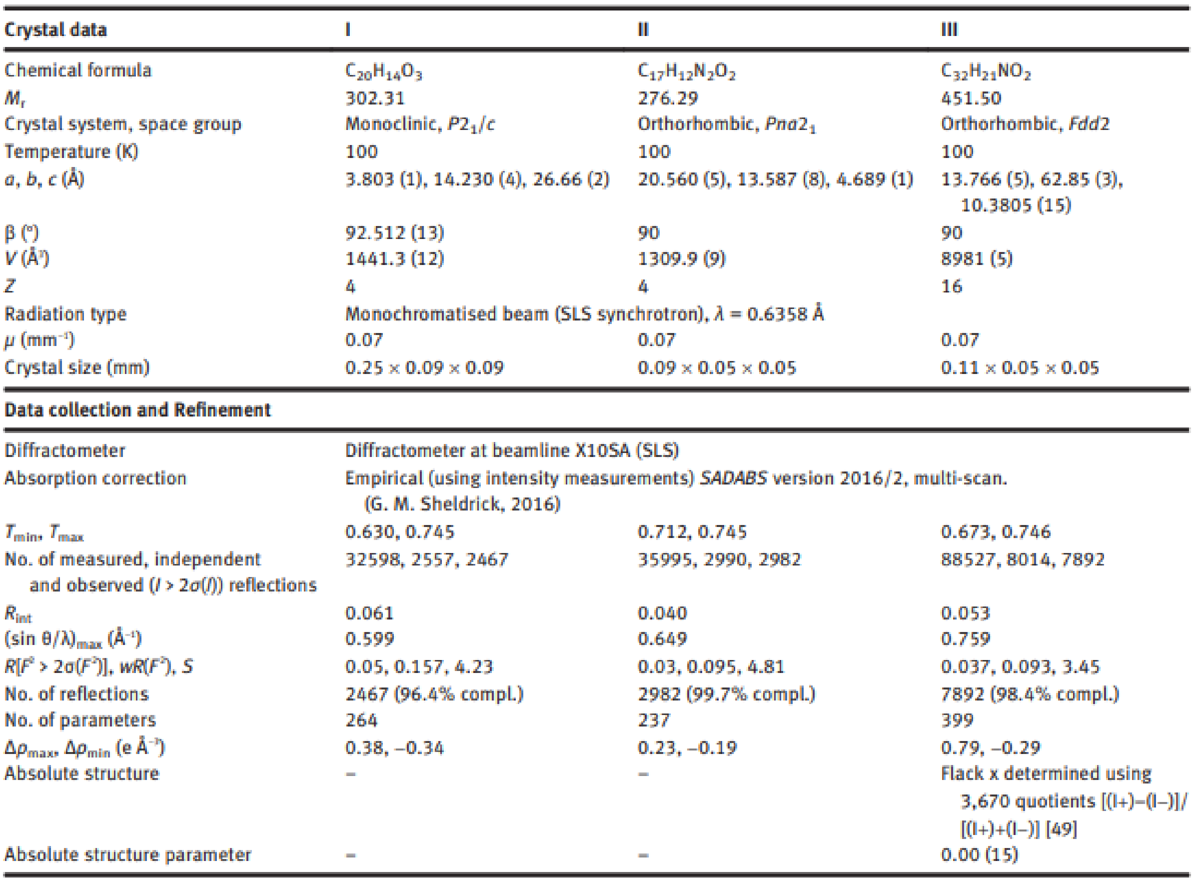

Crystal data	**I**	**II**	**III**
Chemical formula	$C_{20}H_{14}O_3$	$C_{17}H_{12}N_2O_2$	$C_{32}H_{21}NO_2$
M_r	302.31	276.29	451.50
Crystal system, space group	Monoclinic, $P2_1/c$	Orthorhombic, $Pna2_1$	Orthorhombic, $Fdd2$
Temperature (K)	100	100	100
a, b, c (Å)	3.803 (1), 14.230 (4), 26.66 (2)	20.560 (5), 13.587 (8), 4.689 (1)	13.766 (5), 62.85 (3), 10.3805 (15)
β (°)	92.512 (13)	90	90
V (Å^3)	1441.3 (12)	1309.9 (9)	8981 (5)
Z	4	4	16
Radiation type	Monochromatised beam (SLS synchrotron), λ = 0.6358 Å		
μ (mm^{-1})	0.07	0.07	0.07
Crystal size (mm)	0.25 × 0.09 × 0.09	0.09 × 0.05 × 0.05	0.11 × 0.05 × 0.05
Data collection and Refinement			
Diffractometer	Diffractometer at beamline X10SA (SLS)		
Absorption correction	Empirical (using intensity measurements) *SADABS* version 2016/2, multi-scan. (G. M. Sheldrick, 2016)		
T_{min}, T_{max}	0.630, 0.745	0.712, 0.745	0.673, 0.746
No. of measured, independent and observed ($I > 2\sigma(I)$) reflections	32598, 2557, 2467	35995, 2990, 2982	88527, 8014, 7892
R_{int}	0.061	0.040	0.053
$(\sin \theta/\lambda)_{max}$ (Å^{-1})	0.599	0.649	0.759
$R[F^2 > 2\sigma(F^2)]$, $wR(F^2)$, S	0.05, 0.157, 4.23	0.03, 0.095, 4.81	0.037, 0.093, 3.45
No. of reflections	2467 (96.4% compl.)	2982 (99.7% compl.)	7892 (98.4% compl.)
No. of parameters	264	237	399
$\Delta\rho_{max}$, $\Delta\rho_{min}$ (e Å^{-3})	0.38, −0.34	0.23, −0.19	0.79, −0.29
Absolute structure	–	–	Flack x determined using 3,670 quotients [(I+)−(I−)]/[(I+)+(I−)] [49]
Absolute structure parameter	–	–	0.00 (15)

3 Results and discussion

The Holstein plot in Figure 4 and Supplementary Figure S1 shows the fragmentation of the molecules into invarioms and the model compounds that were necessary to generate them. The molecular electron density can then be reconstructed from these fragments. To obtain the Holstein plot and invariom name, the local connectivity of an atom with the respective bond-distinguishing parameter, as provided by the preprocessor program INVARIOMTOOL [53], was evaluated. This invariom string was then re-interpreted to give the required model compounds. To facilitate the reproduction of this work, the SMILES string is also provided. It would have been easier to simply calculate the molecular electron density once, if the purpose had been to model the electron density of only one of the molecules. However, for a series of molecules the model compounds are the same, apart from a few additional ones in each case. Invarioms are available from a database. Since computations of model compounds for invarioms present in the database do not need to be repeated, computation time is saved overall. At the same time the coverage of existing model compounds is continuously expanded, directly covering even more compounds.

Figure 5 shows the result of including aspherical electron density in the scattering factor model for the three molecules in form of a deformation electron density plot. As has been shown earlier, e.g., in [55], the residual electron density is usually reduced after invariom refinement, unless there is disorder or there are other crystallographically important effects that can be overlooked more easily in IAM refinement. Residual electron density due to covalent bonding is absent and faithfully taken into account in all three invariom refinements. Isotropic displacement parameters for hydrogen atoms are also visualized in Figure 5, and from their size one can see that the hydrogen atoms participating in the strong O–H···O hydrogen bond in **I** and **II** have a larger vibrational amplitude than the other hydrogen atoms, similar to methyl hydrogens prone to rotational disorder. While there is residual electron density in **III** behind and in between the O–H···O oxygen atom of 0.15 e, the hydrogen atom can be located rather precisely in **I**, **II**, and **III**. The highest residual electron density peak in **III** is higher in invariom than in IAM refinement, but close to C14, which links the two extended ring systems, i.e., far away from the hydrogen atom of interest. From all three aspherical-atom structure analyses of **I**, **II** and **III** it can be seen that the hydrogen atoms of interest are localized at only one of the two possible oxygen atoms. While the situation still corresponds to an LBHB in these substituted 9-HP derivatives, the hydrogen atoms are located on average in only one of the two possible energy minima throughout the whole crystal. Further details on the exact hydrogen bonding situation are provided in Table 3.

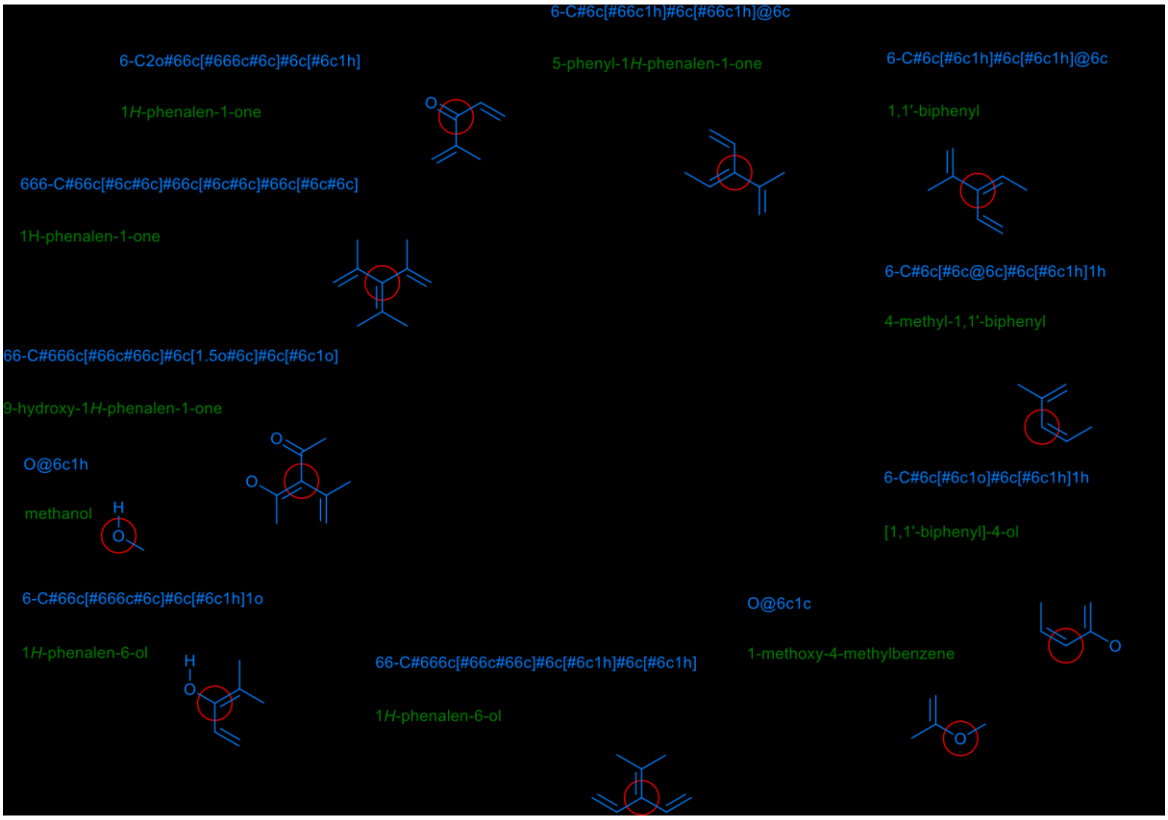

Figure 4: A representation of model compounds used to reproduce aspherical electron densities for 9-hydroxy-5-(4-methoxyphenyl)-1Hphenalen-1-one. Blue color was used for the invariom name of an atom of interest. SMILES and IUPAC names are also provided. The latter describe whole molecules, while the invariom notation defines the local chemical environment of an atom.

4 ONIOM computations

Inlight of the challenge to understand the apparently different analytical results of SC-XRD, IR, NMR and XPS, it is desirable to have a complementary method that probes the solid state to support our interpretation. Therefore, two layer QM/MM ONIOM [57] computations were performed on the asymmetric unit molecules (all structures have $Z'= 1$) in the surrounding of their nearest neighbor molecules that were generated from space-group symmetry using the program BAERLAUCH [58]. Before we discuss the results of a geometry optimization of the central molecule in the cluster, we start discussing the role of space-group symmetry, since this aspect can be relevant for the formation of symmetric or unsymmetrical hydrogen bonding (be it static in time or dynamic).

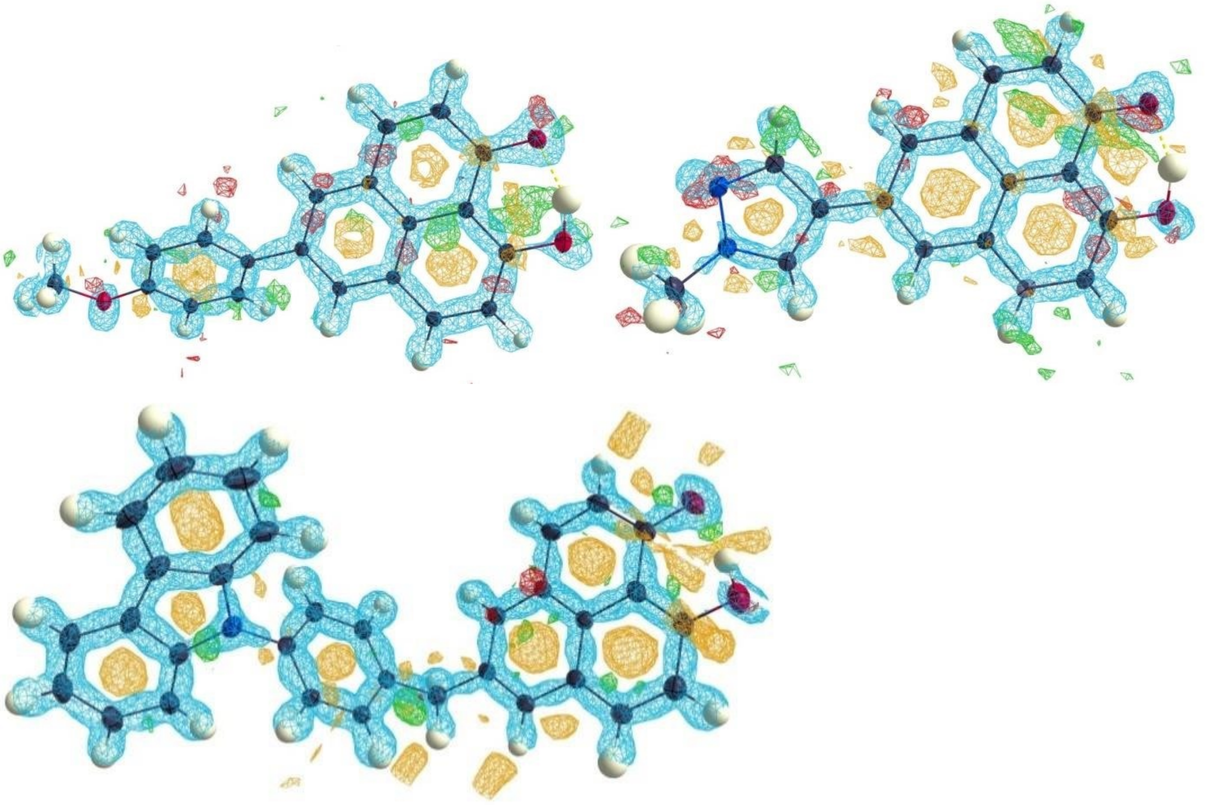

Figure 5: A combination of an ORTEP plot of anisotropic/isotropic displacement parameters (50% probability), the deformation electron density and the remaining residual electron density shown for all three molecules. For **I** (top left) only residuals above 0.2 e are shown, for **II** (top right) this threshold value was set to 0.1 e and for **III** (below) it was 0.15 e. Figures were generated with MOLECOOLQT [56]

Table 3: Hydrogen-bonding scheme (Å,°) in the three derivatives of 9-HP.

O1–H1···O2	**I**	**II**	**III**
D-H	0.99 (3)	1.04 (2)	0.89 (2)
H···A	1.62 (3)	1.56 (2)	1.640 (19)
D···A	2.529 (2)	2.520 (2)	2.5127 (18)
D-H···A	151 (2)	152 (2)	166.7 (18)

Compound **I** fulfills the symmetry of the common monoclinic space group P21/c in the solid, and one can see from the illustration (Figure 6) of neighboring molecule in the cluster that the combination of a 21 screw axis and a c-glide plane leads to an inversion center, so that for all O–H···O moieties there is an O···H–O pendant due to symmetry. Therefore, the in-plane dipole-moment contributions of the intramolecular hydrogen bonds will cancel out in the crystal. Due to the glide plane the situation is analogous in **III**, space group Fdd2, where however no inversion center is present (the only structure for which a Flack-parameter is reported). In **II**, which crystallizes in the non-centrosymmetric space group Pna21, there is also one site for the hydrogen atom only, and molecular in-plane contributions cancel due to π-stacking. We therefore think that the electric field of the crystals does not play the decisive role in the hydrogen position in the O–H···O hydrogen bond. We note that the dipole moment contributions also cancel when there is a dynamic exchange in between them. This is supported by the result of the ONIOM B3LYP/6- 31G(d,p): UFF geometry optimization of the central molecules in their respective clusters as generated from the invariom refined structures. Figure 6 shows exemplarily the cluster of **I** with 15 molecules, emphasizing the central molecule of the asymmetric unit. The number of molecules (**II**: 17 molecules, **III**: 16 molecules) depends on space-group symmetry and crystal packing. A molecule was included in the clusters when a surrounding atom in a neighboring molecule was within 3.75 Å of any of the atoms in the asymmetric unit. Bond distances from these computations corresponding to those given for the experimental structures from invariom refinement are given in Table 4 alongside the experimental data. These data show that the global minimum of the DFT optimized asymmetric unit molecule in a cluster of MK point charges [59], with the molecular surrounding subjected to a UFF force field treatment [60], fully confirm the hydrogen positions of the structures **I**, **II**, and **III**. It inspires confidence how well experiment and theory agree, not only among themselves, but also for all three compounds. The only outlier is the experimentally short O1-H1 bond in **III**, which also affects the bond angle δ. Otherwise there is often quantitative agreement within 3 σ.

5 Discussion: does the LBHB lead to a shared H position in the middle of the two oxygen atoms?

After re-refining three crystal structures of 9-HP derivatives with aspherical scattering factors of the invariom database we find no convincing evidence for a symmetric “resonance assisted” hydrogen bond in these molecules, and a symmetric hydrogen bond can be clearly ruled out at the measurement temperature of 100 K. Although in **III** residual electron density is in the order of magnitude of the signal of covalent bonding, and these signals remain after invariom refinement, residual electron density features are far away from the hydrogen atom in question and do not compromise this result. The experimental results are also in nice agreement with two layer ONIOM computations, and both methods provide a consistent answer. In these computations the coordinates of the experimental crystal structure provide the cluster molecules after applying symmetry, and only the central molecule is optimized. The cluster environment is representative of the crystal field, and the method permits to identify the hydrogen-atom position corresponding to the solid-state energy minimum. So how do these results with local C_S symmetry fit together with the original C_{2v} symmetric high-temperature structure determination for 9-HP [18]? The results for **I**, **II**, and **III** apparently agree only with the low-temperature form of 9-HP (refcode HXPHOL11), where again located hydrogen atoms were found by SC-XRD, but not with the room-temperature structure. Therefore, we have also performed ONIOM computations analogous to those described earlier for **I**, **II**, and **III** on the 9-HP room temperature structure using the deposited refcode HXPHOL as input. A difference was that we had to add several missing hydrogen atoms, so we added a pre-optimization step of the central molecule in the cluster with the XTB program [61]. Since in space group is P21/c there were two possible input structures for the missing hydrogen atom of interest, both of them were computed. Like for **I**, **II**, and **III** both these structures have located hydrogen positions after optimization. Their energy is similar, the relative energy difference for the central molecule in the cluster is 4.1 kcal/mol, which is probably within the accuracy of the computational method. The temperature-dependent disorder (and the phase transition) in 9-HP commences when the energy difference between the lower energy and the higher energy structure can be overcome. H atoms are thus not shared between the two oxygen atoms, and are alternating between molecules related by mirror plus glide plane according to space-group symmetry, again canceling the local dipole moments. We conclude that the room-temperature structure of 9-HP is, analogous to the NMR results, a disordered overlay of the two possible individual structures. We have to remind ourselves that in SC-XRD we obtain positions from a time and space average of a large number of unit cells. When for 9-HP the thermal motion of the atoms increases, the average of the individual structures starts to agree with higher spacegroup symmetry, which also leads to an apparently shared hydrogen atom between the oxygen atoms. Other factors are the resolution of the experiment, which is necessarily limited, and tunneling. However, individual contributor structures still have localized hydrogen atoms. Even measuring diffraction data to higher resolution would not change this apparent C_{2v} symmetry, whereas smaller thermal motion (lowering the temperature) leads to the phase transition in 9-HP. Hydrogen atoms in individual molecules remain located at one oxygen atom in both contributing structures for time periods longer than can be probed by an SC-XRD measurement, despite but still in agreement with the higher symmetry at room temperature.

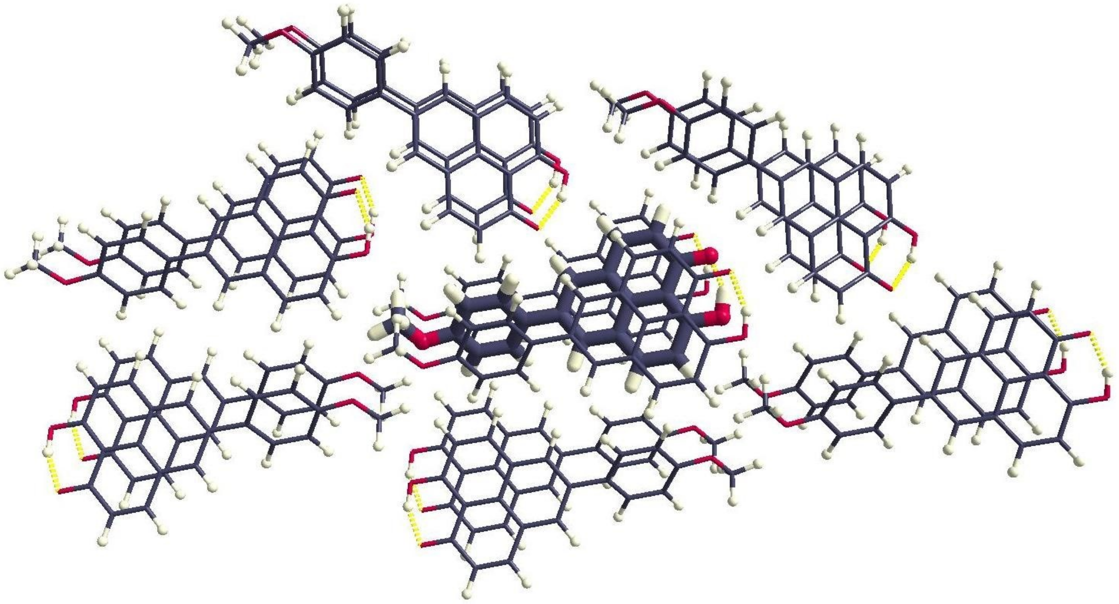

Figure 6: Depiction of the cluster used in the ONIOM B3LYP/6-31G(d,p):UFF computation of I. The central molecule is emphasized. The invariom result, including the hydrogen atom positions after invariom refinement, was used to generate the input.

Table 4: Selected distances (Å) for the three 5-substituted 9-HP samples used in this study.[a]

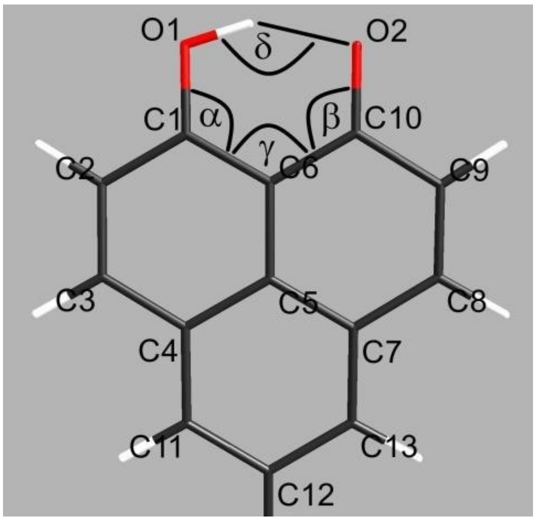

	I-xrd	**I-ONIOM**	**II-xrd**	**II-ONIOM**	**III-xrd**	**III-ONIOM**
O1-C1	1.333(2)	1.3265	1.3368(16)	1.3255	1.3195(18)	1.3262
O2-C10	1.284(2)	1.2603	1.2765(16)	1.2595	1.2660(18)	1.2580
O1-H1	0.99(3)	1.0202	1.04(2)	1.0243	0.888(19)	1.0142
C1-C6	1.424(2)	1.4115	1.4192(17)	1.4094	1.4117(15)	1.4085
C1-C2	1.438(2)	1.4222	1.4310(17)	1.4229	1.4196(19)	1.4212
C2-C3	1.380(2)	1.3712	1.3840(18)	1.3721	1.3685(19)	1.3716
C3-C4	1.434(2)	1.4214	1.4410(17)	1.4277	1.4298(14)	1.4239
C4-C11	1.419(2)	1.4087	1.4200(17)	1.4083	1.4125(18)	1.4132
C4-C5	1.431(2)	1.4201	1.4270(19)	1.4238	1.4098(18)	1.4207
C5-C6	1.429(2)	1.4166	1.4298(18)	1.4149	1.4189(18)	1.4163
C5-C7	1.431(2)	1.4237	1.4316(17)	1.4232	1.4169(13)	1.4207
C6-C10	1.456(2)	1.4558	1.4544(19)	1.4555	1.4510(19)	1.4595
C7-C13	1.408(2)	1.3929	1.4016(17)	1.3907	1.3921(18)	1.3896
C7-C8	1.455(2)	1.4444	1.4509(19)	1.4446	1.4446(19)	1.4399
C8-C9	1.366(2)	1.3592	1.3656(17)	1.3590	1.3558(19)	1.3555
C9-C10	1.463(2)	1.4557	1.4649(17)	1.4534	1.4462(16)	1.4525
α	120.78(13)	121.19	120.66(9)	120.89	120.91(12)	121.07
β	120.72(13)	120.70	120.77(10)	120.55	121.02(10)	121.21
γ	120.00(13)	119.35	119.93(9)	119.30	119.71(11)	119.77
δ	151(2)	152.47	152(2)	153.35	166.7(18)	152.33

[a] xrd = X-ray diffraction and ONIOM = two layer ONIOM computation.

6 Conclusion

While room-temperature SC-XRD using the IAM for 9-HP apparently disagreed initially with other spectroscopic results, cluster computations in addition to earlier lowtemperature SC-XRD data collection and analysis falsify the presence of a C_{2v} symmetric RAHB in 9-HP. These results are fully supported by IAM as well as more precise invariom refinements of three more substituted 9-HP derivatives reported here. ONIOM cluster computations complement and nicely confirm the analysis. Residual electron density obtained after invariom refinement was shown to be a useful validation tool in this context – recent technical progress in evaluating single crystal Xray diffraction data does provide an unambiguous result in full agreement with other spectroscopic results as well as DFT computations on clusters of molecules that represent the solid state.

Acknowledgements

We thank the DFG, project DI 921/6-1, for financial support.

Author contribution: All the authors have accepted responsibility for the entire content of this submitted manuscript and approved submission.

Research funding: B.D. acknowledges funding from the Deutsche Forschungsgemeinschaft DFG, project DI 921/6-1.

Conflict of interest statement: The authors declare no conflicts of interest regarding this article.

References

(1) G. A. Jeffrey, An Introduction to Hydrogen Bonding. Oxford University Press: New York, 1997.

(2) G. R. Desiraju, T. Steiner, The Weak Hydrogen Bond in Structural Chemistry and Biology. Oxford University Press: New York, 1999.

(3) S. J. Grabowski, Hydrogen Bonding - New Insights; Ed.; Springer: Dordrecht, The Netherlands, 2006.

(4) S. Scheiner, Ed., Molecular Interactions: From van der Waals to Strongly Bound Complexes, Wiley, Chichester, UK, 1997.

(5) M. Garcia-Viloca, A. González-Lafont, J. M. Lluch, J. Am. Chem. Soc. 1997, 119, 1081–1086.

(6) M. Garcia-Viloca, R. Gelabert, A. González-Lafont, M. Moreno, J. M. Lluch, J.

Phys. Chem. A 1997, 101, 8727–8733.

(7) C. L. Perrin and J. B. Nielson, Annu. Rev. Phys. Chem. 1997, 48, 5, 11–44.

(8) T. Mochida, A. Izuoka, T. Sugawara, Y. Moritomo, and Y. Tokura, J. Am. Chem. Soc. 1994, 101, 7971–7974.

(9) L. A. Malaspinna, Al. J. Edwards, M. Woińska, D. Jayatilaka, M. J. Turner, J. R. Price, R. Herbst-Irmer, K. Sugimoto, E. Nishibori, and S. Grabowsky, Cryst. Grow. Des. 2017, 17, 3812–3825.

(10) F. Hibbert, J. Emsley, J. Adv. Phys. Org. Chem. 1990, 26, 255–379.

(11) J. Emsley, Struct. Bond. 1984, 57, 147–191.

(12) G. Gilli, F. Bellucci, V. Ferretti, V. Bertolasi, J. Am. Chem. Soc. 1989, 111, 1023−1028.

(13) V. Bertolasi, P. Gilli, V. Ferretti, G. Gilli, Chem. Eur. J. 1996, 2, 925–934.

(14) K. T. Mahmudov, A. J. L. Pombeiro, Chem.-Eur. J. 2016, 22, 16356−16398.

(15) R. S. Brown, A. Tse, T. Nakashima, and R. C. Haddon, J. Am. Chem. Soc. 1979, 101, 3157–3162.

(16) Y. Demura, T. Kawato, H. Kanatomi, I. Murase, Bull. Chem. Soc. Jpn. 1975, 48, 2820–2824.

(17) C. Svensson, S. C. Abrahams, J. L. Bernstein, and R. C. Haddon, J. Am. Chem. Soc. 1979, 101, 5759–5764.

(18) C. Svensson, S. C. Abrahams, Acta Crystallogr., Sect. B: Struct. Sci. 1986, 42, 280–286.

(19) L. M. Jackman, J.C. Trewella, and R. C. Haddon, J. Am. Chem. Soc. 1980, 102, 2519–2525.

(20) R. Rossetti, R. C. Haddon, and L. E. Brus, J. Am. Chem. Soc. 1980, 102, 6913–6916.

(21) H. Hameka and J. R. de la Vega, J. Am. Chem. Soc. 1984, 106, 25, 7703–7705.

(22) P. Gilli, V. Bertolasi, V. Ferretti, and G. Gilli, J. Am. Chem. Soc. 1994, 116, 3, 909–915.

(23) G. Gilli, P. Gilli, The Nature of Hydrogen Bond, Oxford University Press, New York, 2009.

(24) A. Kovács, V. Izvekov, K. Zauer, K. Ohta, J. Phys. Chem. A 2001, 105, 5000–5009.

(25) S. K. Pal, M. E. Itkis, R. W. Reed, R. T. Oakley, A. W. Cordes, F. S. Tham, T. Siegrist, R. C. Haddon, J. Am. Chem. Soc. 2004, 126, 1478–1484.

(26) A. Pariyar, G. Vijaykumar, M. Bhunia, S. K. Dey, S. K. Singh, S. Kurungot, S. K. Mandal, J. Am. Chem. Soc. 2015, 137, 5955–5960.

(27) A. Das, T. M. Scherer, P. Mondal, S. M. Mobin, W. Kaim, G. K. Lahiri, Chem. Eur. J. 2012, 18, 14434–14443.

(28) S. K. Dey, A. Honecker, P. Mitra, S. K. Mandal, A. Mukherjee, Eur. J. Inorg. Chem. 2012, 35, 5814–5824.

(29) T. Mochida, R. Torigoe, T. Koinuma, C. Asano, T. Satou, K. Koike, T. Nikaido, Eur. J. Inorg. Chem. 2006, 3, 558–565.

(30) Y. -J. Gu, B. Yan, Inorg. Chim. Acta 2013, 408, 96–102.

(31) C. F. Koelsch, J. A. Anthes, J. Org. Chem. 1941, 6, 558–565.

(32) A. Das, T. K. Ghosh, A. Dutta Chowdhury, S. M. Mobin, G. K. Lahiri, Polyhedron 2013, 52, 1130–1137.

(33) S. K. Mandal, S. Samanta, M. E. Itkis, D. W. Jensen, R. W. Reed, R. T. Oakley, F. S. Tham, B. Donnadieu, R. C. Haddon, J. Am. Chem. Soc. 2006, 128, 1982–1994.

(34) G. He, Y. Hou, D. Sui, X. Wan, G. Long, P. Yun, A. Yu, M. Zhang, Y. Chen, Tetrahedron 2013, 69, 6890–6896.

(35) L. Bensch, I. Gruber, C. Janiak, T. J. J. Müller, Chem. Eur. J. 2017, 23, 10551–10558.

(36) C. Engdahl, A. Gogoll, U. Edlund, Magn. Reso. Chem. 1991, 29, 54–62.

(37) H. Ozeki, M. Takahashi, K. Okuyama, and K. Kimura, J. Chem. Phys. 1993, 99, 56–66.

(38) K. L. Kunze, J. R. de la Vega, J. Am. Chem. Soc. 1984, 106, 6528–6533.

(39) C. Svensson and S. C. Abrahams, J. Appl. Cryst. 1984, 17, 459–463.

(40) B. Dittrich, T. Koritsanszky, P. Luger, Angew. Chem. Int. Ed. 2004, 43, 2718–2721.

(41) B. Dittrich, J. Lübben, S. Mebs, A. Wagner, P. Luger, R. Flaig, Chem. Eur. J. 2017, 23, 4605–4614.

(42) B. Dittrich, C. B. Hübschle, K. Pröpper, F. Dietrich, T. Stolper and J. J. Holstein, Acta Crystallogr. 2013, B69, 91–104

(43) R. F. Stewart, Acta Cryst. A. 1976, 32, 565–574.

(44) N. Hansen, P. Coppens, Acta Crystallogr. A 1978, 34, 909–921.

(45) L. Bensch, T. J. J. Müller et al., to be published.

(46) W. Kabsch, Acta Cryst. D 2010, 66, 125–132.

(47) G. M. Sheldrick, Acta Cryst. C 2015, 71, 3–8.

(48) L. Krause, R. Herbst-Irmer, G. M. Sheldrick and D. Stalke, J. Appl. Cryst. 48, 2015, 3–10.

(49) Parsons, Flack and Wagner, Acta Cryst. B 2013, 69, 249-259.

(50) A. Volkov, P. Macchi, L. J. Farrugia, C. Gatti, P. Mallinson, T. Richter, & T.

Koritsánszky, XD2006, University at Buffalo, NY, USA, University of Milan, Italy, University of Glasgow, UK, CNRISTM, Milan, Italy, and Middle Tennessee State University, TN, USA.

(51) D. Weininger, J. Chem. Inf. Comp. Sci. 1988, 28, 31–36

(52) Gaussian 09, Revision D.01, M. J. Frisch et al., Gaussian, Inc., Wallingford CT, 2013.

(53) Jayatilaka, D. & Grimwood, D. J., Comput. Sci. 2003, 2660, 142–151.

(54) Hübschle, C. B. & Dittrich, B., J. Appl. Cryst. 2011, 44, 238–240.

(55) Dittrich, B., Hübschle, C. B., Luger, P. & Spackman, M. A., Acta Cryst. D 2006, 62, 1325–1335.

(56) C. B. Hübschle. B. Dittrich, J. Appl. Cryst. 2011, 44, 238–240.

(57) M. Svensson, S. Humbel, R. D. J. Froese, T. Matsubara, S. Sieber, K. Morokuma, J. Phys. Chem. 1996, 100, 19357–19363.

(58) B. Dittrich, S. Pfitzenreuter, C. B. Hübschle, Acta Crystallogr. Sect. A 2012, 68, 110–116.

(59) B. H. Besler, K. M. Merz Jr., P. A. Kollman, J. Comput. Chem 1990, 11, 431439.

(60) A. K. Rappe, C. J. Casewit, K. S. Colwell, W. A. Goddard, W. M. Skid, E. R. Bernstein, J. Am. Chem. Soc. 1992, 114, 10024–10039.

(61) C. Bannwarth, S. Ehlert, S. Grimme, J. Chem. Theory Comput. 2019, 15, 1652–1671.

Supplementary Material: The online version of this article offers supplementary material (https://doi.org/10.1515/zkri-2020-0022).

Supplementary information for manuscript entited:

Studying of the hydrogen atom position in the strong-short intramolecular hydrogen bond of pure and 5-substituted 9-hydroxyphenalenones by invariom-model refinement and ONIOM cluster computations

Irina Gruber,[a] Lisa Bensch,[b] Thomas J. J. Müller,[b] Christoph Janiak,[a] Birger Dittrich[a,*]

[a] *Institut für Anorganische Chemie und Strukturchemie, Heinrich-Heine-Universität Düsseldorf, Universitätsstraße 1, 40225 Düsseldorf, Germany. E-mail: janiak@uni-duesseldorf.de, dittrich@hhu.de,*

[b] *Institut für Organische Chemie und Makromolekulare Chemie, Heinrich-Heine-Universität Düsseldorf, Universitätsstraße 1, 40225 Düsseldorf, Germany.*

Supplementary Figure **S1**: Fragmentation into invarioms of the central molecules 9-hydroxy-5-(1-methyl-1H-pyrazol-4-yl)-1H-phenalen-1-one (**II,** this page) and 5-[4-(9H-carbazol-9-yl) benzyl]-9-hydroxy-1H-phenalen-1-one (**III,** next page) into invarioms and the model compounds that were necessary to generate them.

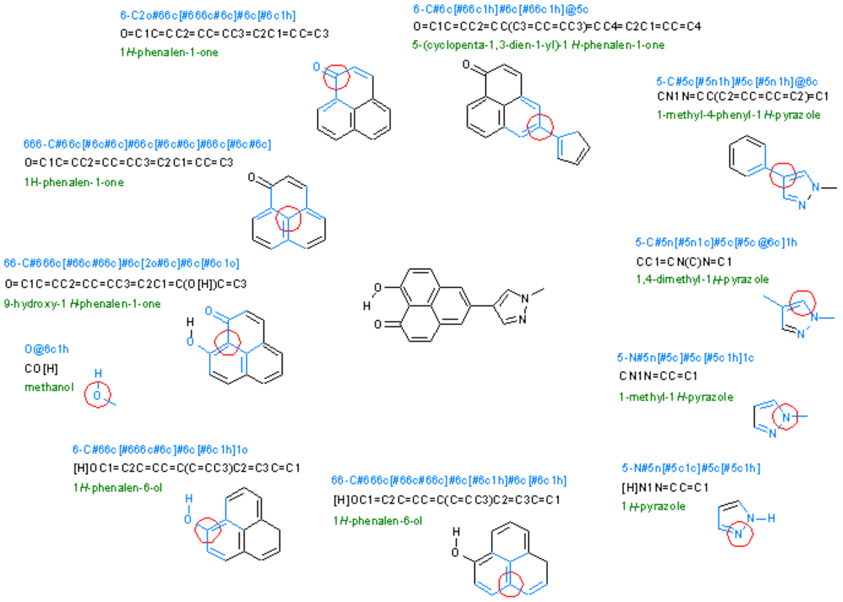

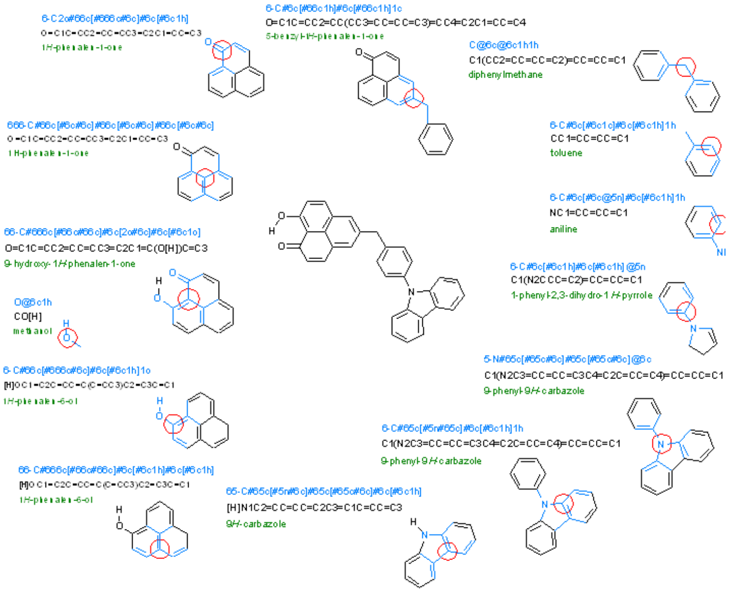

For more information see:

B. Dittrich, C. B. Hübschle, K. Pröpper, F. Dietrich, T. Stolper and J. J. Holstein, Acta Crystallogr. 2013, B69, 91–104

.

3.3 5-(Hetero)aryl Substituted 9-Hydroxyphenalenones - Synthesis and Electronic Properties of Multifunctional Donor-Acceptor Conjugates

Lisa Bensch, Irina Gruber, Christoph Janiak, Thomas J. J. Müller
Chem. Eur. J. 2017,23,10551–10558
DOI: 10.1002/chem.201700553

5-(Hetero)aryl substituted 9-hydroxyphenalenones (9-HP) can be readily synthesized by Suzuki coupling of 5-bromo 9-HP with (hetero)aryl boronic acid (derivatives) void of protection of the hydroxyl functionality with moderate to excellent yields (57-94%). A library of 5-(hetero)aryl substituted 9-HP with broad substituent variation was studied with respect to their electronic properties (absorption and emission spectroscopy, cyclic voltammetry) and their computed electronic structure. All compounds show reversible reductive potentials between -1230 and -1110 mV and the donor-substituted representatives possess irreversible oxidation potentials around 600 mV. Compounds with electron rich donors even show reversible oxidation potentials. Especially the donor-substituted 9-HPs display emission bands between 466 and 567 nm with quite large Stokes shifts (up to 4100 cm-1). TD-DFT calculations nicely reproduce the spectroscopic data and Hammett correlations underline a pronounced resonance substituent influence on the photophysical properties.

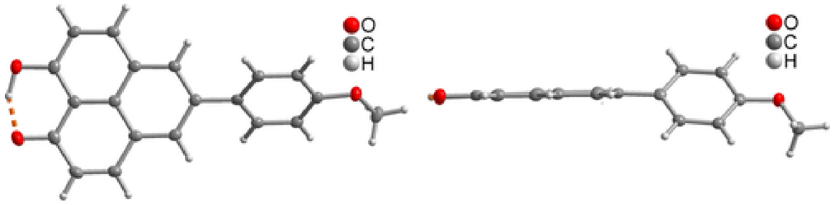

Figure 19. Molecular structure of 3 a (50 % thermal ellipsoids), showing the intramolecular O−H···O bond as dashed orange line. H-bonding details O−H 1.06(3) Å, H···O 1.51(3) Å, O···O 2.508(2), O−H···O 153(2)°. The angle of 47° is the dihedral angle between the plane defined by the carbon atoms of the 9-hydroxyphenalenone fragment and the 5-anisyl moiety (See Supporting Information Figure S1 for graphic with atom numbering; details of bond lengths and angles are given in section 7.1 in the Supporting Information). Reprinted with permission from ref. 233. Copyright 2017, with permission from WILEY- VCH.

<u>Author's share of work:</u>

- Carrying out the X-ray crystallography measurements, evaluating crystal data, structure refinement and displaying the X-ray molecular structures

3.4 Urea-based flexible dicarboxylate linkers for three-dimensionalmetal-organic frameworks

Sebastian Glomb, Gamall Makhloufi, Irina Gruber, Christoph Janiak
Inorganica Chimica Acta, 2018, 475, 35-46
DOI: 10.1016/j.ica.2017.09.029

The metal-organic frameworks (MOFs) 3D-[$Mn_2(L1)_2(DMF)$]·2DMF (**1**), 3D-[$Cd_2(L2)_2(DMF)_3$] (**3**), [$Zn_2(L2)_2(DMF)_3$] (**4**) and 3D-[$Mn_2(L2)_2(DMF)_3$] (**5**) are the first examples of three-dimensional metal-organic networks constructed from a single ditopic dicarboxylate linker (i.e., without bridging co-ligands) with an urea group in the linker axis ($L1^{2-}$ = 4,4′-(carbonylbis(azanediyl))dibenzoate; $L2^{2-}$ = 4,4′-(carbonylbis(azanediyl))bis(3-methylbenzoate), DMF = dimethylformamide). From $Cd^{2+}$and $L1^{2-}$ a 1D coordination polymer 1D-[$Cd(L1)(DMF)_3$] (**2**) is formed. The urea group is engaged in hydrogen bonding with the C(4)[$R^1_2(6)$] motif to an oxygen atom of a DMF solvent (in **1**) or a metal-coordinated carboxylate group (in **3**–**5**). Network **1** has infinite channels with parallelepiped cross sections and 30% solvent-filled volume. The 3 D frameworks **3**–**5** are of diamond (6,6), **dia** topology with a single framework having large voids with 17.6 Å and 19.7 Å nodal separation. Thus, four symmetry-related nets interpenetrate, organized via H-bonds in the C(4)[$R^1_2(6)$] motif, still leaving about 50% solvent-filled void volume in the fourfold interpenetrated structure.

<u>Author's share of work:</u>

- Carrying out the X-ray crystallography measurements, evaluating crystal data, structure refinement and displaying the X-ray molecular structures

3.5 Facile synthesis of nano-sized MIL-101(Cr) with the addition of acetic acid

Tian Zhao, Ling Yang, Peiyong Feng, Irina Gruber, Christoph Janiak, Yuejun Liu
Inorganica Chimica Acta, 2018, 471, 440-445
DOI: 10.1016/j.ica.2017.11.030

MIL-101(Cr), one of the best investigated and widely used metal–organic frameworks, has been easily synthesized with particle diameters in the range from 387(28) nm to 90(10) nm by using acetic acid as a modulator. The particle size of MIL-101(Cr) decreased with increasing acetic acid concentration. The decrease of size in high concentration of acetic acid may be explained with the efficient suppression of the framework extension. In a selected condition, MIL-101(Cr) possessing an average diameter of about 90 nm can be prepared easily and reproducibly in gram-scale, with high BET-surface areas (3200–3500 m^2/g) and fairly good yield (60–75%).

Author's share of work:

- Providing list of references

3.6 Silver, Gold, Palladium, and Platinum N-heterocyclic Carbene Complexes Containing a Selenoether-Functionalized Imidazol-2-ylidene Moiety

Karsten Klauke, Irina Gruber, Tim-Oliver Knedel, Laura Schmolke, Juri Barthel, Hergen Breitzke, Gerd Buntkowsky, Christoph Janiak
Organometallics 2018, 37, 3, 298-308
DOI: 10.1021/acs.organomet.7b00678

The selenoether-functionalized imidazolium salt N-[(phenylseleno)methylene)]-N′-methylimidazolium chloride (LH^+Cl^-) was transformed into the metal–carbene complexes $[AgCl(L)]$, $[AuCl(L)]$, $[PdCl_2(L)]$, and $[PtCl_2(L)]$ by the reaction with Ag_2O and an additional transmetalation reaction of $[AgCl(L)]$ with $[(THT)AuCl]$, $[(COD)PdCl_2]$, and $[(COD)PtCl_2]$, respectively (THT = tetrahydrothiophene, COD = cyclooctadiene). The compound $[AuI_2Cl(L)]$ was prepared by oxidation of $[AuCl(L)]$ with elemental iodine. The microwave-assisted decomposition of $[PdCl_2(L)]$ in the ionic liquid 1-butyl-3-methylimidazolium bis(trifluoromethylsulfonyl)imide ($[BMIm]NTf_2$) or in propylene carbonate led to the formation of $Pd_{17}Se_{15}$ nanoparticles of 51 ± 17 or 26 ± 7 nm diameter, respectively. The decomposition of the platinum complex resulted in either small Pt clusters around 1 nm size from the ionic liquid suspension or Pt nanoparticles of 3 ± 1 nm diameter in propylene carbonate. High-resolution X-ray photoelectron spectroscopy (HR-XPS) and ^{13}C cross-polarization magic-angle spinning (CP MAS) NMR indicated that the surface of Pt clusters and crystalline Pt nanoparticles is formed by an amorphous Pt(II)/Se shell and by carbene ligand residues.

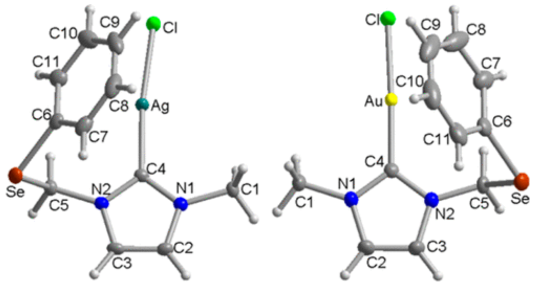

Figure 20. Molecular structures of compounds **2** (left) and **3a** (right) (50% thermal ellipsoids, H atoms of arbitrary radii). Reprinted with permission from ref. 241, Copyright 2018, with permission from American Chemical Society.

<u>Author's share of work:</u>

- Carrying out the X-ray crystallography measurements, evaluating crystal data, structure refinement and displaying the X-ray molecular structures

3.7 Three-component Activation−Alkynylation−Cyclocondensation (AACC) Synthesis of Enhanced Emission Solvatochromic 3-Ethynyl Quinoxalines

Franziska K. Merkt, Simon P. Höwedes, Dr. Charlotte F. Gers-Panther, Irina Gruber, Christoph Janiak, Thomas J. J. Müller
Chem. Eur. J. 2018, 24, 8114–8125
DOI: 10.1002/chem.201800079

2-Substituted 3-ethynylquinoxaline chromophores can be readily synthesized by a consecutive activation–alkynylation–cyclocondensation (AACC) one-pot sequence in a three-component manner. In comparison with the previously published four-component glyoxylation starting from electron-rich π-nucleophiles, the direct activation of (hetero)aryl glyoxylic acids allows the introduction of substituents that cannot be directly accessed by glyoxylation. By introducing *N*,*N*-dimethylaniline as a strong donor in the 2-position, the emission solvatochromicity of 3-ethynylquinoxalines can be considerably enhanced to cover the spectral range from blue–green to deep red–orange with a single chromophore in a relatively narrow polarity window. The diversity-oriented nature of the synthetic multicomponent reaction concept enables comprehensive investigations of structure–property relationships by Hammett correlations and Lippert–Mataga analysis, as well as the elucidation of the electronic structure of the emission solvatochromic π-conjugated donor–acceptor systems by DFT and time-dependent DFT calculations with the PBEh1PBE functional for a better reproduction of the dominant charge-transfer character of the longest wavelength absorption band.

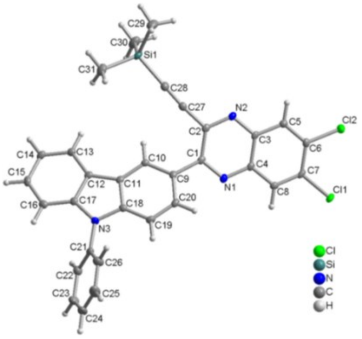

Figure 21. Molecular structure of compound **4 u** (thermal ellipsoids shown at the 50 % probability level). Reprinted with permission from ref. 242, Copyright 2018, with permission from Wiley-VCH.

Author’s share of work:

- Carrying out the X-ray crystallography measurements, evaluating crystal data, structure refinement and displaying the X-ray molecular structures

3.8 Broad-Range Spectral Analysis for Chiral Metal Coordination Compounds: (Chiro)optical Superspectrum of Cobalt(II) Complexes

Gennaro Pescitelli, Steffen Lüdeke, Anne-Christine Chamayou, Marija Marolt, Viktor Justus, Marcin Górecki, Lorenzo Arrico, Lorenzo Di Bari, Mohammad Ariful Islam
Irina Gruber, Mohammed Enamullah, Christoph Janiak
Inorg. Chem. 2018, 57, 21, 13397-13408
DOI: 10.1021/acs.inorgchem.8b01932

Chiroptical broad-range spectral analysis extending from UV to mid-IR was employed to study a family of Co(II) N-(1-(aryl)ethyl)salicylaldiminato Schiff base complexes with pseudotetrahedral geometry associated with chirality-at-metal of the Δ/Λ type. While common chiral organic compounds have well-separated absorption and circular dichroism spectra (CD) in the UV/vis and IR regions, chiral Co(II) complexes feature an almost unique continuum of absorption and CD bands, which cover in sequence the UV, visible, near-IR (NIR), and IR regions of the electromagnetic spectrum. They can be collected in a single (chiro)optical superspectrum ranging from the UV (230 nm, 5.4 eV) to the mid-IR (1000 cm-1, 0.12 eV), which offers a fingerprint of the structure and stereochemistry of the metal complexes. Each region of the superspectrum contributes to one piece of information: the NIR-CD region, in combination with TDDFT calculations, allows a reliable assignment of the metal-centered chirality; the UV-CD region facilitates the analysis of the Δ/Λ diastereomeric equilibrium in solution; and the IR-VCD region contains a combination of low-lying metal-centered electronic states (LLES) and ligand-centered vibrations and displays characteristically enhanced and monosignate VCD bands.

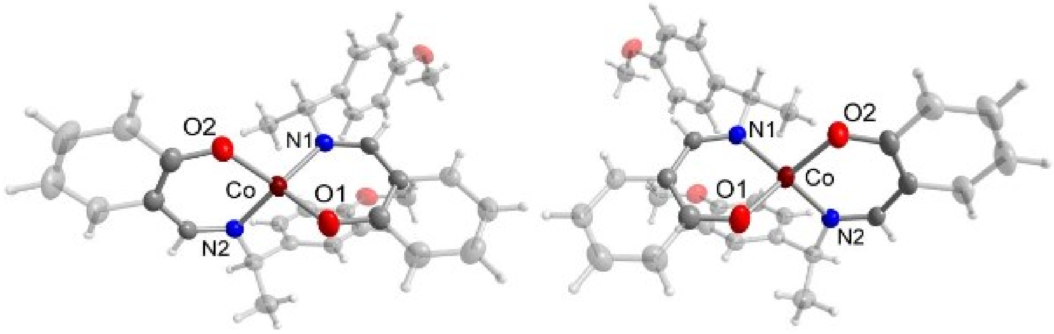

Figure 22. Molecular structure of Λ-(R)-2 (left) and Δ-(S)-2 (right) (50% thermal ellipsoids). See Table S-B2 for bond lengths and angles. Reprinted with permission from ref. 243, Copyright 2018, with permission from American Chemical Society.

<u>Author's share of work:</u>

- Carrying out the X-ray crystallography measurements, evaluating crystal data, structure refinement and displaying the X-ray molecular structures

3.9 Emission solvatochromic, solid-state and aggregation-induced emissive α-pyrones and emission-tuneable 1 H -pyridines by Michael addition–cyclocondensation sequences

Natascha Breuer, Irina Gruber, Christoph Janiak and Thomas J. J. Müller
Beilstein J. Org. Chem. 2019, 15, 2684–2703
DOI: 10.3762/bjoc.15.262

Starting from substituted alkynones, α-pyrones and/or 1H-pyridines were generated in a Michael addition–cyclocondensation with ethyl cyanoacetate. The peculiar product formation depends on the reaction conditions as well as on the electronic substitution pattern of the alkynone. While electron-donating groups furnish α-pyrones as main products, electron-withdrawing groups predominantly give the corresponding 1H-pyridines. Both heterocycle classes fluoresce in solution and in the solid state. In particular, dimethylamino-substituted α-pyrones, as donor–acceptor systems, display remarkable photophysical properties, such as strongly red-shifted absorption and emission maxima with daylight fluorescence and fluorescence quantum yields up to 99% in solution and around 11% in the solid state, as well as pronounced emission solvatochromism. Also a donor-substituted α-pyrone shows pronounced aggregation-induced emission enhancement.

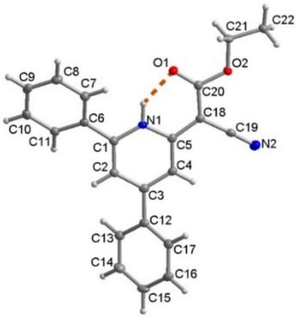

Figure 23. Molecular structure of 1*H*-pyridine **5a** (50% thermal ellipsoids), showing the intramolecular N–H···O bond as dashed orange line. H-bond details N1–H 0.90(2) Å, H···O1 1.87(2) Å, N1···O2 2.624(2) Å, O1–H···O2 140(1)°. Reprinted with permission from ref. 244. Copyright 2019 by Breuer et al.; licensee Beilstein-Institut.This figure is distributed under the terms of the Creative Commons Attribution 3.0 License, which permits unrestricted use, distribution, and reproduction in any medium, provided the original work is properly cited.

<u>Author's share of work:</u>

- Carrying out the X-ray crystallography measurements, evaluating crystal data, structure refinement and displaying the X-ray molecular structures

4. Conclusion and Outlook

4.1 The first research focus - metal-organic frameworks and mixed matrix membranes

Mixed matrix membranes (MMMs) show potential for economically sustainable separation processes. They are a promising approach to increase the performance of polymeric membranes by combining polymer materials with metal-organic framework particles. In order to fulfil this approach, the selected metal-organic framework (MOF) must have gas transport properties.[245] Another important factor is the size and the shape of the MOF filler particles. A smaller particle size is not only more beneficial for making dense MMMs, smaller particles also have higher surface area to volume ratios. This higher surface area to volume ratios can result in enhanced mass transfer between the two phases (i.e., between polymer matrix and filler particles). This thesis deals with MOF based mixed-matrix membranes for gas separation. Therefore, in this last chapter a brief reflection on the results achieved in this work is given, followed by an outlook on the future.

The microwave-assisted synthesis of the metal-organic framework MIL-101Cr has been investigated. The MOF size was determined using dynamic light scattering, transmission electron microscopy, and scanning electron microscopy. It was shown that the size of the MOF particles can be significantly reduced by a combination of microwave, emulsions, modulators, and ultrasound. As shown in this thesis, direct emulsion with the phase-inversion-temperature method yielded nano/microsized MIL-101Cr particles and high BET surface areas (2900 $m^2 g^{-1}$) in good yields (45 %). It was observed that with increasing reaction time and temperature, the particles became more crystalline and showed higher N_2 uptakes, as well as larger total pore volumes. The microwave-assisted emulsion synthesis in the presence of a modulator can be further investigated by varying the modulator and by varying its concentration. In addition to sodium oleate, other monocarboxylic acids such as benzoic acid or lauric acid can be researched. It remains to be seen how other modulators and their concentrations changes the sorption properties, particle morphology, particle size, and pore size. In this context, the template effect of the modulator and the associated mesoporosity of MOFs are particularly relevant. In general, mesoporous MOFs could play an important role in the future in the areas of energy storage, energy conversion and the uptake of larger biomolecules. In the areas of gas storage, gas separation and catalysis, too, it is assumed that mesoporous MOFs will increase efficiency.

Here, the use of nano/microsized MIL-101Cr in mixed-matrix membranes allowed for the preparation of 24 wt% filler mixed-matrix membranes. The increased filler amount improved the gas permeability. The approach, to surpass the normally obtainable filler wt% fraction by a nanosized filler in a mechanically still stable membrane, is a promising result with wider implications. It can therefore be investigated whether other nanoscale MOF materials can be synthesized using the microwave approach. Relevant properties such as their uptake and release behaviour of guest molecules can be investigated as well. After incorporating different nanosized MOF filler particles into MMMs the performance of the resulting membranes needs to be evaluated in terms of gas separation enhancement. In this context, the problems associated with the permeability-selectivity trade-off (Robeson upper bound) and CO_2 induced plasticization in MOF-mixed-matrix membranes need to be further investigated. In the literature, the main focus of MMMs is on the separation of CO_2/CH_4 for the purification of natural gas. The separation of CO_2/N_2 for cleaning flue gases also is a widely studied topic in MMM research. In this context, the use of different nano/microsized MOF filler particles in MMMs for the separation of CO_2/CH_4 and CO_2/N_2 needs to be investigated. The nano-scale MIL-101Cr particles play an important role in mixed-matrix membranes. There are some well-known challenges in preparation techniques for MMMs. They include the proper selection of the polymer material, the homogeneous dispersion of filler particles in the polymer matrix, and the defect-free polymer and filler particle interface. The MMMs produced in this work are based on the commercially available polymer Matrimid. Despite that Matrimid exhibits good separation properties, membranes based on Matrimid suffer from low stability and plasticize in high pressure CO_2 streams. Although there are many studies on the plasticization behaviour of Matrimid, there are only few studies on the plasticization behaviour of mixed-matrix membranes.[246] The currently used MMMs preparation methods can be improved by an enhanced selection of the solvent and fabrication procedure. Hence, a systematic study on the selection of the best solvents, mixtures of solvents, and optimal casting processes for the fabrication of MMMs would be very interesting. Although many studies have shown that fast evaporating solvents limit the penetration of polymer chains in the MOF pores they lead to high residual stresses after evaporation. Further studies regarding the kinetics, i.e., the diffusion of gases through a specific MOF, need to be performed because the number of previously published studies on this topic is manageable. Generally speaking, MMMs suffer from insufficient adhesion between the polymer matrix and the filler particles resulting in the formation of non-selective voids at the polymer-filler interface. This formation leads to high fluxes but low selectivities. This is the reason why in many cases MMMs do not show the predicted separation performance.[247] Nanoparticles which are incorporated in mixed-matrix membranes can agglomerate, especially at higher loadings. Higher loadings of filler particles can result in so called non-selective voids between the particles and minimize the separating effectiveness. In future work, the adhesion between nanosized MOF filler particles and the polymer matrix should be investigated, therefore.

There also is the opportunity to incorporate a second system into the MMMs. By using specific ionic liquids which have favourable interactions with the polymer as well as with the MOF, the compatibility between polymer and MOF can be optimised. The ionic liquid can act as a filling agent at the interface leading to a performance well above the Robeson upper bound.[248] A systematic screening of nanosize MOF filler particles and the use of different kinds of ionic liquids, which would be a time-consuming process, could be very helpful to understand the influence of nanosize MOFs on the polymer matrix. This includes adsorption studies related to mixed-gases which are of great importance due to their more realistic conditions.

Controlled modifications of the external surface of nano/microsized MOF particles through, e.g., the introduction of functional groups through post-synthetic modifications, are also important as they might have a direct impact on permeability and selectivity. The post-synthetic modification also can have an impact on the chiral separation. Homochirality was successfully incorporated into achiral MIL-53-NH_2 nanocrystals by post-synthetic modification with amino acids, such as L-histidine (L-His) and L-glutamic acid (L-Glu). The MIL-53-NH-L-His and MIL-53-NH-L-Glu nanocrystals were then embedded into a polyethersulfone matrix to form homochiral MMMs, which exhibited excellent enantioselectivity for racemic 1-phenylethanol.[249] There is also the opportunity to functionalize MOFs with polymer compatible moieties. This can improve the interface adhesion between MOF filler particles and polymer matrix. Another opportunity is to use mixed-linker MOFs or to functionalize the external surface of the MOF nanoparticles in order to initiate the monomer polymerization. The functionalization of MOFs by grafting of amines onto the surfaces of MOF materials to enhance adsorption of the acidic CO_2 is one of the strategies to enhance the gas separation properties and adhesion between the polymer matrix and the MOF filler particles.[250] Chemical bonding between the polymer phase and MOF filler particles can also be examined to improve the adhesion and gas separation performance.

Metal-organic frameworks are among the most promising scientific advances of our generation. As shown in the introduction, many unique properties of these materials make new applications possible. However, it must be highlighted that it is still important to do a lot more basic research. To quote the father of these remarkable structures: “Scientists have just scratched the surface of the essentially limitless applications of the technology”.

4.2 The second research focus - resonance-assisted hydrogen bonds

While room-temperature single-crystal X-ray diffraction using the independent atom model (IAM) for 9-hydroxyphenalenone apparently disagreed initially with other spectroscopic results, cluster computations in addition to earlier low temperature single-crystal X-ray diffraction data collection and analysis falsify the presence of a C_{2v} symmetric resonance-assisted hydrogen bond in 9-hydroxyphenalenone. These results are fully supported by independent atom model (IAM) as well as more precise invariom refinements of three more substituted 9-hydroxyphenalenone derivatives reported here. ONIOM cluster computations complement and nicely confirm the analysis. Residual electron density obtained after invariom refinement was shown to be a useful validation tool in this context – recent technical progress in evaluating single crystal X-ray diffraction data does provide an unambiguous result in full agreement with other spectroscopic results as well as density-functional theory (DFT) computations on clusters of molecules that represent the solid state.

5. References

[1] O. M. Yaghi, G. Li and H. Li, *Nature* **1995**, *378*, 703-706.

[2] O. M. Yaghi, “Limitless applications: the magic powder that could prevent future crises.” *The Guardian*, Jul. 07, 2017.

[3] T. Schareina, C. Schick, B.F. Abrahams, R. Kempe, *Z. Anorg. Allg. Chem.* **2001**, *627*, 1711-1713.

4 K. Abu-Shandi, H. Winkler, B. Wu, C. Janiak, *CrystEngComm* **2003**, *5*, 180-189.

[5] C. Janiak, *Dalton Trans.* **2003**, *14*, 2781-2804.

[6] N. Stock, A. Stoll, T. Bein, *Micropor Mesopor Mater* **2004***, 69,* 65-69.

[7] G. Férey, *Chem. Soc. Rev.* **2008**, *37*, 191-214.

[8] S. Kitagawa, R. Kitaura, S.-i. Noro, *Angew. Chem. Int. Ed.* **2004**, *43*, 2334-2375.

[9] P. B. Venuto, E. T. Habib, Jr., *Chemical Industries, Vol. 1: Fluid Catalytic Cracking with Zeolite Catalysts*, **1979**, *28*, 228-228.

[10] O.K. Farha, I. Eryazici, N.C. Jeong, B.G. Hauser, C.E. Wilmer, A.A. Sarjeant, R.Q. Snurr, S.T. Nguyen, A. Özgür Yazaydn, J.T. Hupp, *J. Am. Chem. Soc.* **2012**, *134*, 15016-15021.

[11] T. Tian, Z. Zeng, D. Vulpe, M.E. Casco, G. Divitini, P.A. Midgley, J. SilvestreAlbero, J.-C. Tan, P.Z. Moghadam, D. Fairen-Jimenez, *Nat. Mater.* **2017**, *17*, 174-179.

[12] D. DeSantis, J. A. Mason, B. D. James, C.y Houchins, J. R. Long, M. Veenstra, *Energy Fuels* **2017**, *31*, 2024-2032.

[13] C. Schlüsener, M. Xhinovci, S.-J. Ernst, A. Schmitz, N. Tannert, C. Janiak, *Chem. Mater.* **2019**, *31*, 4051−4062.

[14] H. Reinsch, S. Waitschat, N. Stock, *Dalton Trans.* **2013**, *42*, 4840−4847.

[15] O. M. Yaghi, M. O'Keeffe, N. W. Ockwig, H. K. Chae, M. Eddaoudi, J. Kim, *Nature* **2003**, *423*, 705–714.

[16] C. Janiak, J. K. Vieth, *New J. Chem.* **2010**, *34*, 2366-2388.

[17] L. R. MacGillivray, *Metal-Organic Frameworks:Design and Application*, Wiley, Hoboken, New Jersey, **2010**.

[18] R. Seetharaj ,P. V. Vandana, P. Arya, S. Mathew, *Arab. J. Chem.* **2019**, *12*, 295-315.

[19] H. Kim, M. S. Lah, *Dalton Trans.* **2017**, ***46***, 6146-6158.

[20] M. H. Rosnes, F. S. Nesse, P. D. C. Dietzel, *Micropor Mesopor Mater* **2019**, *275*, 207-213.

[21] J. J. Perry, J. A. Perman, M. J. Zaworotko, *Chem. Soc. Rev.* **2009**, *38*, 1400–1417.

[22] A. Alshammari, Z. Jiang, K. E. Cordova, Metal Organic Frameworks as Emerging Photocatalysts, Semiconductor Photocatalysis - Materials, Mechanisms and Applications, Wenbin Cao, IntechOpen **2016**, 301-341. DOI: 10.5772/63489. Available from: https://www.intechopen.com/books/semiconductor-photocatalysis-materials-mechanisms-and-applications/metal-organic-frameworks-as-emerging-photocatalysts

[23] S. T. Batten, R. Robson, *Angew. Chem. Int. Edn Engl.* **1998**, *37*, 1460-1494.

24 M. Wickenheisser, C. Janiak, *Micropor Mesopor Mater* **2015**, *204*, 242-250.

[25] G. Férey, C. M. Draznieks, C. Serre, F. Millange, J. Dutour, S. Surble, I. Margiolaki, *Science* **2005**, *309*, 2040-2042.

[26] T. Zhao, F. Jeremias, I. Boldog, B. Nguyen, S. K. Henninger, C. Janiak, *Dalton Trans.* **2015**, *44*, 16791-16801.

[27] F. Jeremias, S. K. Henninger, C. Janiak, *Dalton Trans.* **2016**, *45*, 8637-8644.

[28] T. Loiseau, C. Serre, C. Huguenard, G. Fink, F. Taulelle, M. Henry, T. Bataille, G. Férey, *Chem. Eur. J.* **2004**, *10*, 1373–1382.

[29] A. Dhakshinamoorthy, M. Alvaro, H. Chevreau, P. Horcajada, T. Devic, C. Serre, H. Garcia, *Catal. Sci. Technol.* **2012**, *2*, 324-330.

[30] N. A. Ramsahye, G. Maurin, S. Bourrelly, P. Llewellyn, T. Loiseau, G. Férey, *Phys. Chem. Chem. Phys.* **2007**, *9*, 1059-1063.

[31] W. Lu, Z. Wei, Z.-Y. Gu, T.-F. Liu, J. Park, J. Park, J. Tian, M. Zhang, Q. Zhang, T. Gentle III, M. Bosch, H.-C. Zhou, *Chem. Soc. Rev.* **2014**, *43*, 5561-5593.

[32] M. E. Casco, Y. Q. Cheng, L. L. Daemen, D. Fairen-Jimenez, E. V. Ramos-Fernández, A. J. Ramirez-Cuesta, J. Silvestre-Albero, ***Chem. Commun.*** **2016**, *52***,** 3639-3642.

[33] B. Zheng, Y. Pan, Z. Lai, K.-W. Huang, Langmuir 2013, 29, 28, 8865-8872.

[34] Y. Xiong, Y.-Z. Fan, Z.-W. Wei, C.-X. Chen, S. Chen, D. Wang, M. Barboiu, J.-J. Jiang, C.-Y. Su, *RSC Adv.* **2019,** 9**,** 37222-37231.

[35] M. Eddaoudi, D. B. Moler, H. Li, B. Chen, T. M. Reineke, M. O'Keeffe, O. M. Yaghi, *Acc. Chem. Res.* **2001**, *34*, 319-330.

[36] V. Guillerm, Ł. J. Weseliński, Y. Belmabkhout, A. J. Cairns, V. D'Elia, Ł. Wojtas, K. Adil, M. Eddaoudi, *Nature Chem* **2014**, *6*, 673-680.

[37] W. J. Rieter, K. M. L. Taylor, H. An, W. Lin, W. Lin, *J. Am. Chem. Soc.* **2006**, *128*, 9024-9025.

[38] W. Lin, W. J. Rieter, K. M. L. Taylor, *Angew. Chem. Int. Ed.* **2009**, *48*, 650-658.

[39] T. Shen, J. Luo, S. Zhang, X. Luo, *J. Environ. Chem. Eng.* **2015**, *3*, 1372-1383.

[40] H. V. Doan, H. A. Hamzah, P. K. Prabhakaran, C. Petrillo, V. P. Ting, *Nano-Micro Lett.* **2019**, 11:54.

[41] H. Li, K. Wang, Y. Sun, C. T. Lollar, J. Li, H.-C. Zhou, *Mater. Today* **2018**, *21*, 108-121.

[42] O. M. Yaghi, H. Li, C. Davis, D. Richardson, T. L. Groy, *Acc. Chem. Res.* **1998**, *31*, 474-484.

[43] G. Férey, *J. Solid State Chem.* **2000**, *152*, 37-48.

[44] O. M. Yaghi, M. O'Keeffe, M. G. Kanatzidis, *J. Solid State Chem.* **2000**, *152*, 1-2.

[45] S. Kitagawa, M. Kondo, *Bull. Chem. Soc. Jpn* **1998**, *71*, 1739-1753.

[46] R. Grünker, V. Bon, P. Müller, U. Stoeck, S. Krause, U. Mueller, I. Senkovskaa, S. Kaskel, *Chem. Commun*. **2014**, *50*, 3450-3452.

[47] J. E. Mondloch, M. J. Katz, N. Planas, D. Semrouni, L. Gagliardi, J. T. Hupp, O. K. Farha, *Chem. Commun.* **2014**, *50*, 8944– 8946.

[48] A. J. Howarth, A. W. Peters, N. A. Vermeulen, T. C. Wang, J. T. Hupp, O. K. Farha, *Chem. Mater.* **2017**, *29*, 26-39.

[49] J. E. Mondloch, O. Karagiaridi, O. K. Farha, J. T. Hupp, *CrystEngComm* **2013**, *15*, 9258– 9264.

[50] M. Arjmandi, M. Pakizeh, *Acta Metall. Sin. (Engl. Lett.)* **2013**, *26*, 597-601.

[51] D. O. Kim, J, Park, G, R. Ahn, H. J. Jeon, J. S. Kim, D. W. Kim, M. S. Jung, Sang W. Lee, S. H. Shin, *Inorg. Chim. Acta* **2011**, *370*, 76-81.

[52] J.-R. Li, R.J. Kuppler, H.-C. Zhou, *Chem. Soc. Rev.* **2009**, *38*, 1477-1504.

[53] P. Horcajada, R. Gref, T. Baati, P. K. Allan, G. Maurin, P. Couvreur, G. Férey, R. E. Morris, C. Serre, *Chem. Rev.* **2012**, *112*, 1232-1268.

[54] H. B. Tanh Jeazet, C. Staudt, C. Janiak, *Chem. Commun.* **2012**, *48*, 2140-2142.

[55] B. Chen, L. Wang, Y. Xiao, F. R. Fronczek, M. Xue, Y. Cui, G. Qian, *Angew. Chem. Int. Ed.* **2009**, *48*, 500-503.

[56] M. H. Beyzavi, C.J. Stephenson, Y. Liu, O. Karagiaridi, J. T. Hupp, O. K. Farha, *Front. Energy Res.* **2015**, 2:63.

[57] C. Janiak, S. K. Henninger, *Nachr. Chem.* **2013**, *61*, 520-523.

[58] I. Erucar, S. Keskin, *Front. Mater.* **2018**, 5:4.

[59] A. N. V. Azar, S. Keskin, *Front. Chem.* **2018**, 6:36.

[60] R. Antwi-Baah, H. Liu, *Materials* **2018**, 11:2250.

[61] G. Cao, Nanostructures and nanomaterials, Properties and Applications, World Scientific Publishing Co. Pte. Ltd., London, **2011**.

[62] A. Zimpel, T. Preiß, R. Röder, H. Engelke, M. Ingrisch, M. Peller, J. O. Rädler, E. Wagner, T. Bein, U. Lächelt, S. Wuttke, *Chem. Mater.* **2016**, *28*, 3318-3326.

[63] A. M. Spokoyny, D. Kim, A. Sumrein, C. A. Mirkin, Chem. *Soc. Rev.* **2009**, *38*, 1218-1227

[64] W. Lin, W. J. Rieter, K. M. L. Taylor, *Angew. Chem*. **2009**, *121*, 660-668.

[65] G. Nichols, S. Byard, M. J. Bloxham, J. Botterill, N. J. Dawson, A. Dennis, V. Diart, N. C. North, J. D. Sherwood, *J. Pharm. Sci.* **2002**, *91*, 2103-2109.

[66] A. Albanese, P. S. Tang, W. C. Chan, *Annu. Rev. Biomed. Eng.* **2012**, *14*, 1-16.

[67] C. C. D. Wang, W. C. H. Choy, C. Duan, D. D. S. Fung, W. E. I. Sha, F.-X. Xie, F. Huang, Y. Cao, *J. Mater. Chem.* **2012**, *22*, 1206-1211.

[68] A. P. Alivisatos, *Science* **1996**, *271*, 933-937.

[69] P. Hirschle, T. Preiß, F. Auras, A. Pick, J. Völkner, D. Valdepérez, G. Witte, W. J. Parak, J. O. Rädler, S. Wuttke, ***CrystEngComm*** **2016**,*18*, 4359-4368.

[70] C. V. McGuire, R. S. Forgan, *Chem. Commun.* **2015**, *51*, 5199–5217.

[71] H. Guo, G. Stan, Y. Liu, ***Soft Matter*** **2018**,*14*, 1311-1318.

[72] Y. Sakata, S. Furukawa, M. Kondo, K. Hirai, N. Horike, Y. Takashima, H. Uehara, N. Louvain, M. Meilikhov, T. Tsuruoka, S. Isoda, W. Kosaka, O. Sakata, S. Kitagawa, *Science* **2013**, *339*, 193-196.

[73] D. Tanaka, A. Henke, K. Albrecht, M. Moeller, K. Nakagawa, S. Kitagawa, J. Groll, *Nat. Chem.* **2010**, *2*, 410-416.

[74] Y. Hijikata, S. Horike, D. Tanaka, J. Groll, M. Mizuno, J. Kim, M. Takata, S. Kitagawa, *Chem. Commun.* **2011**, *47*, 7632-7634.

[75] J. Jiang, G. Oberdörster, P. Biswas, *J. Nanopart. Res.* **2009**, *11*, 77–89.

[76] R. A. Sperling, T. Liedl, S. Duhr, S. Kudera, M. Zanella, C.-A. J. Lin, W. Chang, D. Braun, W. J. Parak, *J. Phys. Chem. C* **2007**, *111*, 11552–11559.

[77] F. Zhang, Z. A. F. Amin, A. Feltz, M. Oheim, W. J. Parak, *ChemPhysChem* **2010**, *11*, 730–735.

[78] E. Caballero-Díaz, C. P., L. Kastl, P. Rivera-Gil, B. Simonet, M. Valcárel, J. Jiménez-Lamana, F. Laborda, W. J. Parak, *Part. Part. Syst. Charact.* **2013**, *30*, 1079–1085.

[79] P. Rivera-Gil, D. J. De Aberasturi, V. Wulf, B. Pelaz, P. del Pino, Y. Zhao, J. M. de la Fuente, I. Ruiz de Larramendi, T. Rojo, X.-J. Liang, W. J. Parak, *Acc. Chem. Res.* **2013**, *46*, 743-749.

[80] H. T. Kwon, H.-K. Jeong, A. S. Lee, H. S. An, T. Lee, E. Jang, J. S. Lee, J. Choi, *Chem. Commun.* **2016**, ***52***, 11669-11672.

[81] C. Orellana-Tavra, R. J. Marshall, E. F. Baxter, Isabel Abánades Lázaro, Andi Tao, A. K. Cheetham, R. S. Forgan, D. Fairen-Jimenez, *J. Mater. Chem. B 2016*, *4*, 7697-7707.

[82] N. Stock, S. Biswas, *Chem. Rev.* **2012,** *112,* 933–969.

[83] T. Chalati, P. Horcajada, R. Gref, P. Couvreur, C. Serre, *J. Mater. Chem.* **2011**, *21*, 2220-2227.

[84] X. Sun, S. Dong, E. Wang, *J. Am. Chem. Soc.* **2005**, *127*, 13102-13103.

[85] M. Oh, C. A. Mirkin, *Nature* **2005**, *438*, 651-654.

[86] L. H. Wee, M. R. Lohe, N. Janssens, S. Kaskel, J. A. Martens, ***J. Mater. Chem.*** **2012**, ***22***, 13742-13746.

[87] J. Li, Q. Wu, J. Wu, Synthesis of Nanoparticles via Solvothermal and Hydrothermal Methods. In: Aliofkhazraei M. (eds) Handbook of Nanoparticles. Springer, Cham, **2016**.

[88] N. A. Khan, I. J. Kang, H. Y. Seok, S. H. Jhung, *Chem. Eng. J.* **2011**, *166*, 1152-1157.

[89] L. Huang, H. Wang, J. Chen, Z. Wang, J. Sun, D. Zhao, Y. Yan, *Micropor Mesopor Mater* **2003**, *58*, 105-114.

[90] I. Gruber, A. Nuhnen, A. Lerch, S. Nießing, M. Klopotowski, A.Herbst, M. Karg, C. Janiak, *Front. Chem*. **2019**, 7:777.

[91] N. A. Khan, S. H. Jhung, *Coord. Chem. Rev.* **2015**, *285*, 11-23.

[92] B. Zhang, Y. Luo, K. Kanyuck, N. Saenz, K. Reed, P. Zavalij, J. Mowery, G. Bauchan, *RSC Adv.* **2018**, *8*, 33059-33064.

[93] C. P. Li, M. Du, *Chem. Commun.* **2011**, *47*, 5958– 5972.

[94] R. Ding, C. Huang, J. Lu, J. Wang, C. Song, J. Wu, H. Hou, Y. Fan, *Inorg. Chem.* **2015**, *54*, 4, 1405-1413.

[95] Y.-H. Huang, W. S. Lo, Y.-W. Kuo, W.-J. Chen, C.-H. Lin, F.-K. Shieh, ***Chem. Commun.*** **2017**, ***53***, 5818-5821.

[96] V. V. Boldyrev, *Powder Technol.* **2002**, *122*, 247-254.

[97] D. Lv, Y. Chen, Y. Li, R. Shi, H. Wu, X. Sun, J. Xiao, H. Xi, Q. Xia, Z. Li, *J. Chem. Eng. Data* **2017**, *62*, 2030-2036.

[98] R. Zhang, C. A.Tao, R. Chen, L. Wu, X. Zou, J. Wang, *Nanomaterials* **2018**, 8:1067.

[99] K. Leng, Y. Sun, X. Li, S. Sun, W. Xu, *Cryst. Growth Des.* **2016**, *16*, 3, 1168-1171.

[100] S. A. Galema, ***Chem. Soc. Rev.*** **1997**, *26*, 233-238.

[101] K.-Y. A. Lin, Y.-T. Hsieh, J. Taiwan, *Inst. Chem. Eng.* **2015**, *50*, 223-228.

[102] M. Kandiah, M. H. Nilsen, S. Usseglio, S. Jakobsen, U. Olsbye, M. Tilset, C. Larabi, E. A. Quadrelli, F. Bonino, K. P. Lillerud, *Chem. Mater.* **2010**, *22*, 24, 6632-6640.

[103] I. A. Ibarra, S. Yang, X. Lin, A. J. Blake, P. J. Rizkallah, H. Nowell, D. R. Allan, N. R. Champness, P. Hubberstey, M. Schröder, ***Chem. Commun.*** **2011**, 47, 8304-8306.

[104] S. Diring, S. Furukawa, Y. Takashima, T. Tsuruoka, S. Kitagawa, *Chem. Mater.* **2010**, *22*, 4531-4538.

[105] D. Bogdal, Microwave-Assisted Organic Synthesis. New York: Elsevier, 2006.

[106] A. Huang, L. Wan, *Caro Mater. J. Res. Bull*. **2018**, *98*, 308-313.

[107] B. Zhang, J. Zhang, C. Liu, X. Sang, L. Peng, X. Ma, T. Wu, B. Han, G. Yang , *RSC Adv.* **2015**, *5* , 37691-37696.

[108] F. Wang, H. Guo, Y. Chai, Y. Li , C. Liu, *Micropor Mesopor Mater* **2013**, *173* , 181-188.

[109] C. Xin, H. Zhan, X. Huang, H. Li, N. Zhao, F. Xiao, W. Wie, Y. Sun, *RSC Adv.* **2015**, *5*, 27901-27911.

[110] Y. Mao, B. Su, W. Cao, J. Li, Y. Ying, W. Ying, Y. Hou, L. Sun, X. Peng, *ACS APPL MATER INTER* **2014**, *6*, 15676-15685.

[111] D. Jiang, A. D. Burrows, K. J.Edler, *CrystEngComm* **2011**, *12*, 6916-6919.

[112] S. Du, F. Li, Q. Sun, N. Wang, M. Jia, J. Yu, *Chem. Commun.* **2016**, *52*, 3368-3371.

[113] D. Bradshaw, S. El-Hankari, L. Lupica-Spagnolo, *Chem. Soc. Rev.* **2014**, *43*, 5431-5443.

[114] E. R. Parnham, R. E. Morris , *Acc. Chem. Res.* **2007**, *40* , 1005-1013.

[115] E. R. Cooper, C. D. Andrews, P. S. Wheatley, P. B. Webb, P. Wormald, R. E. Morris, *Nature* **2004**, *430*, 1012-1016.

[116] T. P. Vaid, S. P. Kelley, R. D. Rogers, *IUCrJ* **2017**, *4*, 380-392.

[117] M. R. Gao, J. Yuan, M. Antonietti, *Chem.-Eur. J.* **2017**, *23*, 5391-5403.

[118] K. S. Suslick, Kirk-Othmer Encyclodpedia of Chemical Technology, Sonochemistry, Fourth Edition, vol. 26, John Wiley & Sons, Inc., New York, USA, **1998**, 516-541.

[119] Y.-S. Wu, S.-C. Ngai, B.-H. Goh, K.-G. Chan, L.-H. Lee, L.-H. Chuah, *Front. Pharmacol.* **2017**, 8:761.

[120] C. S. Carr, D. F. Shantz, *Micropor Mesopor Mater* **2005**, *85*, 284-292.

[121] L. Salvia-Trujillo, M. Artiga-Artigas, A. Molet-Rodríguez, A. Turmo-Ibarzand, O. Martín-Belloso, *Food Syst.* **2018**, 2:79.

[122] C. P. Whitby, L. Lotte, C. Lang, *Soft Matter* **2012**, *8*, 7784-7789.

[123] N. A. Khan, E. Haquea, S. H. Jhung, *Phys. Chem. Chem. Phys.* **2010**, *12*, 2625-2631.

[124] K. Shinoda, H. Saito, *J. Colloid Interface Sci.* **1969**, *30*, 258-263.

[125] S. N. Kale, S. L. Deore, *Sys. Rev. Pharm.* **2017**, *8*, 39-47.

[126] S. Wang, C. M. McGuirk, A. d'Aquino, J. A., Mason, C. A. Mirkin, *Adv. Mater.* **2018**, *30*, 1-14.

[127] K. M. L. Taylor, W. J. Rieter, W. Lin, *J. Am. Chem. Soc.* **2008**, *130*, 14358-14359.

[128] M. A. Basith, D.-T. Ngo, A. Quader, M. A. Rahman, B. L. Sinha, B. Ahmmad, F. Hirose, K. Mølhave, *Nanoscale* **2014**, ***6***, 14336-14342.

[129] J. Jordens, T. Appermont, B. Gielen, T. Van Gerven, L. Braeken, *Cryst. Growth Des.* **2016**, *16*, 11, 6167-6177.

[130] L.-G. Qiu, Z.-Q. Li, Y. Wu, W. Wang, T. Xu, X. Jiang, *Chem. Commun.* **2008**, 31, 3642–3644.

[131] D. Tanaka, A. Henke, K. Albrecht, M. Moeller, K. Nakagawa, S. Kitagawa, J. Groll, *Nat Chem* **2010**, *2*, 410-416.

[132] A. Carné-Sánchez, I. Imaz, M. Cano-Sarabia, D. Maspoch, *Nat Chem* **2013**, *5*, 203-211.

[133] F. Grieser, M. Ashokkumar, J. Z. Sostaric, Sonochemistry and sonoluminescence in colloidal systems. In: Crum, L.A., Mason, T.J., Reisse J.L., Suslick, K.S. (Eds.), Sonochemistry and Sonoluminescence NATO ASI Series. Kluwer Academic Publishers, Netherlands, **1999**, 345–362.

[134] K. Hunger, N. Schmeling, H. B. Tanh Jeazet, C. Janiak, C. Staudt, K. Kleinermanns, *Membranes* **2012**, *2*, 727-763.

[135] T. Graham, On the law of the diffusion of gases, Phil. Mag. 2 **1833**, 175, 269 and 351.

[136] R. W. Baker, *Ind. Eng. Chem. Res.* **2002**, *41*, 6, 1393-1411.

[137] S. Loeb, S. Sourirajan, Sea water demineralization by means of an osmotic membrane, *Adv. Chem. Ser*. **1962,** 38:117.

[138] S. Loeb, S. Sourirajan, The preparation of high-flow semi-permeable membranes for separation of water from saline solutions, US Patent 3,133,132, **1964**.

[139] B. Seoane, J. Coronas, I. Gascon, M. Etxeberria Benavides, O. Karvan, J. Caro, F. Kapteijn, J. Gascon, *Chem. Soc. Rev.* **2015**, *44*, 2421-2454.

[140] J. M. Duval, B. Folkers, M. H. V. Mulder, *J. Membr. Sci.* **1993**, *80*, 189-198.

[141] R. Mahajan, R. Burns, M. Schaeffer, W. J. Koros, *J. Appl. Poly. Sci.* **2002**, *86*, 881-890.

[142] J. Dechnik, C. J. Sumby, C. Janiak, *Cryst. Growth Des.* **2017**, *17*, 4467-4488.

[143] S. Wiederhorn, R. Fields, S. Low, G.-W. Bahng, A. Wehrstedt, J. Hahn, Y. Tomota, T. Miyata, H. Lin, B. Freeman, S. Aihara, Y. Hagihara, T. Tagawa, Mechanical Properties. In *Springer Handbook of Materials Measurement Methods*; H. Czichos, T. Saito, L. Smith, Eds. Springer: Berlin, Heidelberg, 2006; Chapter 7, pp 283-397.

[144] R. Mahajan, W. J. Koros, *Ind. Eng. Chem. Res.* **2000**, *39*, 2692-2696.

[145] R. Mahajan, W. J. Koros, *Polym. Eng. Sci.* **2002**, *42*, 1420-1431.

[146] R. Mahajan, W. J. Koros, *Polym. Eng. Sci.* 2002, 42, 1432-1441.

[147] A. Nuhnen, D. Dietrich, S. Millan, C. Janiak, *ACS Appl. Mater. Interfaces* **2018**, *10*, 33589-33600.

[148] M. Galizia, W. S. Chi, Z. P. Smith, T. C. Merkel, R. W. Baker, B. D. Freeman, *Macromolecules* **2017**, *50*, 20, 7809-7843.

[149] B. Zornoza, S. Irusta, C. Téllez, J. n. Coronas, *Langmuir* **2009**, *25*, 5903-5909.

[150] D. Bastani, N. Esmaeili, M. Asadollahi, *J. Ind. Eng. Chem.* **2013**, *19*, 375-393.

[151] T. W. Pechar, S. Kim, B. Vaughan, E. Marand, M. Tsapatsis, H. K. Jeong, C. J. Cornelius, *J. Membr. Sci.* **2006**, *277*, 195-202.

[152] D. Q. Vu, W. J. Koros, S. J. Miller, *J. Membr. Sci.* **2003**, *211*, 311-334.

153 T.-H. Weng, H.-H. Tseng, M.-Y. Wey, *Int. J. Hydrogen Energ.* **2010**, *35*, 6971-6983.

[154] L. Ge, Z. Zhu, V. Rudolph, *Sep. Purif. Technol.* **2011**, *78*, 76-82.

[155] L. Ge, Z. Zhu, F. Li, S. Liu, L. Wang, X. Tang, V. Rudolph, *J. Phys. Chem. C* **2011**, *115*, 6661-6670.

[156] T. Yang, Y. Xiao, T.-S. Chung, *Energ. Environ. Sci.* **2011**, *4*, 4171-4180.

[157] R. Adams, C. Carson, J. Ward, R. Tannenbaum, W. Koros, *Micropor Mesopor Mater* **2010**, *131*,13-20.

[158] K. Sumida, D. L. Rogow, J. A. Mason, T. M. McDonald, E. D. Bloch, Z. R. Herm, T. H. Bae, J. R. Long, *Chem. Rev.* **2012**, *112*, 724-781.

[159] B. Zornoza, C. Tellez, J. Coronas, J. Gascon, F. Kapteijn, *Micropor Mesopor Mater* **2013**, *166*, 67-78.

[160] M. Carreon, G. Dahe, J. Feng, S. R. Venna, World Scientific Series in Membrane Science and Technology: Biological and Biomimetic Applications, Energy and the Environment. Chapter 1: Mixed Matrix Membranes for Gas Separation Applications, **2017**.

[161] B. Zornoza, P. Gorgojo, C. Casado, C. Tellez, J. Coronas, *Desalin. Water Treat.* **2011**, *27*, 42-47.

[162] H. Cong, M. Radosz, B. F. Towler, Y. Shen, *Sep Purif. Techol.* **2007**, *55*, 281-291.

[163] D. Manimaran, Z. A. Jawad, C. T. Leng, *J. App. Membr. Sci. Technol.* **2019**, *23*, 11-28.

[164] A.M.W. Hillock, S.J. Miller, W.J. Koros, *J. Membr. Sci.* **2008**, *314*, 193-199.

[165] O. Talu, S. Y. Zhang, D. T. Hayhurst, *J. Phys. Chem.* **1993**, *97*, 12894-12898.

[166] M. Sadrzadeh, M. Rezakazemi, T. Mohammadi, Transport Properties of Polymeric Membranes **2018**, 391-423.

[167] C. M. Zimmerman, A. Singh, W. J. Koros, *J. Membr. Sci.* **1997**,*137*, 145-154.

[168] L. M. Robeson, *J. Membr. Sci.* **1991**, *62*, 165-185.

[169] L. M. Robeson, *J. Membr. Sci.* **2008**, *320*, 390-400.

[170] Tanh Jeazet, H. B.; Staudt, C.; Janiak, C. *Dalton Trans.* **2012**, *41*, 14003-14027.

[171] D. Wang, K. Li, W. K. Teo, *J. Membr. Sci.* **1996**, *115*, 85-108.

[172] W. J. Koros, G. K. Fleming, *J. Membr. Sci.* **1993**, *83*, 1-80.

[173] J. Koresh, A. Soffer, *Sep. Sci. Technol.* **1987**, *22*, 973-982.

[174] W. J. Koros, G. K. Fleming, S. M. Jordan, T. H. Kim, H. H. Hoehn, *Prog. Polym. Sci.* **1988**, *13*, 339-401.

[175] R. Mahajan, Formation, characterization and modeling of mixed matrix membrane materials, Ph.D. Thesis, The University of Texas at Austin, **2000**.

[176] L. Pilato, L. Litz, B. Hargitay, R. Osborne, A. Farnham, J. Kawakami, P. Fritze, J. McGrath, *ACS Polymer* **1975**, 16:42.

[177] G. Lei, Carbon Nanotube-based Membranes for Gas Separation, in, University of Queensland, **2012**.

[178] A. Fernández-Barquín, C. Casado-Coterillo, M. Palomino, S. Valencia, A.Irabien, *Sep. Purify. Technol.* **2016**, *157*, 102-111.

[179] Y. Li, T.-S. Chung, S. Kulprathipanja, *AIChE* **2007**, *53*, 610-616.

[180] J. D. Wind, C. Staudt-Bickel, D. R. Paul, W. J. Koros, *Ind. Eng. Chem. Res.* **2002**, *41*, 6139-6148.

[181] M. Zhang, L. Deng, D.Xiang, B. Cao, S. S. Hosseini, P. Li, *Processes* **2019**, 7:51.

[182] W. Koros, Y. Ma, T. Shimidzu, *J. Membr. Sci.* **1996**, *120*, 149-159.

[183] W. J. Koros, C. Zhang, *Nat. Mater.* **2017**, *16*, 289–297.

[184] D. Q. Vu, W. J. Koros, S. J. Miller, *J. Membr. Sci.* **2003**, *211*, 335-348.

[185] K. M. Gheimasi, T. Mohammadi, O. Bakhtiari, *J. Membr. Sci.* **2013**, *427*, 399-410.

[186] R. H. B. Bouma, A. Checchetti, G. Chidichimo, E. Drioli, *J. Membr. Sci.* **1997**, *128,* 141-149.

[187] R. Pal, *J. Colloid Interface Sci.* **2008**, *317*, 191-198.

[188] B. Shimekit, H. Mukhtar, T. Murugesan, *J. Membr. Sci.* **2011**, *373*, 152-159.

[189] T. T. Moore, W. J. Koros, *J. Mol. Struct.* **2005**, *739*, 87-98.

[190] H. Vinh-Thang, S. Kaliaguine, *Chem. Rev.* **2013**, *113*, 4980–5028.

[191] R. Mahajan, D. Q. Vu, W. J. Koros, *AICHE Journa* **2004**, *50*, 311–321.

[192] D. A. G. Bruggeman, *Annalen der Physik* **1935**, *416*, 636-664.

[193] R. Pal, *J. Reinf. Plast. Compos.* **2007**, *26*, 643-651.

[194] *O. Bakhtiari, N. Sadeghi, Int. J. Chem. Eng. App.* ***2014**, 5, 198-203.*

[195] B. Shimekit, H. Mukhtar, S. Maitra, *J. App. Sci.* **2010**, *10*, 1204-1211.

[196] M. A. Aroon, A. F. Ismail, T. Matsuura, M. M. Montazer-Rahmati, *Sep. Purif. Technol.* **2010**, *75*, 229-242.

[197] B. Shimekit, H. Mukhtar, T. Murugesan, *J. Membr. Sci.* **2011**, *373*, 152-159.

[198] S. Hosseini, L. I. Y. T. Chung, Y. Liu, *J. Membr. Sci.* **2007**, *302*, 207-217.

[199] S. Kanehashi, G. Q. Chen, C. A. Scholes, B. Ozcelik, C. Hua, L. Ciddor, P. D. Southon, D. M. D'Alessandro, S. E. Kentish, *J. Membr. Sci*. **2015**, *482*, 49-55.

[200] Y. Huang, X. Wang, D. R. Paul, *J. Membr. Sci.* **2006**, *277*, 219-229.

[201] S. Sorribas, B. Zornoza, C. Téllez, J. Coronas, *J. Membr. Sci.* **2014**, *452*, 184-192.

[202] G. Liu, V. Chernikova, Y. Liu, K. Zhang, Y. Belmabkhout, O. Shekhah, C. Zhang, S. Yi, M. Eddaudi, W. J. Koros, *Nature Materials* **2018**, *17*, 283-289.

[203] M.G. Miricioiu, C. Iacob, G. Nechifor V.-C. Niculescu, *Front. Chem.* **2019**, 7:332.

[204] P. Chowdhury, S. Mekala, F. Dreisbach, S. Gumma, *Micropor Mesopor Mater* **2012**, *152*, 246-252.

[205] E. V. Perez, K. J. Balkus Jr, J. P. Ferraris, I. H. Musselman, *J. Membr. Sci.* **2009**, *328*, 165-173.

[206] I. Gruber, L. Bensch, T. J. J. Müller, C. Janiak, B. Dittrich, *Z. Kristallogr.* **2020**, 235, 225-235.

[207] G. A. Jeffrey, An Introduction to Hydrogen Bonding. Oxford University Press: New York, **1997**.

[208] G. R. Desiraju, T. Steiner, The Weak Hydrogen Bond in Structural Chemistry and Biology. Oxford University Press: New York, **1999**.

[209] S. J. Grabowski, Hydrogen Bonding - New Insights; Ed.; Springer: Dordrecht, The Netherlands, **2006**.

[210] S. Scheiner, Ed., Molecular Interactions: From van der Waals to Strongly Bound Complexes, Wiley, Chichester, UK, **1997**.

[211] M. Garcia-Viloca, A. González-Lafont, J. M. Lluch, *J. Am. Chem. Soc.* **1997**, *119*, 1081-1086.

[212] M. Garcia-Viloca, R. Gelabert, A. González-Lafont, M. Moreno, J. M. Lluch, *J. Phys. Chem. A* **1997**, *101*, 8727-8733.

[213] L. A. Malaspinna, Al. J. Edwards, M. Woińska, D. Jayatilaka, M. J. Turner, J. R. Price, R. Herbst-Irmer, K. Sugimoto, E. Nishibori, S. Grabowsky, *Cryst. Grow. Des.* **2017**, *17*, 3812-3825.

[214] F. Hibbert, J. Emsley, *J. Adv. Phys. Org. Chem.* **1990**, *26*, 255-379.

[215] J. Emsley, *Struct. Bond.* **1984**, *57*, 147-191.

[216] G. Gilli, F. Bellucci, V. Ferretti, V. Bertolasi, *J. Am. Chem. Soc.* **1989**, *111*, 1023−1028.

[217] V. Bertolasi, P. Gilli, V. Ferretti, G. Gilli, *Chem. Eur. J.* **1996**, *2*, 925–934.

[218] K. T. Mahmudov, A. J. L. Pombeiro, *Chem.-Eur. J.* **2016**, *22*, 16356−16398.

[219] P. Gilli, V. Bertolasi, V. Ferretti, and G. Gilli, *J. Am. Chem. Soc.* **1994**, *116*, 909-915.

[220] G. Gilli, P. Gilli, The Nature of Hydrogen Bond, Oxford University Press, New York, **2009**.

[221] A. Kovács, V. Izvekov, K. Zauer, K. Ohta, *J. Phys. Chem. A* **2001**, *105*, 5000–5009.

[222] S. K. Pal, M. E. Itkis, R. W. Reed, R. T. Oakley, A. W. Cordes, F. S. Tham, T. Siegrist, R. C. Haddon, *J. Am. Chem. Soc.* **2004**, *126*, 1478–1484.

[223] A. Pariyar, G. Vijaykumar, M. Bhunia, S. K. Dey, S. K. Singh, S. Kurungot, S. K. Mandal, *J. Am. Chem. Soc.* **2015**, *137*, 5955–5960.

[224] A. Das, T. M. Scherer, P. Mondal, S. M. Mobin, W. Kaim, G. K. Lahiri, *Chem. Eur. J.* **2012**, *18*, 14434–14443.

[225] S. K. Dey, A. Honecker, P. Mitra, S. K. Mandal, A. Mukherjee, *Eur. J. Inorg. Chem.* **2012**, *35*, 5814–5824.

[226] T. Mochida, R. Torigoe, T. Koinuma, C. Asano, T. Satou, K. Koike, T. Nikaido, *Eur. J. Inorg. Chem.* **2006**, *3*, 558–565.

[227] Y. Demura, T. Kawato, H. Kanatomi, I. Murase, *Bull. Chem. Soc. Jpn.* **1975**, *48*, 2820–2824.

[228] Y. -J. Gu, B. Yan, *Inorg. Chim. Acta* **2013**, *408*, 96–102.

[229] C. F. Koelsch, J. A. Anthes, *J. Org. Chem.* **1941**, *6*, 558–565.

[230] A. Das, T. K. Ghosh, A. Dutta Chowdhury, S. M. Mobin, G. K. Lahiri, *Polyhedron* **2013**, *52*, 1130–1137.

[231] S. K. Mandal, S. Samanta, M. E. Itkis, D. W. Jensen, R. W. Reed, R. T. Oakley, F. S. Tham, B. Donnadieu, R. C. Haddon, *J. Am. Chem. Soc.* **2006**, *128*, 1982-1994.

[232] G. He, Y. Hou, D. Sui, X. Wan, G. Long, P. Yun, A. Yu, M. Zhang, Y. Chen, *Tetrahedron* **2013**, *69*, 6890–6896.

[233] L. Bensch, I. Gruber, C. Janiak, T. J. J. Müller, *Chem. Eur. J.* **2017**, *23*, 10551-10558.

[234] C. Svensson, S. C. Abrahams, J. L. Bernstein, R. C. Haddon, *J. Am. Chem. Soc.* **1979**, *101*, 5759–5764.

[235] C. Svensson, S. C. Abrahams, *Acta Crystallogr.* **1986**, *B42*, 280-286.

[236] R. S. Brown, A. Tse, T. Nakashima, R. C. Haddon, *J. Am. Chem. Soc.* **1979**, *101*, 3157–3162.

[237] C. Engdahl, A. Gogoll, U. Edlund, *Magn. Reso. Chem.* **1991**, *29*, 54-62.

[238] T. Mochida, A. Izuoka, T. Sugawara, Y. Moritomo, Y. Tokura, *J. Am. Chem. Soc.* **1994**, *101*, 7971–7974.

[239] H. Ozeki, M. Takahashi, K. Okuyama, K. Kimura, *J. Chem. Phys.* **1993**, *99*, 56-66.

[240] K. L. Kunze, J. R. de la Vega, *J. Am. Chem. Soc.* **1984**, *106*, 6528–6533.

[241] K. Klauke, I. Gruber, T.-O. Knedel, L. Schmolke, J.Barthel, H. Breitzke, G. Buntkowsky, C. Janiak, *Organometallics* **2018**, *37*, 3, 298-308

[242] F. K. Merkt, S. P. Höwedes, C. F. Gers-Panther, I. Gruber, C.Janiak, T. J. J. Müller, *Chem.Eur.J.* **2018**, *24*, 8114–8125.

[243] G. Pescitelli, S. Lüdeke, A.-C. Chamayou, M. Marolt, V. Justus, M. Górecki, L. Arrico, L. Di Bari, M. A. Islam, I. Gruber, M.Enamullah, C. Janiak, *Inorg. Chem.* **2018**, *57*, 13397-13408.

[244] N. Breuer, I. Gruber, C. Janiak, T. J. J. Müller, Beilstein *J. Org. Chem.* **2019**, *15*, 2684–2703.

[245] R. Adams, C. Carson, J. Ward, R. Tannenbaum, W. Koros, *Micropor Mesopor Mater* **2010**, *131*, 13-20.

[246] A. Bos, I.G.M. Pünt, M. Wessling, H. Strathmann, *Sep. Purif. Technol.* **1998**, *14*, 27-39.

[247] G. Dong, H. Li, V. Chen, *J. Mater. Chem. A* **2013**, *1*, 4610-4630.

[248] R. C. Dutta, S. K. Bhatia, *J. Phys. Chem. C* **2020**, *124*, 594-604.

[249] Y. Lu, H. Zhang, J. Y. Chan, R.Ou, H.Zhu, M. Forsyth, E. M. Marijanovic, C. M. Doherty, P. J. Marriott, M. M. Banaszak Holl, H. Wang, *Angew. Chem. Int. Ed.* **2019**, *58*, 16928-16935.

[250] B. Zornoza, A. Martinez-Joaristi, P. Serra-Crespo, C. Tellez, J. Coronas, J. Gascon, F. Kapteijn, *Chem. Commun.* **2011**, *47*, 9522-9524.